

DISSERTATION

FEMTOSECOND TO NANOSECOND TRANSIENT ABSORPTION STUDIES OF AQUEOUS
SOLVATION AND DEPROTONATION DYNAMICS IN CONFINEMENT

Submitted by

Richard Leo Cole

Department of Chemistry

In partial fulfillment of the requirements

For the Degree of Doctor of Philosophy

Colorado State University

Fort Collins, Colorado

Summer 2011

Doctoral Committee:

Advisor: Nancy Levinger

Elliot Bernstein
Branka Ladanyi
Alan Van Orden
Randy Bartels

ABSTRACT

FEMTOSECOND TO NANOSECOND TRANSIENT ABSORPTION STUDIES OF AQUEOUS SOLVATION AND DEPROTONATION DYNAMICS IN CONFINEMENT

We explore the use of logarithmic based optical delay in time-resolved data collection. We show that logarithmic spacing of data points provides an economical way to collect data over many decades of time which speeds data collection. We present a simple algorithm to generate time delay points for application in time-resolved data collection. We test the use of logarithmic vs. linear data collection over six orders of magnitude by measuring broadband femtosecond transient absorption (BFTA) spectra of HPTS in pH-7 water from femtoseconds to nanoseconds. Statistical analysis of logarithmic and linear data collection show that linear data collection shows a clear advantage by requiring a fewer number of time-delay points to achieve a given precision in subsequent data analysis.

We investigate solvation dynamics (SD) via coumarin 343 (C343) in Aerosol OT (sodium bis(2-ethylhexyl) sulfosuccinate, AOT) reverse micelles with varying water content through broadband femtosecond transient absorption experiments. These studies build upon our previous studies of SD in the AOT reverse micelles through time-resolved fluorescence Stokes shift (TRFSS) experiments (*J. Phys. Chem. B*, **1998**, *102*,

2705) which limited data collection to approximately 100 ps. We extend the experimental time window to 2 nanoseconds and recover the entire solvation response. These results combined with steady-state spectra and reorientation dynamics indicate that C343 exists in two distinct populations within the reverse micelles which correlate with interfacial and core water. Our results suggest that translational motion of C343 may contribute to the total observed solvation response.

We study excited state proton transfer (ESPT) of HPTS (8-hydroxypyrene-1,3,6-trisulfonic acid trisodium salt) in cationic (cetyltrimethylammonium bromide, CTAB), anionic (AOT), and nonionic (polyoxyethylene (5) isooctylphenyl ether, IGE) reverse micelles by BFTA. For larger AOT RM, ESPT dynamics are found to be approximately equal to the dynamics found in bulk water. As the size of the AOT RM approaches the size of the probe molecule, ESPT becomes increasingly quenched. For all sizes of CTAB RM, HPTS ESPT is found to be 10-20 times slower than HPTS ESPT in bulk water. This result combined with reorientation measurements suggest that HPTS resides at the interfacial region in CTAB RM and thus remains immobilized. In IGE RM, ESPT is 4-10 times slower than bulk water behavior which we contribute to immobilization of HPTS in the micelle interface. HPTS reorientational motion is hindered with respect to bulk HPTS motion. We measure the kinetic isotope effect (KIE) on HPTS ESPT dynamics and results suggest that the solvent plays a significant role in the observed dynamics only in the largest IGE reverse micelles. Steady-state absorption measurements show that HPTS exists in a unique environment within IGE RM which contrasts with HPTS in other nonionic reverse micelle systems.

DEDICATION

I dedicate this dissertation to my dad, Roger William Cole. The pride and love in my accomplishments will never be forgotten.

ACKNOWLEDGEMENTS

First and foremost I would like to thank my wife, Jennifer, who kept me motivated to complete my thesis work and attack the daunting task of putting all of my work together into this thesis. She always kept me well fed and rested so I could focus and perform at my best. I never could have done it without you sweetie! I also would like to thank the many Levinger group members who I've worked and learned with during my studies at CSU including Bridget Gourley, Ruth Riter, Mariano Correa, Xihua Zhao, Laura Swafford, Mike Harpham, Ben Langdon, George Bullock, Myles Sedgwick, Colleen Woodward, Ben Wiebenga-Sanford, Ryan Trott, Ryan Davis, and Jessica Stover. Many stimulating and enlightening conversations have gotten me to this point. I also acknowledge extended family, both my wife's and my own, who have constantly supported me towards completing my graduate studies; they were always there especially when there seemed to be no light at the end of the tunnel. I thank my advisor Nancy Levinger whose enthusiasm about science has always been infectious. Finally, I thank anyone and everyone that has helped me in any way towards completing this work. It has been a long haul and I will never forget the support I have had from my family, friends, and colleagues to keep going forward. THANKS!

TABLE OF CONTENTS

ABSTRACT OF DISSERTATION.....	ii
DEDICATION.....	iv
ACKNOWLEDGEMENTS.....	v
TABLE OF CONTENTS.....	vi
LIST OF TABLES.....	x
LIST OF FIGURES.....	xii
LIST of ABBREVIATIONS.....	xvii
CHAPTER 1. INTRODUCTION.....	1
1. Motivation.....	1
2. Systems and Spectroscopic Probes.....	3
a. Reverse Micelles (RM).....	3
b. Spectroscopic Probe Molecules.....	7
i. C343 as a probe of solvation dynamics (SD).....	7
ii. HPTS as a probe of excited state proton transfer (ESPT).....	11
3. Time-Resolved Spectroscopic Techniques.....	13
a. Ultrafast Pulses.....	13
b. Spectral Dispersion.....	14
c. Dispersion Management.....	17
i. prism compressors.....	19
ii. grating compressors.....	23
iii. grating stretchers.....	24
d. Ultrafast Pump-Probe Spectroscopy.....	25
i. ultrafast pump-probe experiments.....	25
ii. broadband femtosecond transient absorption spectroscopy.....	26
References for Chapter 1.....	30
CHAPTER 2. EXPERIMENTAL METHODS	34
1. Laser System.....	34
a. Kerr-Lens Mode Locked Oscillator.....	34
b. Regenerative Amplifier.....	37
i. stretcher.....	37
ii. regenerative amplifier.....	40
iii. compressor.....	44
c. Laser System Diagnostics.....	46
i. intensity autocorrelation.....	48

	ii. frequency resolved optical gating (FROG).....	50
2.	Broadband Femtosecond Transient Absorption (BFTA) Apparatus.....	52
	a. Second Harmonic Generation (SHG).....	54
	b. White Light Continuum (WLC) Generation.....	55
	c. Pump/Probe Spatial Overlap.....	59
	d. Time-Delay Control.....	60
	e. Signal Modulation and Detection.....	61
	f. Polarization/Attenuation Control and Monitoring.....	62
3.	BFTA Data Collection.....	63
	a. MatLab Software.....	63
	i. time-delay stepping.....	63
	ii. spectra collection.....	65
	iii. signal averaging.....	67
	b. LabView Software.....	67
	c. Data Collection Operations.....	68
	i. signal optimization.....	68
	ii. time-zero determination.....	68
	iii. emission spectra.....	69
	iv. polarization anisotropy measurements.....	69
4.	Data Analysis Methods.....	70
	a. Lifetime Corrections.....	70
	b. Reorientation Dynamics.....	70
	c. Stokes Shift Dynamics.....	72
	i. spectral lineshape fitting method.....	73
	ii. spectral first derivative method.....	73
	iii. singular value decomposition (SVD) method.....	74
	d. Deprotonation Dynamics.....	75
	References for Chapter 2.....	76

CHAPTER 3.	Logarithmic Based Optical Delay for Time-Resolved Data Collection.....	78
1.	Introduction.....	79
2.	Logarithmic Based Delay Stepping.....	81
	a. Logarithmic Delay Algorithm.....	82
	b. Advantages and Limitations.....	83
	c. Statistical Analysis of Stepping Methods.....	91
3.	Sample Data.....	92
	a. Experimental Methods.....	93
	b. Multiple Timescale Transient Absorption Data.....	95
	c. Statistical Analysis of Collected Data.....	100
4.	Summary.....	102
	References for Chapter 3.....	103

CHAPTER 4. Femtosecond to nanosecond dynamics of confined

	coumarin 343 by transient absorption.....	105
1.	Introduction.....	106
2.	Experimental Methods.....	108
	a. Sample Preparation.....	108
	b. Transient Absorption Spectrometer.....	109
	c. Data Collection.....	110
	d. Data Analysis.....	111
	i. transient spectrograms.....	111
	ii. time-resolved anisotropy.....	113
3.	Results.....	114
	a. Steady-State Absorption and Emission.....	114
	b. Solvation Dynamics.....	116
	c. Time-resolved Anisotropy Measurements.....	122
4.	Discussion.....	125
5.	Summary and Conclusions.....	132
	References for Chapter 4.....	133
CHAPTER 5.	Deprotonation Dynamics of HPTS in Aqueous Cationic, Anionic, and Nonionic Reverse Micelles.....	138
1.	Introduction.....	138
2.	Experimental Methods.....	140
	a. Transient Absorption Spectrometer.....	140
	b. Data Collection.....	141
	c. Data Analysis.....	142
	i. reorientation dynamics.....	142
	ii. ESPT dynamics.....	143
	d. Sample Preparation.....	143
	i. reverse micelle samples.....	143
	ii. simulations of the IGE reverse micelle environment.....	144
3.	Results.....	145
	a. Steady-state Absorption and Emission.....	145
	b. Reorientation Dynamics.....	148
	c. ESPT Dynamics.....	148
	i. BFTA spectrograms.....	148
	ii. ESPT dynamics.....	153
	d. Simulating the IGE RM Environment.....	162
	i. HPTS in other neat nonionic surfactants.....	162
	ii. HPTS in hydrated tetraethylene glycol.....	162
	iii. HPTS in D ₂ O and D ₂ O/IGE/cyclohexane RM.....	165
4.	Discussion.....	165
5.	Summary.....	172
	References for Chapter 5.....	173
CHAPTER 6.	Summary and Concluding Remarks.....	177

References for Chapter 6.....	179
APPENDIX A. Source Code for Data Collection and Analysis.....	180
1. Data Collection Functions.....	180
2. Ocean Optics Spectrometer Functions.....	182
3. Physik Instrumente Translation Stage Functions.....	185
4. Data Processing Functions.....	189
APPENDIX B. Supplemental Materials.....	204
1. Analysis of C343 BFTA Data.....	204
2. Steady-state Emission of HPTS in D ₂ O/IGE/cyclohexane RM.....	206
References for Appendix B.....	207
APPENDIX C. Independent Research Proposal.....	208
1. Abstract and Specific Aims.....	208
2. Background and Motivation.....	209
a. Biological energy transport mechanisms.....	209
b. Vibrational soliton theory.....	210
c. Experimental evidence for vibrational solitons.....	213
i. Steady-state infrared spectra.....	214
ii. IR pump-probe experiments.....	219
3. Proposed Research.....	226
4. Research Methods.....	229
a. Characterization of soliton formation.....	229
b. Characterization of soliton propagation.....	232
References for Appendix C.....	238

LIST OF TABLES

Table 1.1	Commonly used pulse shapes.....	15
Table 1.2	Calculated spectral dispersion coefficients for common optical materials.....	18
Table 2.1	Laser system diagnostics.....	46
Table 3.1	Analysis of the statistical “efficiency” of HPTS/pH-7 water deprotonation fitted parameters.....	101
Table 4.1	AOT/cyclohexane/water reverse micelle water pool diameters, estimated number of water molecules per micelle, absorption/emission maxima, and calculated Stokes shifts for C343 in bulk (acidic, basic) water and in AOT RM.....	117
Table 4.2	Multi-exponential fit parameters from equation 4.11 to time-dependent spectral shifts of the broadband femtosecond transient absorption stimulated emission band maximum of C343 in bulk water and in cyclohexane/AOT/water reverse micelles.....	121
Table 4.3	Single exponential, double exponential and wobble-in-a-cone parameters to measured C343 anisotropy curves in bulk water and in cyclohexane/AOT/water reverse micelles.....	124
Table 5.1	Biexponential fit parameters to reorientation decays of HPTS in cationic, nonionic, and anionic RM systems and in bulk water.....	151

Table 5.2	Multi-exponential fitted parameters 560 nm BFTA traces of HPTS in CTAB, IGE, and AOT RM systems and in bulk water.....	157
Table 5.3	Biexponential fitted parameters to integrated BFTA spectra of HPTS in CTAB, IGE, AOT RM systems and in bulk water.....	161
Table 5.4	Biexponential fit parameters to integrated BFTA spectra of HPTS in IGE RM systems formed with water and D ₂ O and in bulk water and D ₂ O.....	168
Table B.1	Multi-exponential fitted parameters to time-dependent spectral shifts of the BFTA signal maximum, stimulated emission maximum, and the first spectral moment of the SE band of C343 in bulk water and in cyclohexane/AOT/water reverse micelles.....	205
Table C.1	Amide bands of polypeptides.....	215

LIST OF FIGURES

Figure 1.1	Reverse micelle (RM) and lipid bilayer structures.....	4
Figure 1.2	Structure of surfactant molecules AOT, CTAB, and IGE.....	6
Figure 1.3	Spectroscopic probes C343 (coumarin 343) and HPTS	8
Figure 1.4	Schematic description of solvation dynamics (SD).....	9
Figure 1.5	Schematic description of intermolecular excited-state proton transfer...12	
Figure 1.6	Bandwidth in nanometers ($\Delta\lambda_p$) needed to support 800 nm, sub-100 fs pulses for common pulse profiles.....	15
Figure 1.7	Basic configurations for prism compressors, grating compressors, and grating stretching.....	20
Figure 1.8	Basic pump-probe experimental design.....	27
Figure 1.9	Energy level diagram for a one state (no excited state transfer processes) probed by BFTA spectroscopy.....	29
Figure 2.1	Basic components of a chirped pulse amplification laser system.....	35
Figure 2.2	Schematic of the KM Labs TS (KML-TS) laser.....	36
Figure 2.3	Schematic of the Clark MXR CPA-1000 (CPA-1000) stretcher.....	38
Figure 2.4	Schematic of the Clark MXR CPA-1000 (CPA-1000) amplifier.....	41

Figure 2.5	Timing of high voltage pulses applied to the Pockels cell (PC) and their effect in the CPA-1000 amplification cavity.....	43
Figure 2.6	Schematic of the Clark MXR CPA-1000 (CPA-1000) grating compressor..	45
Figure 2.7	Schematic of the second harmonic frequency resolved optical gating (SH-FROG) instrument used to measure pulse autocorrelation and FROG traces.....	49
Figure 2.8	Typical SH-FROG spectrogram and intensity autocorrelation trace recorded for the CPA-1000 laser system.....	51
Figure 2.9	Broadband femtosecond transient absorption (BFTA) instrument.....	53
Figure 2.10	Detailed schematic of white light generation (WLG) and detection Within the broadband femtosecond transient absorption (BFTA) instrument.....	56
Figure 3.1	Comparison of logarithmic stepping vs. linear stepping for a simulated observable.....	84
Figure 3.2	Logarithmic stepping value plotted as function of relative index.....	86
Figure 3.3	Logarithmic stepping value plotted as a function of the data point index.....	88
Figure 3.4	Uncorrected vs. linear corrected logarithmic stepping values.....	90
Figure 3.5	Linear and logarithmic broadband ultrafast transient absorption spectrograms of HPTS in pH-7 water.....	96
Figure 3.6	Extracted deprotonation dynamics from HPTS/pH-7 water transient absorption data collected with linear and logarithmic stepping.....	98

Figure 3.7	Extracted Stokes shift dynamics from HPTS/pH-7 water transient absorption data collected with linear and logarithmic stepping.....	99
Figure 4.1	Absorption (a) and emission (b) of C343 in water/AOT/cyclohexane reverse micelles.....	115
Figure 4.2	Broadband femtosecond transient absorption spectrograms of C343 in bulk water and water/AOT/cyclohexane reverse micelles.....	119
Figure 4.3	Normalized time-dependent spectral shift of the stimulated emission band of C343 in bulk water and in water/AOT/cyclohexane reverse micelles.....	120
Figure 4.4	Time-resolved anisotropy decays for C343 in water and in cyclohexane/AOT/water reverse micelles.....	123
Figure 4.5	Ratio of the interfacial population of C343 to interior population of C343 in water/AOT/cyclohexane RM as a function of w_0	131
Figure 5.1	Comparison of UV-Vis absorption of HPTS in CTAB/water/1-octanol/cyclohexane (top), IGE/water/cyclohexane (middle), and AOT/water/cyclohexane (bottom) reverse micelles.....	146
Figure 5.2	Comparison of steady-state fluorescence of HPTS in CTAB/water/1-octanol/cyclohexane (top), IGE/water/cyclohexane (middle), and AOT/water/cyclohexane (bottom) reverse micelles.....	147
Figure 5.3	Comparison of HPTS anisotropy decays in largest CTAB, IGE, AOT RM investigated and in bulk water.....	149

Figure 5.4	Comparison of HPTS anisotropy decays in CTAB (top), IGE (middle), and AOT (bottom) reverse micelles (RM) systems and in bulk water.....	150
Figure 5.5	Comparison of BFTA spectrograms of HPTS in the largest CTAB, IGE, AOT RM investigated and in bulk water.....	152
Figure 5.6	Comparison of BFTA spectrograms of HPTS in water/AOT/cyclohexane reverse micelles (RM).....	154
Figure 5.7	Comparison of BFTA spectrograms of HPTS in water/IGE/cyclohexane reverse micelles (RM).....	155
Figure 5.8	Comparison of BFTA spectrograms of HPTS in water/CTAB/1-octanol/cyclohexane reverse micelles (RM).....	156
Figure 5.9	Comparison of HPTS spectrally integrated signals in the largest CTAB, IGE AOT RM investigated.....	159
Figure 5.10	Absorption spectrum of HPTS in (a) neat BRIJ-30, Triton X-100, and IGE nonionic surfactants, (b) in neat IGE and IGE dispersed in cyclohexane, and (c) HPTS and MPTS in IGE in cyclohexane.....	163
Figure 5.11	Absorption spectra of HPTS in tetraethylene glycol/water (TEG:water) binary mixtures, in neat TEG, and in slightly acidic water pH = 6.5.....	164
Figure B.1	Steady-state emission from HPTS in D ₂ O/IGE/cyclohexane reverse micelles and in D ₂ O.....	206
Figure C.1	Energy level diagram for the refined vibrational soliton theory.....	211
Figure C.2	Comparison of the peptide geometry in ACN and in polypeptides.....	216

Figure C.3	Temperature dependent IR absorption spectra of crystalline ACN in the amide-I region.....	217
Figure C.4	Temperature-squared analysis of ACN amide-I anomalous band at 1650 cm^{-1} and Trp(Ala) ₁₅ amide-A anomalous band at 3195 cm^{-1}	220
Figure C.5	(a) Absorption spectrum of the NH band of crystalline ACN. The inset schematically depicts the one dimensional chain of hydrogen bonded ACN molecules. (b) The proposed scheme of potential energy surfaces with the allowed transitions depicted.....	222
Figure C.6	Fourier transform spectra of the coherent response ACN after impulsive excitation.....	223
Figure C.7	(a) Absorption spectra of PBLG in chloroform with 3% TFA at 293 K (red line, helical conformation), and at 260 K (blue line, random coil). (b) Pump-probe spectra 600 fs after excitation under the same conditions.....	225
Figure C.8	Proposed model α -helix system.....	228
Figure C.9	Simulated pump-probe data based on helical PBLG IR pump-probe data.....	231
Figure C.10	¹³ C ¹⁸ O amide-I isotopic shift.....	234
Figure C.11	2DIR pulse sequence.....	235
Figure C.12	Simulated DF-2DIR spectrum.....	237

LIST OF ABBREVIATIONS

AOT	sodium (2-ethylhexyl) sulfosuccinate, anionic surfactant
BBO	β -barium borate
BFTA	broadband femtosecond transient absorption
BL	bleach
CaF ₂	calcium fluoride
CPA	chirped pulse amplification
CPA-1000	Clark MXR Model CPA-1000 regenerative amplifier laser
CTAB	cetyl trimethylammonium bromide, cationic surfactant
CW	continuous wave
C343	coumarin 343, SD probe molecule
DS	optical delay stage
ESA	excited state absorption
ESPT	excited state proton transfer
FOD	fourth-order dispersion
FROG	frequency resolved optical gating
FWHM	full width at half of maximum
GVD	group velocity dispersion
HPTS	8-hydroxypyrene-1,3,6-trisulfonic acid, ESPT probe molecule

HR	high reflector
IGE	polyoxyethylene (5) nonylphenylether, nonionic surfactant
IVR	intramolecular vibrational relaxation or redistribution
KML-TS	Kapteyn-Murnane Laboratories titanium sapphire laser
LP-S	Lighthouse Photonics Sprout laser
ML	mode locked
NL	non-linear
OC	output coupler
OO-S	Ocean Optics USB2000+ fiber optic spectrometer
PCGP	principle component generalized projection
PD	photodiode
PEM	proton exchange membrane
POL	linear polarizer
Q-527	Quantronix Nd:YLF pump laser
RM	reverse micelle
SD	solvation dynamics
SE	stimulated emission
SH-FROG	second harmonic frequency resolved optical gating
SHG	second harmonic generation
SPF	short pass filter
TA	transient absorption
TOD	third-order dispersion

TRFSS	time-resolved fluorescence stokes shift
Tsap	titanium doped sapphire
WLC	white light continuum
WP	$\lambda/2$ wave plate

CHAPTER 1

INTRODUCTION

1.1 Motivation

Water is life as we know it, and to understand water behavior is to unlock one of nature's most fundamental elements. No other solvent exhibits such unique macroscopic and microscopic properties which facilitate such a wide variety of natural and synthetic processes.¹ For a host of these processes, water finds itself geometrically confined within nanometer (10^{-9} meters) volumes which can alter its already unique behavior. It has been well established in the literature that water behavior under nanoscopic confinement can deviate strongly from bulk water behavior due to the close proximity of interfaces both natural and synthetic.²⁻⁵ In particular, these confinement-induced deviations from bulk behavior can have dramatic effects on physical, chemical, and biological processes such as electron transfer^{6,7}, proton transfer^{8,9}, and mass transport.^{10,11} Thus, understanding behavior of nanoscopically confined water is a first step towards unraveling and potentially controlling physical, chemical and biological phenomena. Results from studies of solvent behavior in nanoscopic confinement have direct impact on future science and engineering endeavors from biology to material synthesis.

The broad aim of the work in this dissertation is focused on understanding how

polar solvents, namely water, behave differently in confinement and, in turn, how they can affect chemical and biological processes. In an effort to generate fundamental information on confinement effects on polar solvents, we have chosen the model class of systems known as reverse micelles (RM) which contain nanoscopic pools of polar solvents. RM have found use in range of fields from biology as simplified mimics of lipid bilayers¹⁰⁻¹² to material science applications in semiconductor and metal nanoparticle synthesis^{11,13-16} to chemistry as “nanobeakers”.¹⁷

The studies presented hereafter utilize time-resolved spectroscopy to probe solvent and proton transfer dynamics in nanoscopic confined water. We use broadband femtosecond transient absorption (BFTA) spectroscopy in combination with the spectroscopic probes coumarin 343 (C343) and 8-hydroxypyrene-1,3,6-trisulfonic acid trisodium salt (HPTS) to probe solvation and proton transfer dynamics within RM systems. Further details about these probes will be outlined in the following section, but both of these probes have been used extensively to probe ultrafast water dynamics in a variety of systems.¹⁸⁻³¹ Studies using C343¹⁸⁻²³ and HPTS^{21,24-31} have yielded great insight into environmental impacts on fundamental processes of solvation and proton transfer dynamics which makes them excellent candidates for RM confinement studies.

BFTA spectroscopy supplements and complements previous time-resolved fluorescence Stokes shift (TRFSS) spectroscopic studies of water dynamics in RM confinement conducted in the Levinger laboratory.^{23,32-35} These TRFSS studies have focused on femtosecond dynamics while the BFTA studies expand our dynamical analysis over a two nanosecond window e.g. from femtoseconds to nanoseconds.

Exploring dynamics over this longer timescale has given a more complete and comprehensive picture of RM confinement dynamics.

1.2 Systems and Spectroscopic Probes

1.2.a Reverse Micelles (RM)

RM are a model class of systems that generate nanoscopic volumes of polar solvents. RM consist of a nanoscopic pool of polar solvent that is sequestered by surfactant molecules surrounded by a bulk non-polar solvent as illustrated in Figure 1.1. RM can be considered to be a simplified mimic of biological systems as the interior is analogous to a lipid/water interface found in cells. The size of the RM polar solvent pool, or more importantly the degree of confinement, is controlled by adjusting the ratio of surfactant to polar solvent concentrations,

$$w_0 = \frac{[\text{polar solvent}]}{[\text{surfactant}]}. \quad (1.1)$$

For spherical RM, w_0 is proportional to the micelle diameter.

The effective w_0 range generating stable RM microemulsions is determined by the supporting non-polar solvent, polar solvent, and the surfactants and/or co-surfactants employed. Common non-polar solvents used to prepare RM include cyclohexane, *n*-heptanes, *n*-hexanes, *iso*-octane, carbon tetrachloride, and benzene. The polar head groups of surfactants are classified as anionic, cationic, and nonionic. We have chosen a surfactant from each of these groups to explore RM system differences and similarities. Accordingly, our studies employ the surfactants sodium bis(2-

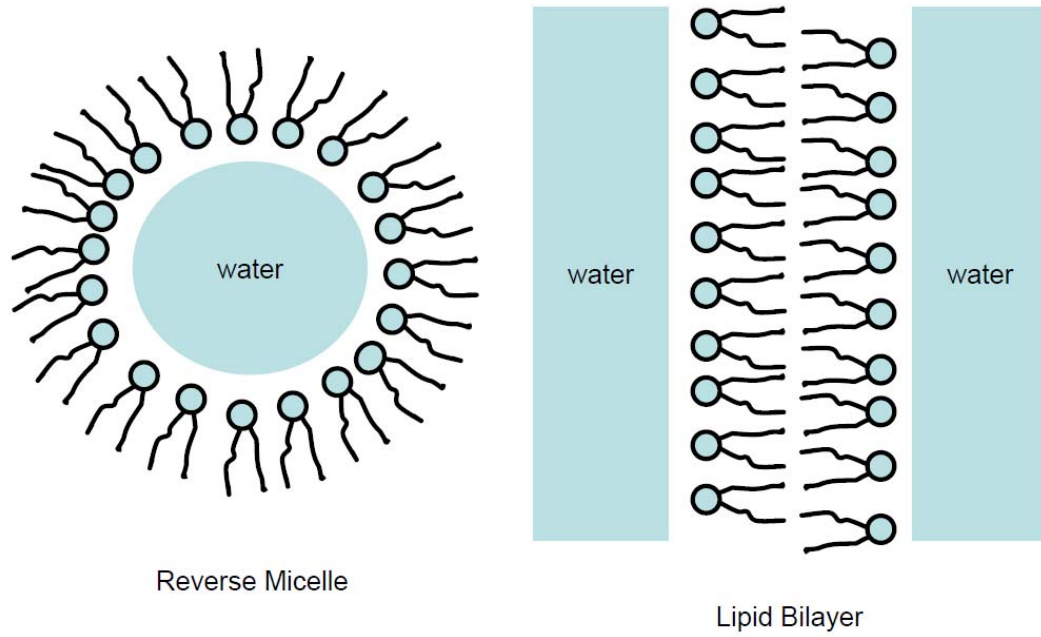


Figure 1.1 Reverse micelle (RM) and lipid bilayer structures. The interior of the RM is similar to a lipid/water interface found in biological systems.

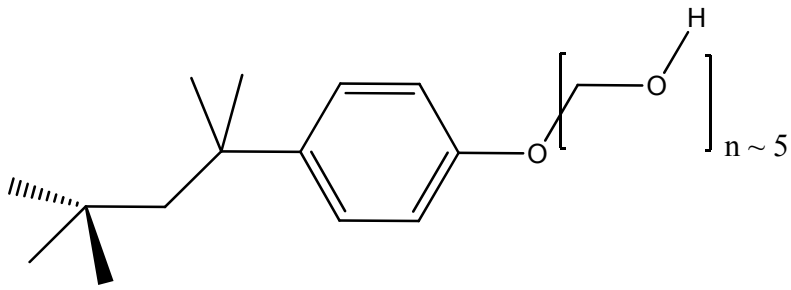
ethylhexyl) sulfosuccinate (AOT), cetyl trimethylammonium bromide (CTAB), and polyoxyethylene (5) nonylphenylether (IGE) which are classified as anionic, cationic, and non-ionic respectively. The structures for these surfactants are shown in Figure 1.2. It is important to note that some surfactants require the addition of a co-surfactant to stabilize RM formation; this is the case for CTAB which requires the addition of a co-surfactant, usually a long-chain alcohol, in the ratio of approximately 5:1 (alcohol:CTAB). Typical alcohols used as CTAB co-surfactants are straight chain 1-decanol, 1-octanol, 1-heptanol, and 1-hexanol.³⁶

Two important values that characterize RM systems are the diameter of the water pool (d) and the surfactant aggregation number (N_{ag}). Reports in the literature have established linear relationships between w_0 and water pool diameters over various w_0 ranges for AOT,³⁷ and IGE³⁸ RM systems through viscosity, dynamics light scattering and small angle neutron scattering (SANS) measurements. These linear relationships and limits are^{39,40},

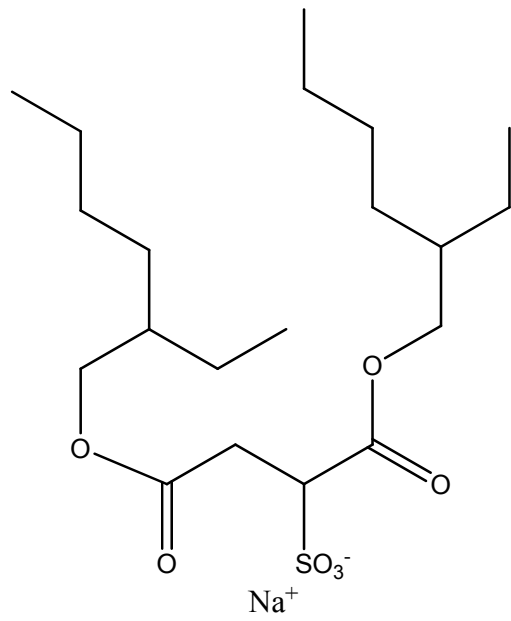
$$d_{AOT} = 0.29\omega_0 + 1.1 \quad 2 \leq \omega_0 \leq 20 \quad (1.2)$$

$$d_{IGE} = 0.38\omega_0 + 1.40 \quad 10 \leq \omega_0 \leq 40. \quad (1.3)$$

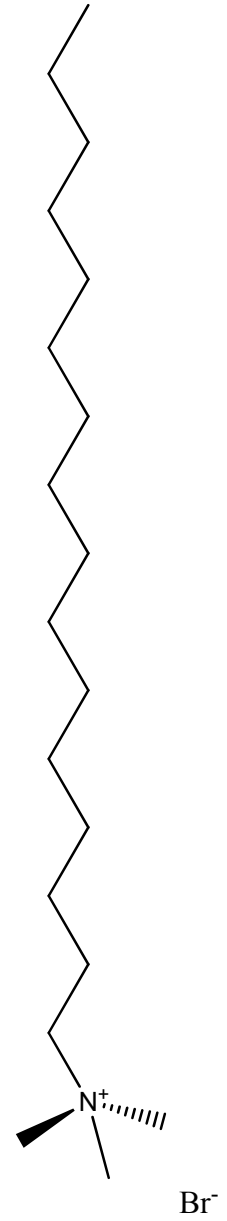
In addition to these measured relationships, mean surfactant aggregation numbers (N , surfactant molecules per RM) have been reported for AOT RM⁴¹, CTAB RM, and IGE RM⁴²⁻⁴⁴ for a variety of w_0 values. In general, N_{ag} increases with w_0 as the surface area of the micelle increases. We use N_{ag} to estimate the number of probe molecules per micelle. Typically the concentration of probe molecules per RM is kept close to unity to



IGE



AOT



CTAB

Figure 1.2 Structure of surfactant molecules AOT, CTAB, and IGE.

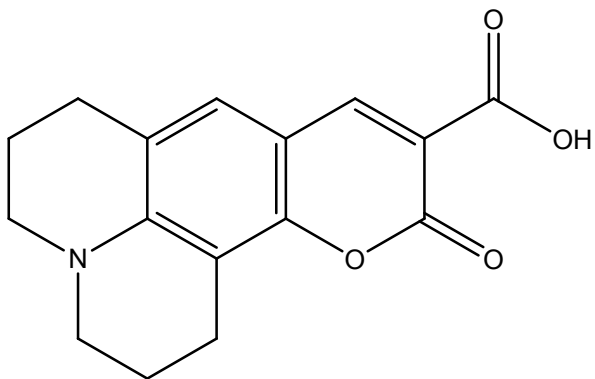
maximize signal intensities and minimize probe-probe molecule interactions. For the studies reported within chapters 4 and 5, we use these established literature values for d and N_{ag} to describe RM microemulsions that were prepared unless otherwise noted.

1.2.b Spectroscopic Probe Molecules

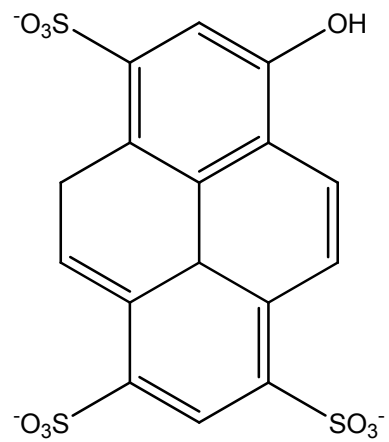
Pump-probe experiments such as the ones later outlined in this work rely on the presence of time-dependent signals following excitation. Time-dependent signals of this type are governed by excited-state processes such as solvation dynamics (SD), excited-state proton transfer (ESPT) dynamics, and inter/intramolecular electron transfer dynamics. The net effect of such processes alters the spectrum of the probe molecule and subsequent analysis of these spectral changes reveals the underlying dynamics of the process itself. The following sections outline the fundamental principles of SD and ESPT and our selection of C343 and HPTS (structures shown in Figure 1.3) to probe these processes in RM systems.

1.2.b.i C343 as a probe of solvation dynamics (SD)

Solvation dynamics (SD) is the response of a solvent to an instantaneous change in the charge distribution on a solvated chromophore upon excitation from the ground electronic state (S_0) to a higher electronic state (S_n). The dynamics represent the relaxation of the solvent to the new charge distribution that lowers the free energy of the excited chromophore. Figure 1.4 gives a schematic representation of the SD process. For chromophores solvated in bulk polar solvents, two types of motion are inherent in SD relaxation: a faster inertial and a slower diffusive motion. The inertial response generally corresponds to individual solvent molecule motion whereas the



C343



HPTS

Figure 1.3 Spectroscopic probes C343 (coumarin 343) and HPTS (8-hydroxypyrene-1,3,6-trisulfonic acid).

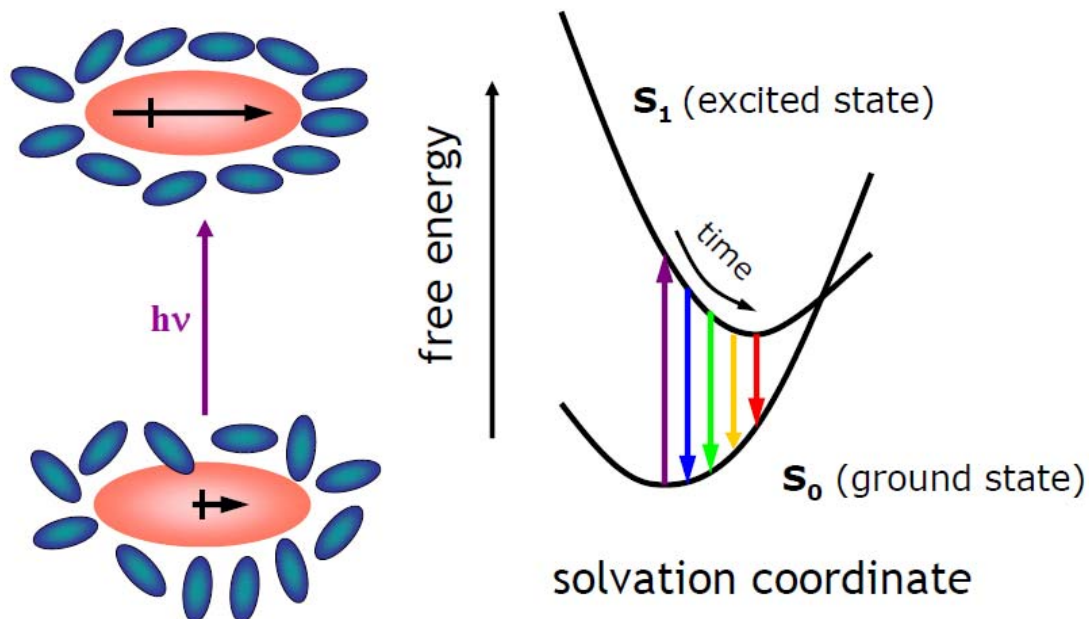


Figure 1.4 Schematic description of solvation dynamics (SD). After excitation of the chromophore, the solvent reorients to lower the free energy of the system in response to the new excited-state charge distribution on the chromophore. This motion on the S_1 surface is reflected in a red shift in the emission (or stimulated emission) spectrum of the chromophore as a function of time.

diffusive response corresponds to collective solvent motion. Intramolecular vibrational relaxation or redistribution (IVR) of the chromophore can also contribute to lowering and modulating the energy of the excited chromophore.⁴⁵ Usually, a chromophore is chosen that has very little structural changes between the S_0 and the S_1 electronic states and thus strong contributions from IVR are typically negligible. The normalized free energy change due to SD is calculated as,

$$S(t) = \frac{\Delta\bar{E}(t) - \Delta\bar{E}(\infty)}{\Delta\bar{E}(0) - \Delta\bar{E}(\infty)} \cong \frac{\nu(t) - \nu(\infty)}{\nu(0) - \nu(\infty)} \quad (1.4)$$

where the average free energy change ($\Delta\bar{E}$) is assumed to be proportional to a spectroscopic observable (ν) such as the frequency of the maximum of the time-dependent chromophore emission spectrum.

Coumarin molecules, such as C343, are ideal probes for SD experiments as they exhibit large dipole changes between the ground (S_0) and first excited (S_1) electronic states and they are rigid molecules.⁴⁶ The magnitude of the dipole change between the S_0 and S_1 states effectively governs the magnitude of the SD response and for C343, the estimated 2.5 Debye change gives a strong, measurable SD signal.⁴⁷ As previously mentioned, IVR contributions to SD are minimized with rigid molecules but conformational motion of the probe molecule is minimized in the SD response as well. For the goals of our SD experiments, we aim to measure just the SD response from solvent motion and the measurement of probe molecule conformational changes due to its inherent physical flexibility (non-rigidity) are unwanted. Thus C343 is a prime

candidate for SD studies of water in RM systems due to its large dipole change upon excitation and its structural rigidity.

1.2.b.ii HPTS as a probe of excited-state proton transfer (ESPT)

Excited-state proton transfer (ESPT) describes proton transfer to, from, or within a molecule that is initiated by the transition to an excited electronic state.⁴⁸ Our discussion focuses on intermolecular ESPT where excitation is photoinitiated. Intermolecular ESPT is a solvent assisted process it is primarily observed only in aqueous systems. Electronic excitation of molecules exhibiting ESPT phenomena are driven by a pK_a jump from the ground state to the excited state. In this case, a particular ESPT molecule becomes a stronger acid upon photoexcitation and the molecule is described as a photo-acid. Thus an ESPT molecule at neutral pH may be protonated in the ground state (ROH) but become deprotonated in the excited state (RO^{*-}) due to the photo initiated pK_a jump, ΔpK_a . Figure 1.5 shows a schematic representation of the intermolecular ESPT process. It is important to note that deprotonation rates are reversible and pH dependent; the steady-state pH of the solvent affects the forward dissociation reaction as well as the reverse recombination reaction.

Time-dependent HPTS spectra display both solvation dynamics and deprotonation dynamics.^{24-26,30} Solvation dynamics manifest as a time-dependent spectral shift that relaxes with a time constant of roughly 1 ps for the HPTS/water system. HPTS is an ideal probe of deprotonation dynamics due to the large magnitude of ΔpK_a which jumps from 7.7 to approximately 1^{49,50} upon excitation of the protonated

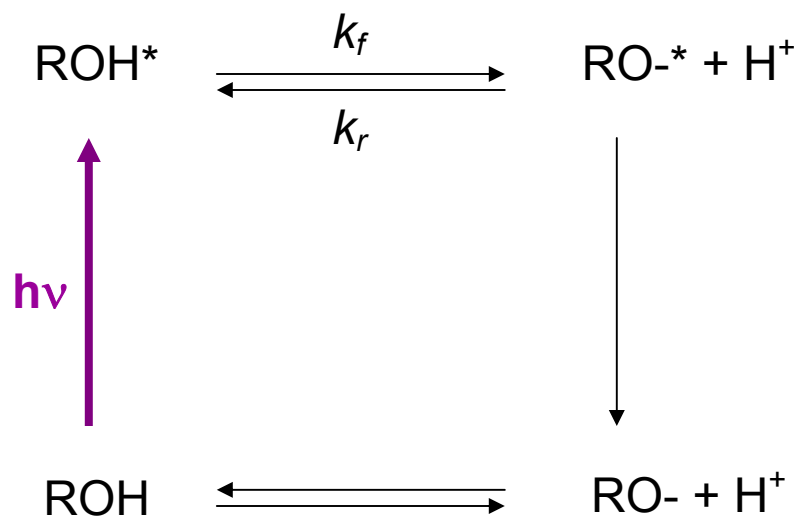
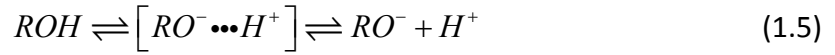


Figure 1.5 Schematic description of intermolecular excited-state proton transfer (ESPT). Photo excitation from the ground electronic state initiates excited state transfer of a proton to the solvent. The observed deprotonation rate depends on forward and backward rate constants which are pH dependent.

state (ROH) which initiates the deprotonation reaction. HPTS deprotonation dynamics follow the mechanism,



where the initial step generates a contact ion pair followed by subsequent diffusion of the proton away from the excited HPTS molecule (ROH^*). Both mechanistic steps depend on the bulk proton concentration which lead to pH dependent deprotonation dynamics. In neutral water (pH=7), the first step in the HPTS deprotonation mechanism occurs on the 2-4 ps timescale while the proton diffusion step occurs on the ~90 ps timescale²⁴⁻²⁶.

1.3 Time-Resolved Spectroscopic Techniques

1.3.a Ultrafast Pulses

Ultrafast pulses are generally considered pulses that have subnanosecond durations ($< 10^{-9}$ seconds) e.g. picoseconds or shorter. Ultrafast pulses are described in the time-domain as,

$$E(t) = A(t) \exp[-i(\omega - \omega_0)t] \exp[\phi(t)] \quad (1.6)$$

where $A(t)$ is the pulse envelope, ω_0 is the carrier oscillation frequency, and $\phi(t)$ is the temporal phase. In this description, the pulse envelope is decoupled from the electric-field oscillations for pulse durations longer than a few optical cycles which is known as the slowly varying envelope approximation.⁵¹ Conversion between the time- and frequency-domains is obtained through the Fourier transform pairs,

$$\tilde{E}(\omega) \sim \int_{-\infty}^{\infty} \tilde{E}(t) \exp[-i\omega t] dt \quad (1.7)$$

$$\tilde{E}(t) \sim \int_{-\infty}^{\infty} \tilde{E}(\omega) \exp[i\omega t] d\omega \quad (1.8)$$

Table 1.1 gives common pulse shapes for $A(t)$ and the corresponding spectral shapes obtained from Fourier transform to the frequency domain, full width at half maximum (FWHM) in both the temporal and spectral domains. The temporal FWHM and spectral FWHM are related through the time-bandwidth product defined as,

$$c_B \geq \Delta\nu_p \cdot \tau_p$$

where the minimum c_B value indicates that a pulse is Fourier transform-limited which is the shortest pulse achievable from a given bandwidth. The pulse shape dictates the minimum value of c_B , and the inverse relation between $\Delta\nu_p$ and τ_p makes an increasing amount of spectral bandwidth a requirement for supporting shorter and shorter pulses. This effect is a result of the Heisenberg uncertainty principle and becomes quite dramatic for sub-100 fs pulse durations. Figure 1.6 plots the required bandwidth to support sub-100 fs pulses centered at 800 nm with Gaussian, Lorentzian, and hyperbolic secant squared (sech^2) pulse profiles.

1.3.b Spectral Dispersion

As previously established, ultrafast pulses require increasing bandwidths to support decreasing duration pulses and consequently frequency dependent delay variations or spectral dispersion will affect ultrafast pulse durations. Thus it is critical to account for spectral dispersion in a given optical system.⁵² In most time-resolved

Table 1.1 Commonly used pulse shapes⁵³.

pulse shape	temporal-domain		spectral-domain		time-bandwidth product (c_B)
	$A(t)$	FWHM (τ_p)	$A(\omega)$	FWHM ($\Delta\omega_p$)	
Gaussian	$\exp[-2(t/\tau_G)^2]$	$1.177 \tau_G$	$\exp[-(\Omega\tau_G)^2/2]$	$2.355/\tau_G$	0.441
Lorentzian	$[1 + (t/\tau_L)^2]^{-2}$	$1.287 \tau_L$	$\exp[-2 \Omega \tau_L]$	$0.693/\tau_L$	0.142
sech^2	$\text{sech}^2(t/\tau_S)$	$1.763 \tau_S$	$\text{sech}^2(\pi\Omega\tau_S/2)$	$1.122/\tau_S$	0.315

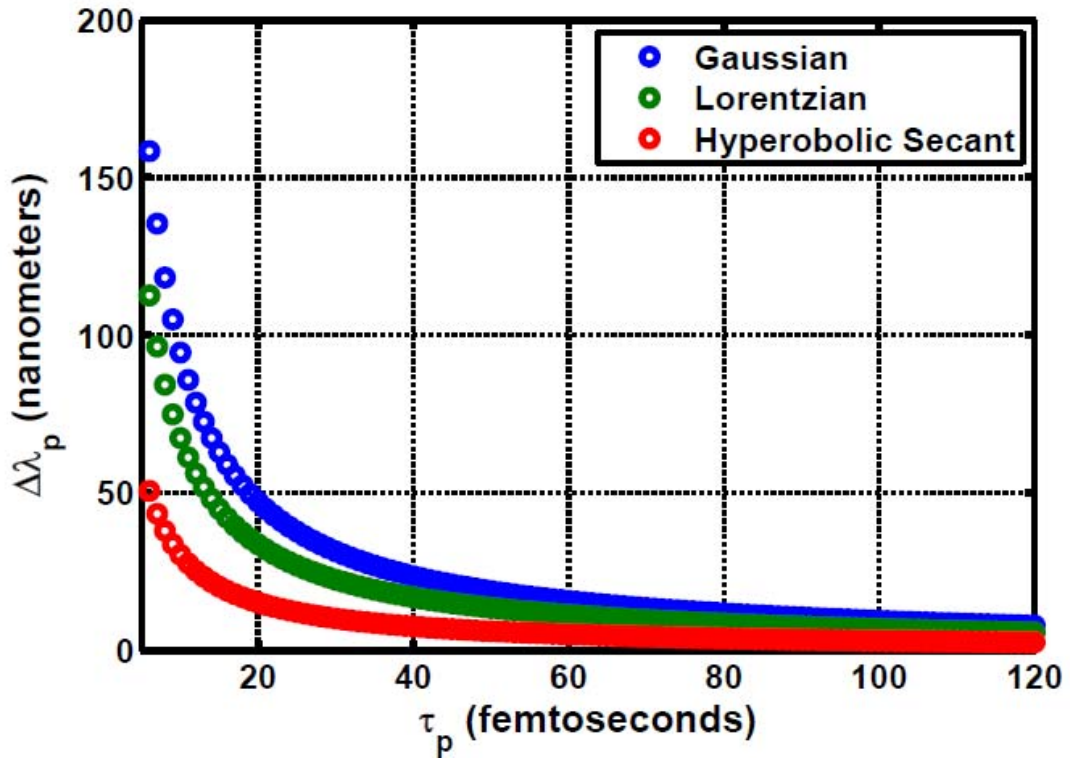


Figure 1.6 Bandwidth in nanometers ($\Delta\lambda_p$) needed to support 800 nm, sub-100 fs pulses for common pulse profiles. Note that for a given bandwidth the transform-limited pulse duration depends on the assumed pulse shape.

spectroscopy applications, it is desirable to deliver the shortest achievable pulse to a sample and therefore spectral dispersion modeling and compensation thereof are essential.

Spectral dispersion is a manifestation of the frequency-dependent refractive index (material dispersion) but it can also be imposed on an ultrafast pulse through angular dispersion introduced by a prism or grating (geometric dispersion). Geometric dispersion will be discussed further in section 1.3.iii. In most cases, the material dispersion accumulated by a pulse in an optical system is compensated for by geometric dispersion of the opposite sign, but in some cases dispersion is added and subtracted geometrically as in chirped pulse amplification (CPA). The amount of material dispersion incurred in an optical system depends on propagation distances and types of materials that a pulse travels through and is given as,

$$\varphi_m(\omega) = \frac{\omega}{c} n(\omega)L \quad (1.9)$$

where ω is frequency, c is the speed of light in a vacuum, L is the length of the material, and $n(\omega)$ is the frequency-dependent refractive index. $n(\omega)$ is usually described via the Sellmeier equation,

$$n^2(\omega) + 1 = \sum_i \frac{B_i}{\omega_i^2 - \omega^2} \quad (1.10)$$

where B_i and ω_i are constants that have been determined experimentally for most optical materials. Spectral dispersion is modeled as a Taylor expansion with respect to the carrier frequency of a pulse (ω_0) of the form,

$$\varphi(\omega) = \sum_n \frac{1}{n!} \varphi^{(n)} \Big|_{\omega_0} (\omega - \omega_0)^n \quad (1.11)$$

where $\varphi^{(n)} \Big|_{\omega_0}$ is the n^{th} derivative of $\varphi(\omega)$ evaluated at ω_0 . The sign of $\varphi^{(n)} \Big|_{\omega_0}$ determines whether the dispersion is considered positive or negative and relative contributions for each term typically decrease by an order of magnitude as n increases. The zero-order and first-order spectral phase have meaning only for the carrier frequency ω_0 and thus they can be neglected in most spectral dispersion calculations. Second-order dispersion also called group velocity dispersion (GVD) is the dominant factor in spectral dispersion with third-order dispersion (TOD) and fourth-order dispersion (FOD) considered cubic and quartic errors, respectively. The sign of GVD has a simple interpretation: positive GVD means that low frequencies (red wavelengths) travel faster through a material than high frequencies (blue wavelengths) while negative GVD means that high frequencies (blue wavelengths) travel faster through a material than low frequencies (red wavelengths). Normal material GVD is positive with negative material GVD rare and considered anomalous. Table 1.2 compiles GVD, TOD, and FOD coefficients for some common optical materials at 800 and 400 nm, the fundamental and second harmonic of the Ti:sapphire laser output, wavelengths relevant to the studies presented here.

1.3.c Dispersion Management

A variety of methods using angular dispersion have been developed that allow spectral dispersion to be managed.⁵¹⁻⁵³ There are two important applications of dispersion management: (1) material dispersion incurred in ultrafast experiments, and

Table 1.2 Calculated spectral dispersion coefficients for common optical materials. These values were calculated from the Sellmeier equation (Equation 1.10) and the resultant spectral phase was calculated from Equation 1.9. Taylor expansion coefficients in Equation 1.11 were calculated as $\varphi^{(n)}|_{\omega_0}$ or $n^{(n)}|_{\omega_0}$ for GVD, TOD, and FOD or $dn/d\lambda$, $d^2n/d\lambda^2$, $d^3n/d\lambda^3$, and $d^4n/d\lambda^4$ respectively.

optical material	λ (nm)	n	$dn/d\lambda$ (1/ μm)	$d^2n/d\lambda^2$ (1/ μm^2)	$d^3n/d\lambda^3$ (1/ μm^3)	$d^4n/d\lambda^4$ (1/ μm^4)	GVD (fs ² /mm)	TOD (fs ³ /mm)	FOD (fs ⁴ /mm)
BK7	800	1.511	-0.0198	0.0492	-0.2887	1.8618	44.59	32.04	-10.56
	400	1.531	-0.1332	1.0766	-12.31	179.6	121.87	40.71	11.58
fused silica	800	1.453	-0.0173	0.0399	-0.2386	1.5293	36.11	27.44	-11.40
	400	1.470	-0.1091	0.8607	-9.60	135.3	97.43	30.20	6.52
CaF ₂	800	1.411	-0.0098	0.0282	-0.1556	0.9952	25.58	15.31	-3.27
	400	1.422	-0.0699	0.5501	-5.99	82.4	62.27	17.91	3.19
sapphire (ordinary)	800	1.569	-0.0281	0.0992	-0.5267	3.3976	89.84	47.69	-0.97
	400	1.603	-0.2393	1.9834	-22.56	327.4	224.53	73.91	20.40
sapphire (extrodinary)	800	1.752	-0.0264	0.0624	-0.3684	2.3638	56.57	41.32	-15.50
	400	1.778	-0.1683	1.3258	-14.73	207.2	150.08	46.05	9.82
BBO (ordinary)	800	1.546	-0.0193	0.0627	-0.3401	2.2209	56.80	32.33	-0.44
	400	1.569	-0.1576	1.3241	-15.41	229.2	149.90	52.71	16.58
BBO (extrordinary)	800	1.661	-0.0304	0.0792	-0.4623	3.0359	71.77	50.86	-10.51
	400	1.693	-0.2189	1.8477	-22.03	335.6	209.16	78.59	27.40

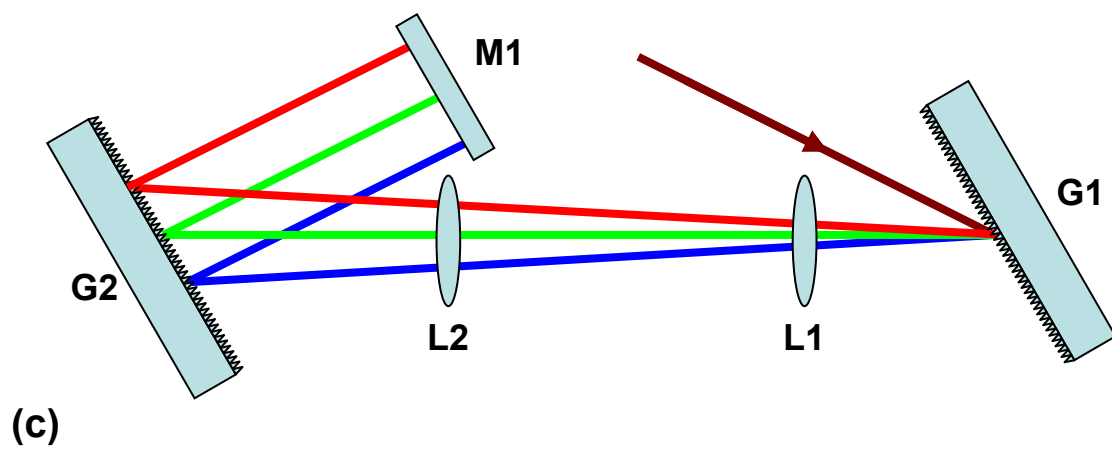
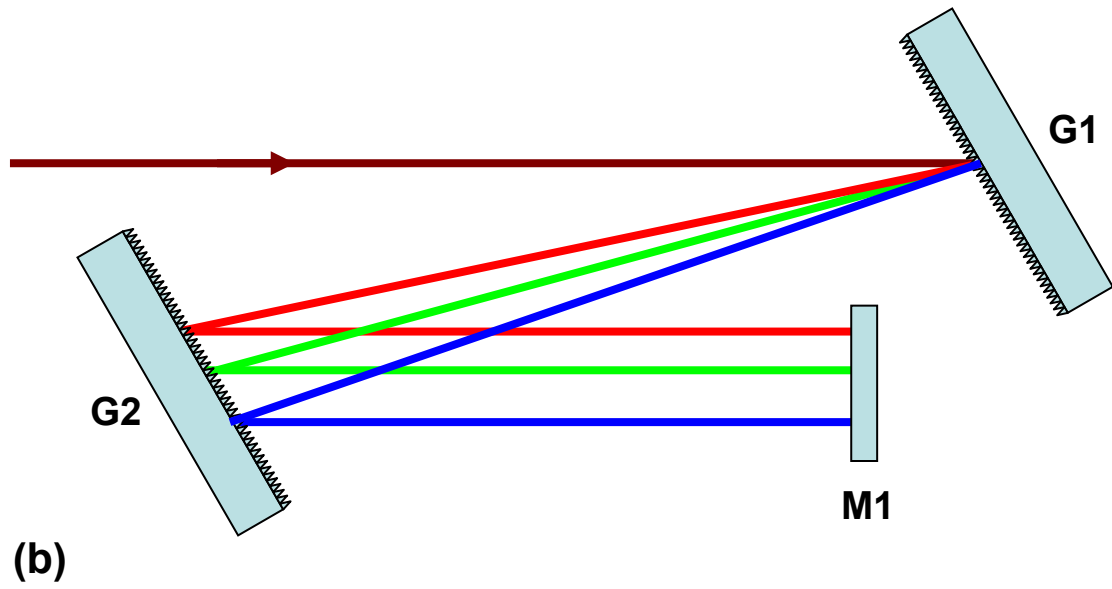
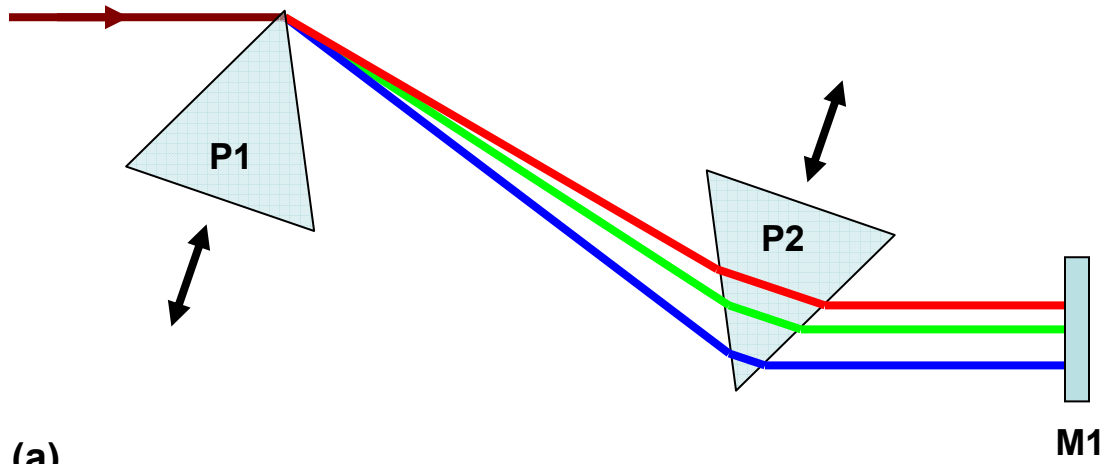
(2) temporal stretching/compressing in CPA. The first application generally uses prism based compressors to compensate for GVD while the second generally uses grating based stretchers/compressors. It is important to note that other methods such as chirped mirrors⁵⁴ have been developed that are not angular dispersion based, but the following discussions focus on the techniques utilized in the work comprised in this dissertation. Discussion begins with a description of material dispersion compensation through the use of prism compressors.

1.3.c.i prism compressors

In ultrafast experiments, a pulse will incur material dispersion before interacting at the measurement position e.g. sample position. Aside from select experiments such as pulse shaping⁵⁵ and coherent control experiments,⁵⁶ it is almost always desirable to deliver the shortest duration pulse to a sample. The shortest pulse condition validates the necessity of dispersion minimization. Material dispersion can be minimized but not entirely eliminated by careful design of an optical system using reflective optics therefore a technique is needed to compensate for material dispersion. Prism compressors accomplish this task.⁵⁷

Figure 1.7(a) shows a schematic of a prism compressor which illustrates its fundamental principles. A typical prism compressor consists of three basic components: (1) a prism (P1) that introduces angular dispersion, (2) a prism (P2) that collimates the spatially dispersed beam, and (3) a retro-reflection mirror that propagates the beam back through P2 and P1 to eliminate the spatial chirp. Both prisms are Brewster prisms, the same material, and arranged at minimum deviation for the input beam which

Figure 1.7 Basic configurations for prism compressors (a), grating compressors (b), and grating stretching⁵⁸ (c).



minimizes loss throughout the prism compressor. The angular dispersion introduced by each prism is governed by the prism's material dispersion and the incidence angle at which the beam strikes the prism. The angular dispersion for P1 and P2 is matched (for near-perfect output collimation) by using minimum deviation configuration (matching incidence angles) and the same material in each prism. The fundamental operating principle of a prism is governed by the introduction of angular dispersion.

Angular dispersion separates the wavelength components of a pulse (or beam) into different propagation directions with lower frequencies (red components) refracting less than higher frequencies (blue components) from the initial propagation direction. Ray tracing in Fig 1.7(a) shows that (1) all of the wavelengths (red to blue) travel through the same amount of prism material giving positive dispersion, and (2) the red wavelengths travel a longer total distance through the prism compressor than the blue wavelengths which delays the red wavelengths with respect to the blue wavelengths giving negative GVD. Thus calculation of the total dispersion for any dispersion order in a prism compressor can be divided into two terms,

$$\varphi_{PC}^{(n)} = \varphi_m^{(n)} + \varphi_L^{(n)} \quad (1.12)$$

where n is the dispersion order, m denotes the prism material dispersion, and L denotes the dispersion from the angular dispersion and prism separation distance. $\varphi_m^{(n)}$ is calculated following the methodology in section 1.3.ii and conversion to the wavelength-domain gives the following expressions for GVD and TOD,

$$\begin{aligned}\varphi_m^{(2)} &= l \left(\frac{\lambda^3}{2\pi c^2} \right) \left(\frac{d^2 n}{d\lambda^2} \Big|_{\lambda_0} \right) \\ \varphi_m^{(3)} &= -l \left(\frac{\lambda^4}{4\pi^2 c^3} \right) \left(3 \frac{d^2 n}{d\lambda^2} \Big|_{\lambda_0} + \lambda \frac{d^3 n}{d\lambda^3} \Big|_{\lambda_0} \right)\end{aligned}\quad (1.13)$$

where l is the mean propagation distance through the prism material (P1 and P2). Added to this term is the angular dispersion term under minimum deviation and Brewster angle conditions which depends on the apex to apex prism separation distance (L) for a given material,⁵¹

$$\begin{aligned}\varphi_L^{(2)} &\approx -4L \left(\frac{\lambda^3}{2\pi c^2} \right) \left(\frac{dn}{d\lambda} \Big|_{\lambda_0} \right)^2 \\ \varphi_L^{(3)} &\approx 6L \left(\frac{\lambda^4}{\pi^2 c^3} \right) \left(\frac{dn}{d\lambda} \Big|_{\lambda_0} \right)^2.\end{aligned}\quad (1.14)$$

Combining equations 1.14 and 1.15 through equation 1.13 gives the total GVD and TOD for a prism compressor,⁵¹⁻⁵³

$$\begin{aligned}\varphi_{PC}^{(2)} &\approx \left(\frac{\lambda^3}{2\pi c^2} \right) \left[l \left(\frac{d^2 n}{d\lambda^2} \Big|_{\lambda_0} \right) - 4L \left(\frac{dn}{d\lambda} \Big|_{\lambda_0} \right)^2 \right] \\ \varphi_{PC}^{(3)} &\approx \left(\frac{-\lambda^4}{\pi^2 c^3} \right) \left[\frac{l}{4} \left(3 \frac{d^2 n}{d\lambda^2} \Big|_{\lambda_0} + \lambda \frac{d^3 n}{d\lambda^3} \Big|_{\lambda_0} \right) - 6L \left(\frac{dn}{d\lambda} \Big|_{\lambda_0} \right)^2 \right]\end{aligned}\quad (1.15)$$

For sufficiently large prism separation distances, GVD is negative and TOD is positive.

Prism compressors are primarily used for material dispersion compensation in ultrafast experiments and in ultrafast oscillators because they utilize material dispersion to generate and adjust the dispersion they introduce. Both of these applications will be discussed in greater detail in the following chapter. In general, application of prism

compressors involves extending L to a point around a target GVD value and translating either prism P1 or P2 which adds or subtracts material dispersion. This gives a controllable adjustment of dispersion for pulse duration optimization at a sample position or for mode locking operation of an ultrafast oscillator. Prism compressors are well suited for these applications because the magnitude of dispersion they introduce is small. Applications such as chirped pulse amplification and optical fiber dispersion compensation require grating-based devices which generate much larger magnitudes of dispersion.

1.3.c.ii grating compressors

The basic design of a parallel grating compressor is shown in Figure 1.7(b). The first description of using a pair of parallel gratings for optical pulse compression was reported by Treacy in 1969⁵⁹ and this design has remained virtually unchanged to date. The grating compressor operates on a similar principle as the prism compressor: the first grating (G1) introduces angular dispersion; the second grating (G2) collimates the spatially chirped beam; and a retroreflection mirror (M1) reflects the beam back onto G2 and G1 which removes the spatial chirp imposed on the beam. Again, ray tracing in Fig 1.7(b) shows that the blue wavelengths travel a shorter distance than the red wavelengths which generates negative GVD.

Analytical expressions have been calculated for the spectral dispersion accumulated in a grating compressor from the grating-induced angular dispersion.^{51,52,59} The following expressions relate the spectral dispersion coefficients to the distance between G1 and G2 (D) for a single pass,⁵¹⁻⁵³

$$\begin{aligned}\varphi_{GC}^{(2)} &= -D \frac{\lambda^3 N^2}{2\pi c^2 \cos^3[\theta(\lambda)]} \\ \varphi_{GC}^{(3)} &= D \frac{3\lambda^4 N^2}{4\pi^2 c^3 \cos^3[\theta(\lambda)]} \left(1 + \frac{\lambda \sin[\theta(\lambda)]}{d \cos^2[\theta(\lambda)]} \right)\end{aligned}\quad (1.16)$$

where N is the grating groove density. $\theta(\lambda)$ is determined from the grating equation,

$$\sin(\theta) = \sin(\gamma) - m\lambda N \quad (1.17)$$

where γ is the grating incidence angle with respect to the grating surface normal, m is the diffraction order, and N is the grating groove density. The coefficients calculated from these equations are multiplied by a factor of 2 for double pass. In practice, grating compressors use reflection gratings, $m = -1$ diffraction orders, and the Littrow condition where $\gamma = -\theta$.

1.3.c.iii grating stretchers

The final device that is used to generate geometric dispersion is the grating stretcher. As discussed in the previous section, parallel grating pairs always generate negative GVD, but it was realized by Martinez that if it was possible to create a situation where the distance between the gratings (D) was negative that the dispersion from the grating pair would change sign and become positive rather than negative.⁵⁸ The basic design for the grating stretcher introduced by Martinez is shown in Fig 1.7(c). The key to generating negative D values was to place a 1:1 imaging lens pair (focal length, f) between the gratings. In this arrangement, the gratings can be symmetrically positioned in three positions: (1) inside f (closer to the lenses); (2) at exactly f ; or (3) outside f (further from the lenses). When the gratings are positioned at f from the

lenses the effective distance between the gratings becomes zero because the image of G2 spatially overlaps with G1; translation of the gratings outside or inside the one f condition gives either positive or negative D values respectively. Translating the gratings outside or away from the lens pair give positive D because the image of G2 remains between G1 and G2 while translating the gratings towards the lens pair gives negative D values because the image of G2 moves behind G1. For these three arrangements, the spectral dispersion coefficients given in equation 1.17 remain valid and only require D to be replaced with the effective distance between the gratings calculated as,

$$D_{eff} = G - 4f \quad (1.18)$$

where G is the distance between the gratings and f is the focal length of the lenses. In practice, grating stretchers use reflective focusing mirrors rather than lenses to eliminate material dispersion contributions, and they fold the optical layout at one focal length between L1 and L2 to conserve space.

1.3.d Ultrafast Pump-Probe Spectroscopy

1.3.d.i ultrafast pump-probe experiments

Pump-probe experiments such as the ones described within this dissertation utilize ultrafast pulses to pump a system into an excited state and subsequently probe the system with another ultrafast pulse at a delayed time.⁶⁰ The time resolution of ultrafast pump-probe experiments depends on the both the duration of the ultrafast pulses used to pump/probe and the resolution of the time delay generated between the

pump and probe pulses. The basic design of all pump-probe experiments follows the schematic shown in Figure 1.8 which is a Michelson interferometer. In this experimental arrangement, an input beam is split into a pump and probe pulse with a beam splitter (BS). The two beams travel separate paths before being recombined (spatially overlapped) at the sample. One of the beams travels down a variable delay path which generates controllable delay between the pump and probe pulses. After impinging the sample the probe beam is routed to a detector. By varying the time delay between the pump and probe, time-dependent dynamics can be mapped out.

Many variations on the basic pump-probe scheme have been developed.^{51,60} In the simplest case, ultrafast pump-probe experiments are one color experiments (pump and probe at the same wavelength) and they measure intensity changes of the probe due to transient absorption changes induced by the pump pulse. In other cases, such as ultrafast fluorescence up-conversion, the probe pulse does not interact with the sample but is instead used to time-gate the fluorescence generated by the pump pulse. In any case, these experiments follow the same recipe: pump...delay...probe. The subsequent discussion focuses on the principles of BFTA spectroscopy, an ultrafast pump-probe spectroscopy.

1.3.d.ii broadband femtosecond transient absorption spectroscopy

Broadband femtosecond transient absorption (BFTA) spectroscopy takes the basic one color transient absorption (TA) experiment and expands it to a broadband regime by generating an ultrafast broadband probe beam. Under the appropriate

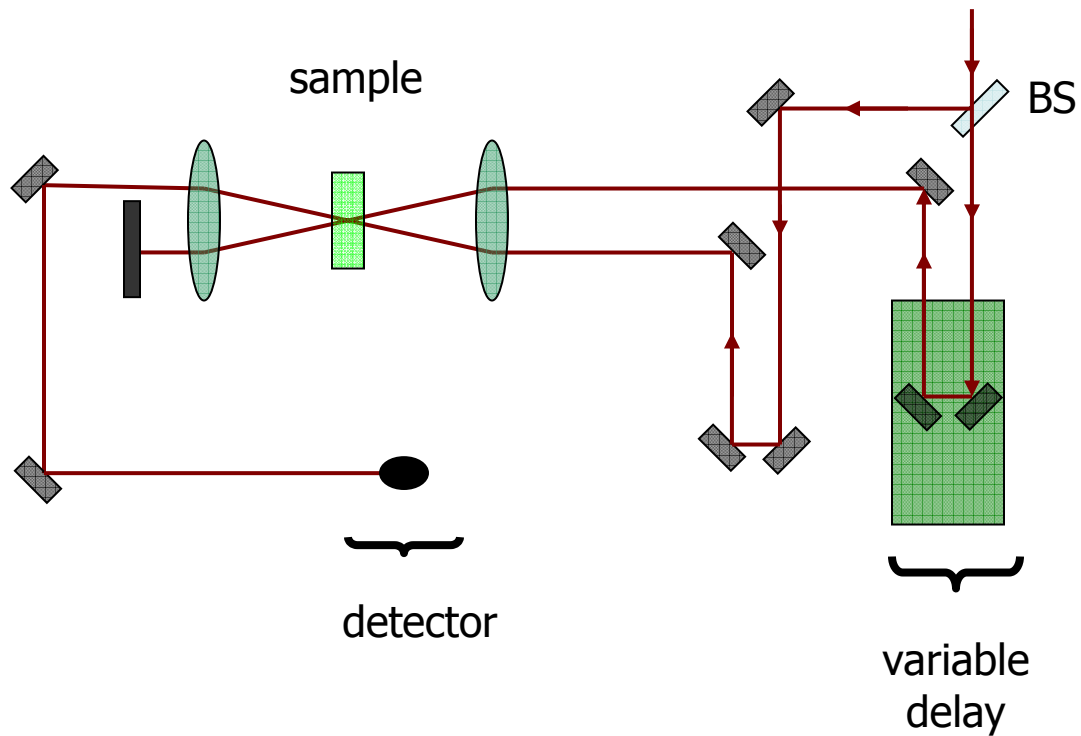


Figure 1.8 Basic pump-probe experimental design, beam-splitter (BS). A pulse impinging BS is split down two different spatial paths. One of the spatial paths is variably controlled to generate time delay between the pump and probe pulses. The time delayed pump and probe pulses are recombined in the sample and the probe beam is detected for subsequent analysis.

conditions an ultrafast pulse can be used to generate a white light continuum (WLC) pulse⁶¹ which generates a broadband, ultrafast probe. Furthermore, the WLC probe can be spectrally resolved giving a great deal more information than the one color experiment.

Spectrally resolved transient absorption signals generated in a broadband pump-probe experiment is described as,

$$S(\nu, \tau) = \log \left(\frac{I_{sig}(\nu, \tau)}{I_{ref}(\nu, \infty)} \right) \quad (1.19)$$

where I_{sig} is the intensity of the probe beam spectrum with the pump beam impinging the sample and I_{ref} is the intensity of the probe beam spectrum with the pump beam blocked. $S(\nu, \tau)$ reflects time-dependent processes initiated by the pump pulse and if we consider a one state system three fundamental signals give the total observed signal (Figure 1.9). These three contributions that comprise $S(\nu, \tau)$ are excited state absorption (ESA), stimulated emission (SE), and ground state bleach (BL). SE and BL contributions indicate the sample absorbing less light while ESA displays an increase in absorption. When $S(\nu, \tau)$ is calculated with equation 1.20, ESA signals are negative and SE/BL signals are positive. We follow this convention throughout the work in this dissertation.

Our BFTA spectrometer uses input ultrafast pulses centered at 800 nm. This input is frequency doubled giving 400 nm pump pulses. The residual 800 nm beam is separated from the 400 nm beam and is subsequently used to generate broadband

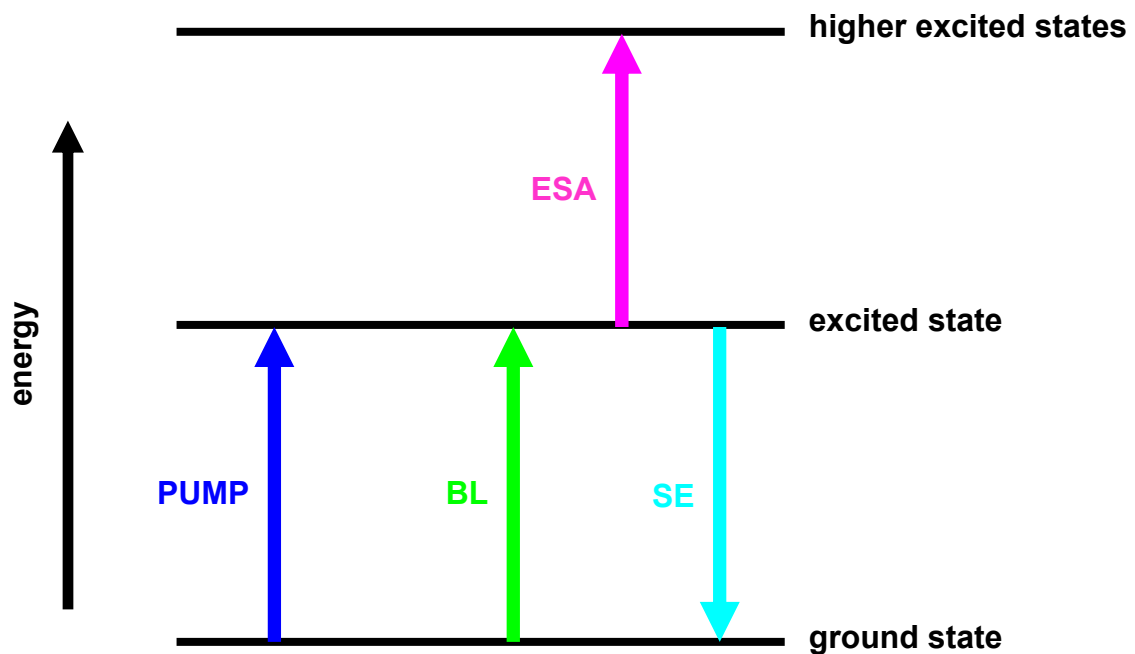


Figure 1.9 Energy level diagram for a one state (no excited state transfer processes) probed by BFTA spectroscopy. The pump pulse (PUMP) prepares population in the excited state. The probed BFTA signal consists of three fundamental transitions from the excited state: ground state absorption or bleach (BL); excited state absorption (ESA) to higher excited states; and stimulated emission (SE) back to the ground state.

fs in duration due to its large bandwidth. Further specific details about our BFTA setup including optimizations and diagnostics will be discussed in the next chapter.

References and Notes

- (1) Lynden-Bell, R. M.; Morris, S. C.; Barrow, J. D.; Finney, J. L.; Jr, C. L. H. *Water and life the unique properties of H₂O*; Woodhead Publishing Ltd.: Cambridge, UK, 2010.
- (2) Kallay, N. *Interfacial Dynamics*; Dekker: New York, NY, 2000.
- (3) Pollack, G. H. *Advances in colloid and interface science* **2003**, *103*, 173.
- (4) Rasaiah, J. C.; Garde, S.; Hummer, G. *Annual Review of Physical Chemistry* **2008**, *59*, 713.
- (5) Mallick, A.; Purkayastha, P.; Chattopadhyay, N. *Journal of Photochemistry and Photobiology, C: Photchemistry Reviews* **2007**, *8*, 109.
- (6) Datta, A.; Mandal, D.; Pal, S. K.; Bhattacharyya, K. *Journal of Physical Chemistry B* **1997**, *101*, 10221.
- (7) Escamilla, E.; Contreras, M.; Escobar, L.; Ayala, G. *Biomolecular Organic Solvents* **1992**, 219.
- (8) Cohen, B.; Huppert, D.; Sontsev, K. M.; Tsfadia, Y.; Nachliel, E.; Gutman, M. *Journal of American Chemical Society* **2002**, *124*, 7539.
- (9) Gil, M.; Martin, C.; Organero, J. A.; Navarro, M. T.; Corma, A.; Douhal, A. *Journal of Physical Chemistry C* **2010**, *114*, 6311.
- (10) Bursing, H.; Kundu, S.; Vohringer, P. *Journal of Physical Chemistry B* **2003**, *107*, 2404.
- (11) Lim, K. T.; Hwang, H. S.; Ryoo, W.; Johnston, K. P. *Langmuir* **2004**, *20*, 2466.
- (12) Luisi, P. L.; Straub, B. E. *Reverse Micelles: Biological and Technological Relevance of Amphiphilic Structures in Apolar Media*; Plenum Press: New York, NY, 1984.
- (13) Chiang, C.-L.; Hsu, M.-B.; Lai, L.-B. *Journal of Solid State Chemistry* **2004**, *177*, 3891.

- (14) Pileni, M. P. *Journal of Physical Chemistry B* **2001**, *105*, 3358.
- (15) Taleb, A.; Petit, C.; Pileni, M. P. *Chemistry of Materials* **1997**, *9*, 950.
- (16) Calandra, P.; Longo, A.; Liveri, V. T. *Journal of Physical Chemistry B* **2003**, *107*, 25.
- (17) Peleni, M. P. *Journal of Physical Chemistry* **1993**, *97*, 6961.
- (18) Grant, C. D.; Steege, K. E.; Bunagan, M. R.; Jr, E. W. C. *Journal of Physical Chemistry B* **2005**, *109*, 22273.
- (19) Jimenez, R.; Fleming, G. R.; Kumar, P. V.; Maroncelli, M. *Nature* **1994**, *369*, 471.
- (20) Martins, L. R.; Skaf, M. S.; Ladanyi, B. M. *Journal of Physical Chemistry B* **2004**, *108*, 19687.
- (21) Uritski, A.; Huppert, D. *Journal of Physical Chemistry A* **2007**, *111*, 10544.
- (22) Wachtveitl, J.; Huber, R.; Spörlein, S.; Moser, J. E.; Grätzel, M. *International Journal of Photoenergy* **1999**, *1*, 153.
- (23) Willard, D. M.; Riter, R. E.; Levinger, N. E. *Journal of the American Chemical Society* **1998**, *120*, 4151.
- (24) C. Prayer, T. G.; Tran-Thi, T.-H. In *AIP Conference Proceedings*; AIP: 1996; Vol. 364, p 333.
- (25) Leiderman, P.; Genosar, L.; Huppert, D. *Journal of Physical Chemistry A* **2005**, *109*, 5965.
- (26) Spry, D. B.; Goun, A.; Fayer, M. D. *Journal of Physical Chemistry A* **2007**, *111*, 230.
- (27) Moilanen, D. E.; Spry, D. B.; Fayer, M. D. *Langmuir* **2008**, *24*, 3690.
- (28) Mojumdar, S. S.; Mondal, T.; Das, A. K.; Dey, S.; Bhattacharyya, K. *Journal of Chemical Physics* **2010**, *132*, 194505.
- (29) Mondala, S. K.; Saha, K.; Pratik Sena, D. R.; Ghosha, S.; Bhattacharyya, K. *Chemical Physics Letters* **2005**, *412*, 228.
- (30) Mohammed, O. F.; Pines, D.; Dreyer, J.; Pines, E.; Nibbering, E. T. J. *Science* **2005**, *310*, 83.

- (31) Tielrooij, K. J.; Cox, M. J.; Bakker, H. J. *Chem Phys Chem* **2009**, *10*, 245.
- (32) Corbeil, E. M.; Riter, R. E.; Levinger, N. E. *Journal of Physical Chemistry B* **2004**, *108*, 10777.
- (33) Corbeil, E. M.; Levinger, N. E. *Langmuir* **2003**, *19*, 7264.
- (34) Riter, R. E.; Willard, D. M.; Levinger, N. E. *Journal of Physical Chemistry B* **1998**, *102*, 2705.
- (35) Pant, D.; Riter, R. E.; Levinger, N. E. *Journal of Chemical Physics* **1998**, *109*, 9995.
- (36) Palazzo, G.; Lopez, F.; Giustini, M.; Colafemmina, G.; Ceglie, A. *Journal of Physical Chemistry B* **2003**, *107*.
- (37) Kinugasa, T.; Kondo, A.; Nishimura, S.; Miyauchi, Y.; Nishii, Y.; Watanabe, K.; Takeuchi, H. *Colloids and Surfaces A* **2002**, *204*, 193.
- (38) Lipgens, S.; Schübel, D.; Schlicht, L.; Spilgies, J.-H.; Ilgenfritz, G. *Langmuir* **1998**, *14*, 1041.
- (39) Kinugasa, T.; Kondo, A.; Nishimura, S.; Miyauchi, Y.; Nishii, Y.; Watanabe, K.; Takeuchi, H. *Colloid Surface A* **2002**, *204*, 193.
- (40) Lipgens, S.; Schubel, D.; Schlicht, L.; Spilgies, J. H.; Ilgenfritz, G.; Eastoe, J.; Heenan, R. K. *Langmuir* **1998**, *14*, 1041.
- (41) Uedal, M.; Schelly, Z. A. *Langmuir* **1988**, *4*, 653.
- (42) Ghosh, S. K.; Khatua, P. K.; Bhattacharya, S. C. *Journal of Colloid and Interface Science* **2004**, *275*, 623.
- (43) Ghosh, S. K.; Khatua, P. K.; Bhattacharya, S. C. *Journal of Colloid and Interface Science* **2004**, *279*, 523.
- (44) Vasilescu, M.; Caragheorghopol, A.; Caldaru, H. *Advances in Colloid and Interface Science* **2001**, *89-90*, 169.
- (45) Larsen, D. S.; Ohta, K.; Xu, Q.-H.; Cyrier, M.; Fleming, G. R. *Journal of Chemical Physics* **2001**, *114*, 8008.
- (46) Horng, M. L.; Gardecki, J. A.; Papazyan, A.; Maroncelli, M. *Journal of Physical Chemistry* **1995**, *99*, 17311.

- (47) Song, X.; Chandler, D. *Journal of Chemical Physics* **1998**, *108*, 2594.
- (48) Kosower, E. M.; Huppert, D. *Annual Review of Physical Chemistry* **1986**, *37*, 127.
- (49) Smith, K. K.; Kaufmann, K. J.; Huppert, D.; Gutman, M. *Chemical Physics Letters* **1979**, *64*, 522.
- (50) Rappoport, Z. *The Chemistry of Phenols*; Wiley: New York, 2003.
- (51) Weiner, A. *Ultrafast Optics*; John Wiley and Sons, Inc.: Hoboken, New Jersey, 2009.
- (52) Walmsley, I.; Waxer, L.; Dorrer, C. *Review of Scientific Instruments* **2001**, *72*, 1.
- (53) Bartels, R. Fort Collins, Colorado, 2006.
- (54) Szipocs, R.; A.Koházi-Kis *Applied Physics B* **1997**, *65*, 115.
- (55) Weiner, A. M. *Review of Scientific Instruments* **2000**, *71*, 1929.
- (56) Ohmori, K. *Annual Review of Physical Chemistry* **2009**, *60*, 487.
- (57) Fork, R. L.; Martinez, O. E.; Gordon, J. P. *Optics Letters* **1984**, *9*, 150.
- (58) Martinez, O. E. *IEEE Journal of Quantum Electronics* **1987**, *QE-23*.
- (59) Treacy, E. *IEEE Journal of Quantum Electronics* **1969**, *5*, 454.
- (60) Fleming, G. R. *Chemical Applications of Ultrafast Spectroscopy*; Oxford University Press: New York, New York, 1986.
- (61) Brodeur, A.; Chin, S. L. *Journal of Optical Society of America B* **1999**, *16*, 637.

CHAPTER 2

EXPERIMENTAL METHODS

2.1 Laser System

The laser system outlined in this section was a combination of a commercially purchased system and a number of custom modifications. The basic laser system consists of a titanium doped sapphire (TSap) based chirped pulse amplifier (CPA) purchased from Clark MXR Model CPA-1000 (CPA-1000) which generated and amplified femtosecond pulses centered at 800 nm. The CPA-1000 laser system was purchased in 1995 and consequently there have been a significant number of advancements in CPA technology. The following sections outline the integration of a number of these advancements into the CPA-1000 laser system to improve its performance. The basic components of a CPA laser system are shown Figure 2.1 and the following sections describe their individual design and operation.

2.1.a Kerr-Lens Mode Locked Oscillator

The laser used to generate ultrafast pulses was a KM Labs Model TS (KML-TS) oscillator pumped with a Lighthouse Photonics Sprout (LP-S) laser (Figure 2.2). The KML-TS laser used Kerr lens mode locking to generate a train of ultrafast pulses. The KML-TS laser had a high degree of flexibility in both the output spectral characteristics

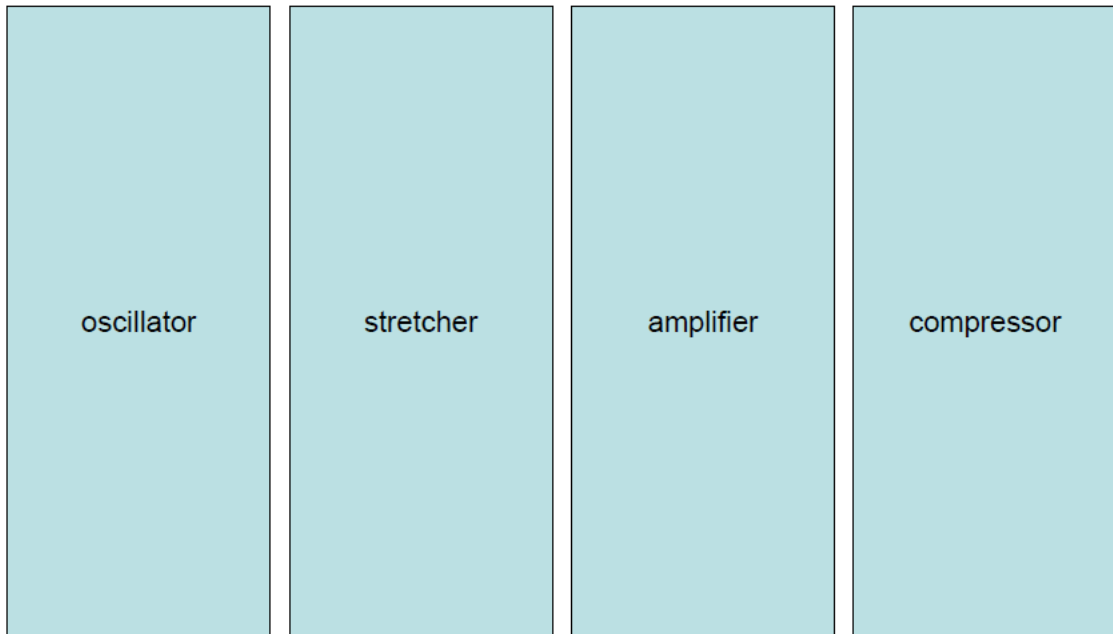


Figure 2.1. Basic components of a chirped pulse amplification (CPA) laser system. An ultrafast pulse is generated (oscillator), temporally stretched (stretcher), amplified (amplifier), and temporal compressed (compressor).

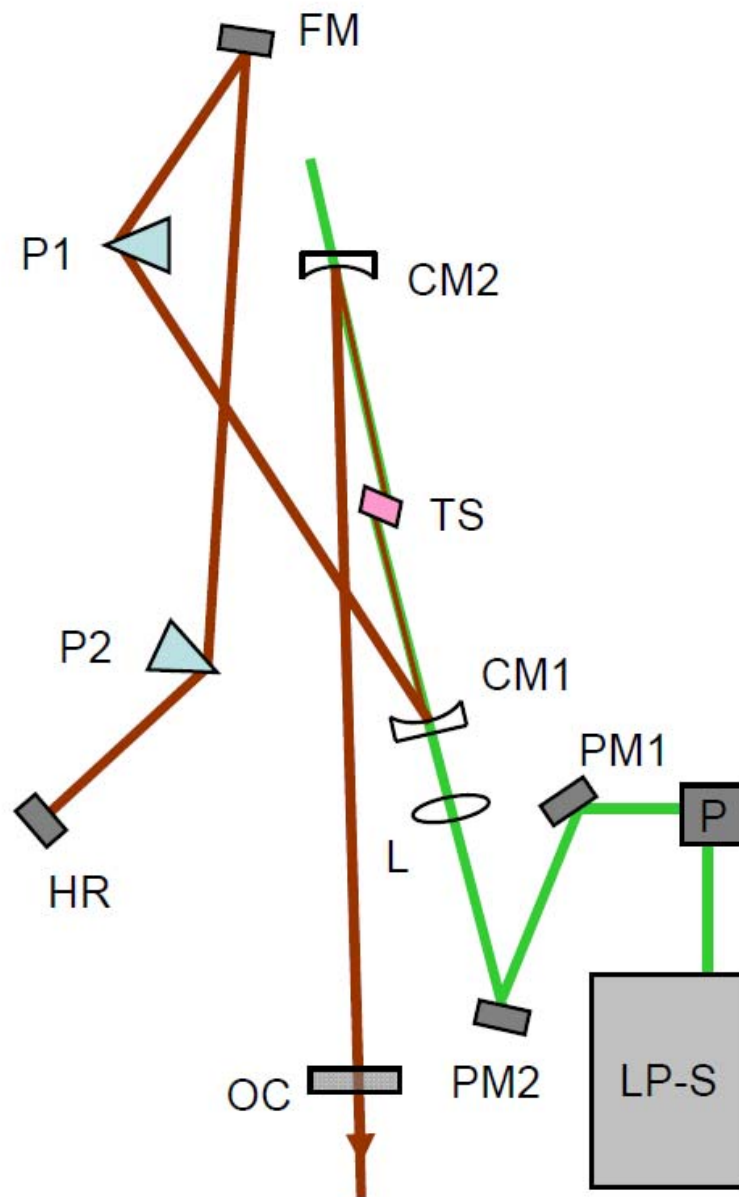


Figure 2.2 Schematic of the KM Labs TS (KML-TS) laser. LP-S (Lighthouse Photonics Sprout pump laser); P (periscope); PM1-PM2 (pump beam turning mirrors); L (pump focusing lens; CM1-CM2 (curved mirrors); TS (TSap crystal); OC (output coupler); FM (cavity folding mirror); P1,P2 (Brewster prisms); HR (high reflector).

and the temporal duration of the pulses generated. The configuration of the KML-TS laser was optimized only in the spectral domain to give a spectrum centered at 800 nm with 50-60 nm of bandwidth. The repetition rate or pulse frequency of the KML-TS laser was approximately 90 MHz and is defined by $c/2L$ where c is the speed of light and L the pulse propagation distance between the output coupler and the high reflector (OC and HR in Figure 2.2 respectively). Details for alignment and diagnostics of the KML-TS laser can be found in its operation manual.¹ The pulses from the KML-TS are used to seed the CPA-1000 regenerative amplifier.

2.1.b Regenerative Amplifier

Amplification of ultrafast pulses without damage to the amplifier optics generally requires a significant reduction in peak pulse intensities to prevent optical damage and nonlinear effects during amplification. This task is accomplished by temporally broadening ultrafast pulses (stretching) to hundreds of picoseconds before the amplification process and subsequently narrowing the pulses (compressing) back to ultrafast durations after amplification. The Clark CPA-1000 operated using a grating based stretcher and compressor and amplification occurs in a TSap laser cavity which is pumped by a CW Q-switched Nd:YLF laser Quantronix Model 527 (Q-527) laser running at a 1 kHz repetition rate. The following sections outline the details of the stretcher, amplifier, and compressor.

2.1.b.i stretcher

The CPA-1000 stretcher followed the basic Martinez design² although utilizing all reflective optics. Using reflective optics minimizes material dispersion in the setup. A

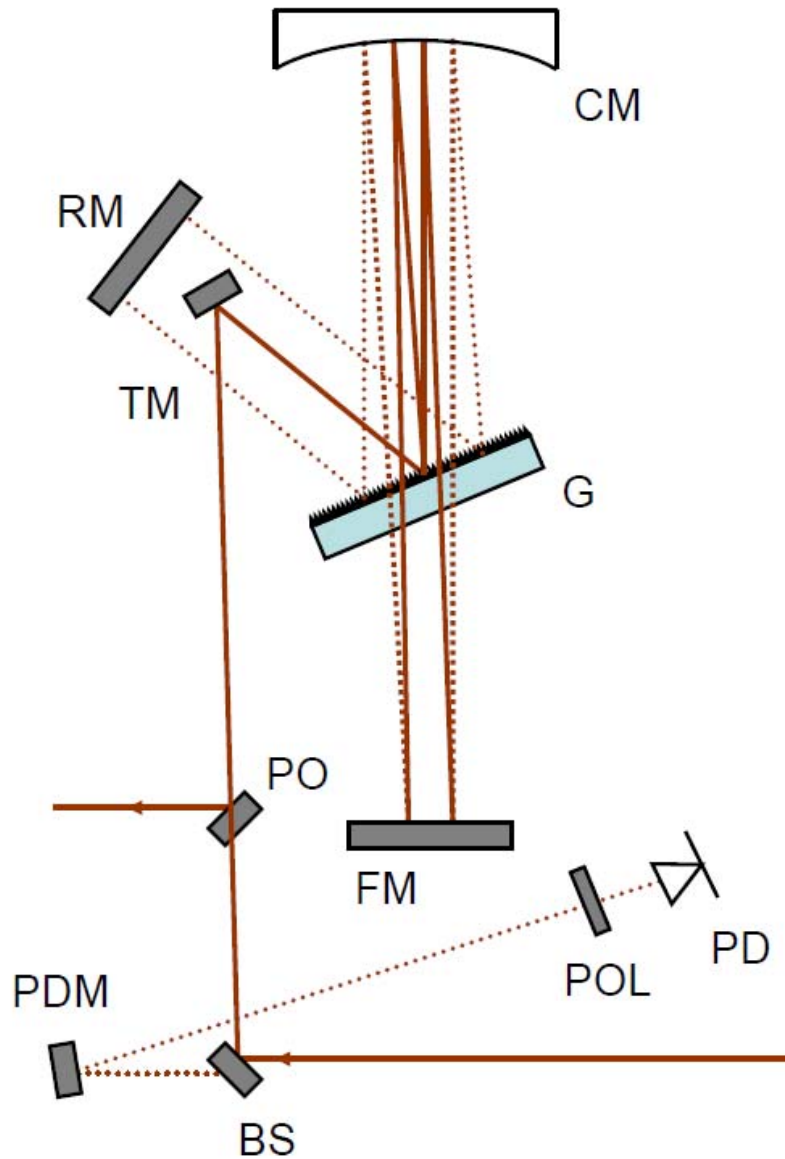


Figure 2.3 Schematic of the Clark MXR CPA-1000 (CPA-1000) laser stretcher. BS (95% reflection beam splitter); PDM (photodiode mirror); POL (linear polarizer); PD (photodiode); TM (turning mirror); G (diffraction grating); CM (curved mirror); FM (folding mirror); RM (retro-reflection mirror); PO (pick-off mirror).

schematic of the CPA-1000 stretcher optical layout is shown in Figure 2.3. The original Martinez design was further simplified by folding with a mirror (FM) at the focus between the two lenses. This optical scheme required only one focusing optic (spherical mirror, CM) and one diffraction grating (G) rather than two of each which saves both space and the total number of optical components required. The incoming beam initially impinged a 95% reflective beamsplitter; the transmitted 5% of the incoming beam was attenuated and strikes a photodiode which serves to synchronize the amplifier to the TSap oscillator. The incoming beam was then routed with TM toward the diffraction grating (G). The diffraction grating spectrally dispersed the beam toward CM which reflected the beam to a folding mirror (FM). TM retro-reflected the dispersed beam back on the same path (CM to G toward TM) albeit slightly higher missing TM and striking the retro-reflection mirror (RR) which routed the beam back through the entire system. The output beam emerged vertically displaced from the input beam on TM and struck a pick-off mirror (PO) which reflected the temporally stretched pulses toward the amplification cavity.

The original CPA-1000 stretcher and compressor used 1400 groove/mm gratings which, combined with the finite size (horizontal widths of reflective surfaces) of the optics, limited the throughput bandwidth of the stretcher and compressors to approximately 15 nm at 800 nm. To improve the bandwidth throughput, we replaced the 1400 groove/mm gratings with 600 groove/mm gratings which increased the throughput bandwidth to approximately 80 nm at 800 nm. The beam incidence angle aligned (γ) was nominally adjusted to align the $m=1$ diffraction order at 800 nm along

the stretcher optical axis. This angle was subsequently tweaked in conjunction with the grating separation distance in the compressor to minimize third-order dispersion in the compressed pulses. The optimized angle (γ) was approximately 7.3 degrees.

To yield positive GVD, the diffraction grating (G) was positioned less than one focal length ($d = 374$ mm) from spherical mirror ($f_l = 914$ mm) which gave an effective grating separation distance of -540 mm. Using the dispersion equations for grating compressors/stretchers (Chapter 1 Section 3.iii.c) this stretcher configuration gave dispersion coefficient of $205,000 \text{ fs}^2$ for GVD. Assuming a transform-limited Gaussian pulse at 800 nm with 60 nm of bandwidth from the KML-TS oscillator, the dispersion added to the pulses lengthens them from 16 fs to 58 ps. This stretching factor reduced the pulse intensity sufficiently for safe amplification.

2.1.b.ii regenerative amplifier

The CPA-1000 amplification cavity is shown in Figure 2.4. Amplification of stretched pulses takes place in a basic folded TSap laser cavity with an intracavity polarizer (POL2) and Pockels cell (POL2 and PC in Figure 2.4 respectively). The POL2/PC serves to Q-switch the cavity and to control injection, cavity dumping during the amplification process. The four cavity optics (CM1-CM4) routed and focused the cavity beam into the TSap crystal which was pumped by the Q-527 pump laser. The Q-527 output was centered at 527 nm with ~ 200 ns pulse durations; this output is focused with a 30 cm focal length lens (L1) through CM1 into the TSap crystal. The original design of the CPA-1000 amplifier cavity pumped the cavity from one direction (through CM1), but an additional lens (L2, focal length 30 cm) and mirror (PM3) were added to reflect and

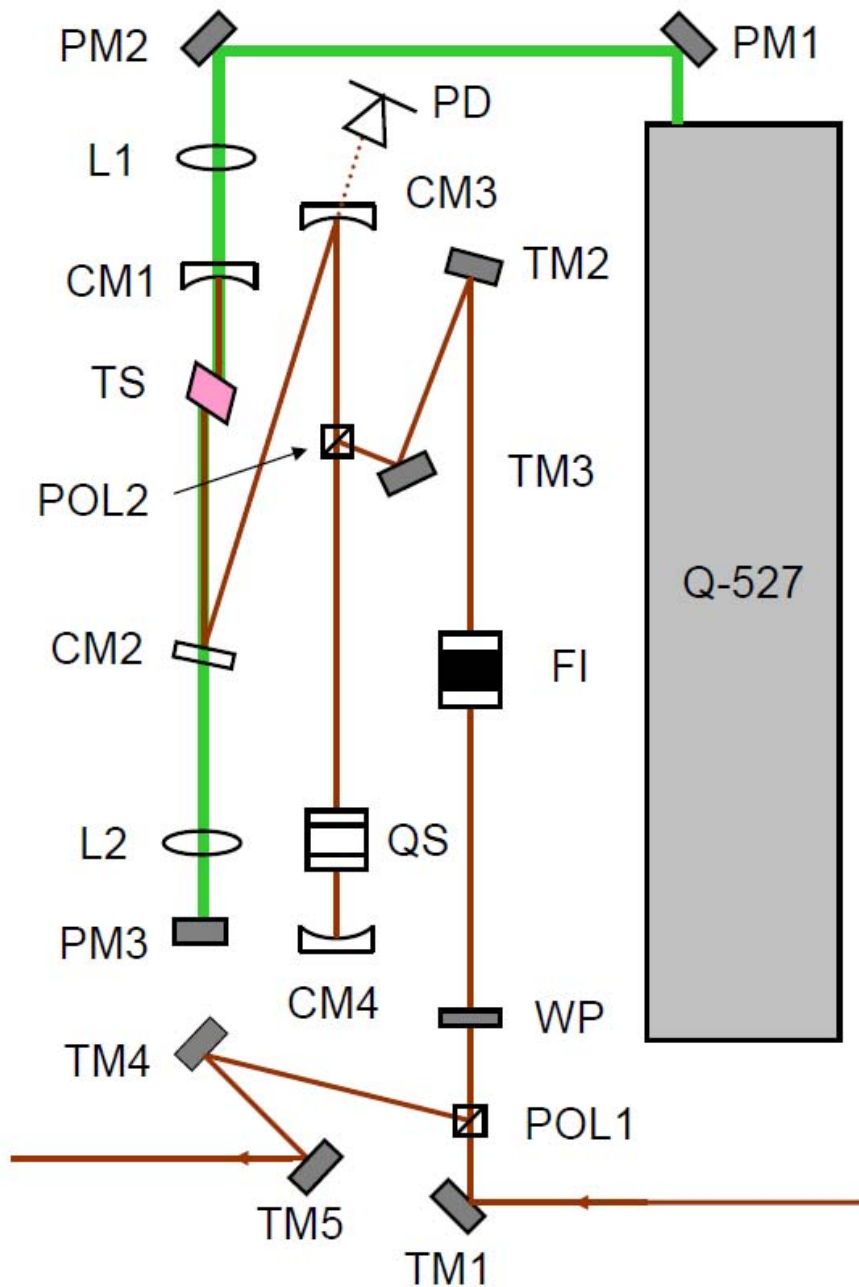


Figure 2.4 Schematic of the Clark MXR CPA-1000 (CPA-1000) amplifier. TM1-TM5 (turning mirrors); POL1-POL2 (polarizers); WP (half-wave plate); FI (Faraday isolator); CM1-CM4 (cavity mirrors); TS (TSap crystal); QS (Q-switch); PD (photodiode); L1-L2 (pump lenses); PM1-PM3 (pump beam mirrors); Q-527 (Quantronix pump laser).

refocus the transmitted pump beam back into the crystal (through CM2). This increased the pump to cavity energy conversion efficiency by approximately 10 percent.

Femtosecond pulses were amplified in this TSap cavity through the use of the POL2/PC which served to reflect within the cavity (trap and amplify) and, after amplification, reflected the pulse out of the amplification cavity (cavity dump). In this process, the repetition rate of the laser was synchronously reduced from the 90 MHz (from the oscillator) to the 1 kHz repetition rate of the Q-527. The timing within CPA-1000 amplification process is depicted in Figure 2.5. POL2 acts as a polarization filter in the cavity which transmits only horizontally polarized light which corresponds with the transmitted polarization allowed by the Brewster cut TSap crystal. PC was aligned to act as a static $\lambda/4$ waveplate which in double pass is a $\lambda/2$ waveplate. The static $\lambda/2$ action of PC rotated the transmitted horizontal polarization (from POL2 toward PC) to vertical polarization when returning to POL2 which subsequently reflected this light out of the cavity. Thus the cavity Q was low and lasing was extinguished. When a single high voltage pulse is applied to PC, the birefringence was stepped up by $\lambda/4$ giving $\lambda/2$, λ operation for single, double pass respectively. In this case three important things happen: (1) the cavity Q is switched high and it was able to lase, (2) any pulses reflected off POL2 during the high voltage pulse were reflected out of the cavity, and (3) any pulse reflected off POL2 into the cavity which also double passes through PC before the high voltage was applied to PC was trapped in the amplification cavity. With the proper timing and short enough rise time (approximately 1-2 nanoseconds) of the high voltage pulse (HV1), a single pulse was trapped in the cavity and amplified. When HV2

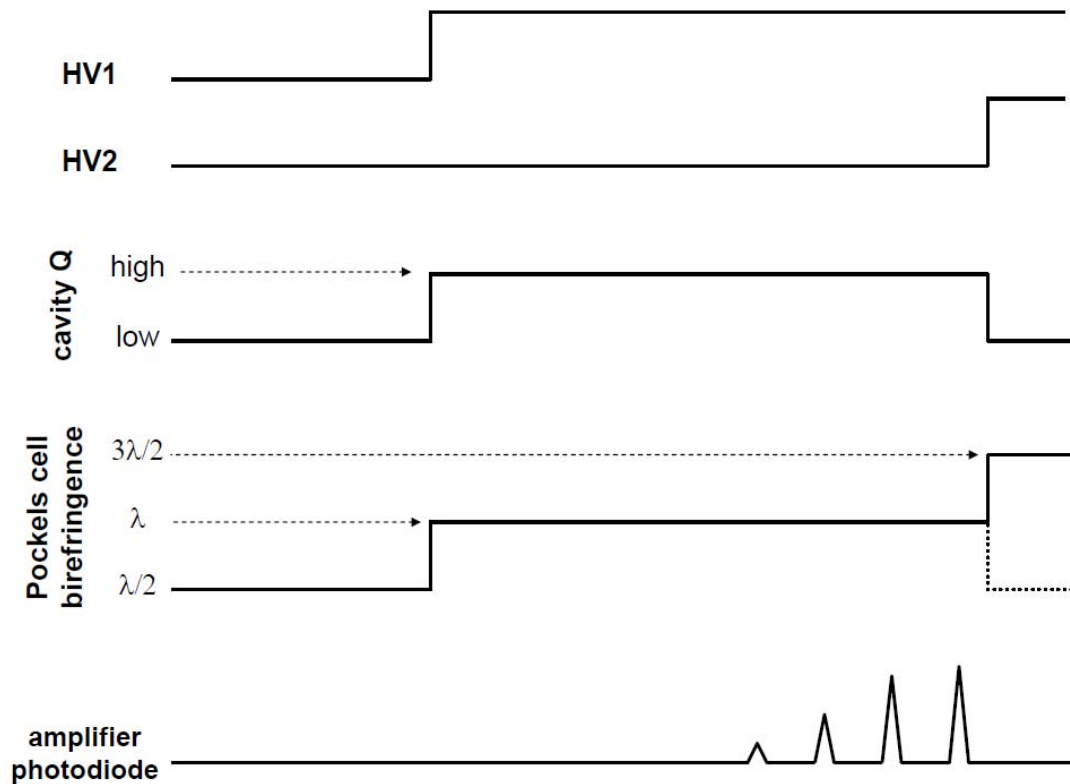


Figure 2.5 Timing of high voltage pulses applied to the Pockels cell (PC) and their effect in the CPA-1000 amplification cavity. HV1 switches the cavity Q to high which allows the cavity to lase wherein one pulse is trapped and amplified. HV2 switches the cavity Q to low and the amplified pulse is reflected out of the amplification cavity (cavity dumping). The cavity build-up and dumping is monitored on the amplifier photodiode (PD, Figure 2.4).

was applied to PC acts as $\lambda/2$ waveplate in double pass which dropped the cavity Q low and light in the cavity (amplified pulse) was rejected from the cavity by POL2 as its polarization is rotated from horizontal to vertical.

The seed pulse (from the KML-TS oscillator) and amplified pulse trains counter propagated between POL1 to POL2 and were separated by use of a Faraday isolator (FI) which acted as a $\lambda/2$ waveplate for propagation through it only one direction. The incoming horizontally polarized seed pulses were rotated by a $\lambda/2$ waveplate (WP, Figure 2.4) to vertical polarization for reflection in the amplification cavity. Propagation through FI from POL1 to POL2 did not rotate the polarization of the seed pulses, but the amplified pulses propagating in the opposite direction were rotated from vertical to horizontal polarization. WP rotated this polarization back to vertical and POL1 reflected the pulses toward the compressor rather than back into the stretcher.

2.1.b.iii compressor

The CPA-1000 grating compressor configuration which followed the design introduced by Traacy³ is shown in Figure 2.6. The optical compression portion of the CPA-1000 compressor consisted of two parallel gratings (G1, G2) and a folding mirror (FM). The incoming amplified beam was first reflected through a polarization rotating periscope (P) which rotates the beam from vertical to horizontal polarization. The amplified beam was expanded by a factor of 2 with a Galilean telescope⁴ (NL, PL) to prevent damage to the diffraction gratings. A turning mirror (TM1) directed the expanded beam to G1. From G1, the $m = -1$ diffraction order was reflected to G2 and from G2 to a folding mirror (FM). FM retro-reflected the spatially chirped beam back to

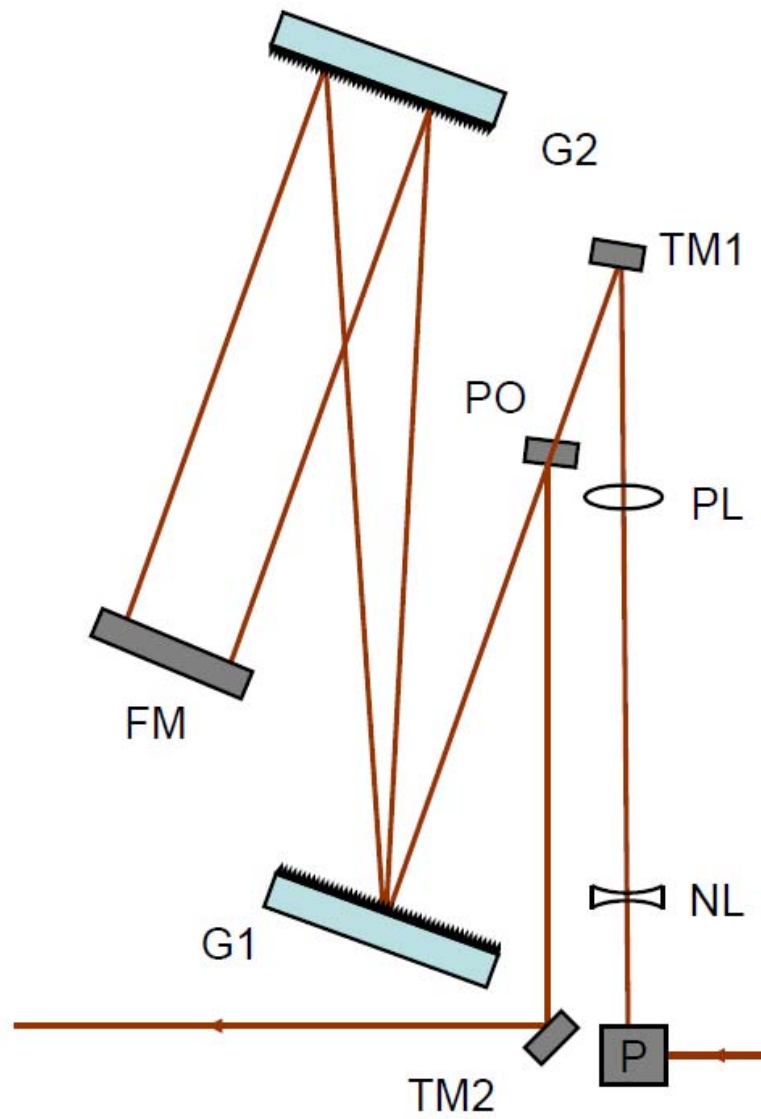


Figure 2.6 Schematic of the Clark MXR CPA-1000 (CPA-1000) grating compressor. P (periscope); NL (negative lens); PL (positive lens); TM1-TM2 (turning mirrors); G1-G2 (diffraction gratings); FM (folding mirror); PO (pick-off mirror).

G2 and G1 albeit vertically displaced and a pick-off mirror (PO) reflected the compressed beam to a turning mirror (TM2) and out of the compressor.

The angle of incidence between the amplified beam and the grating surface normal (γ) was fixed at 5.1 degrees, and compression was initially optimized by varying the distance between G1 and G2. This was typically accomplished by maximizing a second harmonic signal generated from the compressed beam. Further optimization of the compression involved tweaking the stretcher incidence angle and G1/G2 separation distance in conjunction ultrafast pulse characterization techniques. The optimized compressor separation was 776 mm. Typical optimization parameters for the entire CPA-1000 laser system are listed in Table 2.1. The following section outlines the ultrafast pulse characterization techniques that were used to optimize the CPA-1000 laser system.

2.1.c Laser System Diagnostics

Ultrafast pulses temporal characteristics cannot be determined by direct detection as photovoltaic detector responses are approximately limited to hundreds of picoseconds which falls up to 6 orders of magnitude longer than resolution needed for ultrafast pulse characterization. The solution to this problem is to use the pulse itself to resolve its temporal characteristics. This is accomplished through the use of an interferometer which splits the pulse into two replicas, overlaps them spatiotemporally, and measures their non-linear interaction as a function of the path length difference between the two arms of the interferometer. The path length difference is proportional to time delay between the pulses and thus the temporal characteristics of an ultrafast

Table 2.1 Typical optimized parameters of CPA-1000 laser system.

KML-TS Oscillator	
LP-S pump power	4.25 W
average power CW	460 mW
average power ML	650 mW
repetition rate	83 MHz
pulse energy	7.8 nJ/pulse
spectral peak	800 nm
spectral bandwidth	60 nm
CPA-1000 Stretcher	
output power	290 mW
efficiency	45%
distance between G and CM	374 mm
grating incidence angle	7.3 degrees
CPA-1000 Regenerative Amplifier	
Q-527 pump power @ 35 amps	9.5 W
Delay 1	079 B6
Delay 2	082 52
build-up time	115 ns
round trips in cavity	12
cavity dumped power	1.22 W
repetition rate	1 kHz
spectral peak	800 nm
spectral bandwidth	30 nm
CPA-1000 Compressor	
output power	560 mW
efficiency	46%
distance between G1 and G2	776 mm
grating incidence angle	5.1 degrees
pulse energy	560 μ J/pulse
pulse width	50 fs FWHM

pulse can be mapped out. The following sections outline the details of this basic ultrafast characterization methodology.

2.1.c.i intensity autocorrelation

The most utilized method to characterize ultrafast pulses is intensity autocorrelation. Simply put, intensity autocorrelation is an experimental measure of a mathematical convolution expressed as

$$A(\tau) = \int_{-\infty}^{\infty} I(t + \tau)I(t)dt \quad (2.1)$$

where $I(t)$ is the temporal intensity of a pulse in time and $I(t + \tau)$ is this pulse shifted by τ in time. Resultant $A(\tau)$ traces give an over-estimate of actual pulse widths due to a convolution factor which is pulse shape dependent. For Gaussian and sech^2 pulse shape durations (full width at half maximum, FWHM), the convolution factors (A_{FWHM}/I_{FWHM}) are 1.414 and 1.543 respectively.⁵ Actual pulse durations can be estimated from intensity autocorrelation measurements through these relations.

Figure 2.7 shows the scheme of the device that was used to experimentally measure both intensity autocorrelation traces and frequency resolved optical gating (FROG) spectrograms. This device splits an incoming pulse into two pulses with a beam splitter (BS) and directs them down different spatial paths to a measurement position. The path length of one pulse is fixed while the other is varied with a computer-controlled translation stage (DS) to give adjustable delay between two replica pulses. The pulses are focused with a 300 mm focal length curved mirror (CM) and spatially overlapped in a Type I β -barium borate (BBO) second harmonic generation (SHG) crystal. The resultant

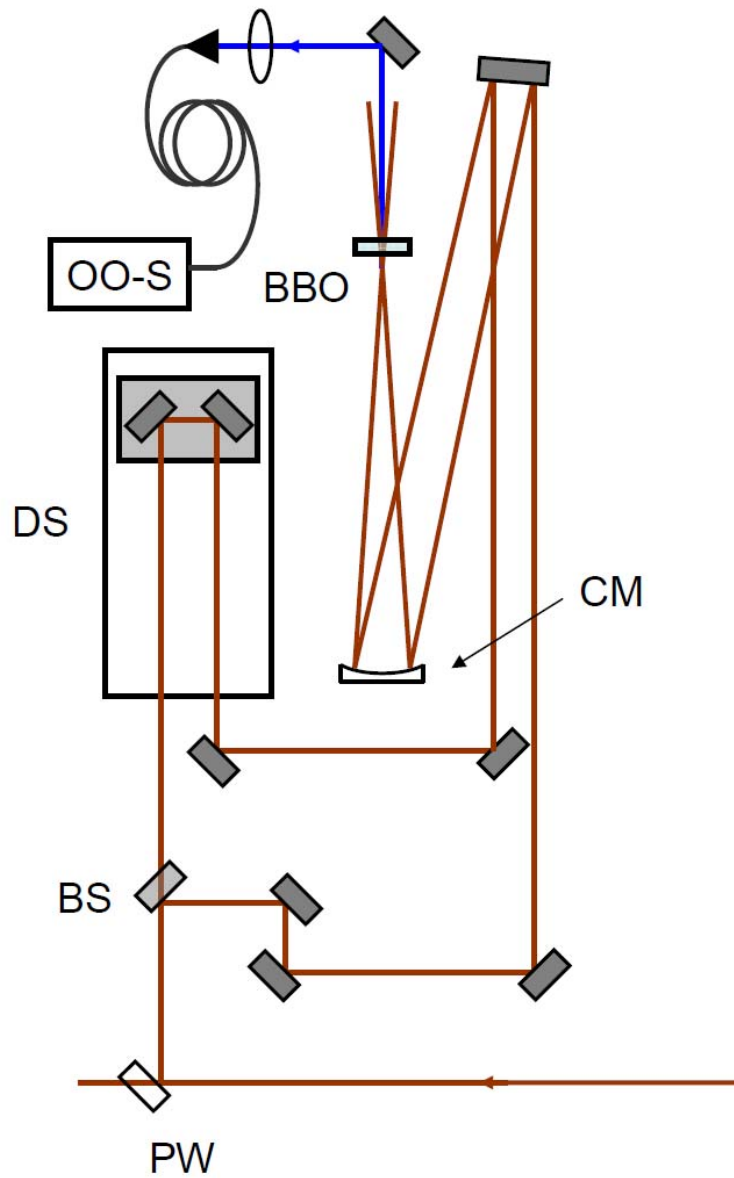


Figure 2.7 Schematic of the second harmonic frequency resolved optical gating (SH-FROG) instrument used to measure pulse autocorrelation and FROG traces. PW (plane parallel window fused silica window); BS (beam-splitter); DS (delay stage); CM (300 mm focal length curved mirror); BBO (β -barium borate Type I doubling crystal); and OO-S (Ocean Optics USB2000+ spectrometer).

SHG signal from the two beams interacting was routed with a mirror to a fiber optic spectrometer (Ocean Optics USB2000+, OO-S). Intensity autocorrelation traces were generated by spectral integration of the signal from the OO-S, but more information is gained from the spectrally resolved signal which is discussed in the following section.

2.1.c.ii frequency resolved optical gating (FROG)

Frequency resolved optical gating (FROG) is akin to intensity autocorrelation with the addition of a spectrometer to spectrally resolve the resultant non-linear (NL) signal. The mechanism for detecting FROG varies depending on the NL signal generated⁶ but we focus our attention on second harmonic FROG (SH-FROG). A schematic for our SG-FROG device is shown in Figure 2.8. The SH-FROG signal intensity is generated from an interaction between the two replica input pulses,

$$F(\tau, \omega) = \left| \int_{-\infty}^{\infty} E(t)E(t-\tau)\exp(-i\omega t)dt \right|^2 \quad (2.2)$$

where the resultant signal intensity is mapped out as a function of both frequency (ω) and the time-delay (τ) between the two replica pulses. Figure 2.8 shows a typical SG-FROG trace collected for the CPA-1000 laser system. The electric field of the pulse $E(t)$ including phase information was extracted from the SH-FROG traces with the principal component generalized projections (PCGP) algorithm developed by Kane and coworkers⁶. Custom functions adapted from published code⁷ were developed in MatLab to implement the PCGP algorithm. The MatLab code for these functions can be found in Appendix A.4. The extracted pulse was fit to a Gaussian giving a FWHM of 60 fs with minimized spectral and temporal phase.

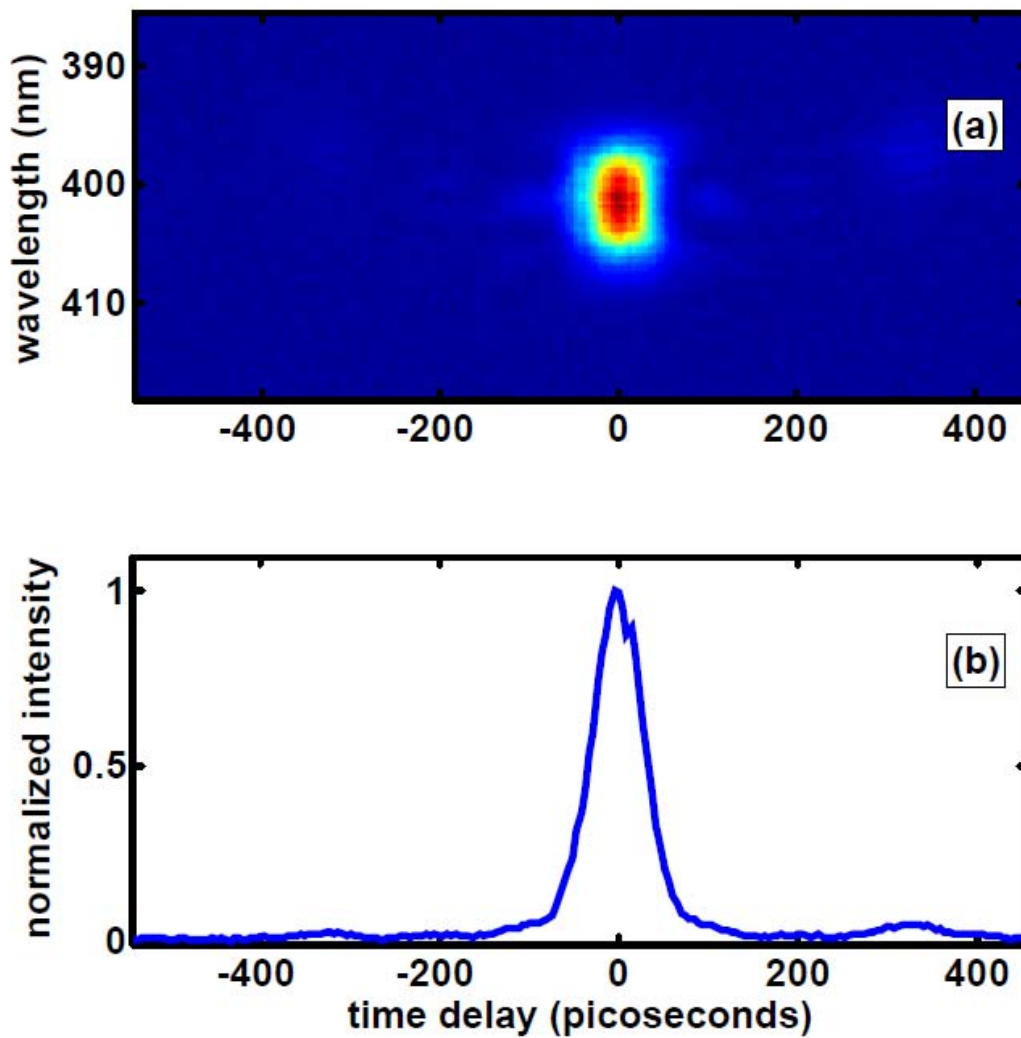


Figure 2.8 Typical SH-FROG spectrogram (a) and intensity autocorrelation trace (b) recorded for the CPA-1000 laser system.

2.2 Broadband Femtosecond Transient Absorption (BFTA) Apparatus

Figure 2.9 shows a schematic of the broadband femtosecond transient absorption apparatus. Input pulses from the CPA-1000 laser first impinged a second harmonic crystal (SHG) with fundamental (800 nm) and second harmonic (400 nm) separated with a dichroic beamsplitter. Both beams subsequently traversed down fused silica prism compressors (PC1, PC2) which precompensate for material dispersion incurred before white light continuum (WLC) generation (for the 800 nm pulses) and the sample position (for the 400 nm pulses). The second harmonic beam traveled down an optical delay stage (DS), through an optical chopper (chopper) and was attenuated with a $\lambda/2$ -linear polarizer pair (WP/POL) before being focused into the sample (sample) with a 250 mm focal length lens (L1). The 800 nm beam was attenuated with a $\lambda/2$ -linear polarizer pair (WP/POL) and focused with a 100 mm focal length lens (L2) into in a 2 mm CaF_2 plate (CaF_2) to generate WLC probe pulses. The resultant probe beam was collimated with a 100 mm focal length concave mirror (CM1) and focused with another 100 mm focal length concave mirror (CM2) into the sample. Samples flowed through a 0.5 mm path length flow cell using a peristaltic pump. After impinging the sample, the WLC probe beam was collimated with a 75 mm focal length acromatic lens (L3), spectrally filtered with a short-pass filter (SPF), polarization filtered with a linear polarizer (POL), and focused with a 50 mm focal length acromatic lens (L4) into a 200 μm fiber optic cable connected to a fiber optic spectrometer (OO-S). The transmitted 400 nm beam was focused onto a photodiode (PD) for pump pulse energy

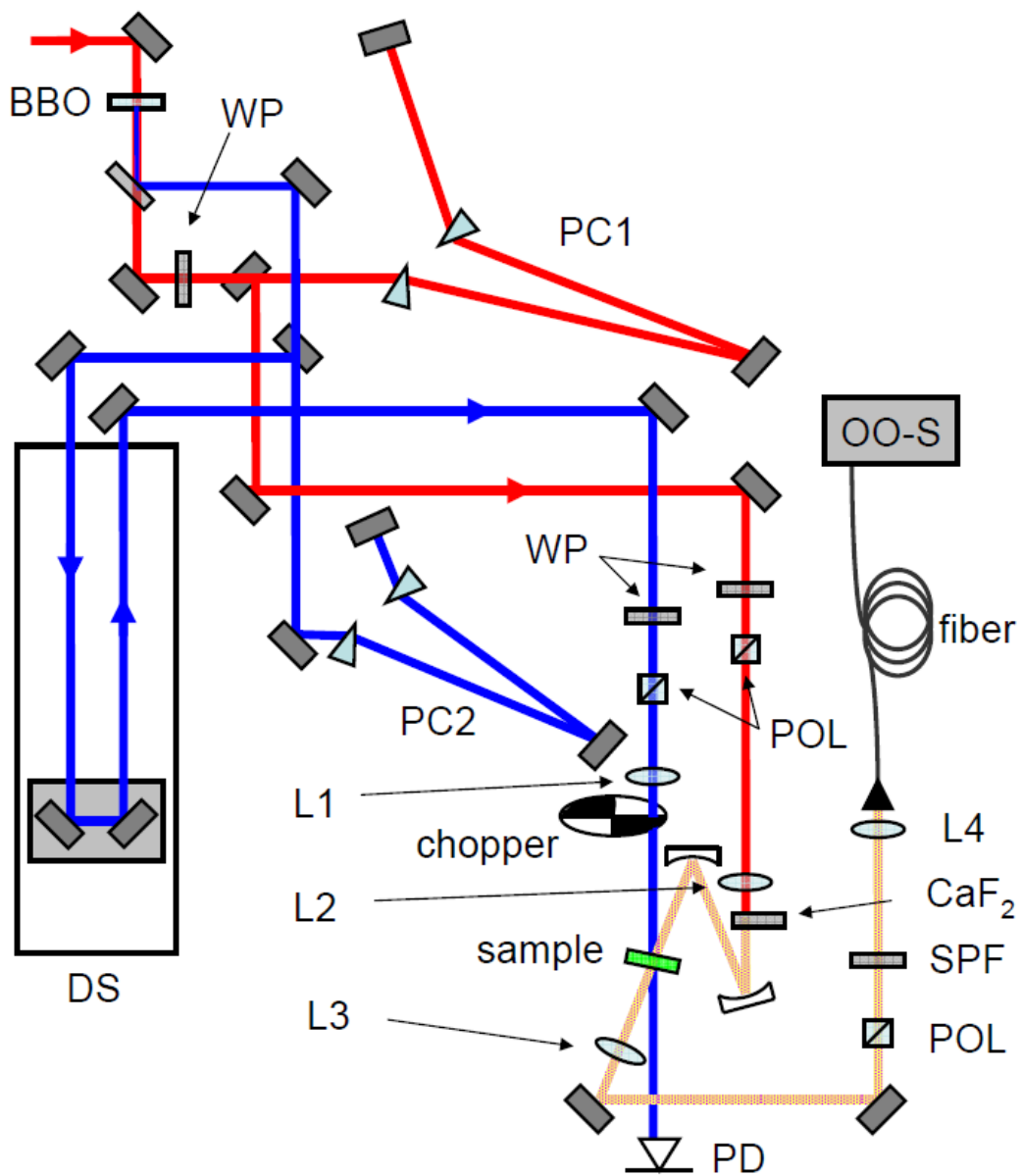


Figure 2.9 Broadband femtosecond transient absorption (BFTA) instrument. BBO (0.1 mm β -barium borate crystal); WP ($\lambda/2$ wave-plate); PC1-PC2 (fused silica prism compressors); DS (optical delay stage); POL (linear polarizer); L1-L4 (focusing and collimation lenses); PD (photodiode); CaF₂ (2 mm calcium fluoride plate); SPF (short pass filter); and OO-S (Ocean Optics spectrometer).

normalization. The following sections discuss the components of the BFTA apparatus in greater detail.

2.2.a Second Harmonic Generation (SHG)

Transient absorption spectroscopy has two basic requirements for pump pulses: (1) the pulse spectrum must overlap with the sample absorption spectrum, and (2) the pulse energy must be sufficient to reach the ground state absorption. For the case of the experiments outlined in this dissertation, we utilize samples that have absorption profiles that overlap with the second harmonic (SH) spectrum of the laser system giving pump pulse centered at approximately 400 nm. As mentioned in section 2.1.b, the laser system is slightly tunable (800 ± 25 nm) which gives a small degree of tunability in SH pump pulses (400 ± 12.5 nm) if needed. In regards to the second requirement, SH pump pulses with sufficient intensity are easily obtained from 400-500 μ J pulses of the CPA-1000 laser system.

SH pump pulses were generated in a 0.1 μ m Type I β -barium borate (BBO) crystal with a usable diameter of approximately 5 mm. BBO was selected because of its high damage threshold and high conversion efficiency (up to approximately 30%). The small thickness of the crystal minimizes the addition of dispersion to the generated SH pump pulse. Approximately 200 μ J pulses (800 nm) from the CPA laser system impinged on the BBO crystal generating 20 μ J SH pulses. Down collimation of the 800 nm beam was not required to fit the beam within the 5 mm BBO crystal aperture. The combination of the large beam size and the short path length of the BBO crystal gave an effective conversion efficiency of approximately 10% that fell well below the achievable

conversion efficiency of 30% but 20 $\mu\text{J}/\text{pulse}$ was more than sufficient to generate measurable BFTA signals.

2.2.b White Light Continuum (WLC) generation

Generation of stable WLC pulses in both spatial and spectral domains was integral to successful operation of the BFTA instrument as transient absorption signals are measured through intensity fluctuations in the probe beam spectrum. Therefore it was essential to generate WLC probe pulses with spectra that were highly stable. The most stable single-filament WLC pulses were generated when the spatial profile of the 800 nm beam was smooth and the temporal duration of the pulses was as short as possible in addition to appropriate focusing and beam attenuation. In addition, the temporal chirp of the WLC was minimized to simplify subsequent data analysis. The following methodology produced WLC pulses stable enough to measure absorption changes to approximately 0.001 absorbance units (1 mOD) with sub-picosecond durations. Figure 2.10 gives a schematic of the WLC generation scheme in the BFTA instrument discussed below.

The WLC generation threshold is material (CaF_2 , sapphire, glass, etc.) dependent, and it depends on the power density achieved in or around the focus of the beam. CaF_2 was chosen over the more commonly utilized sapphire for WLC generation as it yields WLC spectra which extends further into the UV than other materials. For CaF_2 , 1-2 μJ of energy was focused with a 100 mm focal lengths were typically utilized to generate single-filament WLC pulses. It was found that focal lengths of 100 mm or shorter were appropriate while focal lengths longer than 100 mm reduced the WLC

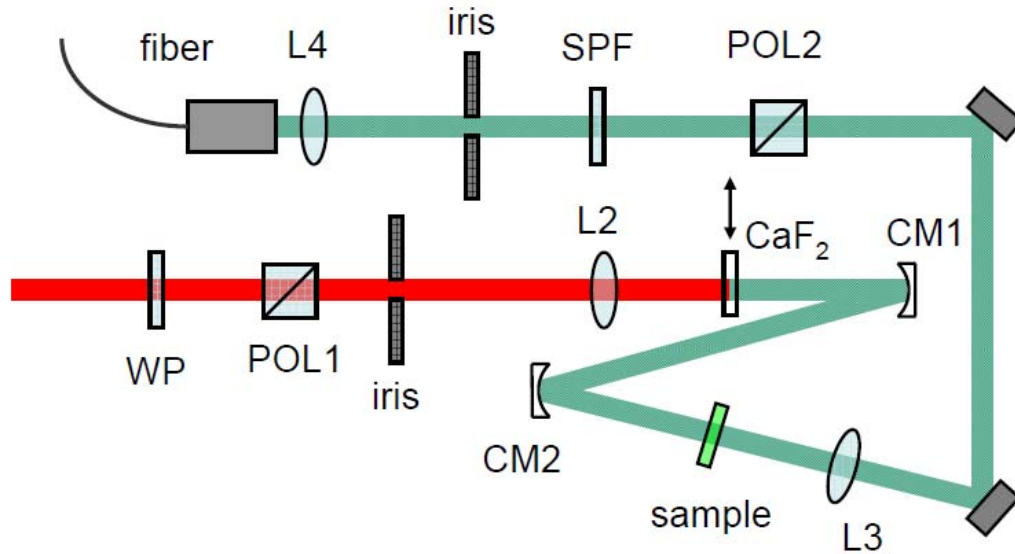


Figure 2.10 Detailed schematic of white light generation (WLG) and detection within the broadband femtosecond transient absorption (BFTA) instrument. WP ($\lambda/2$ waveplate); POL1-POL2 (linear polarizers); iris (adjustable iris); L2 (white light generation lens, 75 mm focal length); CaF₂ (2 mm calcium fluoride plate); CM1 (white light collimation curved mirror, 100 mm focal length); CM2 (white light focusing curved mirror, 100 mm focal length); L3 (white light collimation lens, 75 mm focal length achromatic); SPF (short pass filter, 750 nm cut-off); and L4 (fiber focusing lens, 25 mm focal length achromatic).

spectral intensity in the UV region thus reducing the broadband capability of the transient absorption instrument. In addition, longer focal lengths require more input 800 nm pulse energies after WLC generation which subsequently generated WLC in the sample. Placing the focus just beyond the CaF₂ crystal and increasing beam intensity slightly generally gave the most stable WLC beam/spectrum.

The spatial profile and the power density of the 800 nm continuum generation beam were controlled with an adjustable iris. The beam clipping provides crude yet effective spatially filtering which smoothes the beam profile while also providing an additional adjustment of the beam power density. In addition, focusing on the same spot on the CaF₂ for more than several minutes introduced spatial and spectral instability, and accordingly the CaF₂ crystal was mounted on a translation stage so that periodically a fresh spot on the crystal could be utilized for WLC generation.

The most sensitive parameter that effected stable WLC generation was the temporal duration and shape of the 800 nm femtosecond pulse. The shortest, “cleanest” pulses lowered the required beam energy and gave the most stable WLC spectrum which drastically improved the signal to noise ratio of the BFTA instrument. The 800 nm laser pulses introduced into the BFTA instrument were nominally 40-50 fs FWHM with near Gaussian temporal profiles. The prism compressor that the 800 nm beam traverses in the BFTA instrument (PC1) was configured to preserve the 40-50 fs FWHM duration and Gaussian temporal profile of the input laser pulses. Fine tuning of the pulse duration in the CaF₂ crystal was accomplished by attenuating the beam just below the threshold for WLC generation and adjusting the prism compressor to attempt

to generate WLC by shortening the 800 nm pulses. SG-FROG was used to characterize the WLC generation pulses, and they were found to be approximately 60 fs FWHM with near Gaussian profiles.

The final consideration in WLC was minimization of the temporal chirp. The WLC temporal duration and chirp depend on two parameters: (1) the temporal duration of the 800 nm continuum generation pulse and (2) the amount of material that the WLC propagates through before reaching the sample. The first parameter was addressed by minimizing the 800 nm continuum generation pulse duration pulse through optimizing the prism compressor. As previously mentioned, the pulse shape and duration of the 800 nm continuum generation pulses were characterized with FROG giving near Gaussian pulses with duration of approximately 50-60 fs FWHM. The amount of material that the WLC pulse propagates through was minimized by using only reflective optics to route and focus the WLC beam. Furthermore, the routing/focusing consisted of only two 100 cm focal length concave mirrors: one mirror collimated the WLC beam after generation in CaF_2 and the other focused the WLC beam into the sample. Thus the material that the WLC pulses propagated through before reaching the sample was minimized to the continuum generation crystal (CaF_2), air, and the flow cell window (fused silica). Minimization of the continuum generation pulse duration and the material the continuum pulse propagated through gave WLC pulses with sub-picosecond durations.

2.2.c Pump/Probe Spatial Overlap

Spatial overlap of the pump and probe beams at the sample was an important consideration in the BFTA experiment. Samples flowed through a 0.5 mm path length flow cell with a peristaltic pump (Cole Palmer Model Masterflex PTFE Tubing Pump 77390-00). Flowing samples increased the magnitude of the signal by avoiding local bleaching at the focus. Flow rates varied from 5 – 20 mL/min. The SH pump and WLC probe beams were focused into the sample under varying conditions. The WLC beam was focused with a 100 mm focal length curved mirror into the sample while the SH pump was focused with a 250 mm focal length lens. Under these conditions, the WLC beam focal spot was smaller than and fit within the SH pump focal spot. This insured the largest BFTA signal magnitude and avoided unwanted non-linear effects generated by the SH pump beam. Unwanted NL effects were manifested in only the SH pump beam.

Many unwanted non-linear effects manifest themselves with tight focusing of ultrafast pulses into liquid and solid materials. Non-linear effects are exploited to generate the WLC pulses, but in the case of SH pump focusing into the sample, non-linear effects were minimized. The dominant non-linear effects were WLC generation from and self-focusing of the SH pump in the sample. These two non-linear effects generated unstable BFTA signals as they distorted the SH pump beam profile and generated increased scattered SH pump light.

NL effects from the SH pump were avoided by using a 250 mm focal length lens and placing the focus of the SH beam slightly beyond the sample (closer to the

photodiode, PD). In this configuration, the available SH pulse energy was not sufficient to generate WLC and induce self-focusing. It is important to note that the threshold for these effects occurred at lower pulse energies as the pulse duration become shorter. This effect was used to optimize the configuration of the SH pump prism compressor (PC2) giving sub-100 fs SH pump pulse durations.

2.2.d Time-Delay Control

Relative delay between the WLC and SHG pulses was generated by advancing or delaying the pump pulse arrival time at the sample with an optical delay line consisting of a stepper motor driven translation stage purchased from Physik Instrumente Model PI M 531.5i (PI stage) and a custom retro-reflection mirror mount. The PI stage had a total travel distance of 300 mm with minimum step size of 0.1 mm which corresponds to over 2 nanoseconds of time delay with a resolution of 0.667 fs. The retro-reflector consisted of two mirrors that were oriented 90 degrees relative to each other and 45 degrees with respect to the incoming and exiting beams. This configuration horizontally displaced the incoming beam approximately 105 mm. The PI stage stepping was controlled though a serial port connection (RS-232) with the data collection computer. The PI utility program "PI New Lance" was used to position and define the zero position in experimental setups. Custom programs in both LabView (Version 8.0) and MatLab (Release 2009a) were developed to sequentially step the stage position (delay time) while collecting data. It was found that the MatLab programs were more robust and flexible than the equivalent LabView programs. In the course of this software

development it was found that spacing the delay points logarithmically in time was highly advantageous⁸ and it is the subject of the following chapter.

2.2.e Signal Modulation and Detection

Transient absorption measurements such as those using the BFTA instrument require a reference signal to isolate the transient signal. In the BFTA instrument, a reference signal was generated by blocking the pump pulse and measuring the intensity of the probe spectrum. This reference intensity was compared with the intensity of the probe spectrum through the relation,

$$S(\nu, \tau) = \log \left(\frac{I_{sig}(\nu, \tau)}{I_{ref}(\nu, \infty)} \right) \quad (2.3)$$

which isolates the transient absorption signal from the probe beam spectrum. An optical chopper (Palo Alto Research Model 300 Super Chopper) synchronously blocked and unblocked the pump beam for measurement the reference ($I_{ref}(\nu, \tau)$) and signal ($I_{sig}(\nu, \tau)$) probe spectra respectively. The chopper was synchronized with both the 1 KHz laser pulse train and the spectrometer integration window. The spectrometer response time limited the chopping frequency to 50 Hz which corresponds to 5 pulses per spectrum. The 1 KHz pulse train gave sufficient time (1 ms) for the samples to relax back to equilibrium, and thus each signal and reference spectrum consisted of 5 accumulated measurements of $S(\nu, \tau)$.

Spectra were collected with a fiber optic spectrometer purchased from Ocean Optics Model USB2000+ (OO-S) which is capable of measuring spectra from 350 nm to 1050 nm. The OO-S spectrometer was interfaced to the data collection computer

through a USB connection and operated with custom programs in LabView and MatLab. The OO-S spectrometer was triggered by pulses generated in a digital delay pulse generator (Stanford Research Systems Model DG535). The OO-S spectrometer ran in “synchronous” mode where the trigger pulse low to high edge initiated the integration window and the high to low edge terminated the integration window. Slight adjustments to the timing between the integration window and the chopping window were controlled with the phase adjustment of the chopper to ensure five laser pulses were cleanly measured. The OO-S operation manual gives greater detail on external triggering options and procedures⁹.

2.2.f Polarization / Attenuation Control and Monitoring

The BFTA instrument was capable of measuring molecular reorientation dynamics through polarization control experiments. In these experiments, the BFTA signal was collected with (1) the pump polarization oriented parallel to the probe polarization and (2) the pump polarization oriented perpendicular to the probe polarization. If measured out to long enough delay times, these two extreme measurements contained all the molecular reorientation dynamics for a given sample.

Molecular reorientation dynamics are calculated as,

$$r(\tau) = \frac{I_{\parallel}(\tau) - g \cdot I_{\perp}(\tau)}{I_{\parallel}(\tau) + 2g \cdot I_{\perp}(\tau)} \quad (2.4)$$

where g is an adjustable factor that matches the intensity of I_{\parallel} and I_{\perp} at long delay times where reorientation dynamics have concluded. Typical g values deviated only slightly from unity if the pump beam energy is normalized between I_{\parallel} and I_{\perp}

measurements. To experimentally approach this normalization condition, the attenuated pump beam energy that transmitted through the sample was measured with a photodiode (ThorLabs DET210) and the resultant signal was integrated in time with a gated boxcar integrator (Stanford Research Systems, Model 250). The integrated signal was monitored on an oscilloscope (Tektronix, Model 2465B). The integrated signal was approximated as a square wave which represents the pump-on (high) and pump-off (low) conditions and the pump pulse energy is proportional to the difference between the high and low conditions. From this signal, the relative pulse energy between the parallel and perpendicular pump pulse excitation conditions was normalized. This normalization method was important in cases where the reorientation dynamics exceeded the 2 ns time delay limit of the BFTA instrument.

2.3 Data Collection Operations

2.3.a MatLab Software

The source code for the BFTA instrument Matlab (Release 2009a) software is presented in Appendix A. This code contains all of the data collection, instrument control, and data analysis functions and sub-functions. The following sections outline the basic principles of the software operation.

2.3.a.i time-delay stepping

In the BFTA instrument, adjustable time-delay between the pump and probe was introduced by advancing or retarding the pump pulse arrival at the sample through translating the PI stage. The PI stage was connected to the data collection computer with a serial connection (RS-232) and the data collection computer ran through

Windows XP. Software including LabView drivers, Windows DLL files, and a utility program came with the purchase of the PI stage. Windows DLL files were loaded into MatLab and were used to access all of the necessary stage control functions for data collection. These basic functions of the PI stage were (1) define home (DH); (2) go home (GH); (3) move relative (MR), and (4) move absolute (MA). DH was used to establish the zero or time-zero position where the pump and probe pulses overlapped in time, and GH/MR/MA functions were used during data collection to position the stage at specific delay positions. The resolution of the stage was 0.1 μm which corresponded to 0.667 fs of delay.

Two different stepping methods were used during BFTA data collection. We used linear and/or logarithmic stepping and the selection of the two stepping methods depends on the relevant dynamics of interest. For dynamics that span a few orders of magnitude in time linear stepping is more appropriate while dynamics over many orders of magnitude in time (e.g. fs to ns) logarithmic stepping is more appropriate. In some cases a combination of the two methods is the most efficient approach to data collection. Estimated time steps for linear stepping are calculated as,

$$d_n = n \cdot dn$$

$$dn = \left(\frac{d_{stop}}{N-1} \right) \quad (2.5)$$

and for logarithmic stepping,

$$d_n = 10^{n \cdot dn}$$

$$dn = \log_{10} \left(\frac{d_{stop}}{N-1} \right) \quad (2.6)$$

where n is the data point index, dn is the stepping constant, d_{stop} is the final delay position, and N is the number of data points. From these input functions, we calculated the actual stage steps for each discrete time-delay point (D_n) as,

$$D_n = \mathbf{int} \left(\frac{d_n}{dt} \right) dt \quad (2.7)$$

where dt is the stage resolution, d_n is the input data point, and \mathbf{int} indicates rounding to the nearest integer value. Dividing the resultant time-delay vector by dt gave the stage-position vector (integer values) which was directly implemented with the PI stage functions (MR/MA). The functions that performed these calculations including interfacing to the PI stage are listed in Appendix B.3.

2.3.a.ii spectra collection

The OO-S was operated through MatLab by purchasing Ocean Optics OmniDriver software. This software controls multiple USB spectrometers through a Java platform which is easily implemented in MatLab. Spectra were collected from the OO-S in a synchronous triggered mode through an input digital pulse. In this mode, the integration period was determined by the rising and falling edges of the trigger pulse. Two basic functions were used to operate the OO-S, (1) initialization of the OO-S which extracted the wavelength vector from the spectrometer and placed the OO-S in synchronous triggering mode; and (2) spectra collection. The source code for the OO-S operation is located in appendix A.2. Signal processing of the raw spectra including calculation of the BFTA signal (equation 2.3) were performed with the code in appendix A.4.

Raw probe spectra were collected synchronously with respect to pump pulse chopping at a rate of 200 Hz. The OO-S triggering and integration window were controlled with a square pulse generated from the DG535 digital pulse generator which was synchronized with the 1 KHz CPA-1000 laser pulse train. This corresponds to the “synchronized” triggering option for the OO-S. The integration period was approximately 5 ms which integrated over 5 probe pulses. The chopping frequency was 100 Hz and its phase was adjusted to match the OO-S integration period timing. With the phase selected correctly, two sequential spectra recorded from the OO-S represent spectra collected with the pump-on (signal spectrum, I_{sig}) and pump-off (reference spectrum, I_{ref}) or vice versa. There was no control over the ordering of I_{sig} and I_{ref} so other precautions were needed to ensure that the sign of the calculated BFTA signal (from equation 2.3) remained consistent. Failure to take these precautions resulted in inconsistent BFTA spectral intensities.

The simplest and most effective method developed to keep I_{sig} and I_{ref} consistent throughout data collection was to force the sign of the signal at a particular wavelength to be constant as a function of time. This function was performed by first dividing the calculated BFTA signal at a particular wavelength by its absolute value which determined the absolute sign of the BFTA signal. With the absolute sign known, the BFTA signal could be forced to be positive or negative accordingly to keep the sign of all collected BFTA spectra consistent. One caveat to this approach was the selection of a wavelength where the time-dependent signal did not change sign, in this case forcing the sign to be positive or negative becomes uncertain where the signal crosses zero. In

most cases this was not an issue because a wavelength was selected that had a constant sign as a function of time-delay. Sign consistency was integral to successful signal averaging.

2.3.a.iii signal averaging

Two approaches were utilized to increase the signal to noise (S/N) ratio through signal averaging. The first method was to increase signal averaging for each BFTA spectrum that was collected. The second method averaged spectra collected as separate experiments or “runs.” Increased signal averaging at each time-delay point tended to be very efficient in smoothing collected spectra, but inconsistencies between time-delay points remained. Using multiple runs tended to smooth spectra between time-delay points and thus the entire BFTA data set, but it was time consuming. The best results were obtained with modest averaging (4, 9, or 16) at each data point and averaging over 2 to 3 separate runs. To further increase data collection efficiency, time steps in the forward (positive time steps) and backward (negative time steps) directions were implemented to reduce the wait time for the PI stage to return to the time-zero position.

2.3.b LabView software

One program, “getSpectra,” was developed in LabView to monitor the probe spectrum. This program interfaced to the OO-S and continuously displayed the spectra collected from the OO-S in real-time. This program was used as a diagnostic to tweak the alignment of the probe beam into the OO-S and determine its stability. Furthermore, it was used to determine the approximate cut-off wavelengths (pixel

numbers) for data collection in MatLab. This program was also used to measure the CPA-1000 laser spectrum and the pump spectrum.

2.3.c Data Collection Operations

2.3.c.i signal optimization

The following steps assume that the probe beam spectrum reaching the OO-S has been optimized. The first step in BFTA data collection was to locate and optimize the BFTA signal. These tasks were easily accomplished through the use of a sample that had a strong BFTA signal. A typical sample utilized was 1×10^{-3} M coumarin 153 (C153) in acetonitrile. With this C153 or a similar sample, the focused pump and probe beams could be visually overlapped in the sample by translating the x and y position of the pump focusing lens (PFL). The relative time-delay between the pump and probe was increased to a maximum by translating the PI stage to its furthest positive position. At this point, the MatLab function “signalweek” was used to continuously display the measured BFTA signal. This signal strength was maximized by translating the x and y position of PFL.

2.3.c.ii time-zero determination

From the optimized BFTA signal, time-zero was easily established. The PI stage was translated backwards (toward time-zero) from its maximum delay position while monitoring the BFTA signal. The signal was monitored with “signalweek” and the PI stage was translated with its utility program “NewLance.” Time-zero was defined to be approximately 50 fs before the onset of any BFTA signal. At or before time-zero, the

BFTA signal measured contained only contributions from steady-state emission if the sample was strongly emissive otherwise the BFTA signal averaged to a baseline of zero.

2.3.c.iii emission spectra

The BFTA spectrometer easily measured emission spectra by blocking the probe beam and recording the BFTA signal. The recorded signal was proportional to the steady-state emission spectrum excited at the pump wavelength (centered at approximately 400 nm).

2.3.c.iv polarization anisotropy measurements

BFTA data was collected under the parallel and perpendicular polarization conditions between the pump and probe beam. Data collected in this fashion contain all of the relevant information to calculate the reorientation dynamics and reorientation free BFTA signals. Section 2.2.e outlines the procedure that was used to normalize the parallel and perpendicular BFTA spectra. Briefly the pump pulse energy between the parallel and perpendicular polarization conditions was normalized by rotating the pump beam $\lambda/2$ waveplate (PWP) and monitoring the transmitted pump pulse energy. The integrated signal intensity was matched to the reference intensity (vertical cursor on the oscilloscope) determined from the previous polarization condition. Reorientational free spectra were calculated from the parallel and perpendicular BFTA signals as,

$$S(\nu, \tau) = \frac{1}{3} (S_{\parallel}(\nu, \tau) + 2 \cdot S_{\perp}(\nu, \tau)). \quad (2.8)$$

From this data, a number of analysis procedures were used to extract further dynamical information.

2.3 Data Analysis Methods

2.4.a Lifetime Corrections

Data collected out to the 2 ns limit of the BFTA instrument exhibits decay in the signal due to the finite lifetime of the excited electronic state. A simple procedure was developed to minimize the lifetime decay contribution to the time-dependent BFTA signal. This procedure is as follows: Each spectrally resolved BFTA signal was integrated to yield a single time-dependent trace. This trace was fit to a single exponential from approximately 100 – 2000 ps giving the excited state lifetime decay constant (τ_L). τ_L was used to “lifetime correct” BFTA spectra through,

$$S_L(\nu, \tau) = \frac{S(\nu, \tau)}{\exp[-\tau/\tau_L]}. \quad (2.9)$$

This approach approximately accounts for the finite decay from the excited-state population introduced by the pump pulse excitation. Furthermore, it also provides an estimate of the excited-state lifetime decay constant which was useful to examine environmental impacts on the chromophore.

2.4.b Reorientation Dynamics

Molecular reorientation dynamics were extracted from BFTA data via two methods. The simplest method was to extract a single wavelength trace from the both the parallel and perpendicular spectrograms and calculate the reorientation dynamics from equation 2.4. This method worked quite well when the spectrogram signal to noise ratio was high, but in other cases an additional method was required. To increase the signal to noise of the extracted reorientation dynamics we average over a number of

wavelength traces. The best results were obtained when the wavelength range was chosen to overlap with the strongest signal present in the BFTA data. Care was taken to not integrate the signal over too large of a wavelength window as uncertainty in early time was introduced to the finite chirp (distribution of time-zero across the bandwidth) of the probe pulse. In most cases integration over such broad bandwidths was not required to increase the signal to noise ratio sufficient for dynamical analysis. The Matlab function “anisotropy” (Appendix A.IV) performs all of the previous calculations from input parallel and perpendicular BFTA spectrograms.

Analysis of molecular reorientation dynamics followed a number of procedures which depended on the complexity of the extracted data. The simplest reorientational behavior is represented by a single exponential which reflects simple diffusion in all rotational degrees of freedom (spherical rotor). In this case, the rotational diffusion constant (D_{rot}) is calculated from the fitted reorientational time-constant (τ_{or}) as $D_{rot} = 1/6\tau_{or}$.¹⁰ For most chromophores dissolved in liquids, this analysis is adequate, but for more complex systems such as the reverse micelle (RM) systems reorientational dynamics do not exhibit single exponential behavior and therefore analysis requires more complex models.

Reorientation dynamics that deviate from a single-exponential decay to zero can be described by the wobble-in-a-cone model¹¹⁻¹³ which describes the reorientational decay as,

$$r(t) = \left(Q^2 + (1 - Q^2) \exp[-t/\tau_c] \right) \exp[-t/\tau_{or}] \quad (2.10)$$

where τ_c and Q^2 quantify the wobbling motion within the cone, and τ_{or} is the normal reorientation time-constant. Q^2 values range from 0 to 1 which traverse the unrestricted to fully restricted reorientational motion limits respectively. The semi-cone angle (θ) of the restricted motion is calculated from Q as,

$$Q^2 = \left[\frac{1}{2} (\cos \theta) (1 + \cos \theta) \right]^2. \quad (2.11)$$

This model worked very effectively to quantify the reorientational dynamics observed in RM systems that deviated from single-exponential decay behavior.

2.4.c Stokes Shift Dynamics

Stokes shift dynamics were extracted from BFTA data through a few different methods. It can be difficult to extract solvation dynamics from BFTA data due the complexity of the signal. This complexity arises from three fundamental contributions to the total TA signal: excited-state absorption (ESA), stimulated emission (SE), and ground-state bleach (BL). Solvation dynamics are manifested as time-dependent spectral shifts in the ESA and SE signals added to the generally constant BL signal. The simplest method to extract solvation dynamics from BFTA is to track the maximum of the signal maximum frequency shift. The MatLab function “extractmax” (appendix A.IV) extracts the frequency shift of the maximum of the BFTA data. “extractmax” fits the maximum of the BFTA data to a third-order polynomial and calculates the fitted maximum frequency as a function of time-delay.

2.4.c.i spectral lineshape fitting method

If the ESA/SE/BL signals can be individually distinguished, the total signal can be fit to a sum of peaks,

$$S(\nu) = \sum_n S_n(\nu) \quad (2.12)$$

where $S_n(\nu)$ is the particular spectral lineshape function (Gaussian, Lorentzian, Voigt – symmetric or asymmetric). We choose to represent each contribution to the total BFTA signal as asymmetric Gaussians,

$$SE(\nu) = a \cdot \exp \left[- \left(\frac{\nu - \nu_0}{\Gamma - s \cdot (\nu - \nu_0)} \right)^2 \right] \quad (2.13)$$

where a is the amplitude, p is the peak position, Γ is the width and s is the symmetry parameter. Solvation dynamics were quantified through the SE peak position (ν_0) and also the first moment of the asymmetric Gaussian,

$$M_1 = \nu_0 + \ln 2 \cdot s \cdot \Gamma \quad (2.14)$$

In many cases fitting the BFTA data in this manner was not possible because of overlapping ESA, SE, and BL signals and thus a different approach is needed to extract the time-dependent spectral shifts within the data.

2.4.c.ii spectral first derivative (SFD) method

One global method that is purely numerical and does not require a specific functional form is what we name the spectral first derivative (SFD) method.¹⁴ This method approximates the time-dependent TA signal as a linear combination,

$$S(\nu, \tau) = \alpha \cdot S_0 + \beta \cdot dS_0 \quad (2.15)$$

where S_0 is an early-time TA spectrum; dS_0 is the first derivative of S_0 with respect to frequency ($dS_0/d\nu$); and α, β are scalar quantities that vary with τ . α tracks amplitude changes in the total signal arising from excited-state lifetime decay, and β tracks frequency shifts in the data due to the dynamic Stokes shift. α and β are determined by least-squares fitting and they are the only two adjustable parameters in the fit.

2.4.c.iii singular value decomposition (SVD) method

The final method used to extract solvation dynamics from BFTA data was singular value decomposing (SVD). SVD decomposes 2-dimensional (2D) matrix data \mathbf{X} into three sub matrices,

$$\mathbf{X} = \mathbf{U}\mathbf{S}\mathbf{V}^{-1} \quad (2.16)$$

If \mathbf{X} is $m \times n$ and $m > n$, then \mathbf{U} is $m \times m$; \mathbf{S} is $m \times n$; \mathbf{V} is $n \times n$. In our case, m is the spectral dimension and n is the temporal dimension. Application of SVD methodology is a purely numerical procedure that does not assume functional forms in either the spectral or temporal domains. SVD analysis separates contributions to transient data into spectral and temporal basis functions in the columns of \mathbf{U} and in the columns of \mathbf{V} respectively. Each column in \mathbf{U} and \mathbf{V} is linked by the diagonal values contained in \mathbf{S} . Thus the columns of \mathbf{U} contain the spectral components which that grow or decay according to the temporal components in \mathbf{V} which are weighted by the respective singular values along the diagonal of \mathbf{S} . The singular values indicate the relative

weighting of each spectral component in the total BFTA spectrogram. It should be noted that global analysis of BFTA data through SVD is always useful to identify the number of significant contributions to the time-evolution of the data (the magnitude of the values along the diagonal of \mathbf{S}), but noise present in the data can significantly alter the extracted time-dynamics (\mathbf{V}) of the spectral contributions (\mathbf{U}). Therefore SVD is not always the best global analysis method of BFTA data and it must be used with caution.

2.4.d Deprotonation Dynamics

Extracting deprotonation dynamics from BFTA data followed similar methods as the previously described techniques. The simplest technique that was utilized was to analyze single wavelength traces. Analyzing data in this fashion is sufficient to extract the timescales of the dynamics present in the data, but it lacks the ability to reliably report the amplitudes of the various temporal components. These inconsistencies are greatly minimized through the use of global analysis methods.

For some HPTS data, the solvation and deprotonation timescales overlap, and in these cases we use a simple method to measure the deprotonation dynamics. Solvation dynamics are typically characterized by spectral shifts of SE and/or ESA bands. If one assumes that these shifts preserve the integrated intensity of each band, the SD contribution to the BFTA signal can be minimized via spectral integration,

$$I(\tau) = \int S(\nu, \tau) d\nu. \quad (2.17)$$

This method isolates deprotonation dynamics contributions and it is effectively a simple global analysis method because of the broadband nature of the total BFTA signal.

Despite this, spectrally resolved analysis can yield greater insight and thus a few additional global analysis methods are employed. As established in the previous section, SVD methods are a very powerful and simple way to analyze BFTA data globally without assuming specific spectral or temporal functional forms. A more rigorous approach was to use method that used the concepts from the SVD method.

This analysis method for Stokes shift and deprotonation dynamics has been discussed in detail in the literature, but here we highlight the important aspects. Spry et al.¹⁴ have developed a simple global analysis method for HPTS dynamics, which approximates the time-dependent spectrum of HPTS/water transient absorption data as a linear combination of the protonated (P), deprotonated (D), and derivative of the protonated spectrum (dP), according to the equation:

$$S(\lambda, t) = \alpha(t) \cdot P + (1 - \alpha(t)) \cdot D + \beta(t) \cdot dP \quad (2.18)$$

where $\alpha(t)$ tracks the time-dependent population change between the protonated and deprotonated states yielding the deprotonation dynamics while $\beta(t)$ follows the dynamic Stokes shift of the protonated spectrum. This method gives a very effective way to extract both Stokes shift and deprotonation dynamics from BFTA data.

References and Notes

- (1) *Instruction Manual: Model TS Ti:sapphire laser kit*; Kapteyn-Murnane Laboratories L.L.C: Boulder, CO, 1999.
- (2) Martinez, O. E. *IEEE Journal of Quantum Electronics* **1987**, QE-23.
- (3) Treacy, E. *IEEE Journal of Quantum Electronics* **1969**, 5, 454.

- (4) Moore, J. H.; Davis, C. C.; Coplan, M. A. *Building Scientific Apparatus: A Practical Guide to Design and Construction*, 3rd ed.; Westview Press: Boulder, CO, 2003.
- (5) Webb, C. E.; Jones, J. D. C. *Handbook of Laser Technology and Applications: Laser design and laser systems*; Institute of Physics Publishing: Philadelphia, PA, 2004; Vol. 2.
- (6) Trebino, R. *Frequency-Resolved Optical Gating: The Measurement of Ultrashort Laser Pulses*; Kluwer Academic Publishers: Norwell, Massachusetts, 2000.
- (7) Kane, D. J. *IEEE Journal of Quantum Electronics* **1999**, *35*, 421.
- (8) Cole, R. L.; Barisas, B. G.; Levinger, N. E. *Review of Scientific Instruments* **2010**, *81*, 093101.
- (9) *USB2000+ Fiber Optic Spectrometer: Installation and Operation Manual*; Ocean Optics Inc.: Dunedin, FL, 2010.
- (10) Fleming, G. R. *Chemical Applications of Ultrafast Spectroscopy*; Oxford University Press: New York, 1986.
- (11) Kinosita, K.; Kawato, S.; Ikegami, A. *Biophysical Journal* **1977**, *20*, 289.
- (12) Lipari, G.; Szabo, A. *Biophysical Journal* **1980**, *30*, 490.
- (13) Piletic, I. R.; Moilanen, D. E.; Spry, D. B.; Levinger, N. E.; Fayer, M. D. *Journal of Physical Chemistry A* **2006**, *110*, 4985.
- (14) Spry, D. B.; Goun, A.; Fayer, M. D. *Journal of Physical Chemistry A* **2007**, *111*, 230.

CHAPTER 3

LOGARITHMIC BASED STEPPING ALGORITHM FOR TIME-RESOLVED DATA COLLECTION

A method has been established that generates values spaced according to a mathematical function, specifically the logarithm function that can be applied to a stepper motor. Here, it is applied to yield logarithmically spaced time delay points for subnanosecond interferometric time-resolved experiments using a stepper motor controlled translation stage. Application of this method is discussed in terms of three input parameters: the optical delay stage time resolution, dt ; the time of maximum delay, d_{stop} ; and the desired number of data points, N . The method improves the efficiency of interferometric time-resolved data collection while providing data collection effective to determine decay parameters. In principle, this technique could be generalized to any mathematical function. This work has been published (*Rev Sci Instr* **2010** 81 093101). All of the experimental work and analysis was performed by RLC except for the statistical analysis portion (Sections 3.2.C and 3.3.C) which were contributed by B. George Barisas.

3.1 Introduction

One of the most widely used experimental methods to achieve subnanosecond time resolution in time-resolved spectroscopy enlists optical gating using a Michelson interferometer.¹ Current optical gating interferometry experiments routinely collect data with femtosecond resolution and have recently crossed into attosecond regime.^{2,3} The ultimate, achievable time resolution of the optical gating interferometry method depends on both the duration of the optical gate and the finite delay introduced by the variable path arm of the interferometer. Advances in subnanosecond pulsed laser technology have pushed optical pulse durations from picoseconds to femtoseconds.^{4,5} At the same time, advances in state-of-the-art piezoelectric nanositioning technology provide stepping of nanometers yielding sub-femtosecond resolution.^{6,7} Thus subnanosecond time-resolved experiments using optical gating interferometry methods can measure time-dependent data from attoseconds to nanoseconds.

For many physical, chemical and biological systems, the dynamical response extends over several orders of magnitude. Thus, it is desirable to collect data over a range of timescales *e.g.* femtoseconds to nanoseconds.⁸⁻¹⁰ Collecting data over many decades of time introduces a unique challenge to experimentalists utilizing optical gating interferometry methodology. To capture and accurately measure the shortest time dynamics, data must be collected at a sufficiently high stepping resolution to follow the changes in experimental observables. However, utilizing this high resolution for an entire data set over many orders of magnitude leads to exceedingly long data acquisition times and large data files. Without proper weighting of the data, the high

density of points at long times can improperly emphasize slower processes. So how does one economically collect data over orders of magnitude of time delay with sufficient temporal resolution? The most common and simplest approach to address this challenge is to divide the data collection into timescales utilizing increasing step sizes for longer delays. For instance, for a process occurring over fs to ns, on the shortest timescale data points are collected with femtosecond resolution, followed by an intermediate timescale collected with picosecond resolution and finally on the longest timescale, data are collected with nanosecond resolution.⁸⁻¹⁰ This approach breaks the data collection into regions based on the change in the experimental observable. Thus when the observable is changing rapidly with respect to time delay, the data is recorded at a high time resolution and as the observable changes become smaller the stepping resolution is reduced. This method increases the efficiency of data collection, but it is not the most efficient approach to collect data over many decades of time delay. Furthermore, this method does not necessarily reflect the timescales of the dynamics. The most efficient and appropriate method to collect exponentially decaying data is to divide a given number of data points evenly over the entire time delay range *i.e.* space the points logarithmically.

Here we present a method that maximizes the data collection efficiency with logarithmic based stepping for time-resolved experiments. Although we have devised this method to follow a logarithmic function, in principle this method could be generalized to any mathematical function. Additionally, this method can be applied to any application utilizing a computer controlled stepper-motor driven device. This paper

is organized as follows: Section 3.I outlines general approaches to generating time-resolved data. Section 3.II discusses our logarithmic based delay methodology including a statistical analysis of the method. Section 3.III presents sample data collected with logarithmic based stepping and its evaluation, and Section 3.IV summarizes the paper.

3.2 Logarithmic Based Delay Stepping

Logarithmic based delay stepping provides some advantages over traditional linear stepping methods including more efficient collection of data with improved focus on key parameters of the data. The root advantage of logarithmic stepping arises in relation to the most common time-dependent observables. Specifically, many time decaying signals follow first order kinetics or exponential decay. This translates into dynamics that follow the time variable with a logarithmic dependence, thereby validating a logarithmic-based data collection technique. The data collected with a logarithmic time scale are weighted according to underlying kinetics, yielding an even distribution of data points over a time interval of interest. One important consequence of this scaling is that it reduces the total number of data points needed for a given data set, which speeds data collection.

Our algorithm for logarithmic stepping allows the user to choose the total desired number of data points collected for a single scan in time. For instance, a given interval of 100 ps recorded with even 100 fs steps generates a fixed 1000 data points. Using logarithmic stepping, the user could choose to collect 1000 data points; however, because the point density varies by decade, far fewer points would be needed to obtain

enough data to effectively define the decay characteristics of the data. Thus, the logarithmic stepping algorithm generates a user-selected number of data points which can optimize the number of data points compared to linear evenly spaced steps. Logarithmic stepping provides a huge time saving advantage over linear methods when data is collected over many decades of time delay.

3.2.a Logarithmic Delay Algorithm

In Chapter 2 (Section 2.3.A.i), a general description of stepping methods was introduced, here we present logarithmic stepping in greater detail. Our logarithmic based time stepping algorithm calculates approximate logarithmic time steps using three input parameters, the stage time resolution, dt , the final delay, d_{stop} , and the desired number of data points, N . The time delay at each data point is calculated from the exponential function,

$$d_n = 10^{n \cdot dn} \quad (3.1)$$

where n denotes the index of the data point. dn is a constant that depends on d_{stop} and N ,

$$dn = \log_{10} \left(\frac{d_{stop}}{N-1} \right) \quad (3.2)$$

From equations 3.1 and 3.2, logarithmically spaced data points are calculated. The actual time delay values possible are limited by the linear resolution of the stepping stage. Therefore, the actual time delay or logarithmic stepping values at each step is calculated as,

$$D_n = \text{int} \left(\frac{d_n}{dt} \right) dt \quad (3.3)$$

where dt is the time step resolution defined by the stepper motor driven stage and int indicates rounding to the nearest integer value. Using this function, logarithmic stepping values are generated to position the stepper motor driven stage for each data point in subnanosecond interferometric time-resolved experiments. The following section illustrates examples of the application of our logarithmic based stepping algorithm highlighting the advantages of this stepping method as well as some of its limitations.

3.2.b Advantages and Limitations

One clear advantage of logarithmic based stepping lies in its ability to collect data points over many decades of time delay ,*e.g.*, from femtoseconds to nanoseconds, with spacing between the points that is proportional to the order of magnitude of the time delay. Furthermore, logarithmic stepping introduces a fixed number of data points that does not depend on the starting and stopping conditions. Figure 3.1 shows a comparison of linear stepping (upper trace) versus logarithmic stepping (lower trace) for a fixed number of data points ($N = 150$) from 0 to 1 ns. Linear stepping fixes dt at all time delays which can, as in this example, provides inadequate resolution at short delay times to capture the short time dynamics while providing too many points at the longest delay times. In contrast, logarithmic stepping smoothly varies dt to follow short time dynamics with higher resolution and longer time dynamics with lower resolution. Thus it is apparent that logarithmic stepping provides the economical spacing of data points that more effectively follows the experimental observable dynamics.

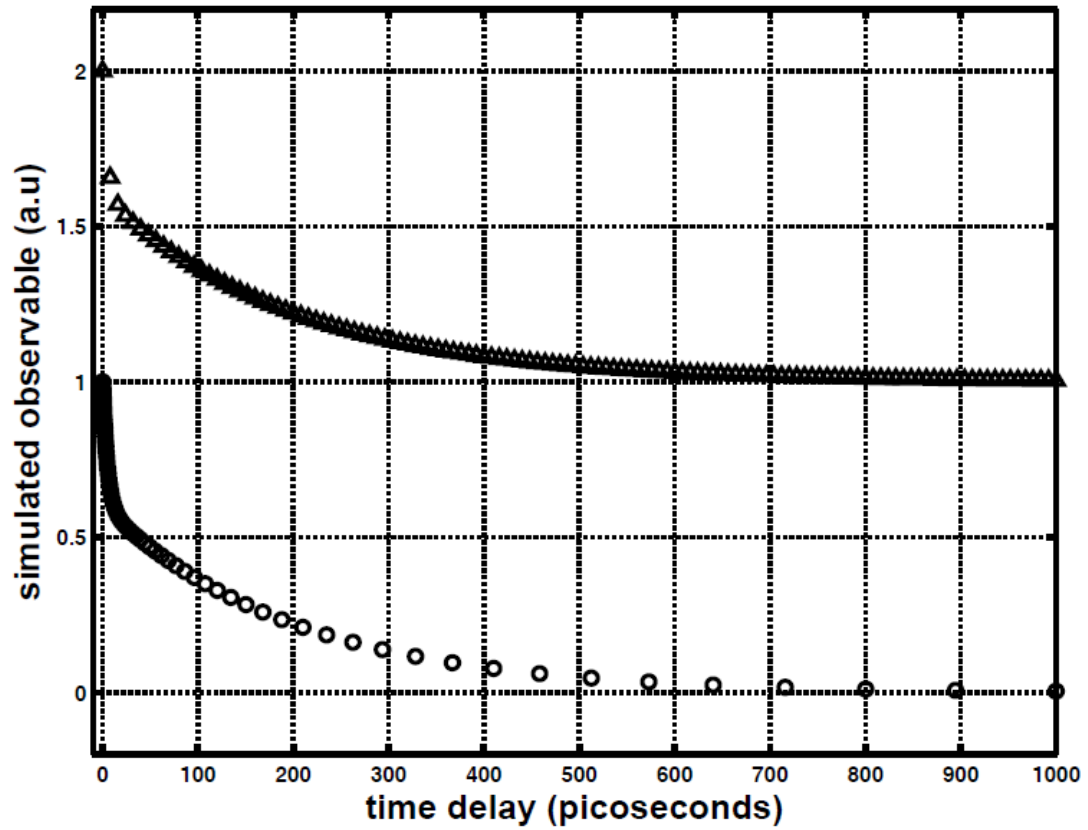


Figure 3.1 Comparison of logarithmic stepping (circles) vs. linear stepping (triangles) for a simulated observable. Top trace, displaced by one unit for clarity, shows evenly spaced points while the bottom trace displays points spaced evenly on a logarithmic scale.

Simply applying equation 3.3 to generate steps for our system results in repeated time points at short delay times as shown in Figure 3.2. This effect arises because the stepping stage has finite resolution. When the density of data points is large, the conversion of d_n to D_n causes small values of d_n to yield identical values of D_n because the logarithmic steps become smaller than the resolution of the stepping stage, dt . This effect becomes more pronounced with increasing total number of points. As N increases from 50 to 200, Figure 3.2, more repeated delay steps occur with a higher density at lower index values or shorter delays. We have found however, that when D_n reaches ten times dt this effect becomes negligible. We also observe repeated values for D_n when d_{stop} approaches the timescale of dt . Figure 3.3 shows the points generated by the logarithmic stepping function, equation 3.3, as a function of the data point index, n , with constant N (50) and dt (0.667 fs) and three different values for d_{stop} . Decreasing d_{stop} causes the density of data points at small delay times to increase which results in time delay stepping that is smaller than the resolution of the delay stage, shown in Figure 3.3(a) to 3.3(c). Finally, varying dt also produces repeated points; it increases the density of data points around the stepping resolution of the delay stage and generates repeated time steps and/or data points. Thus, the number of data points (N), the final delay (d_{stop}), and the stage time resolution (dt) can impose limitations on utilizing the logarithmic stepping function for data collection.

The problem of repeated data points can be addressed in a few ways. One obvious approach is to utilize a stepping stage with more resolution than needed for the

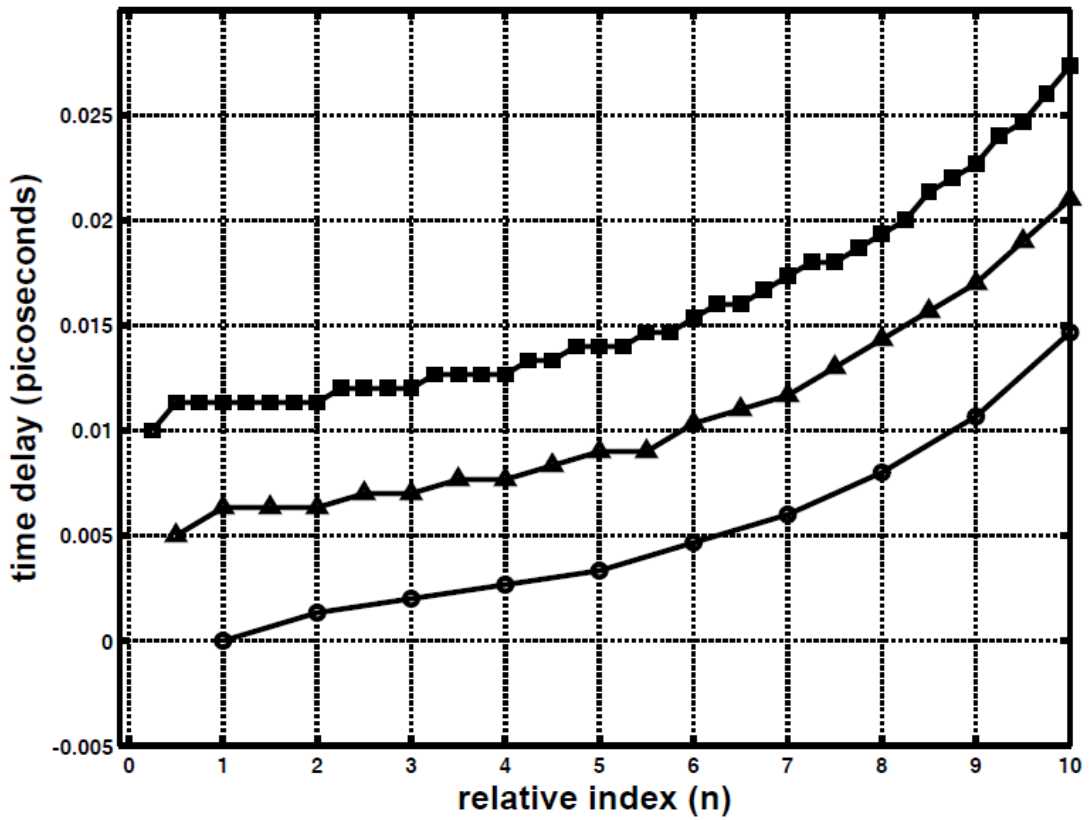


Figure 3.2 Logarithmic stepping value plotted as function of relative index (n) with dt (0.667 fs), d_{stop} (2 ns) and N equal to 50 (circles), 100 (triangles), and 200 (squares). As N increases, the number of repeated data points increases. N equal to 100 and 200 stepping functions have been offset by 0.005 ps and 0.01 ps respectively.

experiment. This solution obviates the problem of repeated points, but this is not practical especially if it requires the purchase of additional, potentially expensive equipment. Be that as it may, with dt more than ten times smaller than the smallest step introduced by d_n , there is adequate stage resolution to preclude repeated data points. For most time-resolved experiments, the shortest time resolution required is on the order of a femtosecond, which leads to an ideal stage resolution of less than 0.1 fs/step for application of this method. This timescale corresponds to linear stepping motion of roughly tens of nanometers per step. This physical distance can easily be reached and surpassed with state-of-the-art piezoelectric nanopositioning technology, but in general the piezoelectric technology does not provide total travel distances beyond a few millimeters, *i.e.*, less than ten picoseconds of delay. For some time-resolved experiments, ten picoseconds of delay is practical but for others it is not and therefore other approaches are needed to minimize or eliminate repeated data points.

Clearly it is preferable to find strategies that address the problem of repeated points that do not require researchers to purchase new equipment. Because the direct application of the logarithmic stepping function in existing experiments does not necessarily allow dt or d_{stop} to be changed, the only truly adjustable parameter is the number of data points, N . Reducing N sufficiently will decrease the number of repeated data points and eventually eliminate them entirely as illustrated in Figure 3.3. However, reducing the total number of points impacts the point density at the longest delay times which could impact data quality. A preferable solution to the repeated points problem is to replace the time interval where the repeated data points arise with evenly spaced

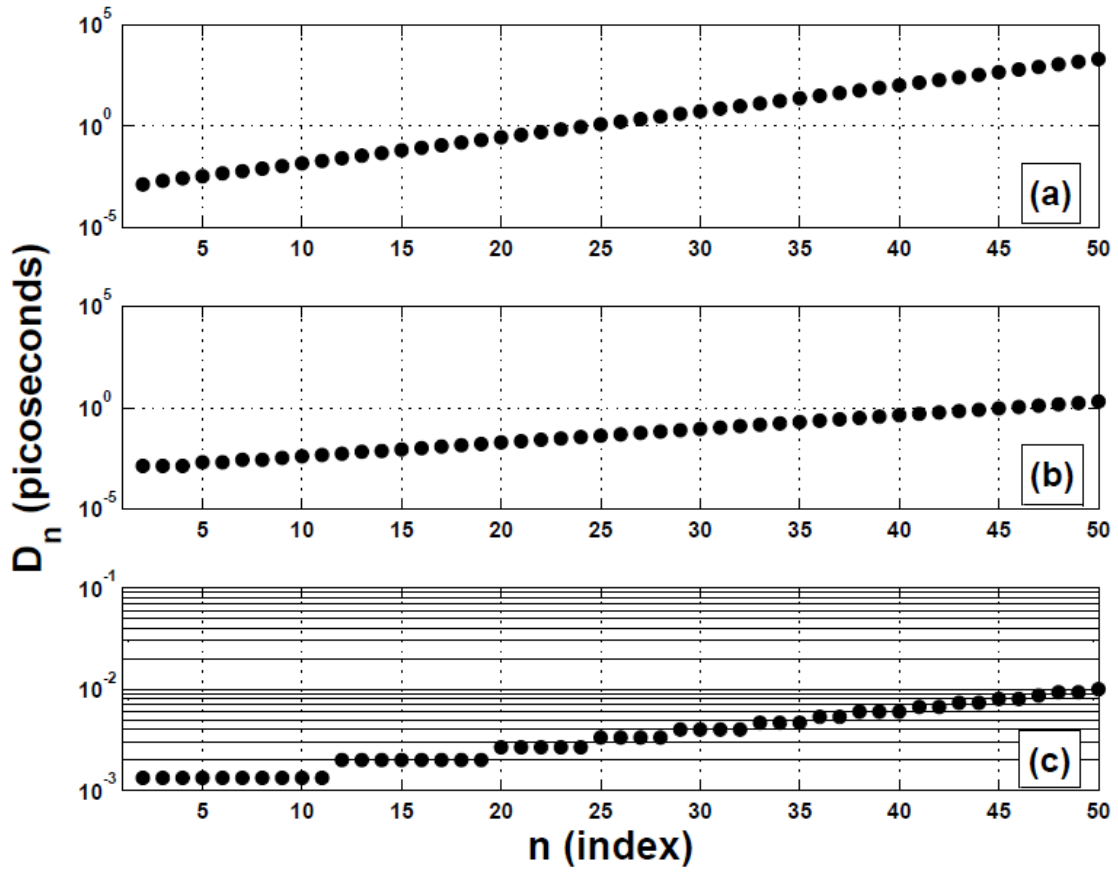


Figure 3.3 Logarithmic stepping value plotted as a function of the data point index (n) with N (50), dt (0.667 fs) constant and d_{stop} equal to (a) 2 ns, (b), 2 ps, and (c) 10 fs. Note the increase in repeated delay steps at early delay time as d_{stop} approaches the timescale of dt .

points with the resolution of the stepping stage. This method is most useful to increase N to generate more data points while still retaining efficiency of logarithmic stepping function. Our logarithmic stepping algorithm identifies repeated data points by taking the first derivative of the logarithmic stepping values; where the derivative is zero the value is not changing. Noting the index values of each repeated data point allows us to replace data points below this index with linearly spaced stepping values at the resolution of the stepping stage, dt . The number of data points in the linear range exactly matches the number of data points up to the largest repeated data point index thus conserving the total number of data points, N . For the given number of repeated data points, a corresponding number of data points are generated which are negative stepping values or time delays before time zero. Figure 3.4 illustrates the linear replacement solution to eliminate repeated data points.

Through any of these methods the limitation from repeated data points can be reduced and/or eliminated but logarithmic stepping does inherently have error with respect to the original logarithmic delay function (d_n). The error that the finite resolution of the stage introduces is calculated as simply the percent difference between d_n and D_n ,

$$error = 100 \cdot \left(\frac{d_n - D_n}{d_n} \right). \quad (3.4)$$

This error is a direct manifestation of the finite stepping of the delay stage and it drops off exponentially as the time delay increases. This inherent error only affects the difference between the logarithmic step function (d_n) and the actual values generated

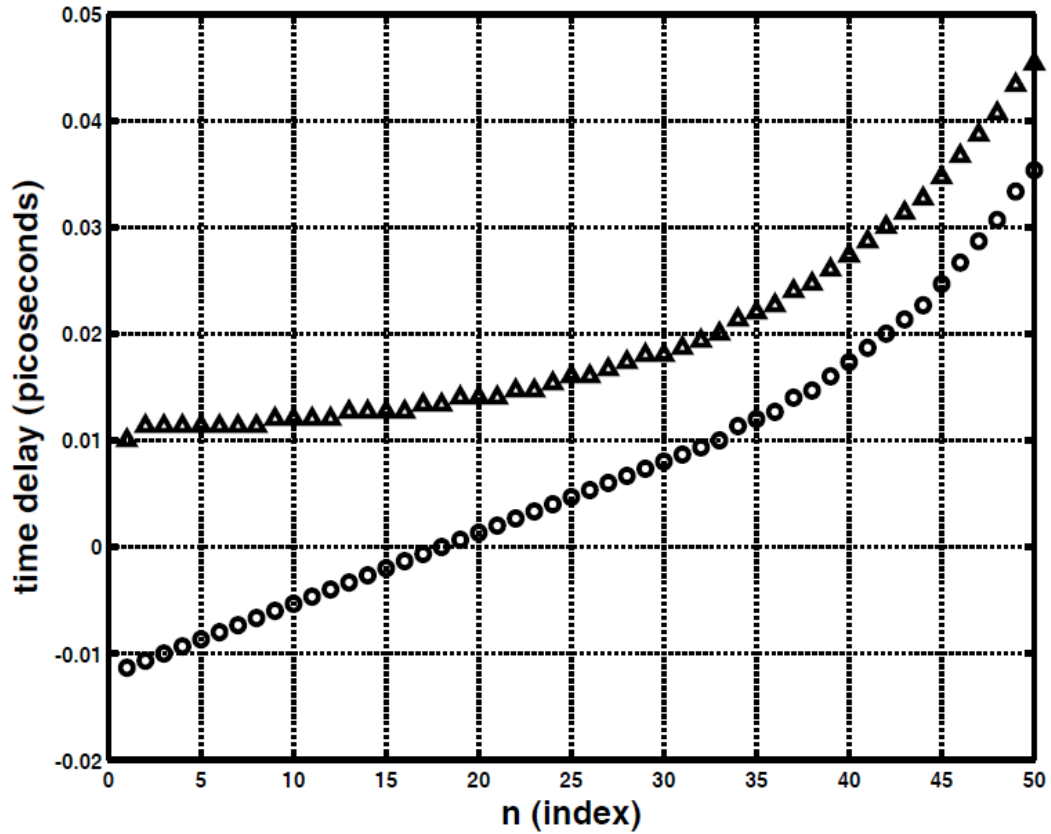


Figure 3.4 Uncorrected (upper trace, triangles) vs. linear corrected (lower trace, circles) logarithmic stepping values with N (200), dt (0.6667 fs), and d_{stop} (2 ns). The uncorrected values include repeated time delay points while the corrected contains no repeated time delay points. The uncorrected values are displaced by 0.01 ps for clarity.

(D_n), and does not impact data collection in any way. The values generated by equation 3.3, D_n , produces the closest achievable delay based on the finite resolution of the stage (dt) to the delay generated in the logarithmic step function.

3.2.c Statistical Analysis of Stepping Methods

Strategies for efficient collection of photometric data depend on the parameters to be evaluated from the data and on how efficiency is defined. Many experimental observables, such as those presented later in Section 3.III.b, involve multiexponential decays. Suppose the decaying quantity y is represented as a sum of exponentials of lifetimes k_i and amplitudes a_i together with a baseline amplitude b ,

$$y(t) = b + \sum_i a_i \exp[k_i t]. \quad (3.5)$$

The parameters c_i that define the decay are then b , k_i and a_i . The “quality” q_n of one of these parameters c_n recovered by data analysis can be defined as the reciprocal of the standard error of the mean of the recovered parameter times the variance of the data.¹¹ This is equivalent to the corresponding diagonal element of the error matrix in a nonlinear least squares scheme,

$$q_n = \frac{1}{A^{-1}_{nn}} \quad (3.6)$$

where

$$A_{ij} = N \frac{\sum_{pts l} \left(\frac{\partial y_l}{\partial c_i} \right) \left(\frac{\partial y_l}{\partial c_j} \right) w_l}{\sum_{pts l} w_l} \quad (3.7)$$

and N is the total number of data points while the weight w_l of the l^{th} point equals the reciprocal of the standard deviation of that point. Clearly, q_n values are proportional to

the number of data points examined and, in the simplest case of data being averaged to obtain a single mean value, q equals the number of data points.

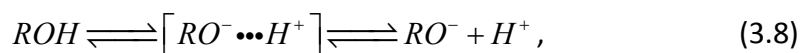
The concept of experimental “efficiency” can be approached from several perspectives. In many instances, the time required to make a mechanical adjustment, such as changing interferometer path, determines the time required to measure a single data point. In such circumstances, the fewer data points collected, the faster the experiment proceeds. Then the experimental procedure that determines a particular q_n with a given quality through analysis of the smallest number of points, N , maximizing q_n/N yields the most efficient experiment. Moreover, photobleaching limits the ultimate number of photons that can be collected from a particular chromophore; hence, in other experimental situations, our key goal may be to use each photon as efficiently as possible to determine decay parameters. The quality of a fitted parameter q_n divided by the total number of photons or integrated light signal S in the points used to determine the parameter is a measure of efficiency in such a case. We enlist both of these statistical analysis methods to analyze the relative efficiency of logarithmic vs. linear data collection below.

3.3 Sample Data

As we have established, logarithmic based stepping is particularly useful in tracking dynamics over many decades of time delay. To illustrate its usefulness, we follow solvation and deprotonation dynamics of the photoacid 8-hydroxypyrene-1,3,6-trisulfonic acid (HPTS) in water using broadband ultrafast transient absorption

spectroscopy. The dynamics of system include several time dependent processes occurring over a range of timescales.¹² Ultrashort pulse excitation of the HPTS protonated state at approximately 400 nm initiates dynamics that span from femtoseconds to nanoseconds.

HPTS transient absorption spectra display both solvation dynamics and deprotonation dynamics.¹² Solvation dynamics manifest as a time-dependent spectral shift that relaxes with a time constant of roughly 1 ps for the HPTS/water system. HPTS deprotonation dynamics follow the mechanism,



where the initial step generates a contact ion pair followed by subsequent diffusion of the proton away from the excited HPTS molecule (RO^-).¹² Both mechanistic steps depend on the bulk proton concentration leading to pH dependent deprotonation dynamics. In neutral water (pH=7), the first step in the HPTS deprotonation mechanism occurs on the 2-4 ps timescale while the proton diffusion step occurs on the ~90 ps timescale.¹² The multiple timescales characterizing the HPTS/water system make it an excellent demonstration for logarithmic stepping interferometric time-resolved experiments.

3.3.a Experimental Methods

The details of the laser system and broadband ultrafast transient absorption apparatus appear in a Chapter 2. Briefly, 125 μ J/pulse of the output of a chirped pulse regenerative amplifier (55 fs FWHM pulses at 804 nm, 1 kHz repetition rate) is used for the transient absorption experiment. Frequency doubling in BBO generates the second

harmonic pump pulses ($\sim 20 \mu\text{J}$). Before reaching the sample, the pump beam is optically chopped to provide a reference signal, double passes a fused silica Brewster prism pair to precompensate for material dispersion, and travels down a variable delay path that provides relative delay between the pump and probe pulses. The residual fundamental beam double passes through a fused silica Brewster prism pair before generating a single filament white light continuum used for the probe pulses. Pump and probe beams are focused onto the sample flowing through a 1 mm cuvette. The diverging probe beam is collimated, spatially filtered, and traverses a short pass dichroic filter to extinguish the spectral intensity around 800 nm. Transient absorption signals are collected using an Ocean Optics spectrometer, which is synchronically triggered externally at twice the frequency of the pump beam modulation.

Data were collected as a function of the delay between the pump and probe pulses, τ , using a program that sequentially measured the white light continuum transmitted through the sample with the pump on (signal), $I_{sig}(\tau)$ and pump blocked (reference) $I_{ref}(\tau)$.

$$S = -\log\left(\frac{I_{sig}}{I_{ref}}\right) \quad (3.9)$$

Transient absorption spectra were compiled to generate a transient absorption spectrogram, $S(\lambda, \tau)$. Logarithmic time delay steps were calculated via the logarithmic stepping function with dt (0.667 fs), d_{stop} (2 ns), and N (200). Linear time delay steps were generated with 100 fs steps to 10 ps, 10 ps steps to 750 ps, and finally 50 ps steps to 2 ns yielding 200 total data points.

Chapter 5 gives studies of the deprotonation dynamics of HPTS in bulk water and reverse micelle media, but here we focus on aqueous samples to illustrate the advantages of logarithmic time-delay stepping. Aqueous HPTS samples were prepared at 0.1 mM at neutral pH yielding an absorbance of 0.25 for the HPTS protonated state absorption band (404 nm) for the 0.5 mm path length used in the transient absorption experiments. Samples were characterized by steady-state absorption measured with a Varian Cary 500 UV/Vis/NIR spectrometer.

3.3.b. Multiple Timescale Transient Absorption Data

Figure 3.5 displays HPTS/water transient absorption spectrograms collected with linear, and logarithmic time delays. Each time step represents a full spectrum reflecting the state of the HPTS/water system at that instant in time. The representations shown in Fig. 3.5 illustrate processes occurring on multiple timescales in the HPTS/water dynamics. Three contributions comprise the transient absorption spectra: excited state absorption (ESA), stimulated emission (SE), and ground state bleach (BL). SE and BL contributions indicate the sample absorbing less light while ESA displays an increase in absorption. We follow the convention of plotting ESA as negative signal (loss of photons) and SE/BL (gain of photons) with a positive signal.

The spectrograms presented in Fig. 3.5(a) reflect evenly spaced data points while data in Fig. 3.5(b) show the logarithmic scale for the data collected. The logarithmic collection and display in Fig. 3.5(b) encourages visual interpretation of the data which shows a smooth blue shift in the spectra occurring from ~ 100 fs to 3 ps, followed by the appearance of the stimulated emission feature around 7 ps. In contrast, although the

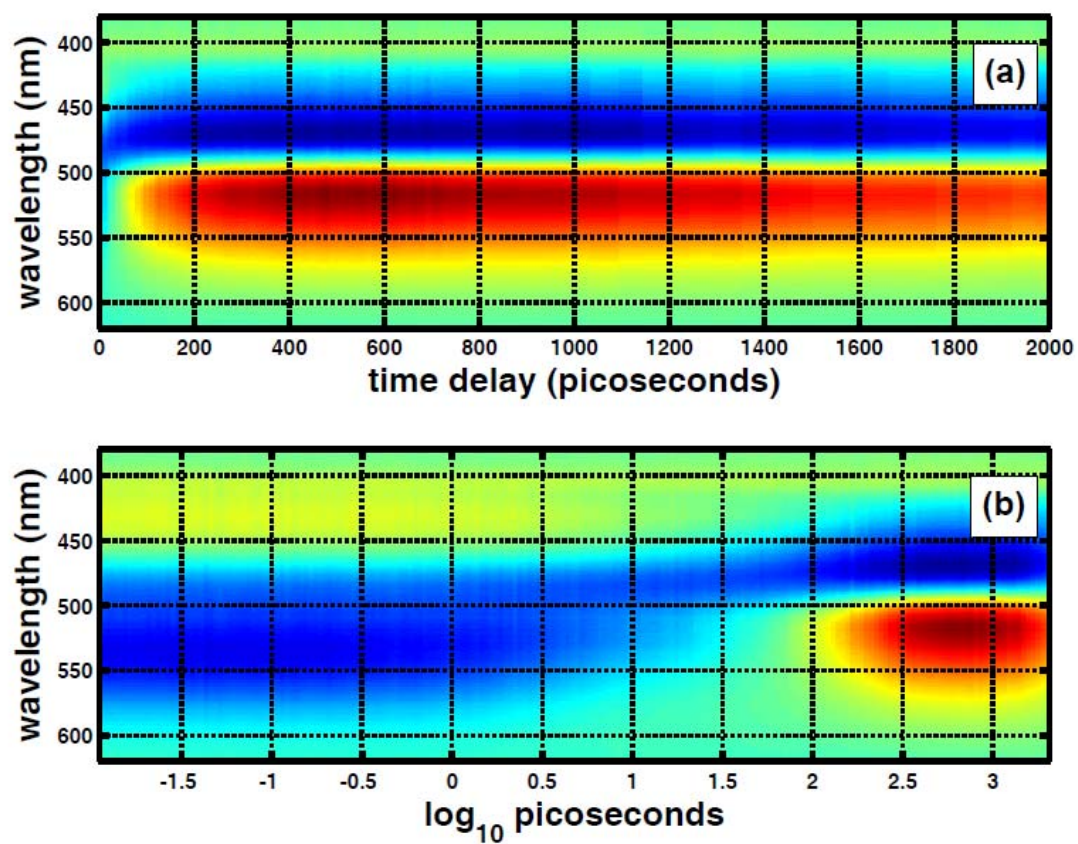


Figure 3.5 Linear (a) and logarithmic (b) broadband ultrafast transient absorption spectrograms of HPTS in pH-7 water. Note that the time delay axis is plotted linearly but represents time delay values with variable linear resolution (a) and logarithmic spacing (b). Both spectrograms contain 200 spectra with final delay equal to 2 ns.

data plotted with a linear scale reveals the stimulated emission appearing near 10 ps delay, this representation obscures all the early dynamics. By dividing the time delay points into regions with different linear resolutions, we can sometimes observe the dynamics of the system but frequently it takes significant analysis to find the timescale of the processes from such data.

Analysis of HPTS/water dynamics demonstrates the advantage of the logarithmic method. Spry et al.¹³ have developed a simple global analysis method for HPTS dynamics, which approximates the time-dependent spectrum of HPTS/water transient absorption data as a linear combination of the protonated (P), deprotonated (D), and derivative of the protonated spectrum (dP), according to the equation:

$$S(\lambda, t) = \alpha(t) \cdot P + (1 - \alpha(t)) + \beta(t) \cdot dP \quad (3.10)$$

where $\alpha(t)$ tracks the time-dependent population change between the protonated and deprotonated states yielding the deprotonation dynamics while $\beta(t)$ follows the dynamic Stokes shift of the protonated spectrum. Application of this global analysis method for linear and logarithmic data collection methods are shown in Figures 3.6 and 3.7. Fig. 3.6(a) and 3.6(b) illustrate that the logarithmic stepping method inherently matches the observed deprotonation dynamics in the HPTS/water transient absorption data while the linear stepping abruptly changes stepping resolution, potentially obfuscating dynamics. In Fig. 3.6(b), the biexponential deprotonation dynamics (2 ps and 90 ps) are clearly visible with the stepping values proportional to the observed change in $\alpha(t)$ over two orders of magnitude. Fig. 3.6(a) shows deprotonation dynamics and the emergence

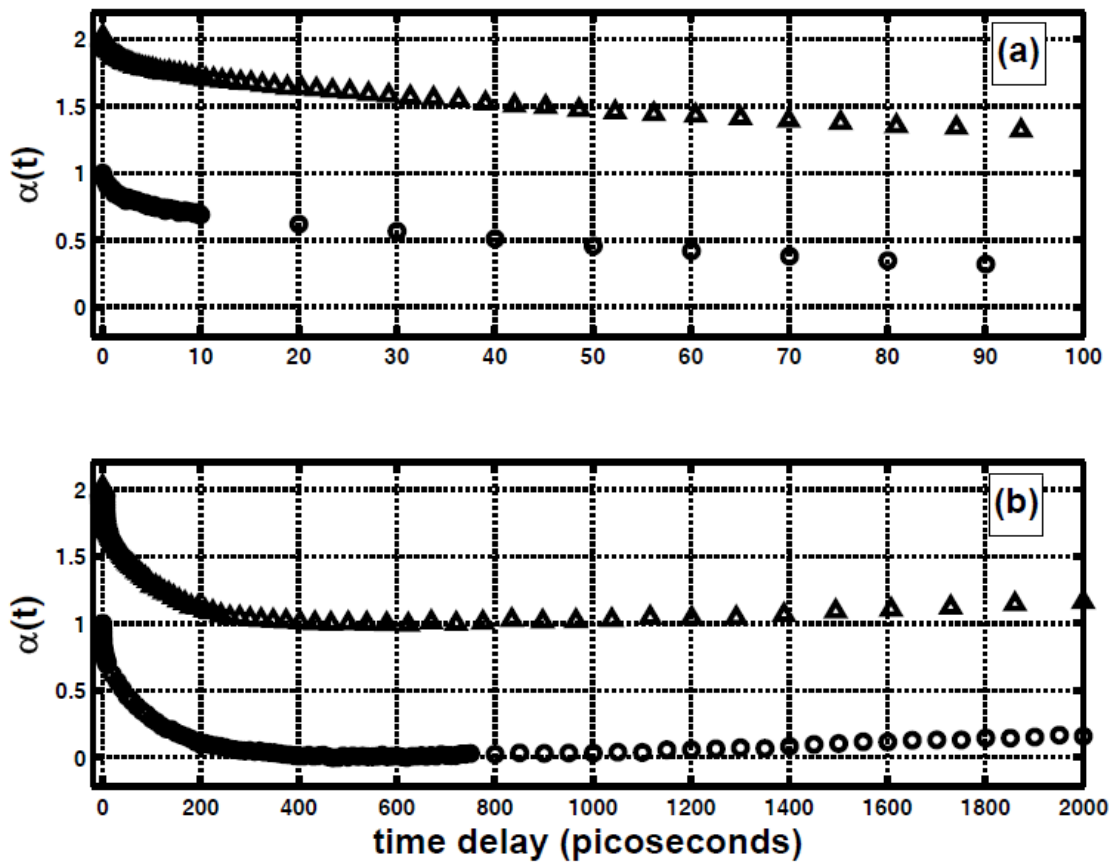


Figure 3.6 Extracted deprotonation dynamics from HPTS/pH-7 water transient absorption data collected with linear (circles) and logarithmic (triangles) stepping. Comparisons between the two methods show that although linear stepping provides effective resolution, logarithmic stepping smoothly adjusts the time stepping on the 10s picosecond (a) and nanosecond (b) timescales. Logarithmic traces (triangles) are displaced by 1 unit for clarity.

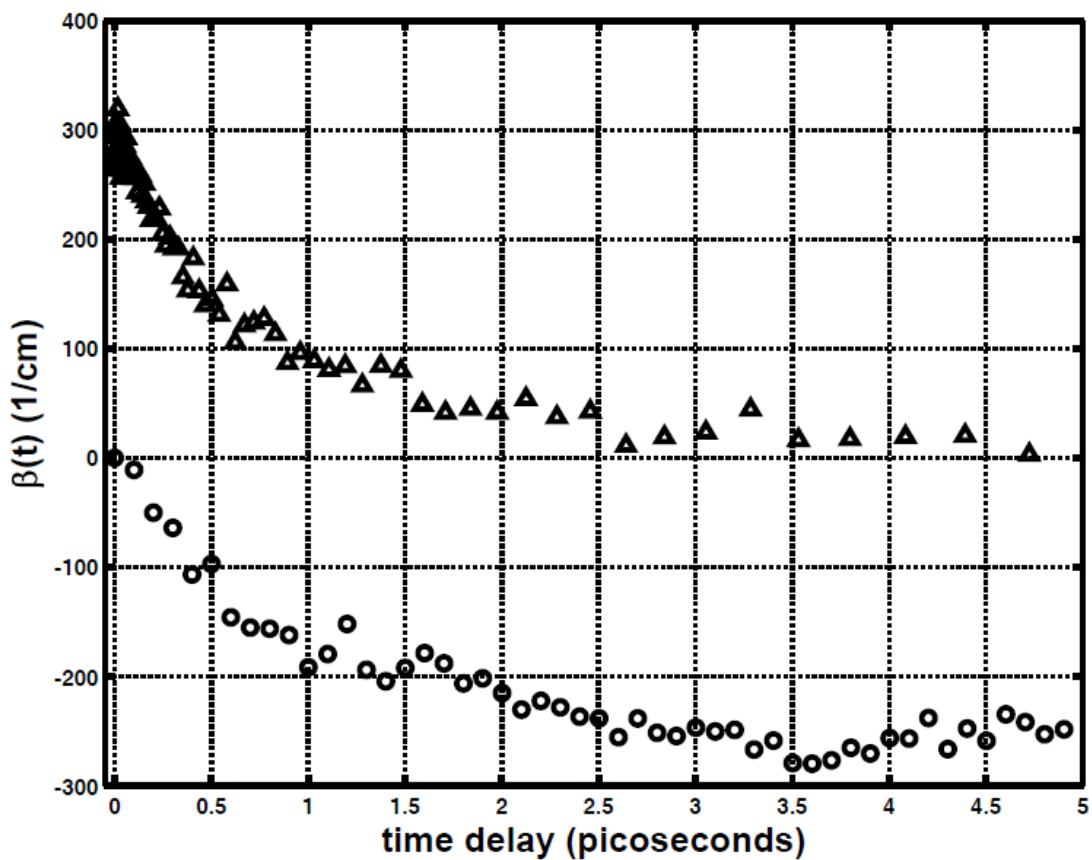


Figure 3.7 Extracted Stokes shift dynamics from HPTS/pH-7 water transient absorption data collected with linear (circles) and logarithmic (triangles) stepping. Comparisons between the two methods show that although linear stepping provides effective resolution, logarithmic stepping smoothly adjusts the time stepping. Logarithmic trace (triangles) is displaced by 300 cm^{-1} for clarity.

of excited state lifetime decay on the order of nanoseconds. In the sub-picosecond regime, Fig. 3.7, adequate time step values resolve the sub-picosecond Stokes shift dynamics, e.g., $\beta(t)$. Over the extended timescale, logarithmic stepping smoothly transitions from high temporal resolution at short delay to lower resolution at longer delay while linear stepping abruptly changes resolution. Logarithmic stepping requires no prior knowledge of the underlying dynamics to determine linear resolution switching points so as to not obscure the dynamics.

3.3.c Statistical Analysis of Collected Data

To further examine the relative efficiency of logarithmic vs. linear data collection, we present statistical analysis (Table 3.1) of the extracted dynamics shown in Fig 3.6 and compare how well each of the model parameters is defined by a given number of data points, regardless of individual point intensities, and by the total optical signal recorded, irrespective of the total number of points. Transient absorption data represent relative small changes in large intensities, so the first columns in Table 3.1 assume a constant uncertainty per point. In this circumstance, for three of five decay parameters, namely a_1 , k_1 and k_2 , log spacing of data points reduces the number of measurement points needed to achieve given precision in a particular fitted parameter. For example, log spacing requires over two-fold fewer measurements than linear spacing, 1/65.0 vs. 1/28, to define the rapid decay amplitude a_1 to a given precision. The advantages of log spacing are much more pronounced when photon-limited data are considered. If the experimental data represented luminescence decay, then Poisson uncertainties in each intensity could be assumed as presented in the rightmost two

Table 3.1 Analysis of the statistical “efficiency” of HPTS/pH-7 water deprotonation fitted parameters.

Parameters ¹	1000xFitted Parameter Quality (q_n) per				Poisson Uncertainty per Point			
	Uniform Uncertainty per Point		Total Signal ³ (S)		Number of Points ² (N)		Total Signal ³ (S)	
	Log spacing	Linear spacing	Log spacing	Linear spacing	Log spacing	Linear spacing	Log spacing	Linear spacing
a_1	65	28	101	49	11.0	2.07	17.0	3.7
$\ln k_1$	1.23	1.04	1.89	1.83	0.21	0.09	0.33	0.16
a_2	56	172	86	172	404	385	623	680
$\ln k_2$	54	88	83	156	29	23	45	40
b	33031	32241	50953	56955	34270	21973	52862	38817

¹ Parameters refer to equation (3.5). Data analysis assumes $a_1=0.25$, $\ln k_1=-1.39$, $a_2=0.75$, $\ln k_2=-4.61$ and $b=0$, these values agreeing well with numbers obtained by analysis of actual data.

² Numbers indicate recovered data quality as calculated from equation (3.6) per point measured, irrespective of intensity differences between points. Higher values indicate more efficient use of experiment time.

³ Numbers indicate recovered data quality as calculated from equation (3.6) per unit total signal measured, irrespective of actual number of points yielding the total signal. Higher values indicate more efficient use of detected photons.

columns of Table 3.1. In such instance, for all five decay parameters, log spacing of data points would reduce the number of measurement points needed to achieve given precision in a particular fitted parameter. Similarly, for four of five parameters, log spacing would require fewer total detected photons to achieve given parameter accuracies. This analysis shows a clear statistical advantage in collecting data logarithmically over linearly.

3.4 Summary

We have established a logarithmic stepping value method that generates logarithmically spaced values and tested its application in subnanosecond time-resolved pump-probe experiments. The logarithmically spaced time delay values are useful to track observables that span a range of timescales. We have found that the logarithmic stepping values obtained from direct application of the logarithmic stepping function (equation 3.2) contain repeated stepping values for small time delays due to the finite resolution of the stepping stage. To alleviate this problem, we introduce linear stepping values at the resolution of the stepping stage to replace the region with repeated points.

We test this method by measuring broadband ultrafast transient absorption of HPTS in water, a system that exhibits dynamics over five decades in time. The logarithmic data collection makes it possible for us to extract the Stokes shift occurring on the hundreds of femtosecond time scale, the biexponential deprotonation dynamics on the picosecond to tens of picosecond timescales, and the lifetime decay of the HPTS

excited state on the nanosecond timescale. The variable time step values introduced from the logarithmic stepping method provides a highly efficient way to collect data that contains all of the relevant dynamics in HPTS/water broadband transient absorption data. Furthermore, statistic analysis of the efficiency of this data collection with linearly-spaced and logarithmically-spaced data points shows that logarithmic data collection determines parameters to a given precision with a five-fold reduction in data points compared to data collected with evenly spaced points.

Although we apply our algorithm to generate points according to a logarithmic function, in principle this method could be used to generate finite resolution steps using any mathematical function. Spacing data points according to the functional form of that the data demonstrate yields data points that reflect the physical process occurring. This allows the user to extract the parameters desired with the highest accuracy and most efficiency.

References and Notes

- (1) Fleming, G. R. *Chemical Applications of Ultrafast Spectroscopy*; Oxford University Press: New York, New York, 1986.
- (2) Bucksbaum, P. H. *Science* **2007**, *317*, 766.
- (3) Kling, M. F.; Vrakking, M. J. J. *Annual Review of Physical Chemistry* **2008**, *59*, 463.
- (4) Backus, S.; III, C. G. D.; Murnane, M. M.; Kapteyn, H. C. *Review of Scientific Instruments* **1998**, *69*, 1207.
- (5) Keller, U. *Nature* **2003**, *424*, 831.

- (6) Lei Gu, X. L.; Bao, H.; Liu, B.; YuelinWang; Liu, M.; Yang, Z.; Cheng, B. *Journal of Micromechanics and Microengineering* **2006**, *16*, 1349.
- (7) Moheimani, S. O. R. *Review of Scientific Instruments* **2008**, *79*, 071101.
- (8) Brauns, E. B.; Madaras, M. L.; Coleman, R. S.; Murphy, C. J.; Berg, M. A. *Physical Review Letters* **2002**, *88*, 158101.
- (9) Furstenberg, A.; Kel, O.; Gradinaru, J.; Ward, T. R.; Emery, D.; Bollot, G.; Mareda, J.; Vauthey, E. *Chemphyschem* **2009**, *10*, 1517.
- (10) Horng, M. L.; Gardecki, J. A.; Papazyan, A.; Maroncelli, M. *Journal of Physical Chemistry* **1995**, *99*, 17311.
- (11) Bevington, P. R.; Robinson, D. K. *Data reduction and error analysis for the physical sciences*; McGraw-Hill Book Company: New York, 2003.
- (12) Leiderman, P.; Genosar, L.; Huppert, D. *Journal of Physical Chemistry A* **2005**, *109*, 5965.
- (13) Spry, D. B.; Goun, A.; Fayer, M. D. *Journal of Physical Chemistry A* **2007**, *111*, 230.

CHAPTER 4

FEMTOSECOND TO NANOSECOND DYNAMICS OF CONFINED COUMARIN 343 BY TRANSIENT ABSORPTION SPECTROSCOPY

Through UV pump/broadband probe transient absorption measurements the dynamics sensed by coumarin 343 (C343) are measured in bulk water and nanoscopically confined in AOT (sodium bis(2-ethylhexyl) sulfosuccinate) reverse micelles. In contrast to Stokes shift dynamics measuring solvation dynamics in bulk water, which conclude after a few picoseconds, dynamics arising from C343 nanoscopically confined in reverse micelles extend to far longer timescales. Analysis of time-dependent Stokes shifts for C343 in AOT reverse micelles reveal two distinct timescales: (1) a fast response (< 10 ps) attributed to solvation dynamics by the liquid environment, and (2) a slow response (> 10 ps) reflecting environmental confinement induced effects. Coupled with anisotropy decays and steady-state spectroscopy, the results indicate that C343 translational motion may play a role in determining the slow dynamics of the C343/AOT reverse micelle system. This work was submitted for publication in the *Journal of Chemical Physics* on June 27, 2011.

4.1 Introduction

The behavior of a supporting solvent can strongly influence fundamental physical and chemical processes. For example, researchers have shown that solvent fluctuations occurring on ultrafast time scales can influence much slower dynamical processes in proteins.^{1,2} Likewise, important chemical processes, such as electron and proton transfer, can often be dictated by solvent dynamics.³⁻⁵ Environmentally induced changes in solvent behavior can influence the direction and rate of physical processes which consequently shift chemical and biological observables.

Historically, researchers have utilized rigid coumarin probe molecules to measure the dynamic response of liquids through the molecule's dynamic Stokes shift.^{4,6,7} In many bulk liquids, this method has proven highly effectively for tracking solvent motion. Recent applications follow the dynamic Stokes shift of coumarins in micro- or nanoheterogeneous media, nominally exploring solvation dynamics of the restricted solvent.⁸⁻²¹ Solvation dynamics follows the response of a solvent to an instantaneous perturbation.⁴ Experimentally, this has been measured by following the spectroscopy of a dye molecule with significantly different ground and excited state molecular dipole moments. The solvent response to the change in dipole manifests in the time varying molecular fluorescence or absorption spectroscopy via

$$C(t) = \frac{f(t) - f(\infty)}{f(0) - f(\infty)} \quad (4.1)$$

where $f(t)$, $f(\infty)$, and $f(0)$ reflect a spectral characteristic, *e.g.*, the peak maximum or first spectral moment, at a variable time t , after the system has relaxed completely, ∞ , and before any dynamic changes occur, 0. This method has proven effective for understanding the response of pure liquids.⁴ More recently, application of solvation dynamics has helped determine the dynamic response in more complex systems such as room temperature ionic liquids²²⁻²⁷ and in macromolecular samples.^{8-10,19-21,28}

One environmental change that significantly influences solvent behavior arises when the solvent is confined to nanoscopic volumes.²⁹⁻³¹ In nanoscopic volumes, solvent properties differ significantly from the properties of a bulk solvent. In general, molecular motion is hindered and slowed when liquids are confined. For example, through time-resolved infrared spectroscopy, Piletic et al. showed that water confined to nanoscopic proportions in reverse micelles has a shell of molecules that interact with the interface and whose properties diverge significantly from bulk water.³² Likewise, in optical Kerr effect experiments, Fourkas and coworkers have shown that confinement to small proportions cause molecules to move more slowly than they do in bulk solvent.³¹ In simulations of methanol in silica pores, Eola et al. showed that confinement impacts the liquid structure near the pore walls and that molecular rotational and translational motions generally slowed in the confined environment.³³ Confining large guest molecules in a supramolecular structure, Mugridge et al. showed that encapsulation increased internal rotational barriers and slowed molecular tumbling.³⁴

Reverse micelles present one common environment used to explore the impact of a confined environment on solvation dynamics.¹¹⁻¹⁸ These structures stabilize small

droplets of water or other polar solvent in a nonpolar solvent using an amphiphilic layer.³⁵ Frequently, reverse micelles possess a spherical form whose radius is proportional to $w_0 = [\text{polar phase}]/[\text{amphiphile}]$. The most common reverse micelle system studied utilizes AOT (sodium dioctylsulfosuccinate) as the surfactant. Researchers have utilized fluorescent probes to explore solvation dynamics in these nanoscopic pools.^{13-16,18,30,36-39} In general, these studies demonstrate differences between solvation occurring in bulk solution and what is observed in confined systems. With increasing w_0 values, most of the systems trend toward bulk behavior. Solvation dynamics experiments have largely focused on systems containing water but some have also probed reverse micelles sequestering nonaqueous interiors.^{15,16,40-42}

The work presented here builds upon previous work in the Levinger group using time-resolved fluorescence Stokes shift studies in AOT reverse micelles.^{17,18,43} Those studies focused primarily on very short time dynamics occurring on the hundred's of fs to ten's of ps timescale. Here we present a study of solvation dynamics utilizing transient absorption spectroscopy methods to probe water and water in AOT reverse micelles. These experiments make it possible for us to explore dynamics up to the nanosecond regime.

4.2 Experimental Methods

4.2.a Sample Preparation

Samples were prepared with coumarin 343 (C343, 97%, Sigma Aldrich), high-purity water (Milli-Q filtered, 18.2 M Ω cm resistivity), AOT (sodium

dioctylsulfosuccinate, 99%, Sigma Aldrich) and cyclohexane (99%, Sigma Aldrich). C343, AOT and cyclohexane were used without further purification. Structures of AOT and C343 are given in Fig. 1.2 and Fig. 1.3 respectively. To prepare reverse micelles, AOT was dissolved in cyclohexane to form a stock solution. A 10 mM stock solution of C343 in water was prepared by the addition of sodium hydroxide to raise the pH to ~ 10.5 . All samples were prepared by mass to approximately 0.4 M AOT in cyclohexane by the following method. An appropriate mass of AOT was dissolved into an amount of cyclohexane under the mass needed for approximately 0.4 M AOT. After dissolving AOT in cyclohexane, an appropriate amount of C343 stock solution was added giving 0.2 mM C343 overall concentrations. Additional water was added to yield samples with w_0 values of 2.5, 5, 10, and 20. Finally, cyclohexane was added to reach approximately 0.4 M AOT for each sample. C343 in AOT RM were compared to 2×10^{-4} M C343 in neat water (pH = 10.5).

Samples were characterized by steady-state absorption measured with a Varian Cary 500 UV/Vis/NIR spectrometer. Fluorescence spectra were recorded from the broadband femtosecond transient absorption instrument by blocking the WLC probe beam and recording the background.

4.2.b Transient Absorption Spectrometer

A description of the laser system and broadband ultrafast transient absorption spectrometer has appeared⁴⁴ and detailed descriptions are given in the supporting information; here we provide a brief summary. 125 $\mu\text{J}/\text{pulse}$ of the output of a chirped pulse regenerative amplifier (50 fs FWHM pulses at 800 nm, 1 kHz repetition rate) is

used for the transient absorption experiment. Frequency doubling in BBO (β -barium borate) generates the second harmonic pump pulses ($\sim 20 \mu\text{J}$). Before reaching the sample, the pump beam is optically chopped to provide a reference signal, double passes a fused silica Brewster prism pair to precompensate for material dispersion, and travels down a variable delay path that provides relative delay between the pump and probe pulses. The residual fundamental beam double passes through a fused silica Brewster prism pair before generating a single filament white light continuum used for the probe pulses. Pump and probe beams are focused onto the sample flowing through a 0.5 mm cuvette. The diverging probe beam is collimated, spatially filtered, and traverses a short pass dichroic filter to extinguish the spectral intensity around 800 nm. Transient absorption signals are collected using an Ocean Optics spectrometer (USB 2000+), which is synchronically triggered externally at twice the frequency of the pump beam modulation 100/200 Hz respectively.

4.2.c Data Collection

Data were collected as a function of the delay between the pump and probe pulses using a custom MatLab (Release 2009a) program that sequentially measured the white light continuum transmitted through the sample with the pump on (signal), $I_{sig}(\nu, t)$ and pump blocked (reference) $I_{ref}(\nu, t)$.

$$S(\nu, t) = -\log\left(\frac{I_{sig}(\nu, t)}{I_{ref}(\nu, \infty)}\right) \quad (4.2)$$

To generate transient absorption spectrograms, signals generated using equation 4.2 were compiled as a function of both time and frequency, $S=S(\nu, t)$. Raw

transient spectra were truncated to 1100 wavelength values over a 380-720 nm range and collected from -100 fs to 2 ns with 200 logarithmically spaced time delays values.⁴⁴ Spectrograms were generated from both parallel and perpendicular pump beam polarizations with respect to the probe beam polarization. Because the WLC has a non-zero temporal chirp, we limited analysis of our data to times longer than 300 fs to avoid spectral shifting arising from the chirp. Further details pertaining to broadband femtosecond transient absorption data collection appear in supporting information.

To extract information about reorientation dynamics from the two dimensional data we used one of two methods. For data with high signal to noise, intensities at single wavelength (~530 nm) as a function of time for both parallel and perpendicular spectrograms yielded effective signals, $S=S(t)$, from equation 4.2. For samples yielding lower signal to noise, we averaged data from several wavelength values near the strongest broadband femtosecond transient absorption signal to yield parallel and perpendicular signals from which reorientational dynamics could be determined.

4.2.d Data Analysis

4.2.d.i transient spectrograms

To measure decay times in the absence of rotational contributions, signals were calculated from parallel and perpendicular polarization spectrograms via,

$$S(\nu, t) = \frac{1}{3} (S_{\parallel}(\nu, t) + 2 \cdot S_{\perp}(\nu, t)) \quad (4.3)$$

Three contributions comprise the transient absorption spectra: excited state absorption (ESA), stimulated emission (SE), and ground state bleach (BL). SE and BL

contributions indicate the sample absorbing less light while ESA displays an increase in absorption. We follow the convention of plotting ESA as negative signal (reduction of the number of photons on the detector) and SE/BL (increase of photons) with a positive signal. Stokes shift dynamics are quantified in transient absorption data through the time-dependent spectral shifts in the SE peak.

The combination of SE, BL and ESA contributions to the transient absorption leads to substantially complicated signals. Because we collected data out to a 2 ns delay, signals include a contribution from the excited state lifetime, which we remove from the data prior to other processing. Integrating $S(\nu, t)$ over all ν values measured generates a signal that decays with the excited state lifetime, τ_L . Fits of the integrated data to a single exponential decay function allows accurate measurement of the excited state lifetime. These values (see Table 4.2) agree well with our previous measurements via time-resolved fluorescence of 4.5 ns.¹⁸ To remove the lifetime contribution from the data, we process each transient spectra as,

$$S_L(\nu, t) = \frac{S(\nu, t)}{\exp[-t/\tau_L]} \quad (4.4)$$

which minimizes the contribution arising from C343 lifetime decay.

After removing contributions to the signal from the excited state lifetime, we note that BL and ESA signals contribute a constant amplitude to the spectrograms at all time delays, indicating that their profiles do not shift during the experiments. This may be attributable to their small amplitude compared with the SE contribution. Because the BL and ESA signals do not display time dependent spectral shifting, we simplify the

dynamical analysis by isolating the SE dynamics from BL and ESA. The contributions of the BL and ESA contributions can be approximated as,

$$BL(\nu) + ESA(\nu) = S_L(\nu, \infty) - a * F(\nu) \quad (4.5)$$

where $aF(\nu)$ is the steady-state emission spectrum with a normalization constant, a , and ∞ is taken as the longest time delay value of our experiment (2 ns). Using this definition, the time-dependent SE signal is calculated from,

$$SE(\nu, \tau) = S_L(\nu, \tau) - [BL(\nu) + ESA(\nu)]. \quad (4.6)$$

Each transient SE spectrum was fit to an asymmetric Gaussian peak,⁴⁵

$$SE(\nu) = a \exp \left[- \left(\frac{\nu - \nu_0(t)}{\Gamma - s(\nu - \nu_0(t))} \right)^2 \right] \quad (4.7)$$

where a is the amplitude, $\nu_0(t)$ is the peak position, Γ is the width and s is the symmetry parameter. We used the SE peak position, $\nu_0(t)$ as the spectral function, $f(t)$ in equation 4.1 to quantify the time-dependent Stoke's shift dynamics. Alternative methods to gauge the solvation dynamics include following the spectral maximum of the spectrograms as a function of time or calculating the first moment of the asymmetric Gaussian. More information about these analyses and comparison to the SE data are given in supporting information.

4.2.d.ii time-resolved anisotropy

Rotational anisotropy decays were calculated via,

$$r(\tau) = \frac{I_{\parallel}(\tau) - g \cdot I_{\perp}(\tau)}{I_{\parallel}(\tau) + 2g \cdot I_{\perp}(\tau)} \quad (4.8)$$

where $S_{//}(t)$ and $S_{\perp}(t)$ are the time-dependent integrated transient absorption spectral intensities for parallel and perpendicular polarization between the pump and probe beams respectively. Because our observed time-resolved anisotropy measurements do not decay completely to zero within the time scale of the experiments, we have applied the standard wobble-in-a-cone model^{46,47} to understand the nature of the C343 dye in these confined systems. This analysis fits decay curves to the following function:

$$r(t) = \left(Q^2 - (1 - Q^2) \exp[-t/\tau_R] \right) \exp[-t/\tau_M] \quad (4.9)$$

where Q and τ_R quantify the degree of restriction and time scale for motion within the cone and τ_M accounts for slower decay components. We obtain the cone semi-angle, θ , from Q by the relation,

$$Q^2 = \left[\frac{1}{2} (\cos \theta) (1 + \cos \theta) \right]^2 \quad (4.10)$$

4.3 Results

4.3.a Steady-State Absorption and Emission

Figure 4.1 shows the steady-state absorption and emission spectra of C343 in bulk and in AOT reverse micelles as a function of wavelength. Both absorption and fluorescence spectra of C343 in AOT reverse micelles are blue-shifted with respect to the steady-state spectra in bulk water. As w_0 increases from 2.5 to 20, both the C343 absorption and emission spectra both shift toward the C343 spectra in bulk aqueous solution. Spectra also display an increasing shift to the blue with decreasing w_0 values. C343 absorption in AOT reverse micelles follows the deprotonated state (RO⁻)

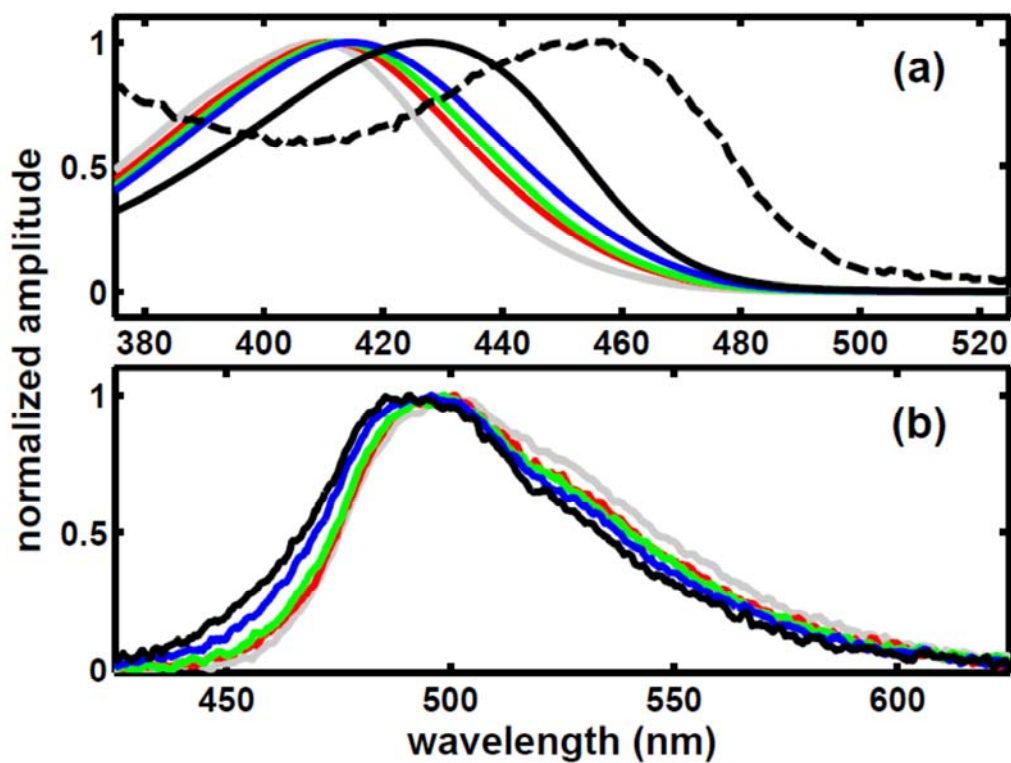


Figure 4.1. Absorption (a) and emission (b) spectra of C343 in water/AOT/cyclohexane reverse micelles with w_0 values of 2.5 (grey), 5.0 (green), 10 (red), and 20 (blue) and in basic water (solid black, pH = 10.5) and acid water (dashed black, pH = 2). Both absorption and emission spectra of C343 in AOT reverse micelles are blue-shifted with respect to C343 in bulk water.

absorption closely. However, the spectra never shift to a point where they overlap the spectra in water. Figure 4.1a also compares the C343 absorption in water/AOT/cyclohexane microemulsions to C343 absorption spectra under basic (pH = 10) and acidic (pH = 2) conditions in water. C343 absorption in AOT reverse micelles corresponds closely with C343 absorption in basic water suggesting that the reverse micelles stabilize the deprotonated C343 state (RO^-). Table 4.1 lists the absorption and emission maxima for C343 in bulk water and in AOT reverse micelles with the calculated Stokes shift values from these data. The Stokes shift for C343 in the AOT reverse micelles increases modestly with decreasing w_0 from 20 to 5; the Stokes shift in the $w_0 = 2.5$ reverse micelles shows a significant increase compared to the values for larger reverse micelles. This increasing Stokes shift primarily reflects the shifting absorption maximum rather than the emission maximum, indicating greater ground-state stabilization over excited-state stabilization of C343 as the water pool volume declines.⁴⁸

4.3.b Solvation Dynamics

Figure 4.2 presents broadband femtosecond transient absorption (BFTA) spectrograms of C343 in water/AOT/cyclohexane reverse micelles and in bulk aqueous solution; the time axis is plotted on a base 10 logarithmic scale with lower and upper limits of $t=0.01$ ps and 2000 ps, respectively ($\log(t)=-2$ to 3.3). The spectrograms in Figure 4.2 are calculated from parallel and perpendicular data using equation 4.3 to yield signals free from contributions of C343 rotation but prior to any processing described in section 4.2.d. Representing the time dependence logarithmically highlights differences in timescales between samples and within a given sample. The positive

Table 4.1 AOT/cyclohexane/water reverse micelle water pool diameters^a, estimated number of water molecules per micelle,^b absorption/emission maxima, static Stokes shifts and reorganization energy (λ) for C343 in bulk (acidic, basic) water and in AOT reverse micelles.

	d_{WP}	n_{water}	V_{ABS}	V_{EMIS}	V_{STOKES}	λ	
bulk (acidic)	--	--	22086	--	--	--	
bulk (basic)	--	--	23416	19954	3462	1731	
w₀	20	6.9	5738	24106	20036	4070	2035
	10	4.0	1118	24215	20081	4134	2067
	5	2.6	290	24319	20186	4133	2066
	2.5	1.8	106	24484	20248	4236	2118

^a Water pool diameters (d_{WP}) were calculated as $d_{WP} = 0.29w_0 + 1.1$ from Ref ⁴⁹

^b The number of water molecules was estimated assuming the molar volume of water (55.4 mol/m³)

signal from the SE band (red "swoosh"), apparent from 450 to 550 nm, dominates all the spectra. Visual examination of the spectrogram in Fig. 4.2a reveals solvation dynamics in bulk water conclude within a few picoseconds in agreement with solvation dynamics data in the literature.⁵⁰ In contrast, the signals for C343 in AOT reverse micelles, shown in Fig. 4.2b-e, show dynamic processes occurring over the entire time window from femtoseconds to nanoseconds.

To quantify the solvation dynamics, we calculate $C(t)$ from equation 4.1 through time-dependent spectral shifts in BFTA spectra, using $f(t)=\nu_0(t)$ from the SE signal maximum determined from equation 4.7. Figure 4.3 shows the solvation dynamic responses occurring over a range of timescales. Data in the supporting information (Appendix B, section B.1) provide similar traces using two alternative methods to gauge the solvation on the basis of the raw transient absorption signal maximum frequency and the first spectral moment of the SE signal. We fit the $C(t)$ data in Fig. 4.3 to a multi-exponential of the form,

$$S(t) = \nu_0 + S_0 \left(\sum_i a_i \exp \left[-\frac{t}{\tau_i} \right] \right) \quad (4.10)$$

where b is the baseline value, measured at $t=\infty$, S_0 is the magnitude of the total observed frequency shift, and a_i and τ_i are the amplitude and time-constant, respectively, for the i th component. The bulk water solvation dynamics are best described by a sum of two exponentials, consistent with data in the literature⁵⁰ while solvation dynamics in reverse micelles require a four exponentials to obtain an effective fit. Fit parameters are compiled in Table 4.2.

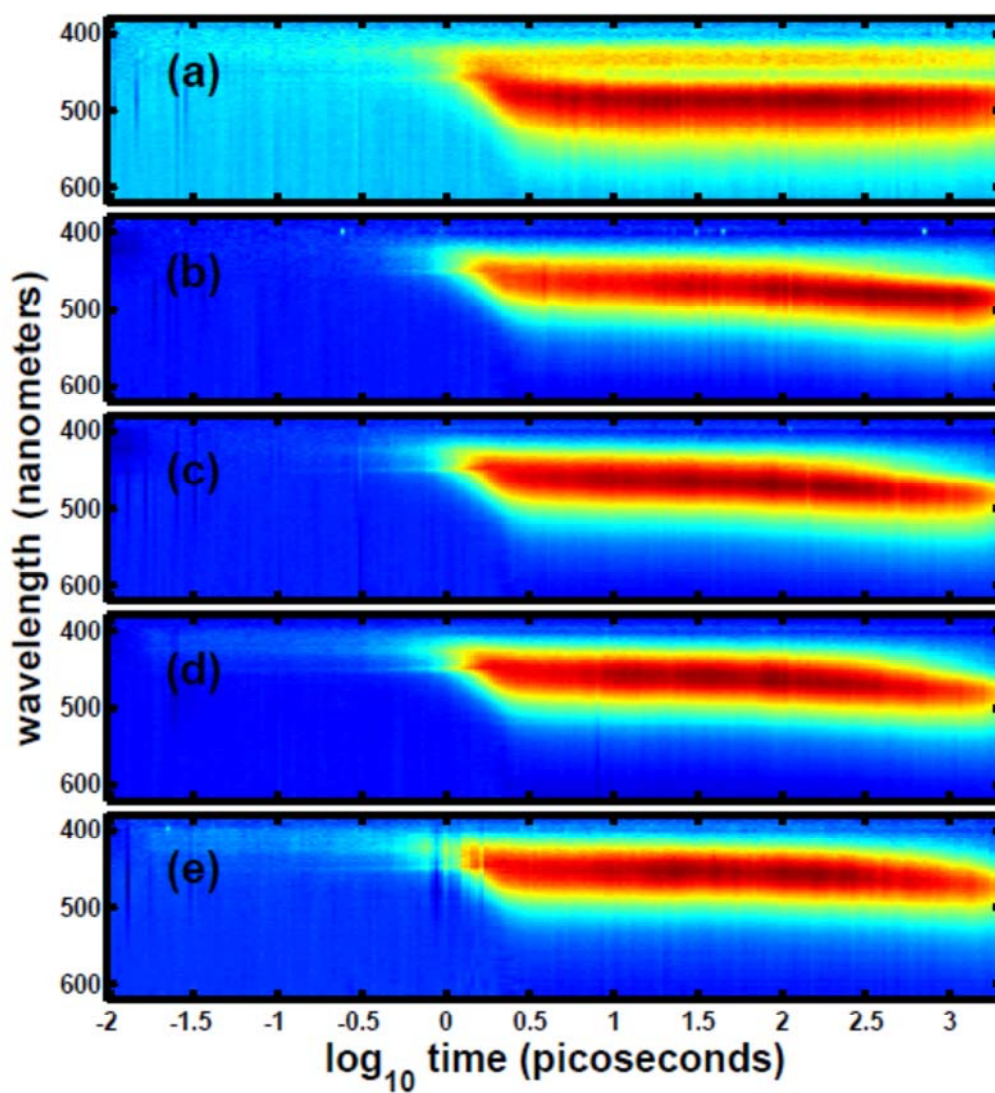


Figure 4.2 Broadband femtosecond transient absorption spectrograms of C343 in a) bulk water and in water/AOT/cyclohexane reverse micelles with w_0 : b) 20, c) 10, d) 5, and e) 2.5. Red hues indicate high intensity while blue hues indicate low intensity with blue hues. All spectrograms are plotted on a base 10 logarithmic scale with the same time limits as spectrogram e) from 10 fs to 2 ns.

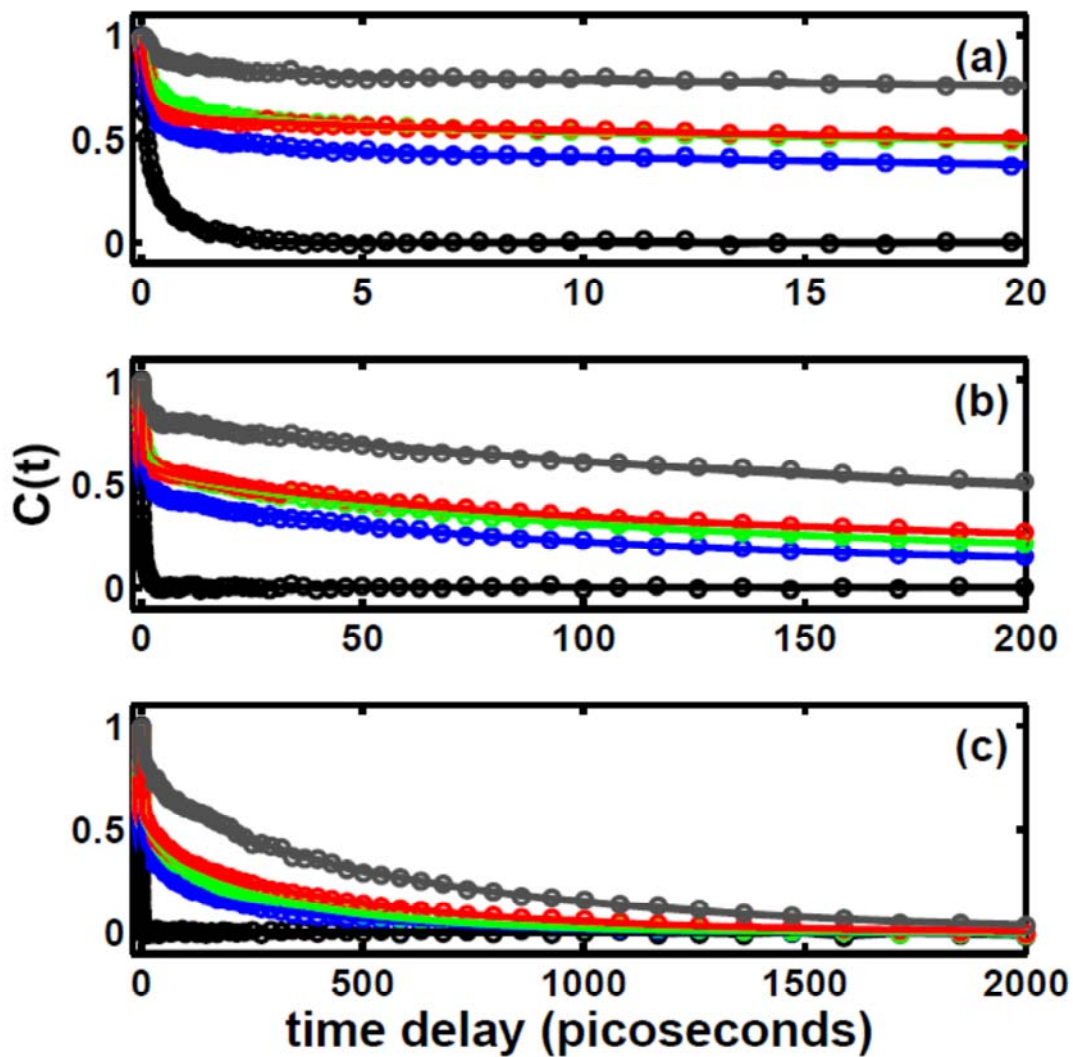


Figure 4.3 Normalized time-dependent spectral shift of the stimulated emission band of C343 in bulk water (black) and in water/AOT/cyclohexane reverse micelles with $w_0=20$ (blue), 10 (green), 5 (red), and 2.5 (grey). Panel a) 0 to 20 ps timescale, b) 0 to 200 ps timescale and c) 0 to 2 ns timescale. Solid curves are multi-exponential fits to the data.

Table 4.2 Multi-exponential fit parameters from equation 4.11 to time-dependent spectral shifts of the broadband femtosecond transient absorption stimulated emission band maximum, of C343 in bulk water and in cyclohexane/AOT/water reverse micelles and extracted excited-state lifetime.

	ν_0 (1/cm)	S_0 (1/cm)	a_1	τ_1 (fs)	a_2	τ_2 (ps)	a_3	τ_3 (ps)	a_4	τ_4 (ps)	τ_L (ns)
bulk	19963(1)	1034(10)	0.61(1)	100(4)	0.39(1)	0.77(0.03)	--	--	--	--	5.3(0.8)
20	20062(6)	1950(10)	0.41(1)	121(4)	0.14(1)	1.6(1)	0.22(1)	61(5)	0.23(1)	386(32)	3.9(0.2)
10	20103(7)	2058(10)	0.29(1)	196(12)	0.14(1)	2.0(2)	0.20(1)	54(5)	0.37(1)	353(19)	3.0(0.2)
5	20194(9)	2042(10)	0.38(1)	187(8)	0.04(1)	2.5(8)	0.19(1)	52(5)	0.39(1)	493(24)	3.4(0.2)
2.5	20193(33)	2396(10)	0.11(1)	315(79)	0.08(1)	2.1(6)	0.20(1)	115(18)	0.60(1)	709(66)	3.6(0.3)

4.3.c Time-resolved Anisotropy Measurements

The anisotropy measurements and selected fits for C343 in bulk water and AOT reverse micelles are shown in Figure 4.4. Anisotropy decays were fit to several different models (equations 4.9 and 4.10),^{46,47} fit results are presented in Table 4.3. The anisotropy decay for C343 in bulk water fits best to a single exponential decay with a time-constant of approximately 90 ps, which agrees well with our previous TRFSS measurements and other reports in the literature.^{18,51} For C343 in AOT reverse micelles, single exponential decays fail to adequately capture the complete anisotropy behavior; the decays display fast (<140 ps) and slow (>500 ps) components and do not reach zero by 2 ns for all measured w_0 values. Both biexponential decay and the wobble-in-a-cone analysis work well to describe the data. As the reverse micelles diameter decreases, normalized amplitudes from the double exponential analysis display a shift in amplitude from the fast component to the slow component as w_0 is decreased. That is, fast rotational motion of C343 in larger reverse micelles comprises a larger fraction of the motion than it does for C343 in the smaller systems.

Because the anisotropy has not decayed by the longest times measured, 2 ns, applying the wobble-in-a-cone model can build insight into this system. This model, characterized by fast probe motion restricted to a cone-shaped space, and a much slower, sometimes constant, decay of the entire system, was developed to describe reorientational relaxation for probes in restricted environments.^{46,47} Fits of our anisotropy data to the wobble-in-a-cone model show that Q^2 values increase as w_0

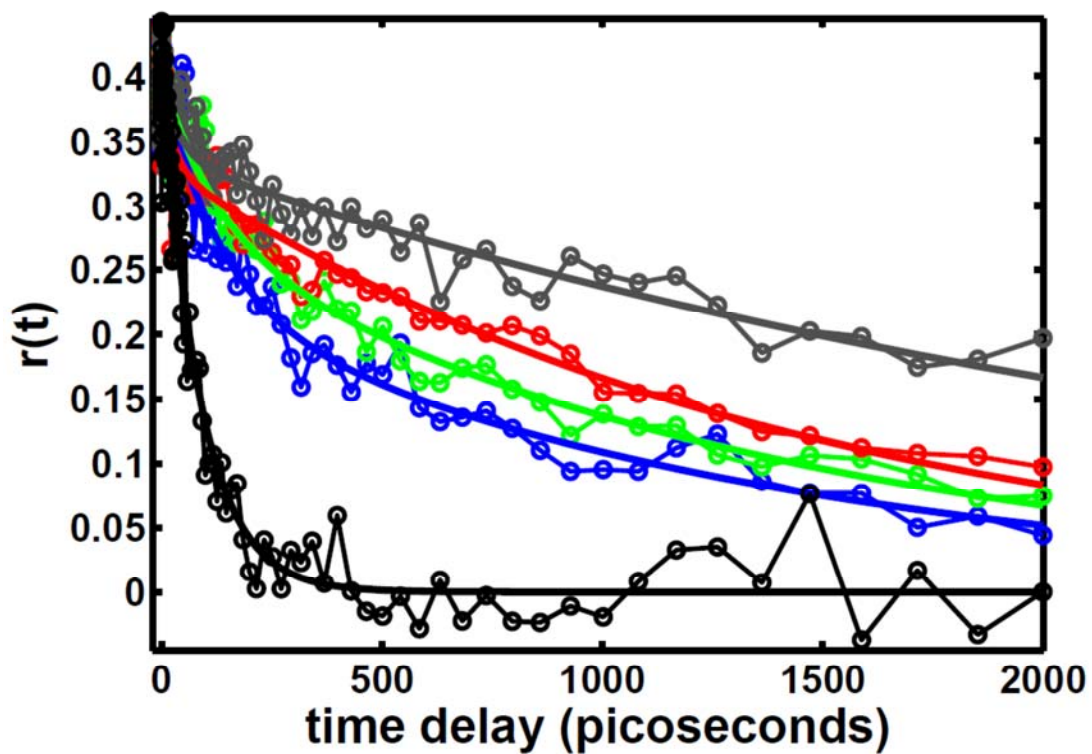


Figure 4.4 Time-resolved anisotropy decays for C343 in bulk water (black) and in water/AOT/cyclohexane reverse micelles with $w_0=20$ (blue), 10 (green), 5 (red), and 2.5 (grey). Solid lines are fits anisotropy decays (double exponential for reverse micelle samples and single exponential for bulk water).

Table 4.3. Single exponential, double exponential and wobble-in-a-cone parameters from fits to measured C343 anisotropy curves in bulk water and in cyclohexane/AOT/water reverse micelles. R corresponds to the total fitted amplitude for each decay and a_1, a_2 in the double exponential analysis are normalized with respect to R . Wobble-in-a-cone values include the semi-cone angle calculated from Eq. 4.5.

	<i>single exponential</i>		<i>double exponential</i>				
	R	τ (ps)	R	a_1	τ_1 (ps)	a_2	τ_2 (ns)
bulk	0.39(0.01)	88(5)	--	--	--	--	--
20	0.35(0.02)	280(20)	0.36(0.02)	0.4(0.1)	130(40)	0.6(0.1)	1.3(1.2)
10	0.39(0.02)	400(30)	0.40(0.02)	0.3(0.1)	130(50)	0.7(0.2)	1.4(1.0)
5	0.35(0.02)	440(40)	0.37(0.02)	0.17(0.02)	25(7)	0.8(0.1)	1.4(0.4)
2.5	0.32(0.02)	400(60)	0.33(0.02)	0.16(0.03)	40(20)	0.8(0.7)	2.8(3.4)

	<i>wobble-in-a-cone</i>				
	R	Q^2	τ_R (ps)	τ_M (ns)	θ (deg)
20	0.358(0.003)	0.78(0.05)	130(40)	0.8(0.1)	23
10	0.396(0.003)	0.85(0.04)	130(30)	1.3(0.1)	19
5	0.369(0.004)	0.911(0.009)	18(5)	1.18(0.06)	14
2.5	0.325(0.004)	0.90(0.02)	50(20)	2.1(0.3)	15

decreases, indicating a shift in amplitude from the fast decay to the slow decay. Semi-cone angles, θ , calculated from Q^2 (equation 4.10) yield angles that decrease with decreasing w_0 to a plateau of 14-15° at $w_0 = 5$. Thus, as the reverse micelles diameter drops, anisotropy measurements exhibit more restricted rotational motion of C343.

4.4 Discussion

The various results presented here build interesting new insight about the nature of the space confined within AOT reverse micelles and how the C343 dye probe exists within that space. The observed dynamics separate naturally into two timescales: (1) faster dynamics occurring on the timescale <10 ps, and (2) slower dynamics occurring on longer timescales (>10 ps). For C343 in all of the AOT reverse micelles studied, the dynamics occurring on the sub 10 ps fit well to a sum of two exponentials. The time constants (τ_1, τ_2) for these two exponentials correspond closely with the time constants observed for C343 solvation dynamics in bulk water albeit with somewhat longer time constants (see Table 4.2). The longer of the two time constants, τ_2 , is roughly twice the value for bulk water and remains relatively constant over the entire w_0 range. The shorter time constant, τ_1 , depends on w_0 ; τ_1 approaches the bulk value, 100 fs, for $w_0 = 20$, reaches a plateau between $w_0 = 5, 10$ and increases sharply at $w_0 = 2.5$. These results suggest that contributions to the dynamic Stokes shift observed arise from solvation of the C343 dye probe by intramicellar water and the micelle

environment. It suggests that the confinement has a more pronounced effect on the inertial water motion than it does on diffusive water motion.

Perhaps the most striking result from Stokes shift analysis of BFTA data of C343 in AOT reverse micelles is the significant portion of the solvation response that occurs on a timescale longer than 10 ps. Solvation dynamics of bulk water do not include dynamics on this longer timescale.⁵⁰ These slower dynamics also decay with biexponential behavior. The shorter time constant, τ_3 stays relatively constant at 50-60 ps for $w_0 = 20$ to 5 and roughly doubles to 115 ps at $w_0 = 2.5$. The slower time constant τ_4 is constant for $w_0 = 20$ and 10 but increases significantly from $w_0 = 10$ to 2.5. Overall we observe that τ_3 and τ_4 increase strongly when the water pool diameter is sufficiently small ($w_0 = 2.5$). Consideration of other data, including steady-state spectra and anisotropy decays helps us to develop understanding of the origin of the dynamics occurring on the tens to hundreds of ps timescale.

Time-dependent Stokes shifts dynamics reflect relaxation on the excited-state potential driven by the C343 dipole change between the ground-state and excited-state.⁴ The total observed Stokes shift, S_0 , (Table 4.2) is proportional to the free energy change due to the system relaxation on the excited-state potential. Our data show consistently larger values for S_0 in reverse micelles than in bulk aqueous solution. This result may appear to contradict our previously reported time-resolved fluorescence Stokes shift studies that showed a consistent decrease in the measured Stokes shift with decreasing w_0 .⁵² However, our previous time-resolved fluorescence Stokes shift studies only included analysis to 10 ps while the BFTA studies reported here extend to 2 ns. The

BFTA data reveal that the 10 ps to 2 ns time window accounts for a significant portion of the total Stokes shift amplitude, dynamics we would have missed previously. This result led us to assess how much of the relaxation our measurements capture.

Comparing the magnitude of dynamic Stokes with reorganizational energy from the steady-state Stokes shift values, v_{STOKES} (Table 4.1) allows us to gauge whether our experiments capture all dynamics occurring or if we miss some fraction. The reorganization energy, λ (see Table 4.1), defined as half the magnitude of the steady-state Stokes shift⁵³, places an upper limit on S_0 . Our results show $S_0/\lambda \approx 0.6$ for C343 in bulk water, indicating that we miss a significant portion of the solvation bulk solvation dynamics that occurs in the first 300 fs. Previous measurements of aqueous solvation dynamics by C343 time-resolved fluorescence Stokes shift⁵⁰ report that a significant portion of the solvation dynamics occurs on the sub 300 fs timescale so it is not surprising that our BFTA measures of the solvation dynamics miss part of the bulk aqueous response. In contrast, values for S_0/λ in AOT reverse micelles approach unity. This indicates that our experiments capture the entire Stokes shifting dynamics occurring in the reverse micelles and suggest that our previous measurements missed some fraction of the dynamic Stokes shift.

The similarity between the shorter time dynamics of C343 in AOT reverse micelles with solvation dynamics in bulk aqueous solution lead us to interpret this response as due to solvation dynamics in the reverse micelles. But what is the nature of the slow solvation response? Solvation dynamics on the tens to hundreds of ps timescale has been observed for a variety of systems including bulk solvents such as

long chain alcohols⁴, ionic liquids²⁷, and in biological systems^{8,10}. The previous discussions have assumed that the measured solvation dynamic responses arise primarily from the dye's solvation response by the environment. Although this is possible for our systems, another mechanism could account for the slowest dynamics observed.

Stokes shifting dynamics are sensitive to any type of molecular motion that lowers the free energy of the system. Traditionally, dynamic Stokes shifts experiments utilize coumarin dyes to follow the dynamic response of the system rather than intramolecular relaxation.⁴ However, in the nanoconfined environment of the reverse micelles, motion of the dye molecule could potentially account for some of the observed dynamics. If C343 resides within the water pool but near the interface in its ground electronic state, the change in dipole occurring upon electronic excitation could provide a driving force causing it to migrate towards the more bulk-like interior of the water pool where more effective solvation lowers the free energy of the system. This motion would be governed by translational motion of C343 and would occur with a much slower rate than the solvation response attributed to water reorientation. Given a translational diffusion constant for C343 in water is $550 \mu\text{m}^2/\text{s}$,⁵⁴ the root mean squared distance that the molecule would move inside the reverse micelle on the τ_4 timescale (Table 4.2) would range from 1.1 to 1.5 nm. This distance, and even smaller distances, could represent displacement of the dye from the interfacial "shell" to the interior "core"³² for all but the smallest reverse micelles studied. Results from steady-state spectroscopy support this interpretation. Migration of C343 from an interfacial to the

reverse micelle interior should lead the steady-state fluorescence spectra to reflect a largely bulk-like environment. Fig. 4.1 shows that the C343 fluorescence spectrum shifts minimally with w_0 and the spectrum is quite close to that for C343 in bulk aqueous solution. Shifting of the absorption spectrum is much more dramatic. Similar time constants obtained for $w_0=20$ and 10 time-resolved anisotropy results (Table 4.3) may indicate that C343 senses similar environments in these reverse micelles.

In simulations, Faeder and Ladanyi explored the location of model chromophores in model AOT reverse micelles.^{11,55} They found only a weak dependence of solvation dynamics of their model I_2^- probe molecule on w_0 and interpreted this to reflect the probe's location in the reverse micelle interior which has an environment similar to bulk water.¹¹ In contrast, data for solvation dynamics of their model I_2^+ show that its position in the reverse micelle interior varies. Feng and Thompson have explored translational diffusion of molecules in model confined environments.^{56,57} They find it difficult to define a diffusion coefficient because a free energy barrier or energy gradient that depends on the radial position can lead to an activated process that may control the timescale of the observed dynamics. Still their results support our interpretation for the slowest dynamics we observe.

Another possible explanation for the slow component to the dynamic Stokes shift observed is that C343 exists in a range of static heterogeneous environments where a fraction of the C343 population is solvated by water near the micelle interface while the interior of the water pool solvates the remaining C343 population. This situation would result in a range of environments for C343 and lead to a distribution of

response times by the C343. The net response would manifest as a fast, bulk-like dynamics from C343 in the interior of the water pool with a slower response from C343 solvated by the interface. Assuming this model, we can estimate the relative populations in each environment. If the fast response (<10 ps) reflects C343 residing in the interior of the water pool and the slower response (>10 ps) is from C343 near the interface, then the amplitude of the slow components divided by the amplitude of the fast components, $(a_3+a_4)/(a_1+a_2)$ should reflect the relative proportion of dye solvated in each environment. Figure 4.5 presents the interfacial to interior C343 population ratio = $(a_3+a_4)/(a_1+a_2)$ versus w_0 values. As the size of the water pool increases, the ratio of the interfacial to interior populations should increase inversely with hydrodynamic radius, $1/R_H$, or, because $w_0 \propto r$, with a $1/w_0$ dependence. This fits the expected surface to volume relationship as a function of w_0 supporting the interpretation that C343 exists in distinct interfacial and interior environments within AOT reverse micelles. However, from this data, we cannot determine the extent to which the two C343 populations may be interchanging or if population transfer occurs while C343 is electronically excited in AOT reverse micelles.

In addition to our observation of dynamics occurring on longer timescales than occur in bulk aqueous solution, we note different trends between the various reverse micelle sizes for the various measurements. In particular, data for $w_0=2.5$ diverge from the trends seen between $w_0=20$ to 5. For example, the increasing overall Stokes shift with decreasing w_0 , ν_{STOKES} in Table 4.1, shows a large increase occurring from $w_0=5$ to 2.5. Likewise, although τ_3 stays relatively constant for $w_0=20$ to 5, it displays a dramatic

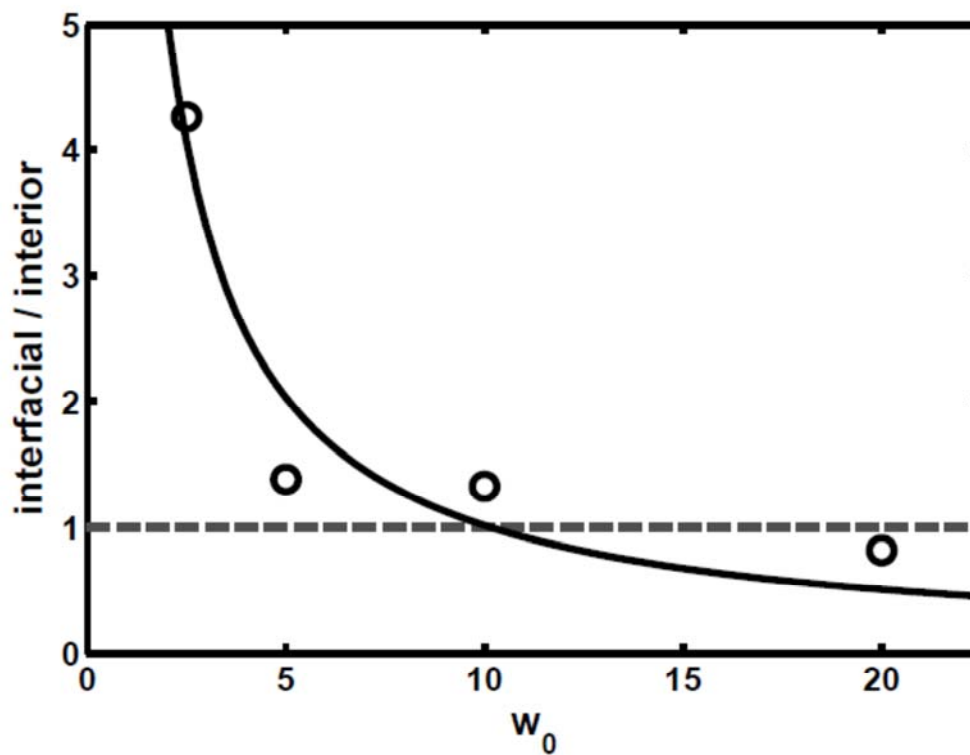


Figure 4.5 Ratio of the interfacial population of C343 to interior population of C343 in water/AOT/cyclohexane RM as a function of w_0 . The dashed line represents a ratio of one to one and the solid line is a $1/r$ fit to the data assuming w_0 is proportional to the micelle radius, r .

increase for $w_0 = 2.5$. The anisotropy decay observed for C343 in $w_0 = 2.5$ shows a highly confined environment. These data support the interpretation that as w_0 decreases, C343 interacts increasingly with the micelle interface due both to the reduced water content and the reduced water pool diameter.

4.5 Summary and Conclusions

We have studied C343 in water/AOT/cyclohexane reverse micelles and in bulk water via broadband ultrafast transient absorption and steady-state spectroscopies. These studies have focused on quantifying the complete evolution of time-resolved Stokes shift dynamics in AOT reverse micelles, which span femtoseconds to nanoseconds. Steady-state absorption and emission indicate that the C343 deprotonated state is stabilized within AOT reverse micelles. Analysis of C343 anisotropy dynamics show that reorientation motion slows as the water pool size shrinks. This is consistent with C343 residing in the water pool and reorientational motion becoming quenched as it interacts more strongly with the micelle interface as the water pool diameter decreases. Analysis of the extracted solvation dynamics agree with our previous TRFSS studies¹⁸ that show hindrance of the solvation response in the <100 ps timescale as the size of the water pool shrinks. We have extended our analysis to 2 ns and recovered the entire solvation response of C343 in AOT reverse micelles. We suggest that the solvation response > 10 ps involves diffusive motion of excited C343 within the reverse micelles to a more energetically favorable location. This interpretation indicates that the excited-state character of C343 plays a role in

determining the overall solvation response of the C343/AOT reverse micelle system and that the assumption that solvation response for fluorescent dye molecules such as C343 is due to solvent motion only is valid in bulk solvents, it is not valid in more complex systems such as reverse micelles. Therefore, measurement of the complete dynamic response e.g from femtoseconds to nanoseconds is essential in detecting and understanding more complex solvation dynamics behavior.

References and Notes

- (1) Agarwal, P. K.; Billeter, S. R.; Rajagopalan, P. T. R.; Benkovic, S. J.; Hammes-Schiffer, S. *Proc. Natl. Acad. Sci. U. S. A.* **2002**, *99*, 2794.
- (2) Nashine, V. C.; Hammes-Schiffer, S.; Benkovic, S. J. *Curr. Opin. Chem. Biol.* **2010**, *14*, 644.
- (3) Barbara, P. F.; Rzeba, W. *Acc Chem Res* **1988**, *21*, 195.
- (4) Horng, M. L.; Gardecki, J. A.; Papazyan, A.; Maroncelli, M. *Journal of Physical Chemistry* **1995**, *99*, 17311.
- (5) Stratt, R. M.; Maroncelli, M. *Journal of Physical Chemistry* **1996**, *100*, 12981.
- (6) Kahlow, M. A.; Jarzeba, W.; Kang, T. J.; Barbara, P. F. *J. Chem. Phys.* **1989**, *90*, 151.
- (7) Fleming, G. R.; Cho, M. H. *Annu. Rev. Phys. Chem.* **1996**, *47*, 109.
- (8) Vajda, Š.; Jimenez, R.; Rosenthal, S. J.; Fidler, V.; Fleming, G. R.; Castner, E. W. *Journal of the Chemical Society, Faraday Transactions* **1995**, *91*, 867.
- (9) Bagchi, B. *Chem. Rev.* **2005**, *105*, 3197.

- (10) Pal, S. K.; Peon, J.; Zewail, A. H. *Proc. Natl. Acad. Sci. U. S. A.* **2002**, *99*, 1763.
- (11) Faeder, J.; Ladanyi, B. M. *J. Phys. Chem. B* **2001**, *105*, 11148.
- (12) Sen, P.; Roy, D.; Mondal, S. K.; Sahu, K.; Ghosh, S.; Bhattacharyya, K. *J. Phys. Chem. A* **2005**, *109*, 9716.
- (13) Shirota, H.; Segawa, H. *Langmuir* **2004**, *20*, 329.
- (14) Adhikari, A.; Dey, S.; Mandal, U.; Das, D. K.; Ghosh, S.; Bhattacharyya, K. *J. Phys. Chem. B* **2008**, *112*, 3575.
- (15) Chakraborty, A.; Seth, D.; Setua, P.; Sarkar, N. *J. Phys. Chem. B* **2006**, *110*, 5359.
- (16) Hazra, P.; Chakraborty, D.; Sarkar, N. *Chem. Phys. Lett.* **2003**, *371*, 553.
- (17) Pant, D.; Levinger, N. E. *Langmuir* **2000**, *16*, 10123.
- (18) Riter, R. E.; Willard, D. M.; Levinger, N. E. *J. Phys. Chem. B* **1998**, *102*, 2705.
- (19) Andreatta, D.; Lustres, J. L. P.; Kovalenko, S. A.; Ernsting, N. P.; Murphy, C. J.; Coleman, R. S.; Berg, M. A. *J. Am. Chem. Soc.* **2005**, *127*, 7270.
- (20) Qiu, W. H.; Zhang, L. Y.; Okobiah, O.; Yang, Y.; Wang, L. J.; Zhong, D. P.; Zewail, A. H. *J. Phys. Chem. B* **2006**, *110*, 10540.
- (21) Zhang, L. Y.; Wang, L. J.; Kao, Y. T.; Qiu, W. H.; Yang, Y.; Okobiah, O.; Zhong, D. P. *Proc. Natl. Acad. Sci. U. S. A.* **2007**, *104*, 18461.
- (22) Shirota, H.; Funston, A. M.; Wishart, J. F.; Castner, E. W. *J. Chem. Phys.* **2005**, *122*.

- (23) Jin, H.; Baker, G. A.; Arzhantsev, S.; Dong, J.; Maroncelli, M. *J. Phys. Chem. B* **2007**, *111*, 7291.
- (24) Ito, N.; Richert, R. *J. Phys. Chem. B* **2007**, *111*, 5016.
- (25) Kashyap, H. K.; Biswas, R. *J. Phys. Chem. B* **2008**, *112*, 12431.
- (26) Lang, B.; Angulo, G.; Vauthey, E. *J. Phys. Chem. A* **2006**, *110*, 7028.
- (27) Samanta, A. *Journal of Physical Chemistry Letters* **2010**, *1*, 1557.
- (28) Nilsson, L.; Halle, B. *Proc. Natl. Acad. Sci. U. S. A.* **2005**, *102*, 13867.
- (29) Fayer, M. D.; Levinger, N. E. In *Ann. Rev. Anal. Chem.* 2010; Vol. 3, p 89.
- (30) Levinger, N. E.; Swafford, L. A. *Annual Review of Physical Chemistry* **2009**, *60*, 385.
- (31) Farrer, R. A.; Fourkas, J. T. *Accounts Chem. Res.* **2003**, *36*, 605.
- (32) Piletic, I. R.; Moilanen, D. E.; Spry, D. B.; Levinger, N. E.; Fayer, M. D. *J. Phys. Chem. A* **2006**, *110*, 4985.
- (33) Elola, M. D.; Rodriguez, J.; Laria, D. *J. Chem. Phys.* **2010**, *133*.
- (34) Mugridge, J. S.; Szigethy, G.; Bergman, R. G.; Raymond, K. N. *J. Am. Chem. Soc.* **2010**, *132*, 16256.
- (35) Luisi, P. L.; Giomini, M.; Pileni, M. P.; Robinson, B. H. *Biochim. Biophys. Acta* **1988**, *947*, 209.
- (36) Bhattacharyya, K. *Accounts of Chemical Research* **2003**, *36*, 95.
- (37) Heisler, I. A.; Kondo, M.; Meech, S. R. *J. Phys. Chem. B* **2009**, *113*, 1623.
- (38) Mitra, R. K.; Sinha, S. S.; Pal, S. K. *Langmuir* **2008**, *24*, 49.
- (39) Das, K.; Jain, B.; Gupta, P. K. *Chem. Phys. Lett.* **2005**, *410*, 160.

- (40) Hazra, P.; Chakrabarty, D.; Sarkar, N. *Chem. Phys. Lett.* **2002**, *358*, 523.
- (41) Pant, D.; Riter, R. E.; Levinger, N. E. *J. Chem. Phys.* **1998**, *109*, 9995.
- (42) Shirota, H.; Horie, K. *J. Phys. Chem. B* **1999**, *103*, 1437.
- (43) Willard, D. M.; Levinger, N. E. *J. Phys. Chem. B* **2000**, *104*, 11075.
- (44) Cole, R. L.; Barisas, B. G.; Levinger, N. E. *Review of Scientific Instruments* **2010**, *81* 093101.
- (45) Stancik, A. L.; Brauns, E. B. *Vibrational Spectroscopy* **2008**, *47*, 66.
- (46) Kinoshita, K.; Kawato, S.; Ikegami, A. *Biophys. J.* **1977**, *20*, 289.
- (47) Lipari, G.; Szabo, A. *Biophys. J.* **1980**, *30*, 490.
- (48) Lakowicz, J. R. *Principles of Fluorescence Spectroscopy* Third ed.; Springer Science + Business Media, LLC: New York, New York, 2006.
- (49) Kinugasa, T.; Kondo, A.; Nishimura, S.; Miyauchi, Y.; Nishii, Y.; Watanabe, K.; Takeuchi, H. *Colloids Surf. A* **2002**, *204*, 193.
- (50) Jimenez, R.; Fleming, G. R.; Kumar, P. V.; Maroncelli, M. *Nature* **1994**, *369*, 471.
- (51) Grant, C. D.; Steege, K. E.; Bunagan, M. R.; Edward W. Castner, J. *J. Phys. Chem. B* **2005**, *109*, 22273.
- (52) Riter, R. E.; Undiks, E. P.; Levinger, N. E. *Journal of the American Chemical Society* **1998**, *120*, 6062.
- (53) Marcus, R. A.; Sutin, N. *Biochimica et Biophysica Acta* **1985**, *811*, 265.
- (54) Dey, S.; Mandal, U.; Sen Mojumdar, S.; Mandal, A. K.; Bhattacharyya, K. *J. Phys. Chem. B* **2010**, *114*, 15506.

(55) Faeder, J.; Ladanyi, B. M. *J. Phys. Chem. B* **2005**, *109*, 6732.

(56) Feng, X. B.; Thompson, W. H. *Journal of Physical Chemistry C* **2007**, *111*,
18060.

(57) Feng, X. B.; Thompson, W. H. *Journal of Physical Chemistry C* **2010**, *114*,
4279.

CHAPTER 5

DEPROTONATION DYNAMICS OF HPTS IN AQUEOUS CATIONIC, ANIONIC, AND NONIONIC REVERSE MICELLES

5.1 Introduction

Proton transfer and transport have the utmost importance in regulating normal biological cell functions¹ and in the development of efficient proton exchange membrane (PEM) fuel cells²⁻⁴. In each of these cases, proton gradients are generated through specific proton transfer and transport mechanisms which in some cases are solvent assisted^{1,5}. Both nanoscopic confinement of water and the proximity of molecular interfaces play the dominant role in these situations as they perturb water mobility and disrupt normal hydrogen bonding networks⁶⁻⁸. Thus a detailed understanding of water behavior in confinement and near interfaces are an essential step towards understanding the role that water plays in proton transfer and transport mechanisms.

One simple, well-behaved class of systems that has been used to confine water is reverse micelles (RM), nanoscopic pools of water that are sequestered by surfactant molecules and surrounded by a bulk non-polar solvent. By adjusting the water to surfactant ratio, the pool radius, and consequently, the degree of confinement and

proximity of the interface can be controlled. Furthermore, the nature of the interface is controlled forming RM from cationic, anionic, and nonionic surfactants. Other studies indicate that confinement, not the nature of the confining interface, impacts observed water hydrogen bonding dynamics.⁹ Building from these results, our studies aim to determine the impact that both confinement and the nature of the interface play in proton transfer reactions.

In continuing efforts to unravel the complexities of confined liquid water, we have probed sub-nanosecond excited state proton transfer (ESPT) dynamics of the photoacid 8-hydroxypyrene-1,3,6-trisulfonic acid (HPTS) with broadband femtosecond transient absorption (BFTA) spectroscopy. HPTS has been utilized to study ESPT in bulk water¹⁰⁻²², Langmuir-Blodgett films²³⁻²⁵, proteins^{26,27}, reverse micelles²⁸⁻³¹, polymer-surfactant aggregates³², and ice^{33,34}. Following photo-excitation, HPTS exhibits ESPT transferring a proton to the solvent. The photo-initiated nature of HPTS ESPT and its spectroscopic characteristics provide a convenient way to initiate and monitor the proton transfer reaction respectively.

Studies of HPTS proton transfer in RM systems have indicated that HPTS is preferentially solvated in the water pool in anionic (AOT)^{29,31,35} and non-ionic (polyoxyethylene(4)lauryl ether, BRIJ-30) RM.^{29,30} In cationic (CTAB) RMs,^{28,30} HPTS resides near the micelle interface. In AOT and BRIJ-30 RMs, proton transfer to the solvent is bulk-like in RM water pools which are larger than the size of the HPTS molecule, that is approximately one nm in length. As the size of the RM approaches the size of HPTS, the ESPT reaction becomes increasingly quenched. These studies prepare

RM from anionic (AOT) and non-ionic (BRIJ-30) surfactants and display little or no difference in behavior between the two surfactant systems. ESPT quenching is only attributed to confinement. In CTAB RM, excitation of the HPTS protonated state [ROH] shows emission from the deprotonated HPTS state [RO⁻] indicating the ESPT process is present albeit the rate of proton transfer is much slower (~ 2000 ps) than bulk ESPT (~ 100 ps). The ESPT rate in CTAB RM is enhanced by adding increasing the acetate concentration within the RM. In this case, the acetate anion within the water pool serves as an acceptor for the proton generated by photo-excitation of HPTS.

In the studies that follow, we aim to further explore the effect that the choice of surfactant molecules plays in determining the observed ESPT reaction rate. Specifically, we explore the use of cationic (cetyl trimethylammonium bromide, CTAB) and nonionic (polyoxyethylene nonylphenylether, IGE) and contrast/compare these results to anionic (sodium dioctyl sulfosuccinate, AOT) and bulk water. The choice of these surfactants allows us to probe the effects of varying interfacial environments on ESPT and varying the size (approximately 1.5 to 10 nm) of the RM determine the significance of confinement on the observed ESPT reaction rate. We follow the ESPT reaction with broadband femtosecond transient absorption spectroscopy from 0 to 2 ns.

5.2 Experimental Methods

5.2.a Transient Absorption Spectrometer

Details of the laser system and broadband femtosecond transient absorption (BFTA) spectrometer are given in previous publication³⁶ and here in Chapter 2; here we

summarize the apparatus. 125 μJ /pulse of the output of a chirped pulse regenerative amplifier (55 fs FWHM pulses at 800 nm, 1 kHz repetition rate) is used for the transient absorption experiment. Frequency doubling in BBO generates the second harmonic pump pulses ($\sim 20 \mu\text{J}$). Before reaching the sample, the pump beam is optically chopped to provide a reference signal, double passes a fused silica Brewster prism pair to precompensate for material dispersion, and travels down a variable optical path that provides relative delay between the pump and probe pulses. The residual fundamental beam double passes through a fused silica Brewster prism pair before generating a single filament white light continuum used for the probe pulses. Pump and probe beams are focused onto the sample flowing through a 0.5 mm cuvette. The diverging probe beam is collimated, and traverses a short pass dichroic filter to extinguish the spectral intensity around 800 nm. Transient absorption signals are collected using an Ocean Optics spectrometer, which is synchronically triggered externally at twice the frequency of the pump beam modulation.

5.2.b Data Collection

Data collection was accomplished via a custom program written in MatLab (Release 2009a). This program sequentially measures the transmission spectra with the reference (pump-off), I_{ref} , and signal (pump-on), I_{sig} , and calculates the average transient absorption signal spectra:

$$S(\nu, t) = \log \left(\frac{I_{sig}(\nu, t)}{I_{ref}(\nu, \infty)} \right) \quad (5.1)$$

Transient absorption spectra were collected as a function of the delay between the pump and probe pulses, τ , and compiled to generate a transient absorption spectrogram, $S(\nu, t)$. Raw transient spectra were truncated to 1100 wavelength values over a 380-720 nm range and collected from -100 fs to 2 ns with 200 logarithmically spaced time steps.³⁷ Spectrograms were generated from both parallel and perpendicular pump beam polarizations with respect to the probe beam polarization. Parallel and perpendicular excitation pulses were normalized by monitoring pump pulse intensities transmitted through the sample with a photodiode trace on an oscilloscope. Subsequent data analysis utilized spectra from approximately 0.5 to 2000 ps to eliminate spectral shifting from the non-zero temporal chirp of the WLC probe.

5.2.c Data Analysis

5.2.c.i reorientation dynamics

Rotational anisotropy decays were calculated via,

$$r(t) = \frac{I_{\parallel}(t) - g \cdot I_{\perp}(t)}{I_{\parallel}(t) + 2g \cdot I_{\perp}(t)} \quad (5.2)$$

where $I_{\parallel}(t)$ and $I_{\perp}(t)$ are the time-dependent integrated transient absorption spectral intensities for parallel and perpendicular polarization between the pump and probe beams respectively. g is a normalization factor that matches the parallel and perpendicular intensities at delay times where $r(t)$ has decayed to zero; typical g values deviated only slightly from 1 (+/- 0.1) due to careful normalization of pulse energies between parallel and perpendicular polarizations during data collection. For

samples where $r(t)$ did not decay completely to zero within the 2 ns time window of the BFTA experiment, we assume that g equals one.

5.2.c.ii ESPT dynamics

Three contributions comprise the transient absorption spectra: excited state absorption (ESA), stimulated emission (SE), and ground state bleach (BL). SE and BL contributions indicate the sample absorbing less light while ESA displays an increase in absorption. We follow the convention of plotting ESA as negative signal (loss of photons) and SE/BL (gain of photons) with a positive signal. For ESPT processes, there is one BL contribution from the protonated state [ROH*] and two contributions of SE/ESA, one from [ROH*] and one from the deprotonated [RO⁻*] state.

We isolate the ESPT through spectral integration of the BFTA data. This approach isolates the ESPT from solvation dynamics (SD) which are manifested as time-dependent spectral shifts, described in Chapter 4. This analysis method assumes that solvation dynamics shift SE and ESA bands but they retain the same integrated oscillator strength. We have found this method to be adequate to minimize SD contributions and isolate ESPT dynamics. Resultant traces were fit to a sum of two exponentials.

5.2.d Sample preparation

Samples were characterized by steady-state absorption measured with a Varian Cary 500 UV/Vis/NIR spectrometer. Fluorescence spectra were recorded from the BFTA instrument by blocking the WLC probe beam and recording the background.

5.2.d.i reverse micelle samples

Samples were prepared with HPTS (97%, Sigma Aldrich), high-purity water (Milli-Q filtered, 18.2 M Ω cm resistivity), AOT (sodium dioctylsulfosuccinate, 99%, Sigma Aldrich), CTAB (cetyl trimethylammonium bromide, Sigma Aldrich), IGE (polyoxyethylene (5) nonylphenylether, Sigma Aldrich), 1-octanol (99%, Sigma Aldrich) and cyclohexane (99%, Sigma Aldrich). HPTS, AOT, IGE and cyclohexane were used without further purification. CTAB was purified by dissolving in absolute ethanol and recrystallizing three times, dried under vacuum filtration, and dried under vacuum.

Samples were prepared at 0.4 M AOT and IGE. For CTAB samples, the surfactant concentration was 0.1 M and 1-octanol was added as a cosurfactant in a ratio of 1:5 (CTAB:1-octanol) to form stable microemulsions. A 20 mM stock solution of HPTS in water was prepared with slightly acidic water (pH = ~6.5). Samples were prepared in approximately 20 mL volumes by mass in the following order: (1) surfactant, (2) 1-octanol (only for CTAB samples), (3) stock solution of HPTS, (4) additional water to reach the target w_0 value and (5) cyclohexane. The amount of additional water was added to yield samples with approximate w_0 values of 1, 2.5, 5, 10, and 20 for AOT, IGE samples and 10, 40 for CTAB samples. All RM samples were approximately 0.2 mM HPTS overall. IGE reverse micelle samples with D₂O (99%, Sigma Aldrich) instead of water were prepared with the previous procedure.

5.2.d.ii simulations of the IGE RM environment

Hydrated tetraethylene glycol (TEG, 99% purity, Arcos) mixtures with HPTS were prepared to simulate the IGE RM environment. Samples were prepared by mass with a stock HPTS water solution following the previously described procedure at TEG to water

ratios of 1, 3, 6, and 20. HPTS was added directly to anhydrous TEG to prepare the neat TEG sample. HPTS was also dissolved directly into the non-ionic surfactants IGE, BRIJ-30 (Sigma Aldrich), and Triton X-100 (polyoxyethylene (10) isooctylcyclohexyl ether, Sigma Aldrich). MPTS (98%, Fluka) was dissolved directly into IGE.

5.3 Results

5.3.a Steady-state Absorption and Emission

Figure 5.1 shows a comparison of the normalized steady-state absorption of HPTS in CTAB, IGE, AOT RM and in bulk water (pH \sim 6.5). HPTS visible absorption spectra display two absorption bands with maxima at \sim 404 nm and \sim 454 nm that correspond to the protonated [ROH] and deprotonated [RO⁻] HPTS states, respectively. The relative amplitude between each of these bands is pH dependent.¹⁴ In CTAB, IGE, and AOT RM, HPTS absorption spectra show the presence of [RO⁻] HPTS albeit with very different w_0 dependences. The HPTS absorption in CTAB RM shows an increase in [RO⁻] state absorption at larger w_0 values; HPTS absorption in IGE RM shows a decrease in [RO⁻] state absorption with increasing w_0 values; and HPTS absorption in AOT RM shows a relatively constant [RO⁻] state absorption with varying w_0 values. This suggests that the environment sensed by the HPTS changes from the aqueous solution from which it was introduced to the RM.

Similar to HPTS absorption spectra, HPTS emission with [ROH] state excitation (Figure 5.2) is characterized by two emission bands, one from the excited protonated

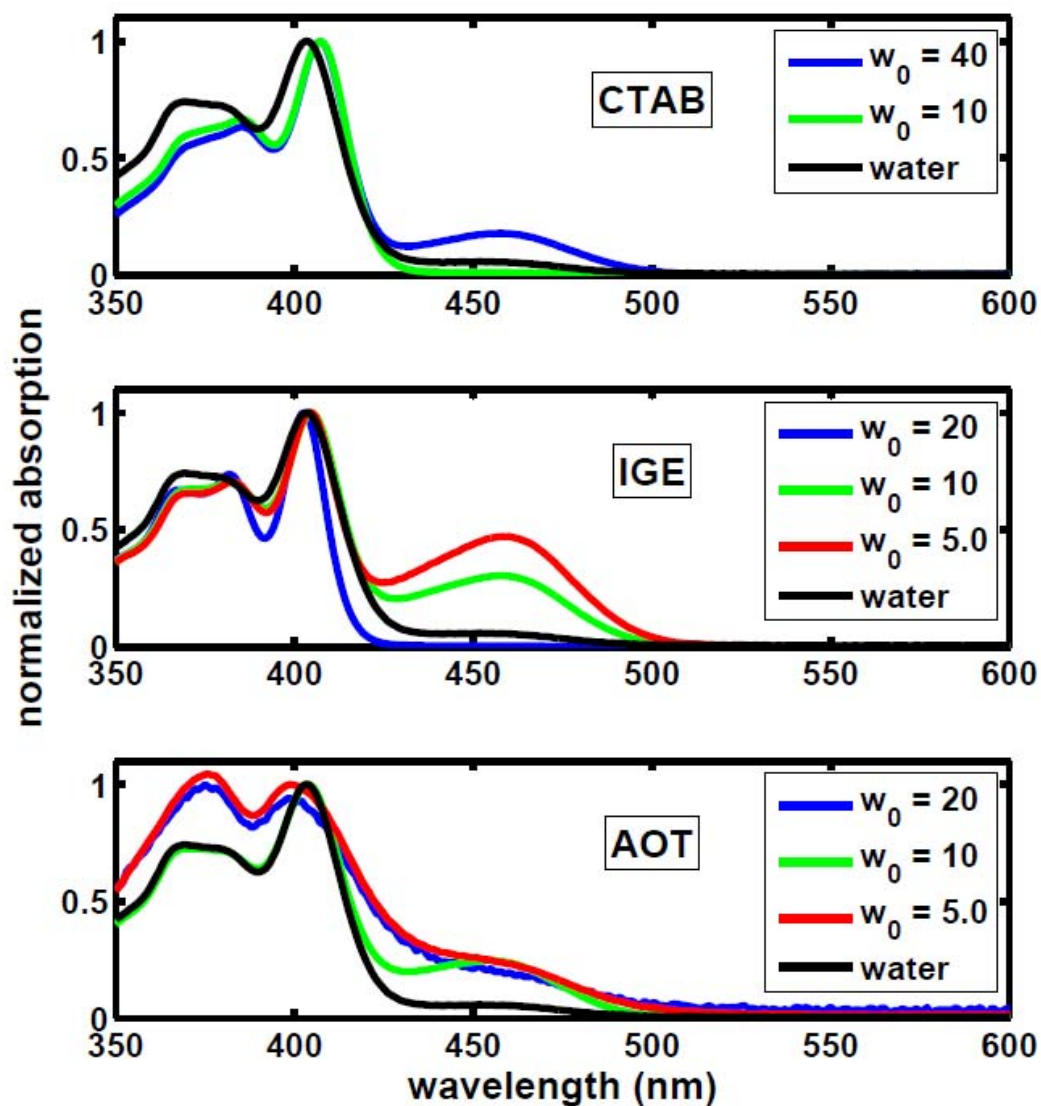


Figure 5.1 Comparison of UV-Vis absorption of HPTS in CTAB/water/1-octanol/cyclohexane (top), IGE/water/cyclohexane (middle), and AOT/water/cyclohexane (bottom) reverse micelles. The absorption spectrum of HPTS in neutral bulk water is included in all three panels for comparison. HPTS absorption in AOT reverse micelles shows relatively constant deprotonated state absorption (454 nm)

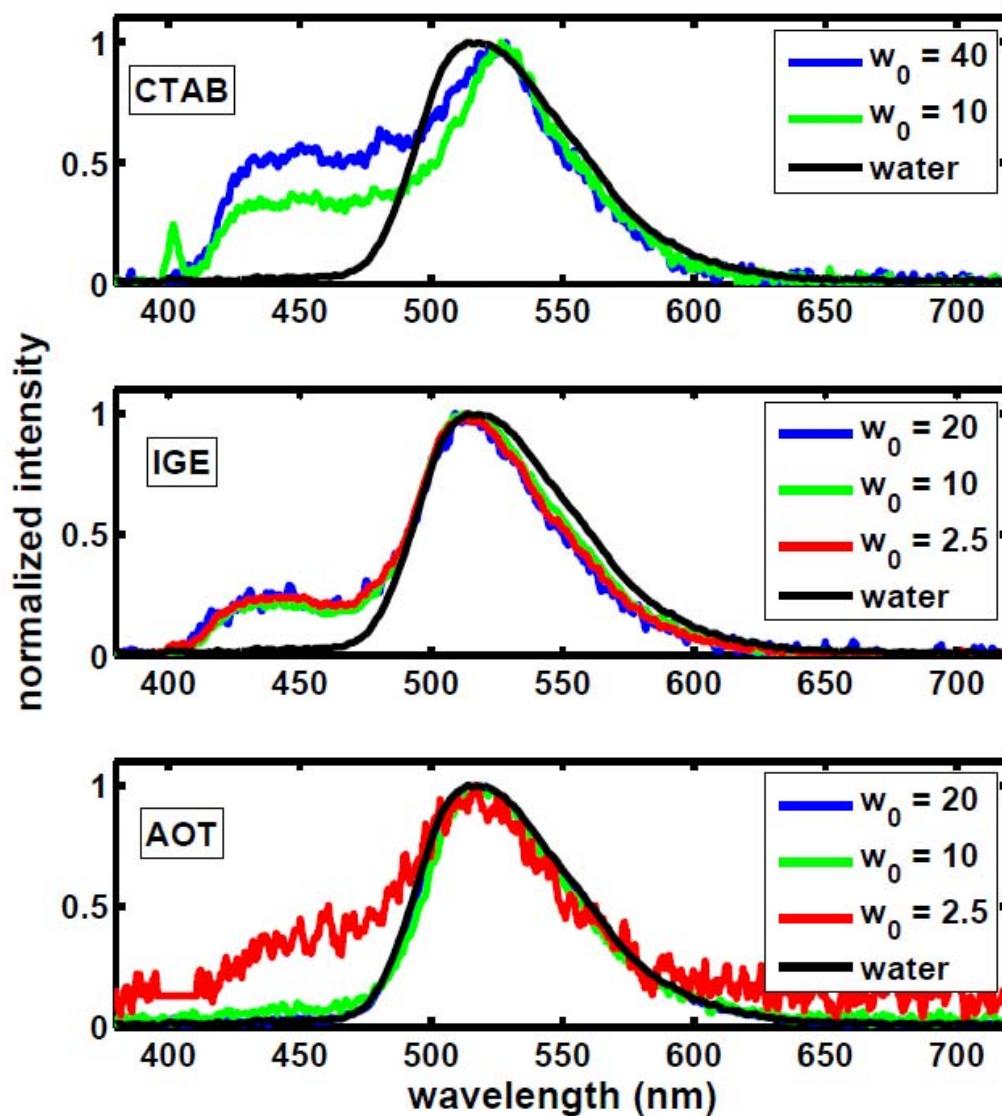


Figure 5.2 Comparison of steady-state fluorescence of HPTS in CTAB/water/1-octanol/cyclohexane (top), IGE/water/cyclohexane (middle), and AOT/water/cyclohexane (bottom) reverse micelles. The emission spectrum of HPTS in neutral bulk water is included in all three panels for comparison. When protonated HPTS in reverse micelles is excited (~ 400 nm) emission from the deprotonated state (~ 530 nm) dominates indicating the presence of excited state proton transfer.

while HPTS absorption IGE and CTAB reverse micelles show deprotonated state absorption that is size dependent. [ROH*] state appearing at shorter wavelength, approximately 430 nm, and the other from the excited deprotonated [RO⁻*] state at longer wavelength, 560 nm.¹⁴ HPTS emission in IGE and CTAB RM display increased emission from the [ROH*] state with respect to both bulk water and AOT RM emission spectra. HPTS in the smallest AOT RM investigated ($w_0 = 2.5$) shows similar behavior to HPTS in CTAB and IGE RM. Slight spectral shifting to shorter wavelengths is observed for HPTS in IGE and AOT RM as w_0 decreases while in CTAB RM HPTS shows an increase in [ROH*] state emission intensity.

5.3.b Reorientation Dynamics

Figure 5.3 shows HPTS anisotropy decays for the largest CTAB, IGE, AOT RM investigated and in bulk aqueous solution. HPTS reorientational decays in large CTAB and IGE RM show much slower decays than HPTS reorientational decays in bulk aqueous solution. The reorientational decay for HPTS in large AOT RM closely approaches the reorientational decay in bulk aqueous solution. These results indicate that HPTS experiences restricted environments in CTAB and IGE RM that is markedly different than bulk aqueous solution while HPTS in all but the smallest AOT RM exists in a largely bulk-like environment. Figure 5.4 shows anisotropy curves for HPTS in water/CTAB/1-octanol/cyclohexane, water/IGE/cyclohexane, and water/AOT/cyclohexane RM with w_0 varied, and in bulk aqueous solution. A strong correlation with w_0 was not observed. Biexponential fit parameters are presented in Table 5.1. HPTS reorientational motion in

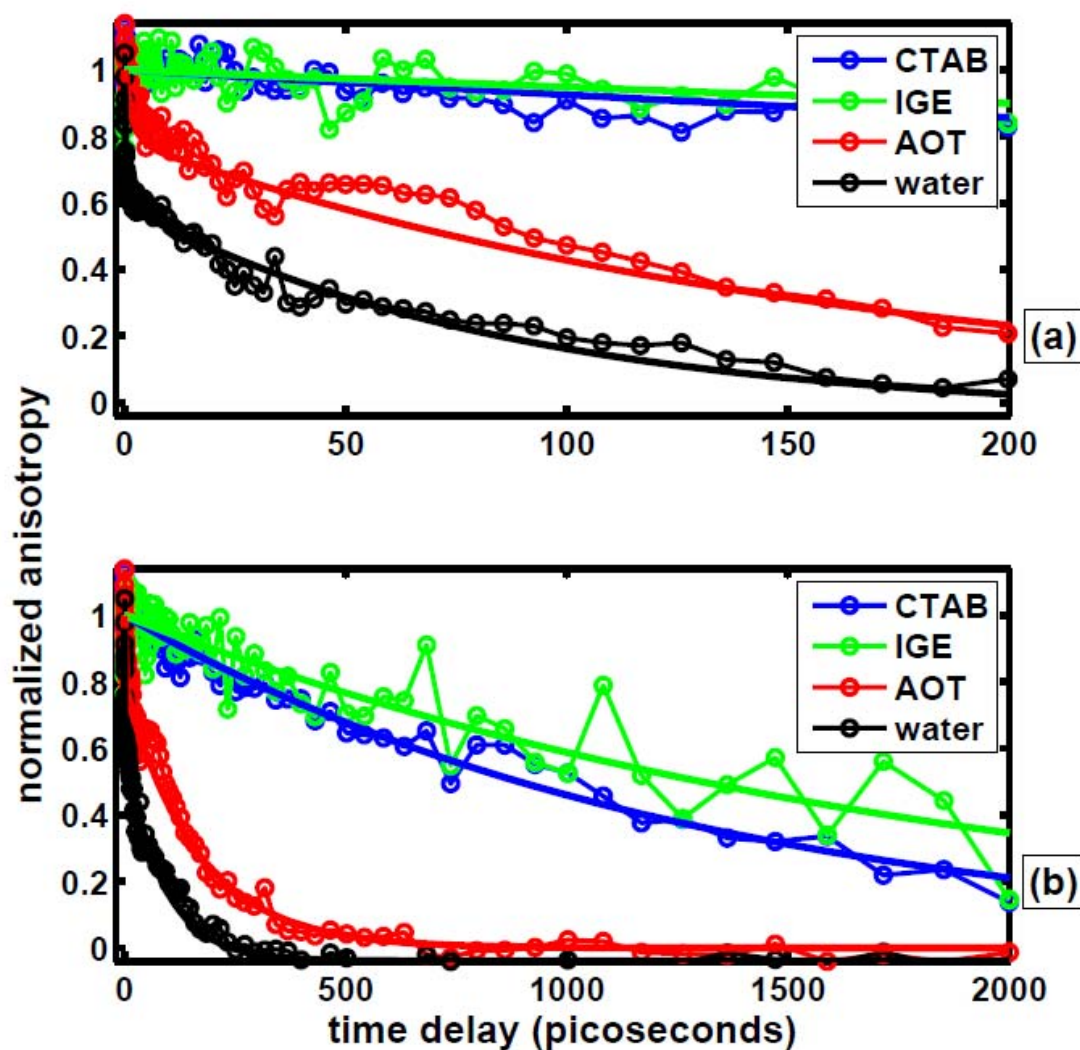


Figure 5.3 Comparison of HPTS anisotropy decays in the largest CTAB, IGE, AOT RM investigated ($w_0 = 40, 20, 20$ respectively) and in bulk water. Solid lines are biexponential fits to the data. HPTS reorientational motion is severely hindered in large IGE, CTAB RM with respect to bulk reorientational motion while HPTS reorientational motion in large AOT RM approaches bulk behavior.

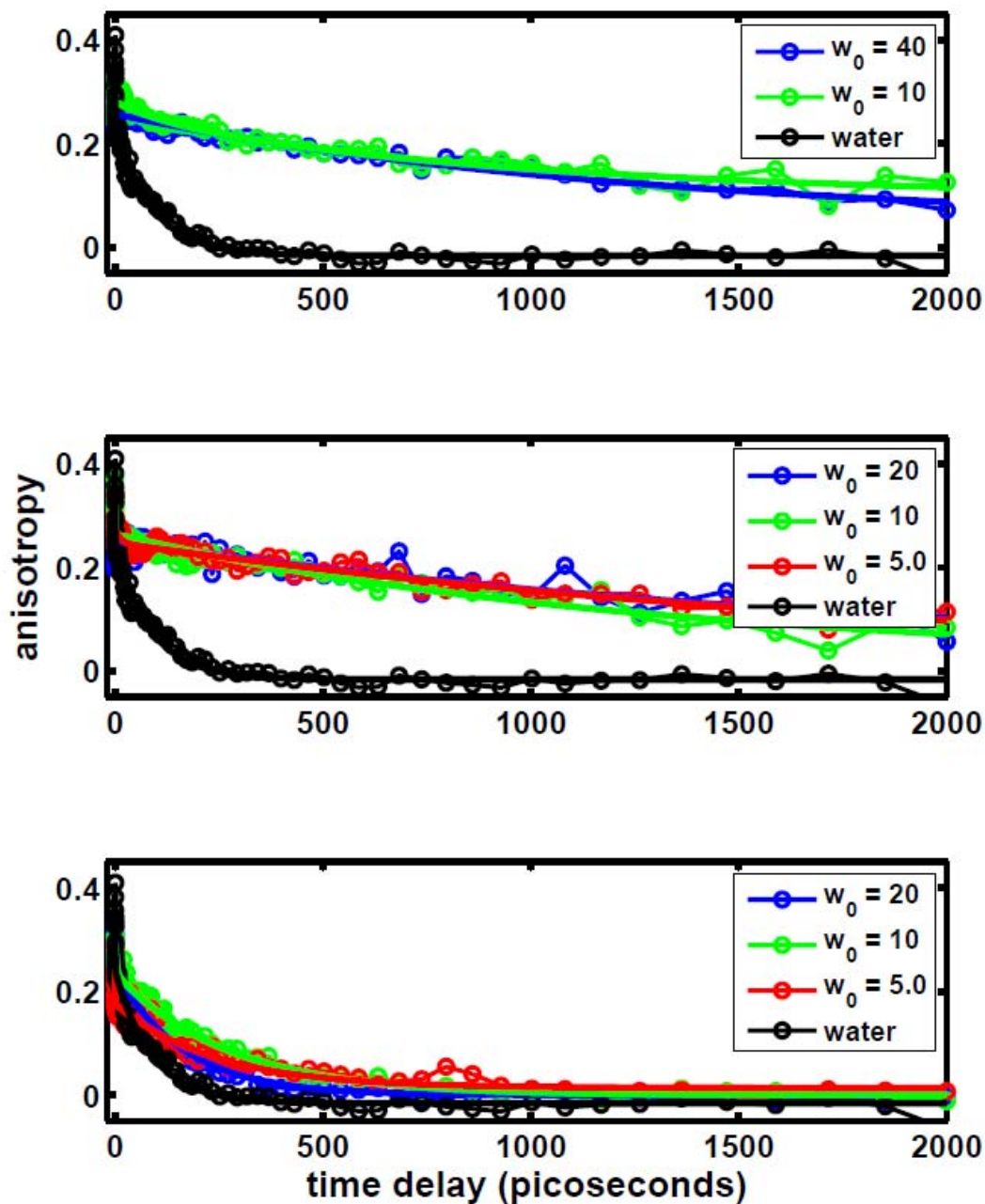


Figure 5.4 Comparison of HPTS anisotropy decays in CTAB (top), IGE (middle), and AOT (bottom) reverse micelles (RM) systems and in bulk water. Biexponential fits are solid lines. No significant w_0 dependences are observed within each RM system.

Table 5.1 Biexponential fit parameters to reorientation decays of HPTS in cationic, non-ionic, and anionic RM systems and in bulk water. The number in parenthesis following each value is the error.

CTAB (cationic)					
	R	a₁	τ₁ (ps)	a₂	τ₂ (ps)
bulk	0.40(0.01)	0.37(0.02)	0.22(0.02)	0.630(0.008)	87(4)
w₀	40	0.21(0.02)	1	1300(200)	--
	10	0.18(0.05)	0.16(0.01)	122(10)	0.84(0.09)
IGE (nonionic)					
bulk	0.40(0.01)	0.37(0.02)	0.22(0.02)	0.630(0.008)	87(4)
w₀	20	0.23(0.01)	1	1900(800)	--
	15	0.26(0.008)	1	440(30)	--
	10	0.30(0.01)	0.19(0.01)	0.30(0.09)	0.81(0.01)
	5	0.27(0.01)	0.10(0.01)	12(5)	0.90(0.01)
	2.5	0.28(0.01)	0.10(0.01)	19(12)	0.90(0.01)
AOT (anionic)					
bulk	0.40(0.01)	0.37(0.02)	0.22(0.02)	0.630(0.008)	87(4)
w₀	20	0.39(0.01)	0.21(0.02)	1.8(0.3)	0.8(0.5)
	15	0.302(0.008)	0.29(0.04)	7(2)	0.7(0.5)
	10	0.289(0.009)	0.19(0.02)	2.8(0.6)	0.8(0.5)
	5	0.25(0.01)	0.35(0.04)	0.21(0.05)	0.6(0.3)
	2.5	0.17(0.03)	1	900(300)	--

CTAB/IGE RM occurs on the nanosecond timescale ($\sim 1\text{-}2$ ns) while reorientational motion in AOT RM occurs on the hundreds of picoseconds timescale ($\sim 100 - 200$ ps).

5.3.c ESPT Dynamics

5.3.c.i BFTA spectrograms

Spectrograms provide a simple and convenient way to qualitatively analyze BFTA data collected under varying conditions. Figure 5.5 shows a comparison of selected HPTS BFTA spectrograms at the largest w_0 values e.g. the largest water pool sizes measured and in bulk water. It is apparent that even at the largest water pool sizes HPTS BFTA spectra deviate strongly from bulk-like behavior in CTAB, IGE RM while HPTS BFTA spectra in AOT RM very closely approach bulk-like behavior. Figure 5.6, 5.7, and 5.8 show spectrograms for HPTS in CTAB, IGE, and AOT RM, respectively, as a function of w_0 . HPTS in CTAB RM shows no evidence of the deprotonated state for all w_0 values measured. In the IGE RM, HPTS the deprotonated state appears but still in the presence of the protonated state and only after a long delay of approximately 500 ps for all w_0 values. HPTS in AOT RM clearly behaves similarly to its bulk aqueous solution behavior. As w_0 is reduced below 10, conversion to the deprotonated state becomes increasingly quenched. Spectrograms provide qualitative information, but further analysis requires quantification of the observed dynamics.

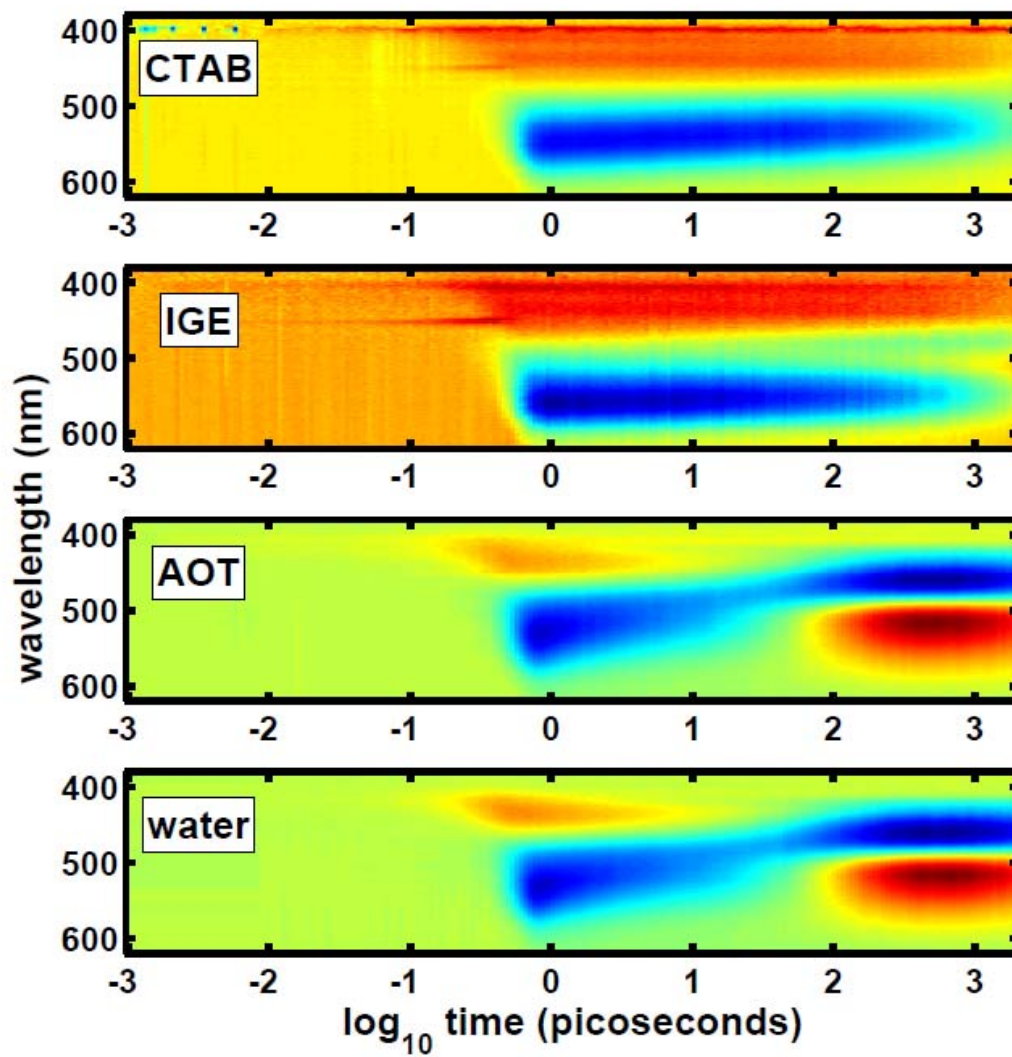


Figure 5.5 Comparison of BFTA spectrograms of HPTS in the largest CTAB, IGE, and AOT RM investigated ($w_0 = 40, 20, 20$ respectively) and in bulk water. Red hues indicate positive signals (ESA) and blue hues indicate negative signals (SE/BL). Bulk-like behavior is observed only for HPTS in AOT RM.

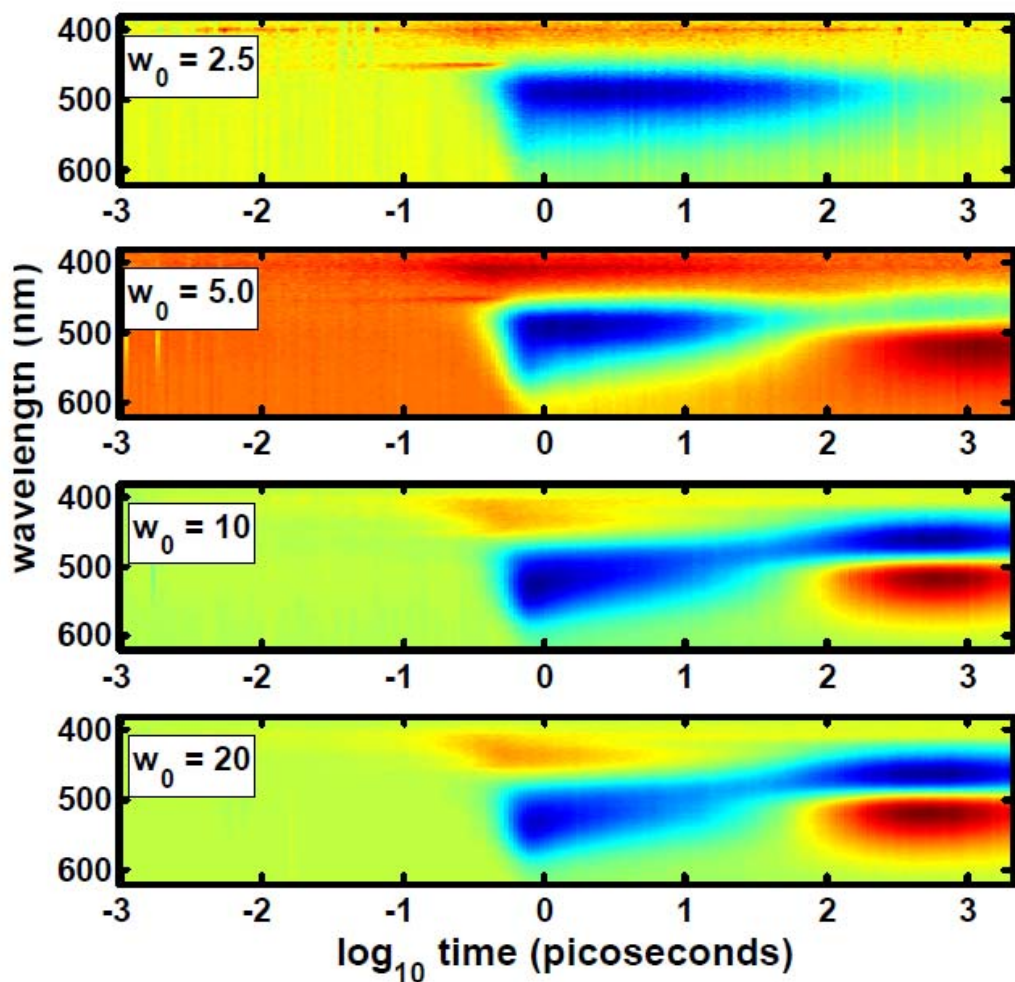


Figure 5.6 Comparison of BFTA spectrograms of HPTS in water/AOT/cyclohexane reverse micelles (RM). Red hues indicate positive signals (ESA) and blue hues indicate negative signals (SE/BL). Complete conversion to the deprotonated state is observed in larger RM ($w_0 = 20, 10$) which is comparable to HPTS behavior in bulk water but conversion to the deprotonated state is increasingly quenched as the size of the water pool is decreased further ($w_0 = 5.0, 2.5$).

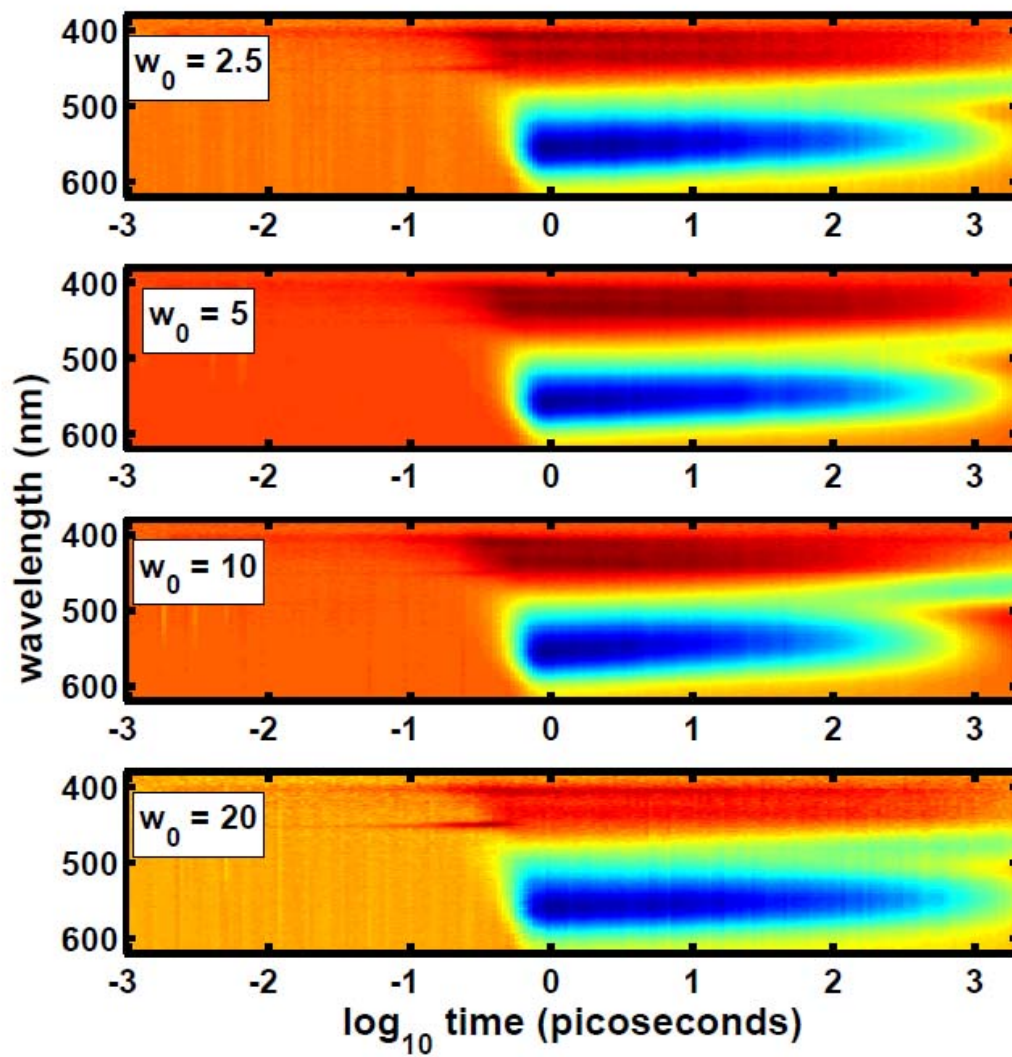


Figure 5.7 Comparison of BFTA spectrograms of HPTS in water/IGE/cyclohexane reverse micelles (RM) as a function of w_0 values (2.5, 5.0, 10, and 20). Red hues indicate positive signals (ESA) and blue hues indicated negative signals (SE/BL). The HPTS deprotonated state immerges late in the time window (~ 500 ps) for all w_0 values. HPTS ESPT in IGE RM shows little dependence on w_0 .

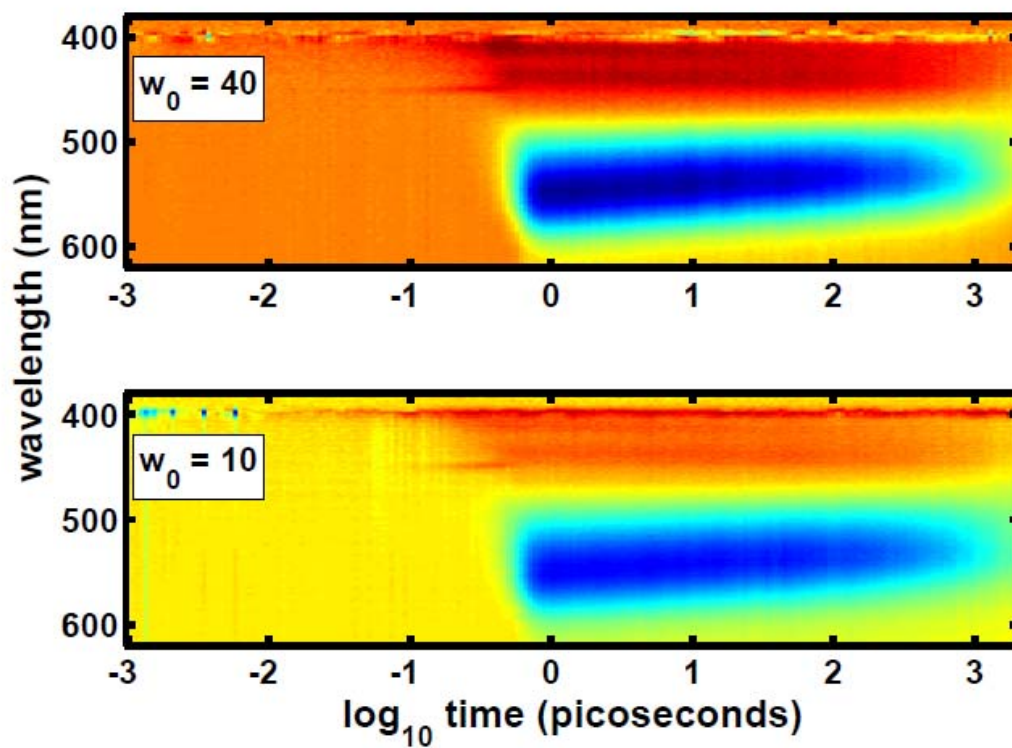


Figure 5.8 Comparison of BFTA spectrograms of HPTS in water/CTAB/1-octanol/cyclohexane reverse micelles (RM) as a function of w_0 values (10, and 40). Red hues indicate positive signals (ESA) and blue hues indicated negative signals (SE/BL). No apparent immergence of the deprotonated state is observed.

5.3.c.ii ESPT dynamics

We first quantify the dynamics present in HPTS BFTA data by fitting the wavelength trace at 560 nm to a multi-exponential decay function. The 560 nm trace was selected because it shows the largest dynamic shift in amplitude (negative to positive) between the [ROH*] and [RO-*] transient spectra. A sum of four exponentials was necessary and adequate to fully describe the observed dynamics. Results for these fits are given in Table 5.2. The fitted parameters display a distinct difference between dynamics observed for HPTS in CTAB and IGE reverse micelles compared to dynamics measured for HPTS in AOT RM and in bulk-water. The fastest time component (τ_1), ~ 0.5 -2 ps, is similar for all RM systems and w_0 values. It is attributed to SD and this value agrees well with the diffusive solvation response of water of 0.89 ps^{21,38}. However, the amplitude of this component (a_1) is roughly a factor of 10 smaller in CTAB and IGE RM than in AOT RM and bulk-water dynamics. In IGE RM, the shortest time component is not measurable at $w_0 = 2.5$. The subsequent longer time dynamics in CTAB and IGE RM are dominated by a 0.6-1.7 ns decay (τ_4) with an amplitude of ~ 0.4 -0.6 (a_4). This decay is only observed in AOT RM at the smallest w_0 value of 2.5. At the intermediate timescale of the experiment results are comparable across all RM investigated and in bulk. These dynamics are split into a 7-20 ps decay (τ_2) and a 90-170 ps decay (τ_3). In CTAB/IGE RM, the amplitudes (a_2 and a_3) are comparable across all w_0 values, but in AOT RM and bulk aqueous solution, a_3 is larger by a factor of approximately three. As

w_0 is reduced (5.0 to 2.5), a_3 decreases and is split into a_4 . These results suggest that HPTS resides in restricted environments in CTAB/IGE RM and this restriction is approached in the smallest AOT RM. Further analysis was conducted to isolate the ESPT component.

Studies of SD in AOT RM via coumarin 343 (C343) have shown dynamics that extend from femtoseconds to nanoseconds³⁶. To separate the overlap of SD and ESPT timescales, we isolate the ESPT by integrating over the entire transient spectrum. This approach minimizes SD contributions which are primarily manifested as spectral shifting leaving ESPT dominant in the integrated signal. Figure 5.9 shows a semilog plot of the normalized integrated signal vs. time delay for the largest CTAB, IGE, and AOT RM prepared and in bulk aqueous solution. Panels (a) and (b) show the same qualitative trend as analysis of the 560 nm traces albeit the decays are simplified requiring only a biexponential decay function for a good fit. Biexponential fit parameters are tabulated in Table 5.3.

For HPTS in AOT RM, a clear trend is observed as w_0 is reduced from 20 to 2.5 which increases the time constants and shifts amplitude from the longer time component (τ_2) to the shorter time component (τ_1). At $w_0 = 20$ in AOT RM, HPTS ESPT is near the values for HPTS in pH = 7 water.²¹ The small discrepancy in our measured bulk water ESPT dynamics are due to the slight acidity of the Millipore water used to prepare the bulk water sample. These results indicate that as the size of the AOT RM is reduced the HPTS ESPT becomes increasingly quenched. HPTS ESPT dynamics in CTAB RM show a similar increase in the time constants for smaller RM although the measured dynamic

Table 5.2 Multi-exponential fitted parameters to 560 nm BFTA traces of HPTS in CTAB, IGE, and AOT RM systems and in bulk water.

Analysis of BFTA data in this fashion does not explicitly separate SD and ESPT dynamics, thus the fastest time component can be attributed to SD and slower dynamics to ESPT. The number in parenthesis is the error.

CTAB (cationic)							
	a_1	τ_1 (ps)	a_2	τ_2 (ps)	a_3	τ_3 (ps)	τ_4 (ns)
bulk	0.24(0.01)	0.78(0.04)	0.10(0.01)	7(1)	0.66(0.01)	133(3)	--
w₀ = 40	0.01(0.01)	0.9(2.0)	0.10(0.01)	8(2)	0.22(0.01)	92(15)	1.3(0.2)
10	0.022(0.009)	0.5(0.5)	0.11(0.01)	7(1)	0.20(0.01)	80(11)	1.4(0.2)
IGE (non-ionic)							
bulk	0.24(0.01)	0.78(0.04)	0.10(0.01)	7(1)	0.66(0.01)	133(3)	--
20	0.04(0.01)	0.14(0.08)	0.11(0.03)	26(8)	0.13(0.04)	167(112)	1.7(0.7)
15	0.13(0.01)	1.4(0.2)	0.19(0.01)	9(1)	0.28(0.02)	108(11)	0.63(0.05)
w₀ = 10	0.07(0.04)	2(1)	0.15(0.03)	9(3)	0.19(0.01)	84(12)	0.78(0.04)
5	0.031(0.008)	1.0(0.5)	0.11(0.01)	13(3)	0.17(0.02)	122(25)	1.3(0.2)
2.5	--	--	0.14(0.02)	10(2)	0.18(0.02)	101(28)	1.1(0.2)
AOT (anionic)							
bulk	0.24(0.01)	0.78(0.04)	0.10(0.01)	7(1)	0.66(0.01)	133(3)	--
20	0.23(0.02)	0.70(0.05)	0.13(0.02)	5.9(0.8)	0.64(0.01)	115(3)	--
15	0.25(0.02)	0.76(0.06)	0.15(0.02)	9(1)	0.60(0.02)	140(6)	--
w₀ = 10	0.23(0.01)	0.73(0.05)	0.18(0.01)	8.3(0.8)	0.60(0.02)	142(5)	--
5	0.27(0.01)	0.93(0.08)	0.32(0.02)	15(2)	0.42(0.02)	137(14)	--
2.5	0.2(0.1)	1(1)	0.11(0.09)	8(16)	0.35(0.08)	75(40)	0.6(0.4)

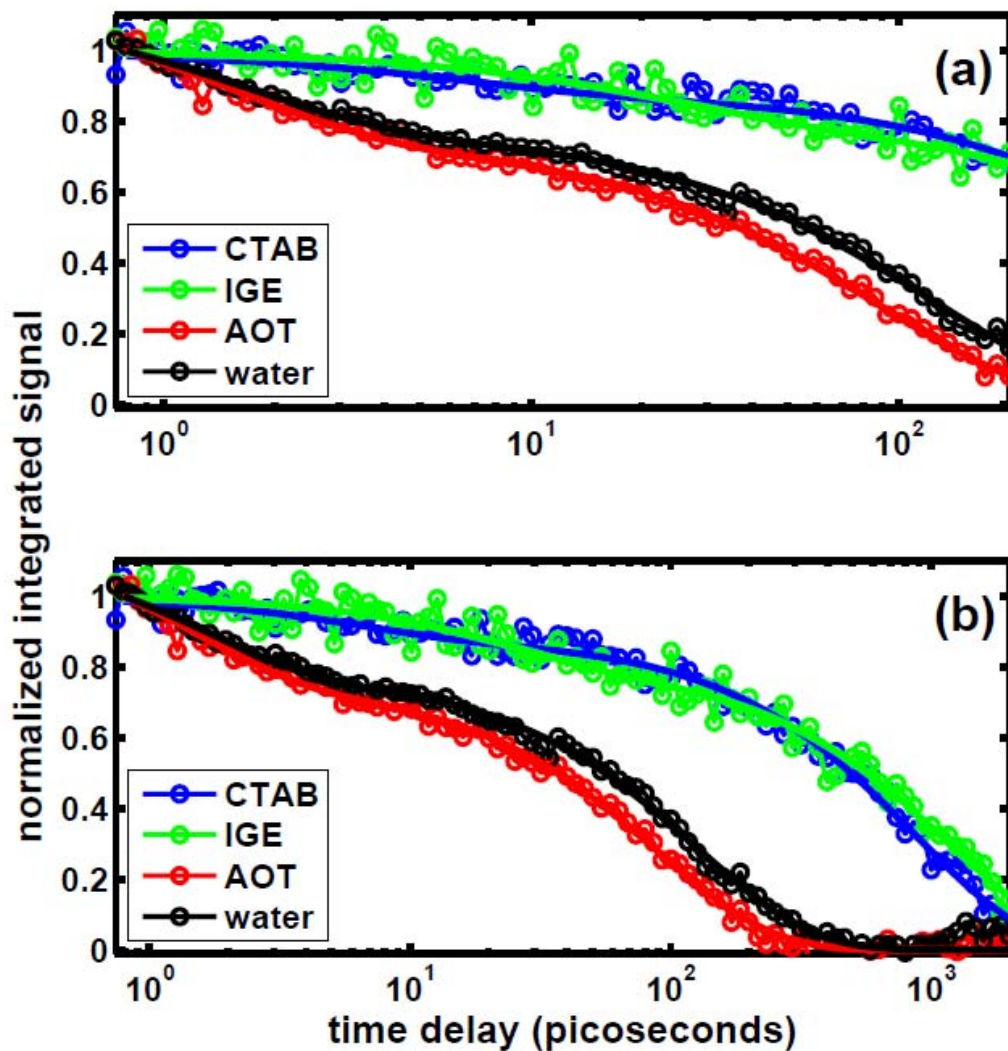


Figure 5.9 Comparison of HPTS spectrally integrated signals in the largest CTAB, IGE, AOT RM investigated ($w_0 = 40, 20, 20$ respectively) and in bulk water from 0 to 200 ps (a) and 0 to 2000 ps (b). Solid lines are biexponential fits to the data. Spectral integration minimizes solvation dynamic contributions to the observed dynamics yielding a clear measurement of ESPT dynamics. HPTS ESPT in AOT RM approaches bulk behavior while HPTS ESPT in CTAB/IGE RM deviates from bulk ESPT behavior.

Table 5.3 Biexponential fitted parameters to integrated BFTA spectra of HPTS in CTAB, IGE, and AOT RM systems and in bulk water. Analysis of BFTA data in this fashion minimizes SD contributions yielding nearly pure measurement of ESPT dynamics. The number in parenthesis is the error.

CTAB (cationic)				
	α_1	τ_1 (ps)	α_2	τ_2 (ns)
bulk	0.230(0.007)	1.6(0.1)	0.770(0.006)	128(3)
w₀ = 40	0.12(0.01)	6(1)	0.88(0.03)	870(60)
10	0.128(0.009)	35(6)	0.9(0.1)	2100(400)
IGE (nonionic)				
bulk	0.230(0.007)	1.6(0.1)	0.770(0.006)	128(3)
20	0.19(0.02)	23(5)	0.81(0.07)	1200(200)
15	0.28(0.01)	11(1)	0.72(0.01)	453(22)
w₀ = 10	0.209(0.007)	8.9(0.8)	0.79(0.01)	670(30)
5	0.158(0.007)	9(1)	0.84(0.02)	890(40)
2.5	0.19(0.01)	12(2)	0.81(0.03)	890(70)
AOT (anionic)				
bulk	0.230(0.007)	1.6(0.1)	0.770(0.006)	128(3)
20	0.25(0.03)	1.5(0.1)	0.745(0.007)	90(3)
15	0.31(0.04)	2.1(0.2)	0.69(0.01)	98(4)
w₀ = 10	0.33(0.03)	3.9(0.3)	0.668(0.009)	103(4)
5	0.67(0.03)	18.9(0.9)	0.33(0.02)	210(20)
2.5	0.5(0.1)	38(6)	0.51(0.05)	340(70)

timescales are larger than in AOT RM and in bulk water. In IGE RM, HPTS ESPT dynamics show much slower decay constants that, in general, do not exhibit a clear dependence on w_0 . The fast time constant varies between 8.9 and 23 ps accounting for about 20% of the total amplitude and the slower component varies from 0.4 to 1.2 ns comprising the remaining amplitude. These results suggest that HPTS in IGE RM resides in a different environment than it does in AOT RM. Due to the strong correlation between AOT and bulk water ESPT dynamics and the deviation from this behavior in IGE RM, one can conclude that HPTS does not reside in a bulk aqueous environment in the IGE RM. Effectively we find that HPTS finds itself solvated differently in each RM system investigated.

5.3.d Simulating the IGE RM Environment

5.3.d.i HPTS in other neat non-ionic surfactants

Figure 5.10 presents a series of absorption studies that probe HPTS behavior in a variety of environments similar to the IGE RM environment. Figure 5.10a shows absorption spectra for HPTS in several neat nonionic surfactants (IGE, BRIJ-30, and Triton X-100). HPTS absorption in BRIJ-30 and Triton X-100 show HPTS to be protonated (~404 nm) while absorption of HPTS in IGE show a significant absorption from the deprotonated state (~465 nm). Figure 5.10b shows a comparison between HPTS absorption in neat IGE and IGE dispersed in cyclohexane to 0.4 M. Absorption of HPTS in neat and 0.4 IGE show very close agreement. Finally in Figure 5.10c HPTS and MPTS absorption in IGE are compared.

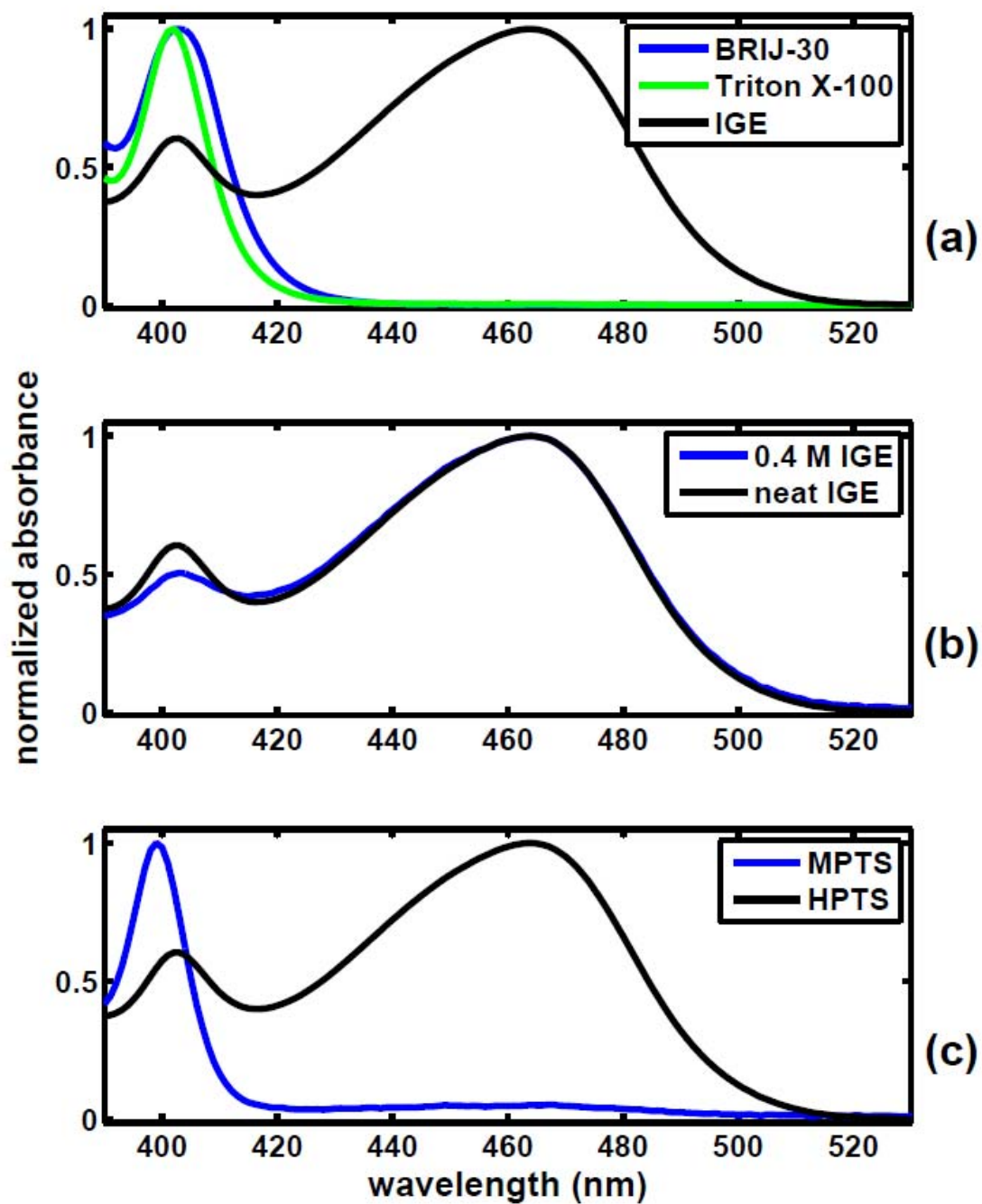


Figure 5.10 Absorption spectrum of HPTS in (a) neat BRIJ-30, Triton X-100 and IGE nonionic surfactants; (b) in neat IGE and in IGE dispersed in cyclohexane; and (c), HPTS and MPTS in IGE in cyclohexane.

5.3.d.ii HPTS in hydrated tetraethylene glycol

Tetraethylene glycol (TEG) was used to simulate the IGE polyethylene oxide headgroup. We dissolved HPTS in solutions containing water/TEG mixtures and recorded the absorption spectra. Figure 5.11 contrasts spectra at a range of hydration levels in addition to HPTS absorption in water and in anhydrous TEG. We observe a continuous shift in the HPTS absorption spectra from the anhydrous spectrum towards the water spectrum as the hydration level increases. All the spectra indicate only the presence of the protonated HPTS molecule with no evidence for deprotonation.

5.4.d.iii HPTS in D₂O and D₂O/IGE/cyclohexane reverse micelles

BFTA data was also collected for HPTS in D₂O and D₂O/IGE/cyclohexane reverse micelles to probe the role that water plays in the observed ESPT dynamics. ESPT decays were extracted from the transient spectra via the spectra integration method and analyzed as outlined in section 5.2.C.ii, biexponential fit results are presented in Table 5.4. Similar trends are observed for D₂O/IGE reverse micelles as in water/IGE reverse micelles albeit the extracted ESPT time constants are slightly slower. The effect that the substitution of D₂O for water has on HPTS proton transfer dynamics is quantified by calculating the ratio of the longer time constant for D₂O over the water value, $\tau_{2,D_2O} / \tau_{2,water}$. This ratio gives an approximate measure of the kinetic isotope effect (KIE). We compare the IGE reverse micelle KIE values to the bulk solvent KIE value.

The calculated KIE value between bulk water and D₂O is approximately 3. In all IGE reverse micelles the KIE values fall short of the bulk value. Aside from a KIE value of 0.6 at $w_0=20$ the calculated KIE generally increase as w_0 is increased. At $w_0 = 15$, the KIE

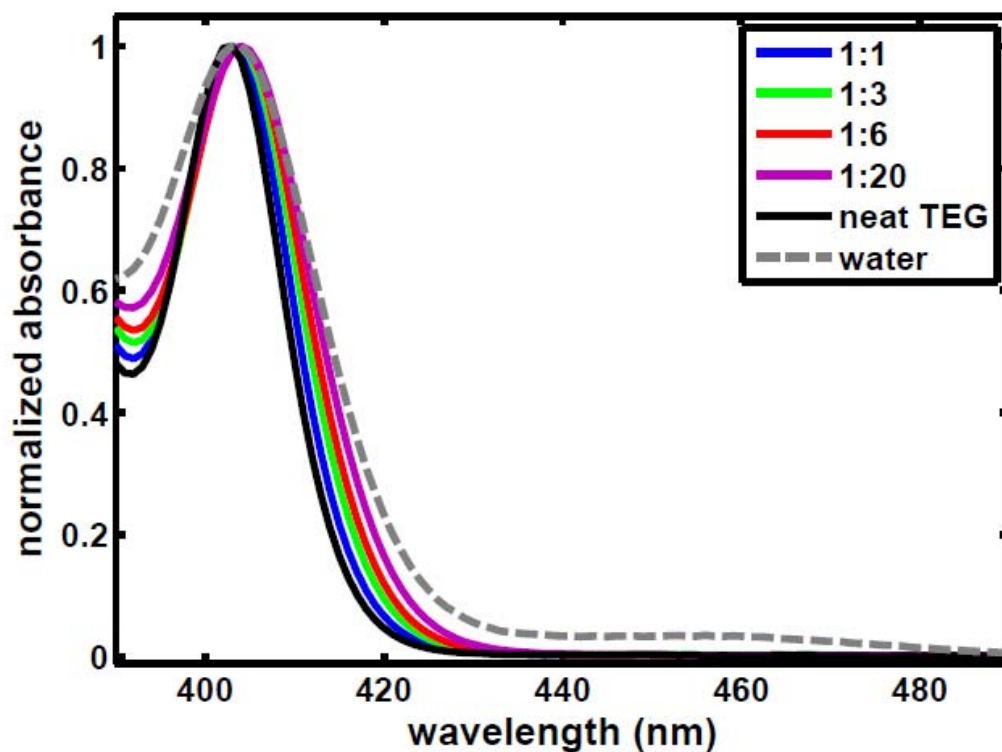


Figure 5.11 Absorption spectra of HPTS in tetraethylene glycol/water (TEG:water) binary mixtures, in neat TEG, and in slightly acidic water pH =6.5. Increasing the hydration of TEG produces HPTS spectra that are comparable to HPTS in water and a shift towards the deprotonated state absorption (454 nm) is not observed.

Table 5.4 Biexponential fit parameters to integrated BFTA spectra of HPTS in IGE RM systems formed with water and D₂O and in bulk water and D₂O. Kinetic isotope effect

(KIE) values are calculated as $\frac{\tau_{2,D_2O}}{\tau_{2,water}}$. KIE values for HPTS in IGE RM fall short of the KIE

value for the bulk solvents and approach unity as w_0 is decreased. The number in parenthesis is the error.

		a_1	τ_1 (ps)	a_2	τ_2 (ps)	KIE
	bulk water	0.230(0.007)	1.6(0.1)	0.770(0.006)	128(3)	3.1(0.1)
	bulk D ₂ O	0.180(0.007)	1.7(0.2)	0.820(0.007)	390(9)	
$w_0 = 20$	water	0.19(0.02)	23(5)	0.81(0.07)	1200(200)	0.6(0.1)
	D ₂ O	0.15(0.01)	10(2)	0.85(0.02)	770(40)	
$w_0 = 15$	water	0.28(0.01)	11(1)	0.72(0.01)	453(22)	2.1(0.2)
	D ₂ O	0.20(0.01)	14(2)	0.80(0.03)	970(80)	
$w_0 = 10$	water	0.209(0.007)	8.9(0.8)	0.79(0.01)	670(30)	1.3(0.1)
	D ₂ O	0.18(0.01)	13(2)	0.82(0.03)	860(70)	
$w_0 = 5$	water	0.158(0.007)	9(1)	0.84(0.02)	890(40)	1.2(0.1)
	D ₂ O	0.20(0.01)	30(4)	0.79(0.04)	1100(100)	
$w_0 = 2.5$	water	0.19(0.01)	12(2)	0.81(0.03)	890(70)	1.1(0.1)
	D ₂ O	0.16(0.01)	17(3)	0.84(0.03)	980(90)	

value is approximately 2 and the values show a gradual decrease towards unity for w_0 values 10 to 2.5. These results imply that water plays a diminished role in HPTS ESPT dynamics in IGE reverse micelles which becomes increasingly valid as the size of the water pool decreases.

5.4 Discussion

Our results clearly indicate that the choice of RM surfactant molecule, anionic, cationic, or non-ionic, dramatically influences the observed ESPT dynamics. Although HPTS is highly soluble in water, our results indicate that HPTS is not solvated in the water pool in IGE and CTAB RM. Both reorientation and ESPT dynamics support this interpretation. The interaction between HPTS and the CTAB interface is easily explained as a Coulomb attraction between the anionic HPTS molecule and the cationic trimethylammonium headgroup of the CTAB surfactant. This places HPTS at the micelle interface and it is embedded such that the HPTS hydroxyl group is inefficiently solvated by water. In this situation, the proton transfer reaction is quenched and does not appear to proceed during the experimental time window (2 ns). It is also possible that the cosurfactant (octanol) partially solvates the HPTS molecule and impedes ESPT dynamics. In any case, it is clear that HPTS is not solvated effectively by water in CTAB reverse micelles.

A similar principle can be used to interpret HPTS behavior in AOT RM; HPTS interfacial interactions in AOT RM are minimized due to a Coulomb repulsion between the anionic HPTS molecule and the anionic sulfonate headgroup of the AOT surfactant.

Thus HPTS in AOT RM shows behavior that is congruent with its behavior in bulk aqueous solution as long as it remains solvated in the water pool. Only when the size of the water pool is reduced sufficiently and HPTS interactions with the AOT RM interface increase does ESPT reaction in HPTS become quenched.

Interpretation of HPTS behavior in IGE RM is less intuitive than for AOT or CTAB. In IGE RM, HPTS exhibits ESPT dynamics that are approximately 10 times slower than the bulk ESPT timescales of 2.5 and 90 ps at neutral pH. ESPT dynamics are present even in the smallest water pool size investigated in IGE RM. Coupling this with the reorientational studies we can conclude that HPTS does not reside in an environment that is like bulk aqueous solution. Structural studies of IGE RM indicate that a distinct water pool forms and that hydration of the polyethylene oxide headgroups is minimal.³⁹ Although this and other studies of IGE RM demonstrate that a significant water pool forms,³⁹⁻⁴¹ we speculate that HPTS resides somewhere in the RM interface. This result and interpretation differs from results from studies of HPTS in BRIJ-30 nonionic RM which report HPTS to be solvated in the water pool.²⁹ The question that remains is, what interactions result in the highly water soluble HPTS molecule to be solvated at the IGE RM interface rather than within the water pool. In efforts to further understand this behavior we have conducted a series of studies to probe specific molecular interactions that HPTS can experience within IGE reverse micelles.

We first consider the role that the structure of IGE impacts our observations. In contrast to CTAB and AOT, which are solids at room temperature, nonionic surfactants are typically viscous liquids at room temperature. We have found that HPTS is soluble in

these liquids. Figure 5.10a highlights differences between HPTS behavior in IGE compared to other nonionic surfactants. In BRIJ-30 and Triton X-100 HPTS remains protonated and the protonated absorbance band (~404 nm) dominates the spectrum. This behavior is expected because deprotonation of HPTS typically requires the presence of water. Figure 5.10b contrasts HPTS in neat IGE and in 0.4 M IGE in cyclohexane with no added water. Because HPTS is completely insoluble in cyclohexane, it is not surprising that the spectra in Fig. 5.10b show that the environment sensed by HPTS is similar whether IGE is neat or dispersed in cyclohexane. Interestingly, absorption spectrum of HPTS in IGE and IGE dispersed in cyclohexane show the opposite behavior; the spectra are dominated by the deprotonated state absorption (~454 nm). Figure 5.10c compares absorption spectra for HPTS and MPTS (8-methoxypyrene-1,3,6-trisulfonate) solutions with IGE in cyclohexane. In MPTS, a methoxy group replaces the hydroxyl group involved in ESPT in HPTS.²¹ Thus, MPTS only displays an excited state without the possibility of proton transfer. The absorption spectra shown in Figure 5.10 suggest different deprotonation dynamics for HPTS in BRIJ-30 RM²⁹ compared to the IGE RM.

Comparison between HPTS and MPTS absorption spectra in Fig. 5.10c helps us to interpret the differences observed for HPTS in IGE solutions. We anticipate that environmental effects or complex formation should be similar for HPTS and MPTS. The dramatic differences between their spectra in the same environment demonstrates that band observed for HPTS in IGE is associated with proton transfer and does not arise from a spectral shift induced by the formation of an HPTS-IGE complex. If IGE were

forming a complex with HPTS, then we would expect similar complex formation for MPTS and their spectra would agree more closely.

To explore the interaction of HPTS with the polyethylene oxide portion of the IGE surfactant, we performed another series of experiments. Small angle neutron scattering (SANS) studies have shown that the water pools formed in IGE RM are very well defined indicating that the PEO head group is not significantly hydrated.³⁹ Likewise, we have observed formation of a real water pool in IGE RM via ^{51}V NMR spectroscopy of decavanadate ($\text{V}_{10}\text{O}_{28}^{6-}$) in IGE RM.⁴⁰ Additionally, time-resolved infrared experiments have supported the SANS results showing the formation of a water pool in the IGE RM.⁹ These results show that complexation of HPTS with the PEO portion of IGE is not responsible for the spectroscopy observed.

At this point it is unclear what role water plays in the ESPT dynamics we have observed in IGE RM and so we have explored water's role by substituting D_2O for water. In bulk solvents (water and D_2O), the kinetic isotope effect (KIE) is approximately 2.2²¹. If water plays a significant role in the observed ESPT dynamics in IGE RM, we should see a similar KIE ratio. If water contributes very little to the observed ESPT dynamics the KIE value should approach unity. For HPTS in water and D_2O , the KIE value (Table 5.3) we measure is approximately 3 which nominally agrees with reported values.^{14,21} In all of the IGE reverse micelles KIE values fall short of the bulk value and decrease as the size of the water pool is reduced. Thus as the size of the water pool decreases the role of the solvent in the observed HPTS ESPT process diminishes nearly to zero. These results (and our previous results) clearly show that HPTS tends to be solvated by the IGE surfactant

rather than water or D₂O. Only at higher hydration levels (water pool diameters) does the solvent impact the HPTS ESPT dynamics indicating that the solvation environment includes water.

HPTS has been studied in a variety of micelle systems containing cationic, anionic, and nonionic surfactants. Bardez et al. have shown that HPTS in CTAB reverse micelles displays emission from both the neutral anionic forms of the molecule indicating the presence of ESPT process, and Bhattacharyya and coworkers measured the ESPT rate constant to be over 200 times slower than the rate in bulk water. Our results confirm that HPTS ESPT is present in CTAB reverse micelles and that the proton transfer rate is 10-20 slower than the bulk water value. We add picosecond reorientation data that indicates that HPTS does reside at the interfacial region of the CTAB reverse micelle and is not effectively solvated within the water pool. Time-resolved fluorescence studies by Spry et al. of HPTS in water/AOT/heptane reverse micelles³⁵ clearly indicate that HPTS is solvated deep in the micelle water pool and interfacial interactions are minimal. Tielrooij and coworkers found through femtosecond transient absorption studies of HPTS in water/AOT/isooctane reverse micelles²⁹ ESPT dynamics are near bulk values and quenching of HPTS ESPT occurs only when the water pool diameter is reduced to a size on the order of the HPTS molecule (~1 nm). They also perform the same study of HPTS in water/BRIJ-30/cyclohexane reverse micelles and recover nearly the identical result; HPTS is solvated in the BRIJ-30 RM water pool. This result contrasts our results for water/IGE/cyclohexane reverse micelles which indicate that HPTS is not solvated fully within the water pool and significant interactions

between HPTS and IGE are present which alter the observed proton transfer dynamics. To the best of our knowledge, HPTS in IGE reverse micelles provides the only example where ESPT is quenched in nonionic reverse micelles.

5.5 Summary

We have presented broadband femtosecond transient absorption (BFTA) studies of solvation dynamics (SD) and excited state proton transfer (ESPT) in cationic, nonionic, and anionic reverse micelles (RM) and in bulk water. Results show that the choice of surfactant has a dramatic effect on the observed ESPT dynamics. HPTS in AOT RM (anionic) shows significantly different behavior from HPTS in CTAB (cationic) and IGE (nonionic) RM which approaches HPTS behavior in bulk water. Both reorientation and ESPT dynamics approach the behavior of HPTS in bulk aqueous solution in AOT RM with the largest water content. These results indicate that HPTS in AOT RM is solvated in the water pool and furthermore quenching of HPTS bulk behavior is observed as the size of the water pool is decreased. These results confirm previously reported studies by Tielrooij and coworkers²⁹. In cationic RM (CTAB), HPTS appears to reside at the interface which is supported by both the slow reorientation and ESPT dynamics with respect to HPTS behavior in bulk water. Similar behavior is observed for HPTS in IGE RM as in CTAB RM and we interpret the slowed dynamics in the same manner. As the water content of both CTAB and IGE RM were varied, no significant correlations were observed. We explain the location of HPTS in CTAB RM in terms of a Coulomb attraction

between the oppositely charged CTAB and HPTS molecules, but the location of HPTS in IGE RM required further study to understand the nature of the HPTS IGE interaction.

References and Notes

- (1) Stryer, L. *Biochemistry*; 4th ed.; Freeman and Company: New York, 1995.
- (2) Barbir, F. *PEM Fuel Cells: Theory and Practice*; Elsevier Academic Press: London, UK, 2005.
- (3) Mehta, V.; Cooper, J. S. *Journal of Power Sources* **2003**, *114*, 32.
- (4) Tawfik, H.; hung, Y.; Mahajan, D. *Journal of Power Sources* **2007**, *163*, 755.
- (5) Deisenhofer, J.; Norris, J. R. *The Photosynthetic Reaction Center*; Academic Press, 1993; Vol. 1.
- (6) Somasundaran, P. *Encyclopedia of Surface and Colloid Science*; 2 ed.; CRC Press: Boca Raton, FL, 2006; Vol. 8.
- (7) Suresh, S. J. *Journal of Chemical Physics* **2007**, *126*, 204705.
- (8) Zhang, J.-X.; Aiello, D.; Aker, P. M. *Journal of Physical Chemistry* **1995**, *99*, 721.
- (9) Moilanen, D. E.; Levinger, N. E.; Spry, D. B.; Fayer, M. D. *Journal American Chemical Society* **2007**, *129*, 14311.
- (10) Cox, M. J.; Bakker, H. J. *Journal of Chemical Physics* **2008**, *128*, 174501/1.
- (11) Cox, M. J.; Timmer, R. L. A.; Bakker, H. J.; Park, S.; Agmon, N. *Journal of Physical Chemistry A* **2009**, *113*, 6599.

- (12) Foerster, T.; Voelker, S. *Zeitschrift fuer Physikalische Chemie* **1975**, *97*, 275.
- (13) Jung, G.; Gerharz, S.; Schmitt, A. *Physical Chemistry Chemical Physics* **2009**, *11*, 1416.
- (14) Leiderman, P.; Genosar, L.; Huppert, D. *Journal of Physical Chemistry A* **2005**, *109*, 5965.
- (15) Leiderman, P.; Gepshtein, R.; Uritski, A.; Genosar, L.; Huppert, D. *Journal of Physical Chemistry A* **2006**, *110*, 5573.
- (16) Mohammed, O. F.; Dreyer, J.; Magnes, B.-Z.; Pines, E.; Nibbering, E. T. J. *Chem Phys Chem* **2005**, *6*, 625.
- (17) Mohammed, O. F.; Pines, D.; Dreyer, J.; Pines, E.; Nibbering, E. T. J. *Science* **2005**, *310*, 83.
- (18) Pines, E.; Huppert, D.; Agmon, N. *Journal of Chemical Physics* **1988**, *88*, 5620.
- (19) Siwick, B. J.; Bakker, H. J. *Journal of Physical Chemistry A* **2007**, *111*, 230.
- (20) Spry, D. B.; Fayer, M. D. *Journal of Chemical Physics* **2008**, *128*, 084508/1.
- (21) Spry, D. B.; Goun, A.; Fayer, M. D. *Journal of Physical Chemistry A* **2007**, *111*, 230.
- (22) Tran-Thi, T.-H.; Gustavsson, T.; Prayer, C.; Pommeret, S.; Hynes, J. T. *Chemical Physics Letters* **2000**, *329*, 421.
- (23) Ray, K.; Nakahara, H. *Journal of Photochemistry and Photobiology, A: Chemistry* **2005**, *173*, 75.

- (24) Tsukamoto, O.; Villeneuve, M.; Sakamoto, A.; Nakahara, H. *Bulletin of the Chemical Society of Japan* **2007**, *80*, 1723.
- (25) Tsukamoto, O.; Villeneuve, M.; Sakamoto, A.; Nakahara, H. *Chemical Physics Letters* **2008**, *454*, 247.
- (26) Seigneuret, M.; Rigaud, J.-L. *Federation of European Biochemical Societies* **1988**, *228*, 79.
- (27) Sharma, J.; Tleugabulova, D.; Czardybon, W.; Brennan, J. D. *Journal of the American Chemical Society* **2006**, *128*, 5496.
- (28) Roy, D.; Karmakar, R.; Mondal, S. K.; Sahu, K.; Bhattacharyya, K. *Chemical Physics Letters* **2004**, *399*, 147.
- (29) Tilrooij, K. J.; Cox, M. J.; Bakker, H. J. *Chem Phys Chem* **2009**, *10*, 245.
- (30) Abou-Al Einin, S.; Zaitsev, A. K.; Zaitsev, N. K.; Kuzmin, M. G. *Journal of Photochemistry and Photobiology A: Chemistry* **1988**, *41*, 365.
- (31) Bardez, E.; Goguillon, B. T.; Keh, E.; Valeur, B. *The Journal of Physical Chemistry* **1984**, *88*, 1909.
- (32) Ghosh, S.; Dey, S.; Mandal, U.; Ahikari, A.; Mondal, S. K.; Bhattacharyya, K. *Journal of Physical Chemistry B* **2007**, *111*, 13504.
- (33) Timmer, R. L. A.; Cox, M. J.; Bakker, H. J. *Journal of Physical Chemistry A* **2010**, *114*, 2091.
- (34) Uritski, A.; Huppert, D. *Journal of Physical Chemistry A* **2008**, *112*, 4415.
- (35) Spry, D. B.; Goun, A.; Glusac, K.; Moilanen, D. E.; Fayer, M. D. *Journal of the American Chemical Society* **2007**, *129*, 8122.

- (36) Cole, R. L.; Levinger, N. E. *To Be Published* **2011**.
- (37) Cole, R. L.; Barisas, B. G.; Levinger, N. E. *Review of Scientific Instruments* **2010**, *81* 093101.
- (38) Jimenez, R.; Fleming, G. R.; Kumar, P. V.; Maroncelli, M. *Nature* **1994**, *369*, 471.
- (39) Lipgens, S.; Schubel, D.; Schlicht, L.; Spilgies, J. H.; Ilgenfritz, G.; Eastoe, J.; Heenan, R. *Langmuir* **1988**, *14*, 1041.
- (40) Sedgwick, M. A.; Crans, D. C.; Levinger, N. E. *Langmuir* **2009**, *25*, 5496.
- (41) Moilanen, D. E.; Levinger, N. E.; Spry, D. B.; Fayer, M. D. *Journal American Chemical Society* **2007**, *129*, 14311.

CHAPTER 6

SUMMARY AND CONCLUSIONS

The goal of the work presented was to understand more completely aqueous solvation and proton transfer in confinement. We approached these goals by using a model system for studies of confinement, the reverse micelle. By varying the hydration level in the reverse micelles we were able to systematically interrogate confinement by preparing reverse micelles with varying water pool diameters. We chose probe molecules that were soluble in water (C343, HPTS), but we found that the nature of the reverse micelle interface can drastically alter the observed dynamics.

To first approach these goals, we constructed a broadband femtosecond transient absorption spectrometer (BFTA) which allows dynamics to be tracked through absorption changes from 0 to 2 nanoseconds. The BFTA instrument allows ultrafast excitation at approximately 400 nm and a spectral probing from 380-720 nm. In the course of optimizing data collection with this instrument a method was developed to collect data with logarithmically spaced time-delay points rather than points spaced linearly in time. This methodology was tested and it was found that it provides both an economical advantage for data collection over many decades of time and a statistical

advantage which allows an observed parameter to be determined with greater precision via fewer number of data points.¹

Solvation dynamics studies using C343 in Aerosol OT (AOT) reverse micelles through BFTA spectroscopy build upon our previous time-resolved fluorescence Stokes shift (TRFSS) study² and we were able to fully recover the solvation response of the AOT reverse micelle system as measured through C343. Measurement of C343 reorientation and solvation dynamics out to 2 nanoseconds revealed that C343 exists in two distinct environments within AOT reverse micelles which approximately correlate with the surface to volume ratio of the water pool. We concluded that the C343 population within AOT reverse micelles was solvated by interfacial and core water which behave differently. We also proposed the idea that dynamic heterogeneity may be present and electronically excited C343 may migrate within the AOT reverse micelles to a more energetically favorable location during the course of the solvation response.

Our investigations of excited state proton transfer (ESPT) from HPTS to water in confinement explored the use of cationic (CTAB), anionic (AOT), and nonionic (IGE) surfactants to form reverse micelles. We questioned what effect the varying nature of the micelle interface would have on the HPTS ESPT process and found some surprising results. Our studies confirmed other literature reports that HPTS appears to be located at the CTAB micelle interface

The reason for the unique attraction between HPTS and IGE which is not observed between HPTS and other nonionic surfactant molecules (BRIJ-30, TRITON-X 100) is still unknown although our studies have narrowed the possibilities.

In conclusion, our investigations of solvation and proton transfer dynamics in confined water were largely a success. We found that understanding the complex dynamical behavior observed in confinement truly requires analysis to the longest timescales possible.

References and Notes

(1) Cole, R. L.; Barisas, B. G.; Levinger, N. E. *Review of Scientific Instruments* **2010**, *81*, 093101.

(2) Riter, R. E.; Willard, D. M.; Levinger, N. E. *Journal of Physical Chemistry B* **1998**, *102*, 2705.

APPENDIX A

MATLAB CODE

A.1 Data Collection

```
function[PI_open_error wave wrapper]=initialINST()  
  
[wave wrapper]=iniUSB2000(0,2,20000); %initialize Ocean Optics  
USB2000+ spectrometer  
  
[PI_open_error PI_initialize_error]=openPI(1); %open serial port and  
initialize delay stage  
  
wave=wave(1:1100);
```

```
function[PI_close_error]=closeINST();  
  
[PI_close_error]=closePI;  
  
closeUSB2000(wrapper);
```

```
function[wave,TAspec]=signalweek(specindex,averaging,Nspec,scale)  
  
[wave wrapper]=iniUSB2000(specindex,2,20000);  
  
wave=wave(1:1100);  
  
TAspec=zeros(size(wave,1),size(wave,2));  
  
figure(1)  
  
for i=1:Nspec  
  
    [TAspec,wrapper]=collectTA2(averaging,wrapper);  
  
    plot(wave,TAspec,'linewidth',3,'color','red');
```

```

formatWLplot;

xlim([wave(1) wave(1100)]);

ylim([-scale scale]);

drawnow;

end

closeUSB2000(wrapper);

function [wave, TAspec]=signaltweek(specindex, averaging, Nspec, scale)

[wave wrapper]=iniUSB2000(specindex, 2, 20000);

wave=wave(1:1100);

TAspec=zeros(size(wave,1), size(wave,2));

figure(1)

for i=1:Nspec

    [TAspec, wrapper]=collectTA2(averaging, wrapper);

    plot(wave, TAspec, 'linewidth', 3, 'color', 'red');

    formatWLplot;

    xlim([wave(1) wave(1100)]);

    ylim([-scale scale]);

    drawnow;

end

closeUSB2000(wrapper);

```

```

%this function will collect data on both an approximate logarithmic
delay scale

function [delay, wave, data]=TAcollect2(stop,Npoints,averaging)

timelog=datestr(now);

[ndelay,delay]=logsteps(stop,Npoints); %define delay points on log10
scale

[PI_open_error]=initialINST; %initializes OO spectrometer and PI
translation stage

if PI_open_error > 0 %aborts data collection if stage communication has
an error
else
    moveA(-1500); %move to collect background
    back=zeros(size(rwave,1),10);
    for i=1:10
        [dat,wrapper]=collectTA(specindex,averaging,wrapper); %collect
background
        back(:,i)=dat;
    end
    [back]=fixsignbyWL(450,back);
    back=sum(back,2)./10;
    PIhome; %position stage before time zero if not there already
    rdata=zeros(size(rwave,1),size(delay,2)); %allocate 'rdata' in
memory
    for i=1:(size(delay,2))
        Amove=ndelay(i); %define step - start at zero

```

```

        delay(i)=moveA(Amove); %move to position & get position

        [TAspec,wrapper]=collectTA(specindex,averaging,wrapper);

        rdata(:,i)=TAspec;

end

PIhome;

closeINST(); %closes PI and OO instrument communication

%DATA PROCESSING

[tdata]=trunwav(rdata,50,1024); %truncate spectrum around data

[wave]=trunwav(rwave,50,1024);

[back]=trunwav(back,50,1024);

[data]=fixsignbyWL(350,tdata); %correct the sign of each spectrum

grid

save back back -ascii -double

save data data -ascii -double

save wave wave -ascii -double

save delay delay -ascii -double

save rdata rdata -ascii -double

save rwave rwave -ascii -double

save timelog timelog

end

timelog=[timelog; datestr(now)];

%this function will collect data on both an approximate logarithmic
delay scale

function[delay,wave,data]=TAcollect3(stop,Npoints,averaging)

[ndelay,delay]=logsteps(stop,Npoints); %define delay points on log10
scale

```

```

[PI_open_error wave wrapper]=initialINST; %initializes OO spectrometer
and PI translation stage

save wave wave -ascii -double

save delay delay -ascii -double

%DATA COLLECTION LOOP

for run=1:10

    if PI_open_error > 0 %aborts data collection if stage communication
has an error

        break

    else

        data=zeros(size(wave,1),Npoints); %allocate 'Fdata' in memory

        %FOWARD DATA COLLECTION

        for i=1:Npoints

            Amove=ndelay(i); %define step - start at zero

            moveA(Amove); %move to position & get position

            [signal,wrapper]=collectTA2(averaging,wrapper);

            data(:,i)=signal;

            figure(1)

            subplot(1,2,1)

            imagesc(data)

            formatspectrogramTAcollect;

            set(gca,'linewidth',2.5)

            title('forward','fontsize',18)

            drawnow

        end

        questdlg('Move CaF2 crystal position!');

        %BACKWARD DATA COLLECTION

        for i=1:Npoints

            Amove=ndelay(Npoints-i+1); %define step - start at zero

```

```

moveA(Amove); %move to position & get position
[signal,wrapper]=collectTA2(averaging,wrapper);
signal=(signal+data(:,Npoints-i+1))./2;
data(:,Npoints-i+1)=signal;
figure(1)
subplot(1,2,2)
imagesc(data)
formatspectrogramTAcollect;
set(gca,'linewidth',2.5)
title('forward + backward','fontsize',18)
drawnow
end
%PLOT DATA FOR EACH RUN
figure(2)
set(gca,'linewidth',2.5)
if run <= 1
    subplot(1,2,1)
    imagesc(data)
    formatspectrogramTAcollect;
    title('Run #1','fontsize',18)
    save data data -ascii -double %no multiple runs, single
data set
    tmp1=data;
else
    tmp2=data;
    [tmp1,tmp2]=fixSPECsign(tmp1,tmp2);
    subplot(1,2,2)
    data=(tmp1+tmp2)./2;
    imagesc(data)

```

```

        formatspectrogramTAcollect;

        title('Averaged','fontsize',18)

        save data data -ascii -double %signal averaged data

    end

    button=questdlg('Collect another run?');

    if strcmp(button, 'Yes')

        else

            break

        end

    end %conditional that PI stage communication has no errors

end %multiple runs loop

closeINST(); %closes PI and OO instrument communication

%this function will collect data on both an approximate logarithmic
delay scale

function[delay,wave,data]=TAcollect4(stop,steps,averaging)

[ndelay,delay]=linspace(1e-15,stop,steps); %define delay points on
log10 scale

[PI_open_error wave wrapper]=initialINST; %initializes OO spectrometer
and PI translation stage

%COLLECT BACKGROUND

moveA(-1500); %move to collect background

wave=trunwav(wave,50,1024);

[back, wrapper]=collectTA(10,wrapper);

save back back -ascii -double

save wave wave -ascii -double

save delay delay -ascii -double

Npoints=size(delay,2);

```

```

%DATA COLLECTION LOOP

for run=1:10

    if PI_open_error > 0 %aborts data collection if stage communication
has an error

        break

    else

        data=zeros(size(wave,1),Npoints); %allocate 'Fdata' in memory

        %FOWARD DATA COLLECTION

        for i=1:Npoints

            Amove=ndelay(i); %define step - start at zero

            moveA(Amove); %move to position & get position

            [signal,wrapper]=collectTA(averaging,wrapper);

            data(:,i)=signal;

            figure(1)

            subplot(1,2,1)

            imagesc(delay,wave,data);

            formatspectrogramTAcollect;

            set(gca,'linewidth',2.5)

            title('forward','fontsize',18)

            drawnow

        end

        questdlg('Move CaF2 crystal position!');

        %BACKWARD DATA COLLECTION

        for i=1:Npoints

            Amove=ndelay(Npoints-i+1); %define step - start at zero

            moveA(Amove); %move to position & get position

            [signal,wrapper]=collectTA(averaging,wrapper);

            signal=(signal+data(:,Npoints-i+1))./2;

            data(:,Npoints-i+1)=signal;

```

```

figure(1)

subplot(1,2,2)

imagesc(delay,wave,data);

formatspectrogramTAcollect;

set(gca,'linewidth',2.5)

title('forward + backward','fontsize',18)

drawnow

end

%PLOT DATA FOR EACH RUN

figure(2)

set(gca,'linewidth',2.5)

if run <= 1

    subplot(1,2,1)

    imagesc(delay,wave,data)

    formatspectrogramTAcollect;

    title('Run #1','fontsize',18)

    save data data -ascii -double %no multiple runs, single
data set

    tmp1=data;

else

    tmp2=data;

    [tmp1,tmp2]=fixSPECsign(tmp1,tmp2);

    subplot(1,2,2)

    data=(tmp1+tmp2)./2;

    imagesc(delay,wave,data)

    formatspectrogramTAcollect;

    title('Averaged','fontsize',18)

    save data data -ascii -double %signal averaged data

end

```

```

        button=questdlg('Collect another run?');
        if strcmp(button, 'Yes')
            else
                break
            end
        end %conditional that PI stage communication has no errors
    end %multiple runs loop
closeINST(); %closes PI and OO instrument communication

```

A.2 Ocean Optics Spectrometer Functions

```

function [wavelength, wrapper]=iniUSB2000 (specindex, trigmode, integration)
    import com.oceanoptics.omnidriver.api.wrapper Wrapper %imports
    Wrapper.class which has spectrometer controls
    wrapper = Wrapper(); %opens a new instance of Wrapper
    wrapper.openAllSpectrometers(); %searches for available
    spectrometers
    wrapper.setIntegrationTime (specindex, integration); %sets
    integration time for spect. '0'
    wrapper.setExternalTriggerMode (specindex, trigmode); %sets trigger
    mode for spectrometer '0'
    wavelength=wrapper.getWavelengths (specindex); %gets wavelength
    vector from spectrometer '0'

function []=closeUSB2000 (wrapper)
    wrapper.closeAllSpectrometers() %closes all spectrometers

function [signal, wrapper]=collectTA (averaging, wrapper)

```

```

averaging=round(averaging./2);
dat1=zeros(2048,1);
dat2=zeros(2048,1);
signal=zeros(1100,averaging);
for i=1:averaging
    wrapper.getSpectrum(0);
    dat1=wrapper.getSpectrum(0);
    dat2=wrapper.getSpectrum(0);
    dat3=wrapper.getSpectrum(0);
    dat4=wrapper.getSpectrum(0);
    ref=(dat1+dat3)./2;
    sig=(dat2+dat4)./2;
    sig=1000.*(log(sig./ref));
    signal(:,i)=smooth(sig(1:1100));
end
signal=fixsignbyWL(400,signal);
signal=sum(signal,2)./size(signal,2);

function [signal,wrapper]=collectTA2(averaging,wrapper)
N=averaging.*2;
dat=zeros(2048,1);
dat2=zeros(1100,1);
signal=zeros(1100,averaging);
for i=1:N
    dat=wrapper.getSpectrum(0);
    dat2(:,i)=(dat(1:1100));
end
for i=1:N/2

```

```

    ref=dat2(:, ((i-1)*2+1));
    sig=dat2(:, i*2);
    signal(:, i)=smooth(1000.*log(sig./ref));
end

%subplot(1,2,1)
%imagesc(signal)
signal=fixsignbyWL(400, signal);
%subplot(1,2,2)
%imagesc(signal)
%save signal signal -ascii -double
signal=sum(signal, 2) ./size(signal, 2);

function [spectrum, wrapper]=getSpec (specindex, wrapper)
[spectrum]=wrapper.getSpectrum (specindex);

function [wrapper]=getSpectra (specindex, Nspec, xmin, xmax, ymin, ymax, integr
ationtime)
trigmode=2;
[wave, wrapper]=iniUSB2000 (specindex, trigmode, integrationtime);
for i=1:Nspec
[spec, wrapper]=getSpec (specindex, wrapper);
drawnow;
plot (wave, spec, 'linewidth', 3)
xlim([xmin xmax])
ylim([ymin ymax])
grid
end

```

A.3 Physik Instrumente Translation Stage Functions

```
%initialize the translation stage

function[COMopen_error, initialize_error]=openPI(COMport)

addpath(['C:\Program Files\MATLAB\Matlab TA Data Collection\PI Matlab
Functions\WindowsDLL'])

loadlibrary NetLib300 %loads DLL file with stage functions

[COMopen_error]=calllib ('NetLib300', 'LAN_open', COMport, 1); %opens
COM port

[initialize_error]=calllib ('NetLib300', 'LAN_init_net');% detects
stages

function[close_error]=closePI

[close_error]=calllib ('NetLib300', 'LAN_close') %closes COM port

unloadlibrary NetLib300

function[position]=getPIpos

[position]=calllib ('NetLib300', 'LAN_getPos', 2); %gets position

[position]=stepstopsdelay(position);

function[delay]=linandlogdelay(linres, linstop, logstop, Nlogpoints)

Nlin=linstop/linres;

lindelay=[1:Nlin]*linres;

a=log10(logstop);

b=log10(linstop);

da=(a-b)/Nlogpoints;
```

```

c=(1:Nlogpoints)*da+b;

logdelay=10.^c;

delay=[0 lindelay logdelay];

function [ndelay, adelay]=linearsteps(dt1,dt2,dt3,t1stop,t2stop,t3stop,stage
resolution)

N1=t1stop./dt1;

t1=[0:N1].*dt1;

N2=(t2stop-t1stop)./dt2;

t2=[0:N2].*dt2+t1stop;

N3=(t3stop-t2stop)./dt3;

t3=[1:N3].*dt3+t2stop;

delay=[t1 t2 t3];

ndelay=round(delay./stageresolution); %calculate steps for stage

adelay=ndelay.*stageresolution*1e12; %convert to picoseconds

function [ndelay, adelay]=linsteps(baseunit, stop, dt)

%constants

fs=1e-15;

ps=1e-12;

stageresolution=0.66667e-15;

%calculate number of points

N=round(stop./dt);

%calculate time delay vector and add 'zero' point

delay=[1:N].*dt;

delay=[0 delay];

%calculate steps for stage

ndelay=round(delay./stageresolution);

```

```

%calculate actual step values
adelay=stageresolution.*ndelay./baseunit;

function[delay]=logdelay(scan,Npoints)

a=log10(scan);
da=a/Npoints;
a=(1:Npoints)*da;
delay=10.^a;

function[ndelay,adelay]=logsteps(stop,Npoints)

%constants
fs=1e-15;
ps=1e-12;
baseunit=fs;
stageresolution=0.6667e-15;
Ntotal=round(Npoints);
N=Ntotal;

%divide exponent by number of points
da=log10(stop/baseunit)/(N-1);

%calculate time delay vector and add 'zero' point
a=[1:(N-1)].*da;
delay=10.^a;
delay=[0 delay];

%calculate steps for stage
ndelay=round(baseunit.*delay./stageresolution);

%find repeated data points
x=diff(ndelay);
x=x+1;

```

```

[index]=find(x<2);
index=index+1;
a=max(index);
b=ndelay(a);
%replace repeated points with linearly spaced points
for i=1:a
    ndelay(a-i+1)=b-i+1;
end
%calculate actual step values
adelay=stageresolution.*ndelay./ps;
adelay=adelay((Ntotal-Npoints+1):Ntotal);
ndelay=ndelay((Ntotal-Npoints+1):Ntotal);

function[delay]=moveA(steps)
calllib('NetLib300','LAN_moveA',2,steps); %moves to absolute
position
calllib('NetLib300','LAN_waitStop',2); %waits for stage to stop
[delay]=getPIpos;

function[delay_fs]=PIhome
moveA(0);
[delay_fs]=getPIpos;

%this function converts picoconds of delay into steps on the stage
function[ndelay,adelay]=psdelaytosteps(delay)
ps=1e-12;
c=2.99792458e8;
microm=1e-6;

```

```

dt=(0.2*microm/c) ./ps;
ndelay=round(delay./dt);
adelay=(ndelay.*dt);

function [nstep, nscan, astep, ascan]=scansetup(scan, step)

fs=1e-15;
c=2.99792458e8;
microm=1e-6;
dt=2*0.1*microm;
nscan=round(scan/step);
nstep=round(step*3/2);
astep=nstep*dt/(c*fs);
ascan=nscan*astep;

function [fsdelay]=stepstopdelay(steps)

ps=1e-12;
microm=1e-6;
c=2.99792458e8;
dstep=0.1*microm;
fsdelay=2*(steps.*dstep) ./ (c.*ps);

```

A.4 Data Processing Functions

```

function [data]=addspec(data1, data2, data3);

m=size(data1,1);
n=size(data1,2);
data=zeros(m,n);

for i=1:n

```

```

temp1=data1(:,i);
temp2=data2(:,i);
temp3=data3(:,i);
a=sum(temp1-temp2,1);
b=sum(temp1+temp2,1);
if a>=b
    temp2=temp2.*-1;
else
end
a=sum(temp1-temp3,1);
b=sum(temp1+temp3,1);
if a>=b
    temp3=temp3.*-1;
else
end
temp=(temp1+temp2+temp3)./3;
data(:,i)=temp;
end

```

```

function[cdata]=correctsign(index,data)
%this function fixes the sign by comparing to an adjacent trace.
%It calculates the difference and the sum between the two values
%at an WL and flips the sign accordingly.
cdata=zeros(size(data,1),size(data,2));
for i=1:(size(data,2)-1)
    a=size(data,2)+1-i;
    temp1=data(:,a);
    temp2=data(:,a-1);

```

```

x=abs(temp1(index)-temp2(index));
y=abs(temp1(index)+temp2(index));
if x<y
else
    temp2=temp2*-1;
end
cdata(:,a-1)=temp2;
end
cdata(:,size(data,2))=data(:,size(data,2));
data=cdata;
save data data -ascii -double
imagesc(cdata)

%This program fits the rawchirp to a polynomial and calculates
%the chirp function for the entire wavelength range based on this fit.

function[chirp]=fitchirp(delay,wave,rchirp,Nstart,Nend,order)

temp1=rchirp(Nstart:Nend)';
temp2=wave(Nstart:Nend);

[fitcoef]=polyfit(temp2,temp1,order);
chirp=polyval(fitcoef,wave);

save chirp chirp -ascii -double

figure(2)

```

```

plot(wave,rchirp,wave,chirp,'linewidth',3)
xlabel('wavelength (nanometers)')
ylabel('time delay (picoseconds)')
title('chirp function')

function[data]=fixsign(data,default)
%fixes the sign of the TA matrix by selecting a wavelength trace that
%should always have a constant sign (pos or neg) and corrects the sign
of
%the collected data accordingly
for i=1:size(data,2)
    [a,index]=max(abs(data(:,i)));
    b=max(data(index,i));
    if index<200
        if index>600
            a=max(abs(data(:,default)));
            b=max(data(:,default));
        else
            end
        end
    end
    test=a/b;
    if test<0
        temp=data(:,i).*-1;
    else
        temp=data(:,i);
    end
    data(:,i)=temp;
end

```

```

%save data data -ascii -double

%imagesc(data)

function[data]=fixsign2(data,pumpindex)

m=size(data,2);

for i=1:m

    a=data(pumpindex,1);

    b=data(pumpindex,i);

    c=a*b;

    if c>0

    else

        data(:,i)=data(:,i).*-1;

    end

end

end

imagesc(data)

save data data -ascii -double

function[data]=fixsignbyWL(index,data)

%fixes the sign of the TA matrix by selecting a wavelength trace that
%should always have a constant sign (pos or neg) and corrects the sign
of
%the collected data accordingly

for i=1:size(data,2)

    a=abs(data(index,1));

    b=data(index,i);

    test=a/b;

    if test<0

```

```

        temp=data(:,i).*-1;
    else
        temp=data(:,i);
    end
    data(:,i)=temp;
end
%save data data -ascii -double
%imagesc(data)
function[data1,data2]=fixSPECsign(data1,data2)
tmp1=sum(sum(data1,1),2);
tmp2=sum(sum(data2,1),2);
a=abs(tmp1+tmp2);
b=abs(tmp1-tmp2);
if a < b
    data2=-data2;
else
end

function[] = formatplot()
grid on
set(gca,'linewidth',2.5)
set(gca,'fontweight','bold')
xlabel('time delay (picoseconds)','fontsize',16)

function[] = formatspectrogram()
%ylim([380 620])
%xlim([-0.75 log10(2000)])
grid on

```

```

set(gca, 'linewidth', 2.5)
set(gca, 'fontweight', 'bold')
xlabel('log_1_0 picoseconds', 'fontsize', 16)
ylabel('wavelength (nm)', 'fontsize', 16)

```

```

function[] = formatspectrogramTAcollect()
hold on
%ylim([380 720])
grid on
set(gca, 'linewidth', 2.5)
set(gca, 'fontweight', 'bold')
xlabel('log_1_0 picoseconds', 'fontsize', 16)
ylabel('wavelength', 'fontsize', 16)
hold off

```

```

function[] = formatWLplot()
xlim([380 720])
grid on
set(gca, 'linewidth', 2.5)
set(gca, 'fontweight', 'bold')
ylabel('\DeltaA (mOD)', 'fontsize', 16)
xlabel('wavelength (nm)', 'fontsize', 16)

```

```

function[data]=quickfix(index, data)
data(:, index)=data(:, index).*-1;
imagesc(data)
save data data -ascii -double

```

```

%This function extracts the maximum of the cross phase modulation
signal
%(XPM) in a pure solvent. It pulls out the time delay as a function of
%wavelength. The time resolution comes from the time resolution at
which
%the XPM data was collected.

```

```

function[rchirp]=rawchirp(delay,wave,data)

```

```

%data=abs(data); %absolute value of data

```

```

N=size(data,1); %wavelength

```

```

rchirp=zeros(N);

```

```

for i=1:N

```

```

    temp=(data(i,:));

```

```

    [C,I]=max(temp);

```

```

    rchirp(i)=delay(I);

```

```

end

```

```

figure(1)

```

```

imagesc(delay,wave,data)

```

```

xlabel('time delay (picoseconds)')

```

```

ylabel('wavelength (nanometers)')

```

```

title('XPM chirp')

```

```

hold on

```

```

plot(rchirp,wave,'linewidth',3,'color','black')

```

```

hold off

```

```

save rchirp rchirp -ascii -double

```

```

function[sdata]=subtractbackground(back,data)
sdata=zeros(size(data));
for i=1:size(data,2);
    sdata(:,i)=data(:,i)-back;
end

```

```

function[sdata]=subtractback(data,numspec)
fback=zeros(size(data,1),numspec);
for i=1:numspec
    temp=data(:,i);
    fback(:,i)=temp;
end

```

```

fback=sum(fback,2)./size(fback,2);
M=size(data,2);

```

```

for i=1:M
    sdata(:,i)=data(:,i)-fback;
end

```

```

save sdata sdata -ascii -double
imagesc(sdata)

```

```

function[sdata]=subtractbackground(back,data)
sdata=zeros(size(data));
for i=1:size(data,2);
    sdata(:,i)=data(:,i)-back;
end

```

```

function [tdelay, tdata]=tcorrect(chirp, delay, wave, sdata, offset)

M=size(sdata,1); %wavelength
N=size(sdata,2); %delay
dt=(delay(3)-delay(2));

shift=round(chirp./dt)+offset; %number of pixels to shift data
spectrogram
tdelay=delay;

tdata=zeros(M,N);
for i=1:M
    s=-1.*shift(i); %shift for time domain trace
    temp=sdata(i,:)' ; %time domain trace
    temp=circshift(temp,s)';
    tdata(i,:)=temp;
    temp=[];
end

N=size(tdata,2);
cut=max(shift);
for i=1:cut
    tdata(:,1-i+N)=[];
    tdelay(1-i+N)=[];
end

```

```

imagesc(tdelay, wave, tdata)

save tdelay tdelay -ascii -double

save tdata tdata -ascii -double

%This function time corrects transient absorption data based on an
chirp
%obtained from the XPM chirp fit. Offset moves shifts the data to put
time
%zero at the "edge" of the data.

function [tdelay, tdata]=timecorrect(delay, wave, data, chirp, offset)

M=size(data,1); %wavelength
N=size(data,2); %delay
dt=(delay(3)-delay(2));

shift=round(chirp./dt)+offset; %number of pixels to shift data
spectrogram
tdelay=delay;

tdata=zeros(M,N);
for i=1:M
    s=-1.*shift(i); %shift for time domain trace
    temp=data(i,:)' ; %time domain trace
    temp=circshift(temp,s)';
    tdata(i,:)=temp;
    temp=[];
end

```

```

N=size(tdata,2);
cut=max(shift);
for i=1:cut
    tdata(:,1-i+N)=[];
    tdelay(1-i+N)=[];
end

figure(1)
subplot(2,1,1)
imagesc(delay,wave,data)
title('raw data','fontsize',20)
subplot(2,1,2)
imagesc(tdelay,wave,tdata)
title('time corrected data','fontsize',20)
save tdata tdata -ascii -double
save tdelay tdelay -ascii -double

function [data]=trunwav(data,start,length)

if size(data,2)>1
    data=data(start:start+length-1,:);
else
    data=data(start:start+length-1);
end

function [xcorr]=xpm(delay,data,I1,I2)
xcorr=abs(data(I1:I2,:));

```

```

xcorr=sum(xcorr,1)./size(xcorr,1);

figure(1)

plot(delay,xcorr,'k','linewidth',3)

xlabel('time delay')

ylabel('integrated signal')

grid

function[anis resid coef]=anisotropy(para,perp,delay,wave)

%This function calculates the anisotropy of TA data collected at 400nm
with
%the ocean optics spectrometer - - it integrates over a spectral range
to
%simplify the anisotropy analysis. N values define integration range
for spectral data (N1,N2) and where to
%start (N3) and end (N4) the linear fit of the log of the anisotropy
data
%(assumes single exponential decay)

N1=200;

N2=600;

N3=105;

N4=200;

N5=size(para,2);

para=intspec(wave,para,N1,N2);

perp=intspec(wave,perp,N1,N2);

%para=para-para(1);

%perp=perp-perp(1);

tmp1=sum(para((N5-3):N5));

```

```

tmp2=sum(perp((N5-3):N5));
g=tmp1./tmp2;
g=1;
%g=para(size(para,2))./perp(size(perp,2));
perp=g.*perp;

figure(1)
subplot(2,1,1)
plot(delay,[para' perp'],'o-','linewidth',3)
grid
xlim([0 2000])
xlabel('time delay (picoseconds)','fontsize',16)
ylabel('integrated signal','fontsize',16)
legend('para','perp')
formatplot;

anis=(para-perp)./(para+2.*perp);
tmp1=delay(N3:N4)-delay(N3);
tmp2=anis(N3:N4);
adelay=delay(N3:size(delay,2))-delay(N3);
anis=anis(N3:size(delay,2));

[fitcoef]=polyfit(tmp1,log(tmp2),1);
[fit]=polyval(fitcoef,adelay);
fit=exp(fit);
resid=anis-fit;
R2=(1-sum(abs(resid),2)./size(resid,2)).^2;
tau=-(1/fitcoef(1));

```

```

r0=exp(fitcoef(2));
coef=real([r0 tau R2])
figure(1)
subplot(2,1,2)
plot(adelay,anis,'o-k','linewidth',3)
hold on
plot(adelay,fit,'r','linewidth',3)
hold off
grid
xlim([0 2000])
ylim([-0.1 0.5])
xlabel('time delay (picoseconds)','fontsize',16)
ylabel('anisotropy','fontsize',16)
formatplot;

anis=[adelay' anis'];
save anis anis -ascii -double
save resid resid -ascii -double
save coef coef -ascii -double
save fit fit -ascii -double

```

APPENDIX B

SUPPLEMENTAL MATERIALS

B.1 Analysis of C343 BFTA Data

The time-dependent Stokes shift in the coumarin 343 (C343) broadband femtosecond transient absorption (BFTA) data were gauged in three ways, as noted in the Chapter 4. After we removing contributions to the signal from the excited state lifetime (equation 4.4), and from the BL and ESA signals (equation 4.6), we used three different methods to gauge the time-dependent Stokes shift. Calculations based on fitting spectrogram traces to an asymmetric Gaussian function are described in the paper. Dynamics were also quantified through the spectral maximum of the spectrograms as a function of time and using the first moment of the asymmetric Gaussian peak¹

$$M_1 = \nu_0 + \ln 2(s \cdot \Gamma) \quad (\text{B.1})$$

Table B.1 gives the exponential fit results. All analysis methods generate the same qualitative trends

Table B.1 Multi-exponential fitted parameters to time-dependent spectral shifts of the BFTA signal maximum, stimulated emission maximum, and the first spectral moment of the SE band of C343 in bulk water and in cyclohexane/AOT/water reverse micelles. The number in parenthesis following each value is the error.

BFTA Signal Maximum Frequency										
	ν_0 (1/cm)	S_0 (1/cm)	a_1	τ_1 (ps)	a_2	τ_2 (ps)	a_3	τ_3 (ps)	a_4	τ_4 (ns)
bulk	20237(4)	1164(10)	0.62(0.03)	0.058(0.008)	0.37(0.02)	1.0(0.1)	**	**	**	**
w₀ = 20	20347(22)	1606(10)	0.38(0.01)	0.16(0.02)	0.15(0.01)	2.3(0.8)	0.19(0.01)	46(15)	0.28(0.01)	431(97)
10	20310(38)	1884(10)	0.40(0.01)	0.09(0.01)	0.11(0.01)	2.3(0.6)	0.20(0.01)	68(16)	0.29(0.01)	662(163)
5	20471(37)	1759(10)	0.28(0.01)	0.14(0.03)	0.10(0.01)	3(1)	0.23(0.01)	37(12)	0.39(0.01)	536(105)
2.5	20714(348)	1493(10)	0.27(0.01)	0.28(0.08)	0.05(0.01)	7(10)	0.31(0.01)	177(126)	0.36(0.01)	1203(2171)
Stimulated Emission (SE) Maximum Frequency										
bulk	19963(1)	1034(10)	0.61(1)	100(4)	0.39(1)	0.77(0.03)	**	**	**	**
w₀ = 20	20062(6)	1950(10)	0.41(1)	121(4)	0.14(1)	1.6(1)	0.22(1)	61(5)	0.23(1)	386(32)
10	20103(7)	2058(10)	0.29(1)	196(12)	0.14(1)	2.0(2)	0.20(1)	54(5)	0.37(1)	353(19)
5	20194(9)	2042(10)	0.38(1)	187(8)	0.04(1)	2.5(8)	0.19(1)	52(5)	0.39(1)	493(24)
2.5	20193(33)	2396(10)	0.11(1)	315(79)	0.08(1)	2.1(6)	0.20(1)	115(18)	0.60(1)	709(66)
Stimulated Emission (SE) First Spectral Moment										
bulk	19694(1)	1036(10)	0.67(1)	129(7)	0.32(1)	1.11(8)	**	**	**	**
w₀ = 20	19835(22)	2085(10)	0.36(1)	286(20)	0.11(1)	3.8(9)	0.27(1)	84(11)	0.25(1)	564(110)
10	19830(69)	2152(10)	0.24(1)	560(64)	0.13(1)	9(3)	0.34(1)	144(37)	0.29(1)	777(370)
5	20015(36)	2091(10)	0.25(1)	485(111)	0.08(1)	4(3)	0.20(1)	52(17)	0.47(1)	548(80)
2.5	19925(58)	2798(10)	0.19(1)	96(10)	0.08(1)	2.2(4)	0.11(1)	83(15)	0.61(1)	1019(87)

B.2 Steady-state emission of HPTS in D₂O/IGE/cyclohexane RM

Emission spectra from HPTS in D₂O/IGE/cyclohexane microemulsions (Figure B.1) clearly indicate the presence of excited state proton transfer (ESPT). Emission spectra were recorded with excitation at ~400 nm from the BFTA instrument which excites the protonated state of HPTS, [ROH]. Emission from [ROH*] and the electronically excited deprotonated state of HPTS, [RO⁻*], is observed. This behavior confirms that the ESPT process is present in D₂O/IGE/cyclohexane reverse micelles.

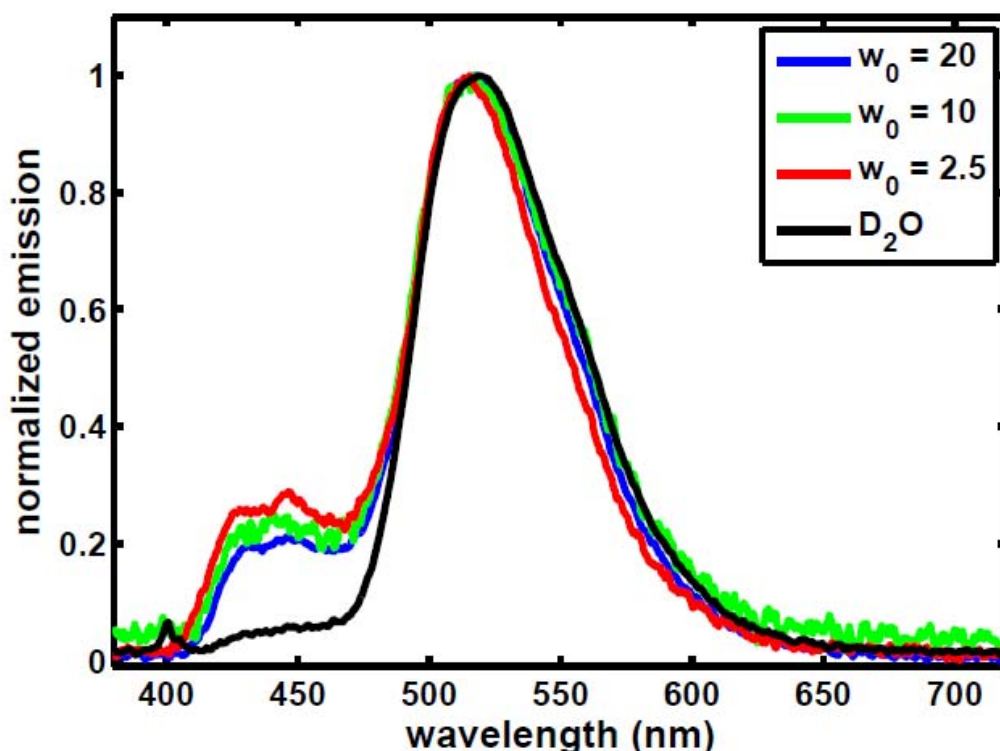


Figure B.1 Steady-state emission from HPTS in D₂O/IGE/cyclohexane reverse micelles and in D₂O. Spectra are very similar to HPTS emission in water/IGE/cyclohexane reverse micelles albeit the protonated state [ROH] emission (~430 nm) increases as the water pool diameter is reduced.

References and Notes

- (1) Stancik, A. L.; Brauns, E. B. *Vibrational Spectroscopy* **2008**, *47*, 66.

APPENDIX C

INDEPENDENT RESEARCH PROPOSAL

C.1 Abstract and Specific Aims

Intramolecular energy transport and storage in biomolecules are highly efficient although extremely elusive¹. In 1973, Davydov introduced a model for energy transport in biomolecules wherein vibrational solitons (localized, self-stabilizing states) travel along α -helices^{2,3}. Solitons are self-stabilizing states that arise from a balance between nonlinearity and dispersive effects, and in the case of Davydov's model, vibrational excitation along the peptide backbone of a α -helix causes lattice distortions that localize quanta of vibrational energy on peptide units¹. There has been a great deal of work developing the theoretical descriptions of the vibrational soliton, but experimental observations have been limited. To date, experimental observations have shown that vibrational solitons exist at biologically relevant temperatures, but there has been no experimental measure of their *formation* and *propagation*. The research outlined in this proposal aims to provide an experimental method that measures and characterizes vibrational soliton *formation* and *propagation* in α -helices at biologically relevant temperatures.

My approach is to use prepared α -helix systems with three characteristics: (i) a tethered chromophore absorber at one end of the α -helix, (ii) isotopic labeling ($^{13}\text{C}^{18}\text{O}$)

at the other end of the α -helix, and (iii) a variable number of peptide units in the helical chain. The chromophore will give the ability to insert energy directionally into the system while the varied chain length and isotopic labeling providing a probe of propagation times. Data will be collected by two ultrafast spectroscopic methods: visible-pump infrared-probe and dual-frequency two-dimensional infrared (DF-2DIR) correlation spectroscopy. The formation of the α -helix vibrational soliton will be monitored via the pump-probe experiments wherein a visible, femtosecond pump pulse introduces energy into the absorbing end of the α -helix and an infrared, femtosecond pulse probes population growth into the soliton vibrational mode. The subsequent soliton propagation time along the α -helix will be characterized via DF-2DIR that will measure the interaction between the soliton vibrational mode and the isotopic labeled vibrational mode at the terminal peptide unit. By systematically varying the length of the α -helix, vibrational soliton propagation dynamics will be determined. This methodology will, for the first time, allow the *formation and propagation* of the elusive Davydov vibrational soliton to be characterized.

C.2 Background and Motivation

C.2.a Biological energy transport mechanisms

One of the fundamental goals in the field of bioenergetics is to unravel transport mechanisms of energy released in adenosine triphosphate (ATP) hydrolysis. ATP hydrolysis facilitates a variety of cell functions with an immediate release of energy ⁴. This energy is typically partitioned and transferred as heat but there is compelling

evidence that suggests intramolecular transport in biomolecules may be an important energy transport mechanism. The small amount of energy released in ATP hydrolysis (~ 10 kcal or 3500 cm^{-1} per mol) suggests that vibrational states may play an important role in intramolecular energy transport. Thus, in 1973 Davydov proposed a transport mechanism wherein self-stabilized vibrational states or vibrational solitons propagate along α -helices^{2,3}.

C.2.b Vibrational soliton theory

Solitons are self-stabilizing states that arise from a balance between nonlinearity and dispersive effects. In Davydov's original model, local vibrational excitations on a peptide unit of a α -helix distort the α -helix structure and in turn this structural distortion traps the vibrational excitation on one or two adjacent peptides^{1,5}. Soliton formation is mediated by the nonlinear nature of the hydrogen bonds that stabilize the α -helix structure. Figure C.1 shows the local structure of the α -helix.

A comprehensive review of Davydov's vibrational soliton theory can be found in Ref.⁵, but in short, theoretical analysis yields two solutions: (1) an *exciton* or *vibron* which is delocalized vibrational excitation induced by a dipole-dipole interaction, and (2) a *soliton* which is considered "phonon dressed" or bound to a specific site (peptide unit) and is self-stabilized. It is important to note that a variety of terms (self-trapped, bound, or phonon dressed) are used to label the soliton which all describe the same state. In addition, the exciton is labeled as a vibron because the excitation is a vibrational transition. The energy of the vibron is described as

$$E_{ex} = E_0 - 2J \tag{C.1}$$

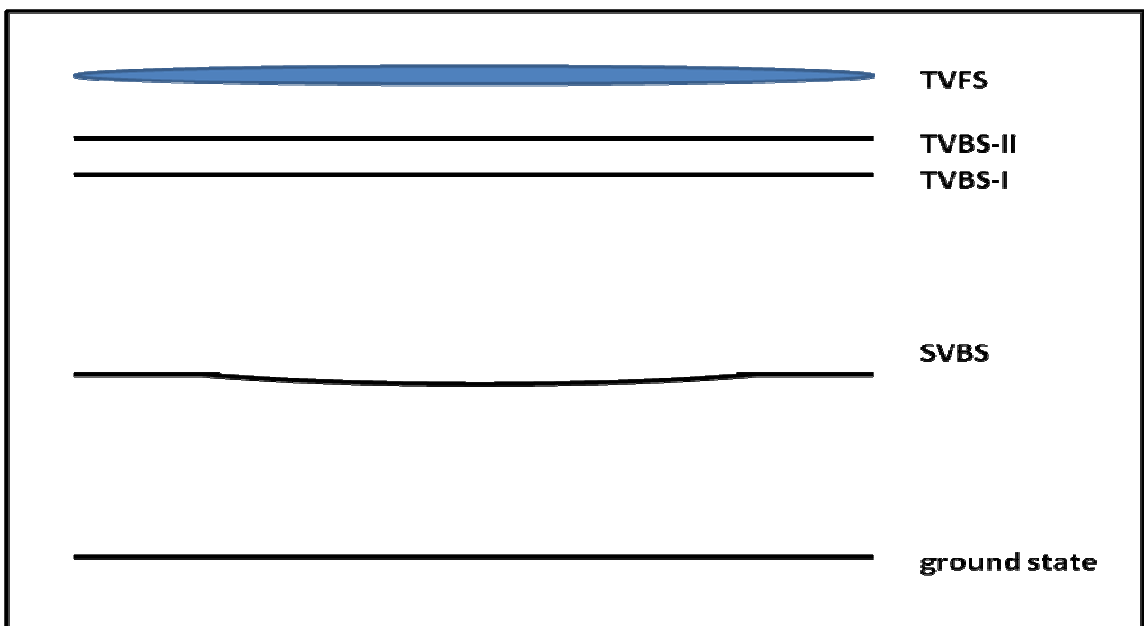


Figure C.1 Energy level diagram for the refined vibrational soliton theory. SVBS, single-vibron bound state; TVBS-I, two-vibron bound state over one peptide unit; TVBS-II two-vibron bound state over two peptide units; and TVFS, two-vibron free state corresponding to two unbound non-interacting vibrons.¹

excitation is a vibrational transition. The energy of the vibron is described as

$$E_{ex} = E_0 - 2J \quad (\text{C.1})$$

and the soliton as

$$E_{sol} = E_0 - \frac{\chi^2}{2W} \quad (\text{C.2})$$

where E_0 the vibrational energy of the uncoupled oscillator is, J is the dipole-dipole coupling parameter, χ is the exciton-phonon coupling parameter, and W is the hydrogen bonding force constant. For soliton formation to occur, it must be energetically favorable and thus the energy difference

$$\Delta E = E_{ex} - E_{sol} = \frac{\chi^2}{2W} - 2J \quad (\text{C.3})$$

must be greater than zero. The most important parameter in this energy difference is the exciton-phonon coupling parameter defined as

$$\chi \equiv \frac{dE_0}{dR} \quad (\text{C.4})$$

where R is the length of the adjacent hydrogen bond. χ effectively determines whether an exciton will collapse into a soliton; exciton-phonon coupling must be sufficiently high for soliton formation to occur. An important feature in this description of a vibrational soliton is that the soliton band will appear to spectroscopically redshifted with respect to the normal excitation band. In addition, the self-stabilizing of

nature the soliton is expected to extend the lifetime beyond that of the exciton which is typically just the vibrational mode lifetime.

Refinement of Davydov's vibrational soliton theory has determined that vibrational soliton exist as single vibron bound states (SVBS), two vibron bound states (TVBS) or two-vibron free states (TVFS)^{6,7}. Figure C.1 shows an energy level diagram for the refined model. The SVBS corresponds exactly with the original Davydov solution; TVFS correspond to two non-interacting unbound vibrons; TVBS-I correspond with two interacting vibrons bound to a single peptide; and TVBS-II corresponds to two interacting vibrons bound to two adjacent peptide units. Further theoretical analysis suggest that the lifetime of SVBS is too short lived to be relevant for energy transport at biological temperatures⁸. On the other hand, TVBS are longer lived while supporting larger quanta of energy. Furthermore, TVBS introduce a convenient mechanism for energy to transfer along the α -helix provided the energy difference between TVBS-I and TVBS-II is below the available thermal energy ($\sim 200 \text{ cm}^{-1}$ at room temperature) which numerical calculations support. Early experimental observations of vibrational solitons utilize Davydov's formalism while more recent studies describe systems in terms of the TVBS model.

C.2.c Experimental evidence for vibrational solitons

In the following experimental studies, it is important to reference various infrared (IR) absorption features found in polypeptide systems. Table C.1 shows the mode designations, approximate frequency range, and approximate descriptions for IR active vibrations in polypeptides⁹. These studies focus on anomalous side bands

around the amide-I region and amide-A region which are dominantly CO stretching and NH stretching, respectively. Experimental evidence for vibrational solitons begins with analysis of anomalous IR absorption features.

C.2.c.i steady-state infrared spectra

The first experimental observation of vibrational solitons was made by Careri and coworkers in 1983¹⁰⁻¹². These studies used crystalline acetanilide (ACN) as a model of a α -helix. ACN is a molecular solid up to 113° C with a structure similar to the α -helix and peptide chains. Figure C.2 shows the similarity in structure of the peptide chain and ACN. The focus of this study was on explaining the anomalous side band at 1650 cm^{-1} of the amide-I band at 1665 cm^{-1} in ACN's infrared absorption spectrum which had been previously observed but not conclusively assigned with conventional molecular spectroscopy analysis¹⁰. Figure C.3 shows the anomalous band and its temperature dependence.

To probe the origin of this anomalous band, the authors conduct a series of experiments with the following explanations:

- Amorphous ACN samples show a very weak band at 1650 cm^{-1} but upon annealing the band intensity recovers. This indicates that regular hydrogen bonding structure in crystalline ACN is a requirement for the band to be present. Thus, hydrogen bonding mediates the formation of the anomalous band.

Table C.1 Amide bands of polypeptides.

Designation	Frequency range (cm ⁻¹) ^a	Description ^c
Amide A	~3300 (s)	NH _s
Amide B	~3100 (s)	NH _s
Amide I	1600-1700 (s)	CO _s (76%), CN _s , (14%), CCN _d (10%)
Amide II	1510-1580 (m)	NH _{ib} (43%), CN _s (29%), CO _{ib} (11%), CC _s (9%)
Amide III	1200-1400 (w)	NH _{ib} (55%), CC _s (19%), CN _s (15%), CO _{ib} (11%)
Amide V	610-710 (w)	CN _t (66%), NH _{ob} (34%)

^a s, strong; m, medium, w, weak.

^b Tamm and Tatulian, 1997.

^c s, stretch; d, deformation; t, torsion, ib, in-plane bend; ob, out-of plane bend.

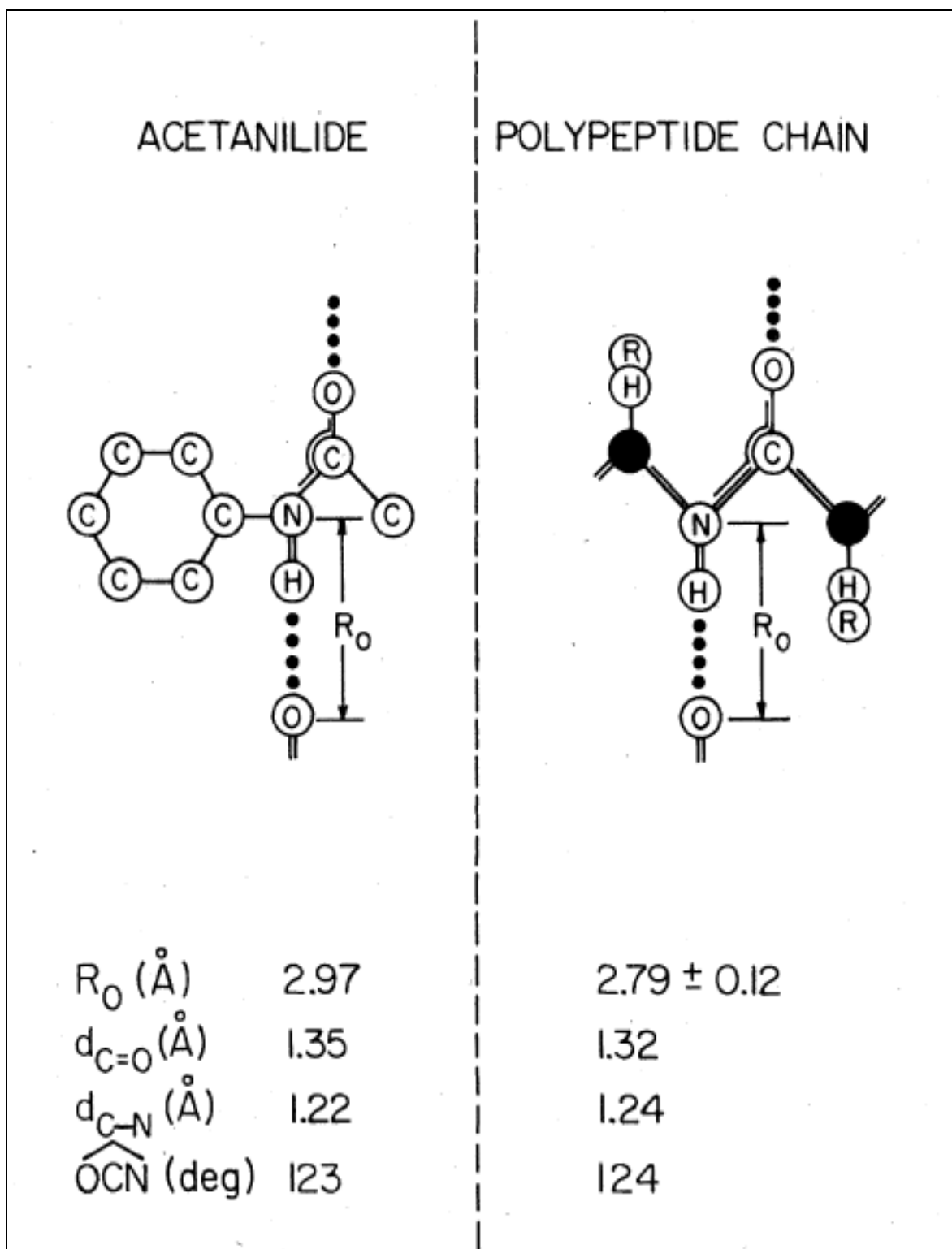


Figure C.2 Comparison of the peptide geometry in ACN and in polypeptides. ¹¹

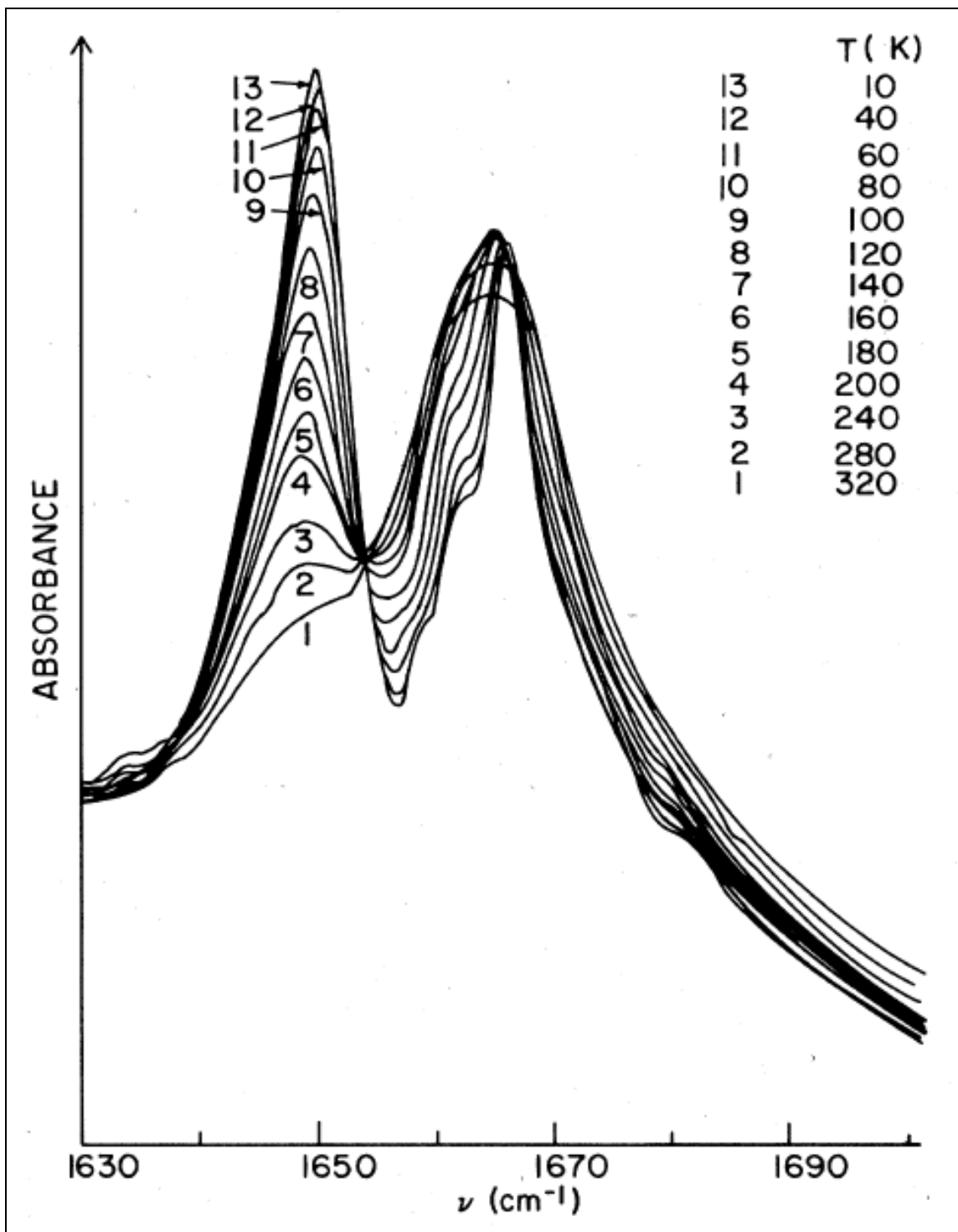


Figure C.3 Temperature dependent IR absorption spectra of crystalline ACN in the amide-I region.¹¹

- Isotopic substitution with ^{15}N shifts the anomalous band (1650 cm^{-1}) in the same magnitude and direction as the amide-I band (1665 cm^{-1}). This shows that the side band is related to the amide-I band.
- Spectra recorded at various temperatures show a clear isosbestic point between the amide-I band (1665 cm^{-1}) and the side band (1650 cm^{-1}). In addition, parallel increases/decreases between the integrated absorbance of the normal amide I band and the anomalous band integrated absorbance are observed. This indicates that the population sampled by the anomalous band originates from population in the normal amide-I mode.

With these observations in mind and with no conventional assignment available for the anomalous band, the authors explain the anomalous band in terms of vibrational soliton theory. First they estimate the value of exciton-phonon coupling parameter, χ by measuring the normal amide-I frequency as a function of the hydrogen bond length in molecular solids similar in structure to ACN (Me-ACN, p-Cl-ACN). χ is calculated with equation C.4 which is estimated to be $6.2 \times 10^{-11}\text{ N}$. Next, the splitting between the anomalous band and the normal amide-I band is used to calculate the hydrogen bonding force constant $W = 4.8\text{ N/m}$ which is a reasonable force constant value for hydrogen bonding. The conclusion is that the anomalous band at 1650 cm^{-1} in the IR absorption spectra of ACN can be explained quite reasonably by vibrational soliton theory. Scott and coworkers also found the same temperature dependence in the amide-I overtone spectrum¹².

This same anomalous temperature dependence was later confirmed in ACN and extended to polypeptide systems by Timonen and coworkers¹³. The main focus of this study was to extend the work of Careri and coworkers to polypeptide systems, and accordingly they chose two model polypeptides that form crystalline α -helices: tryptosine-alanine₁₅ (Try-(Ala)₁₅) and tryptophan-alanine₁₅ (Trp-(Ala)₁₅). These polypeptides consist of a terminal peptide and a chain of fifteen alanine peptide units. No temperature dependence was found in the amide-I region as with ACN, but the polypeptide systems show a similar temperature-dependent side bands in the amide-A region at 3200-3450 cm⁻¹. The origin of the temperature dependence of the polypeptide amide-A mode and ACN amide-I mode was tested by plotting the logarithm of the integrated intensity of each side band vs. temperature squared. Figure C.4 shows this analysis which indicates that both side bands originate from similar mechanisms i.e. coupling to phonons. This result shows that vibrational solitons exist in α -helices but it lacks any time-dependent analysis of these systems.

C.2.c.ii IR pump-probe experiments

More recently ACN and polypeptide systems have been investigated further with IR, femtosecond pump-probe experiments^{1,14}. Pump-probe experiments track time-dependent absorption changes from femtoseconds to picoseconds. Analysis of IR pump-probe data yields information about vibrational lifetimes, vibrational energy transfer (VET), intramolecular vibrational redistribution (IVR), and vibration-phonon coupling. In addition, it can identify transient vibrational states that cannot be detected

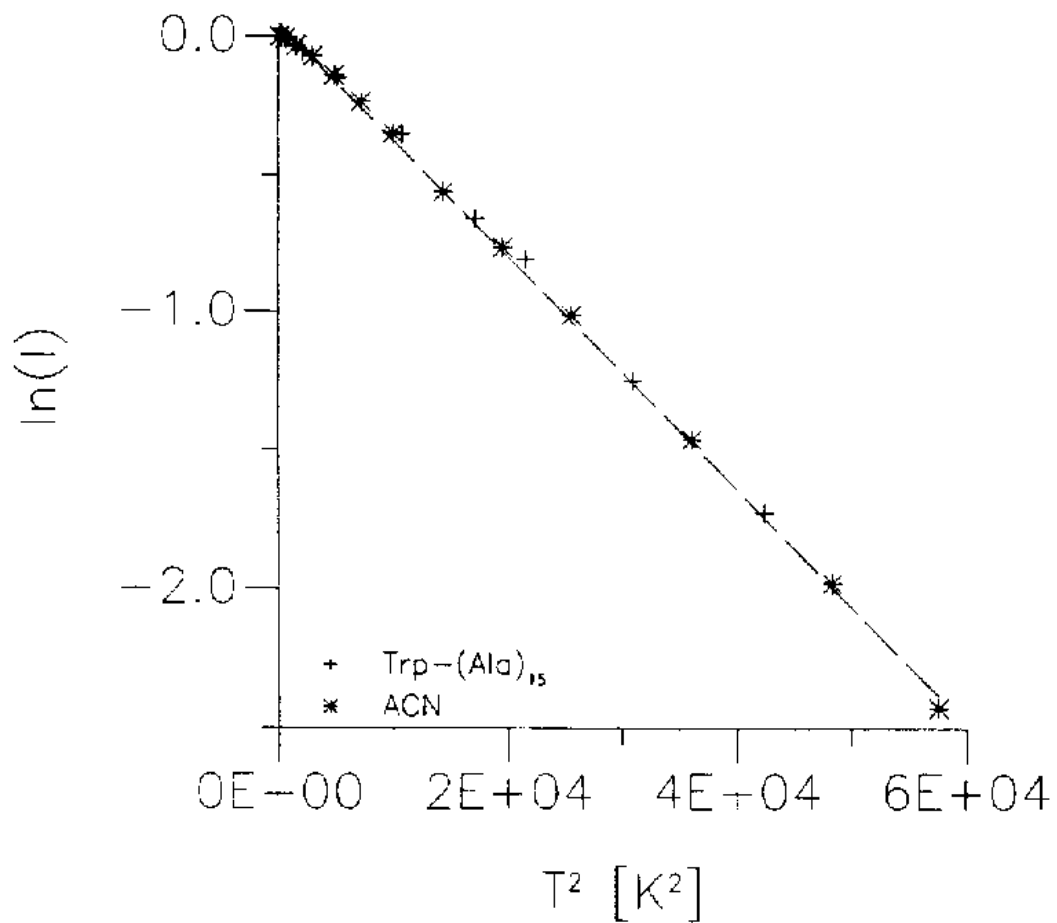


Figure C.4 Temperature-squared analysis of ACN amide-I anomalous band at 1650 cm^{-1} (*) and Trp(Ala)₁₅ amide-A anomalous band at 3195 cm^{-1} (+).¹³

via steady-state spectroscopic methods.

In 2002, Hamm and coworkers conducted time-resolved experiments on room temperature ACN¹⁴. In this study, time-dependent absorbance was probed in the amide-A region wherein the main peak at 3295 cm^{-1} has a sequence of equally spaced satellite peaks to lower energy. This absorption feature has been assigned to a main free exciton (unbound) peak followed by lower energy soliton peaks. Figure C.5 shows the amide-A mode of ACN with satellite peaks and also shows the proposed potential energy diagram for the exciton-soliton system in ACN. To test the validity of this potential energy scheme, two sets of experiments were conducted.

In the first set of experiments, broadband femtosecond pulses were used to excite (pump) and probe the main peak and first three satellite peaks simultaneously. These experiments yielded time-dependent traces at the maxima of the four peaks found in the steady-state absorption spectrum. A surprising feature of these traces is that they all exhibit oscillations out to 8 picoseconds. Fourier transformation of this time-domain data yields spectra with a strong peak at 48 cm^{-1} and a weaker peak at 76 cm^{-1} . Figure C.6 shows the time-domain and Fourier transformed data. These two frequencies match peaks in the non-resonant electronic Raman spectrum for ACN and thus the conclusion is that these peaks are the phonon modes that mediate self-trapping i.e. vibrational solitons.

In the second series of experiments, narrow band, femtosecond pump pulses were used to selectively excite individual peaks followed by a broadband, femtosecond probe. These experiments probe energy transfer between the excited band and the

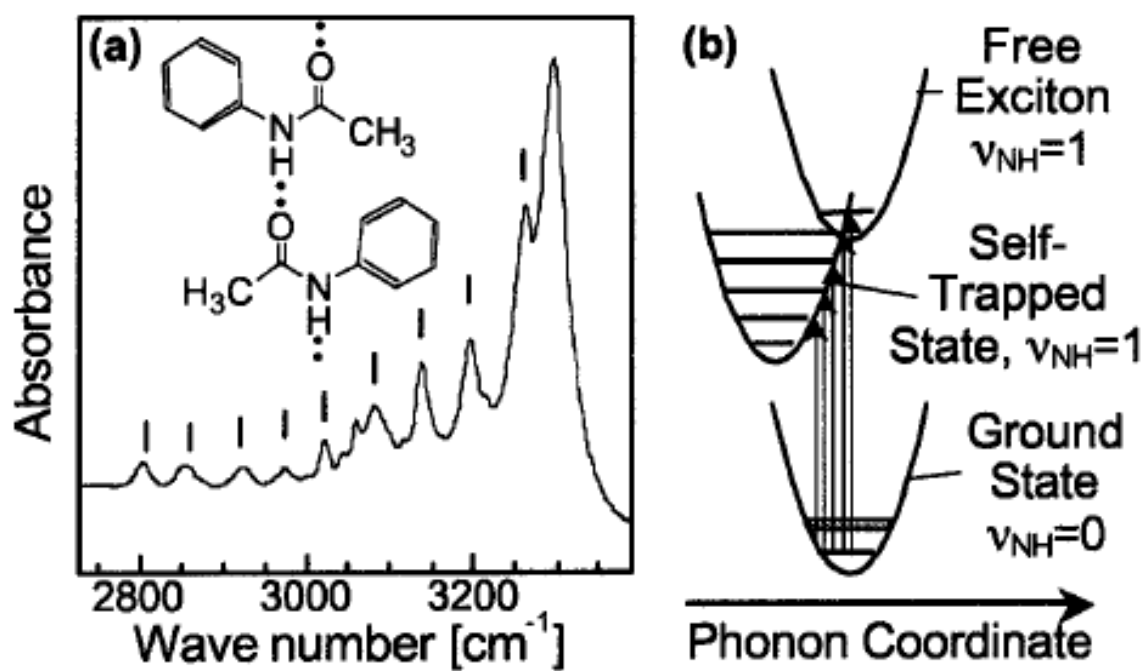


Figure C.5 (a) Absorption spectrum of the NH band of crystalline ACN. The inset schematically depicts the one dimensional chain of hydrogen bonded ACN molecules. (b) The proposed scheme of potential energy surfaces with the allowed transitions depicted.¹⁴

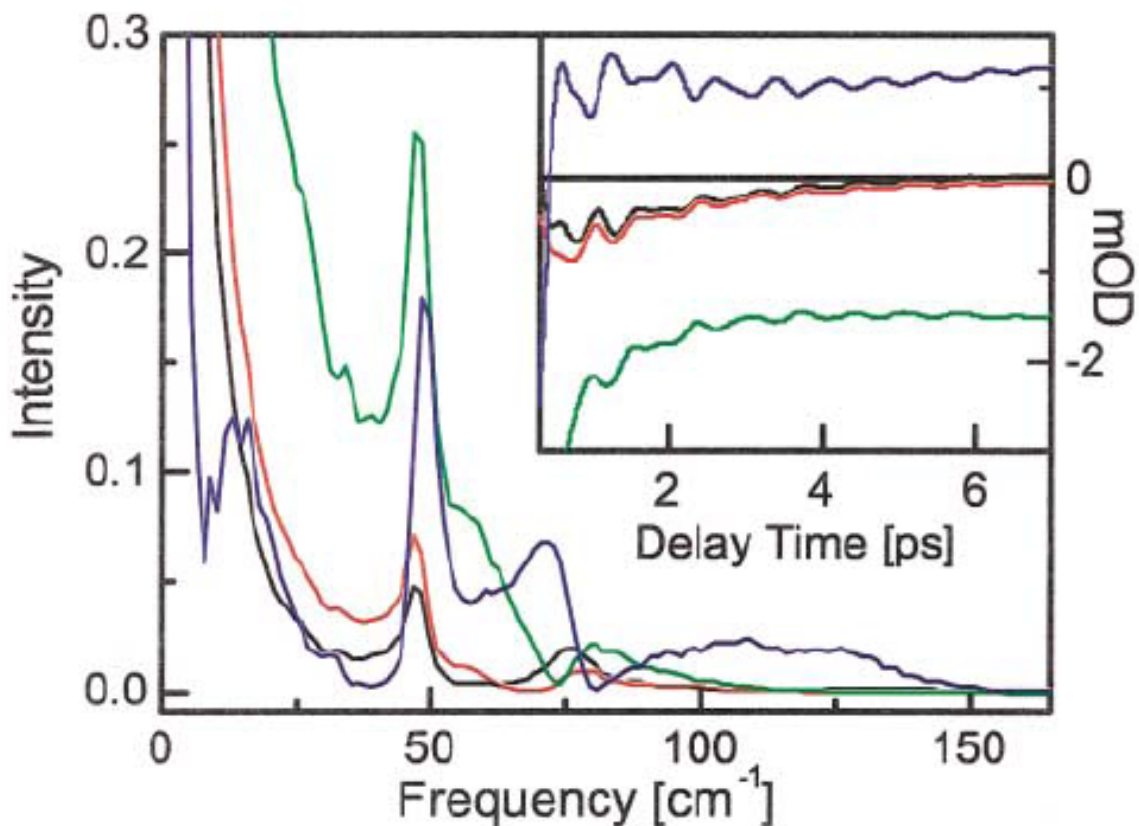


Figure C.6 Fourier transform spectra of the coherent response ACN after impulsive excitation. The inset shows the corresponding signals in the time domain. The four signals correspond to the absorption peaks in the linear spectrum: 3295 cm⁻¹ (blue line), 3260 cm⁻¹ (green line), 3195 cm⁻¹ (red line), and 3137 cm⁻¹ (black line).¹⁴

probed bands. The results show that when the exciton band is excited there is energy transfer to the soliton bands, and excitation at any of the soliton peaks displays no back transfer into the exciton band. Thus, this is a direct observation of vibrational solitons because excitation at the exciton state leads to irreversible population transfer to the soliton states. These results show that the satellite peaks are indeed soliton states and are self-stabilizing because, although it is energetically possible within the available thermal energy for there to be back transfer to the exciton band, no back transfer is observed.

The most recent investigation of vibrational solitons in α -helices was conducted by Hamm and coworkers in 2004¹. In this study, time-dependent absorption in the NH stretching (amide-A and amide-B) region was probed for poly- γ -benzyl-L-glutamate (PBLG). In chloroform, PBLG forms long, stable α -helices both in solution and in films grown from these solutions. PBLG can easily be denatured to form random coils by addition of trifluoroacetic acid (TFA) and a reduction in temperature. Figure C.7 shows the steady-state spectra, pump-probe spectra, and time-domain traces for helical and random coil PBLG in chloroform. The important feature of this data is that the helical pump-probe data exhibit two positive peaks and the random coil pump-probe data show only one positive peak. For an isolated oscillator, a pump-probe spectrum displays two peaks: (1) a negative peak at the fundamental frequency that corresponds with ground state bleach and stimulated emission between $\nu = 0,1$, and (2) a redshifted positive peak to corresponds with excited state absorption, $\nu = 2 \leftarrow 1$. The PBLG random coil spectrum clear shows this characteristic behavior while the PBLG helical

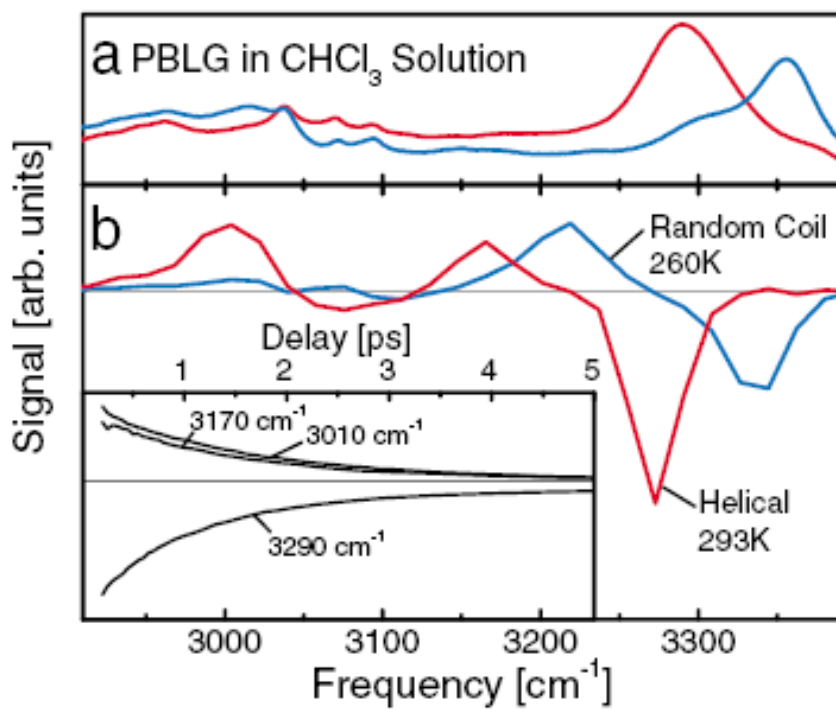


Figure C.7 (a) Absorption spectra of PBLG in chloroform with 3% TFA at 293 K (red line, helical conformation), and at 260 K (blue line, random coil). (b) Pump-probe spectra 600 fs after excitation under the same conditions. Inset: Decay of negative and both positive bands at 293 K.¹

spectrum presents a very different situation.

A variety of experiments were conducted on the PBLG helical system which resulted in the conclusion that the double peak structure originates solely from the NH stretch band and it is coupled to the periodic structure of the α -helix. Thus, Hamm and coworkers used TVBS theory to describe the helical PBLG transient IR spectrum. The pump-probe signal is described in terms of transitions between the four excited states/ground state as depicted in Figure C.1. The pump pulse bleaches the ground state transferring population to the single-vibron state. The probe pulse can either stimulate emission from the single-vibron state back to the ground state or be absorbed by single-vibron population to another excited state (TVFS, TVBS-I, TVBS-II) resulting in a negative signal or positive, respectively. With these possibilities in mind the transient spectrum of helical PBLG can be assigned easily. The positive peaks at 3006 cm^{-1} and 3160 cm^{-1} correspond to excited state absorption from the single-vibron state to TVBS-I and TVBS-II, respectively. The negative peak at 3290 cm^{-1} corresponds to the sum of stimulated emission from the single-vibron state to the ground state (negative signal) and excited state absorption from the single-vibron state to TVFS (positive signal). Hamm and coworkers successfully reproduced the helical PBLG transient absorption spectrum based on the TVBS theory in Ref. ^{6,7}.

C.3 Proposed Research

Reports in the literature show that Davydov's vibrational solitons do indeed exist and that the α -helices can support soliton formation at biological relevant

temperatures.^{1,10-14} This work provides a wealth of information about the nature of the vibrational soliton, but it provides only evidence of soliton existence and no measure of its ability to transfer energy, i.e. to propagate. Thus I propose a method that will probe the formation and propagation of the vibrational soliton in a α -helix system.

Previous studies of vibrational solitons have excited IR transitions directly which limits the study of soliton formation and propagation dynamics in a fundamental way. Direct IR excitation/probing generate signal contributions from random positions along the α -helix making it impossible to distinguish location. Therefore, it inherently provides no way of tracking soliton propagation and formation on the helix. To observe vibrational soliton propagation and formation, energy needs to be introduced into the system via an indirect, directional mechanism. To accomplish this, I propose a model α -helix system with three features: (i) a tethered chromophore at one end of the helix, (ii) isotopic ($^{13}\text{C}^{18}\text{O}$) labeling at the other end (terminal peptide) of the helix, and (iii) a variable number of peptide units in the helical chain. Figure C.8 shows a schematic representation of the model α -helix system indicating the chromophore, variable chain length, and isotopic labeling. The chromophore will allow energy to be directionally injected into the helix and subsequently the formation and propagation of the soliton at the NH stretching frequency. Two spectroscopic methods will measure the soliton dynamics. Pump-probe experiments at the chromophore excitation energy and vibrational soliton mode energy, respectively, will track the dynamics of the soliton formation. Isotopic labeling at the terminal peptide will shift the energy of the mode

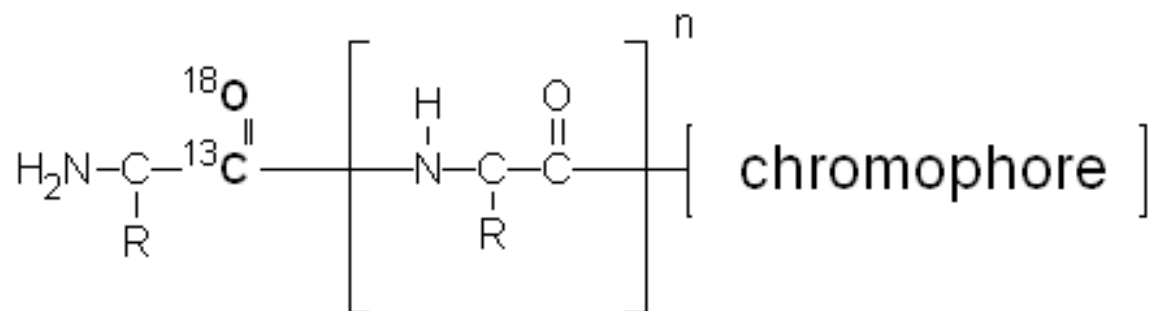


Figure C.8 Proposed model α -helix system. The chromophore is tethered to a variable length α -helix chain. The terminal peptide unit is labeled with $^{13}\text{C}^{18}\text{O}$.

and yield an isolated, local vibrational mode. When the soliton mode resides on the terminal peptide unit, coupling between the soliton mode and the local mode will be probed via dual-frequency two-dimensional infrared (DF-2DIR) spectroscopy. The specifics of these proposed methods will be discussed in detail in the following sections.

C.4 Research Methods

In the following sections I will outline the specific methods that will measure vibrational soliton formation and propagation dynamics in α -helices. Section C.3.a describes the pump-probe experiments used to characterize soliton formation. Section C.3.b discusses soliton propagation characterization utilizing DF-2DIR spectroscopy.

C.3.a Characterization of soliton formation

The IR pump-probe study on PBLG by Hamm and coworkers shows very clearly that population in vibrational soliton states at the NH stretching frequency can easily be probed. Circumventing the problem of defining location on the helix with my model α -helix, I propose pump-probe experiments identical to Hamm and coworkers' albeit with pumping at the chromophore excitation frequency rather than the NH stretch directly. This gives the ability to selectively introduce energy into one end of the helix without random IR excitation along the helix. Excess energy upon electronic excitation of a chromophore is partitioned rapidly (0.1 – 10 picoseconds) through intramolecular vibrational redistribution (IVR)¹⁵. With the selection of a proper chromophore and excitation conditions, electronic excitation will lead to vibrational excitation on the first peptide unit of the α -helix. With excitation of the peptide NH stretch, the formation of

the soliton follows. Following electronic excitation of the chromophore, a variably delayed IR probe pulse will measure transient population growth into the soliton mode.

Pump-probe experiments of this type measure population changes by comparing the time-dependent intensity of the probe pulse (signal) with the steady-state probe pulse intensity (reference) through the following relation,

$$\Delta A(\nu, t) = -\log\left(\frac{I_{sig}(\nu, t)}{I_{ref}(\nu)}\right) \quad (\text{C.5})$$

where ΔA is the time-dependent (transient) absorption signal which is proportional to transient population changes via Beer's law. For each time delay selected between the pump and probe pulse, a transient spectrum is recorded. Figure C.9 shows simulated pump-probe data in the NH stretching region (2900 - 3400 cm^{-1}).

This simulation is based on approximate peak widths and peak positions found in helical PBLG pump-probe data. It assumes single Gaussian peaks where the negative peak (blue) is the free NH stretch and the positive peaks (red) are the soliton peaks. This data illustrates the following expected dynamics: (i) the initial negative rise in the free NH stretch peak corresponds to population growth into the free NH stretch via IVR ($\tau_{IVR} = 0.5$ ps) which is followed by (ii) partial population transfer into the soliton states ($\tau_{sol} = 1.0$ ps), and finally (iii) the overall signal decays with the vibrational lifetime of the free NH stretch ($\tau_{vib} = 5$ ps). These dynamic represent the simplest case scenario where the dynamics are single exponentials and equal population is transferred to both the soliton states. Single exponential dynamics are a reasonable assumption but the dynamics are likely to be more complicated. First, the simulated data assumes equal

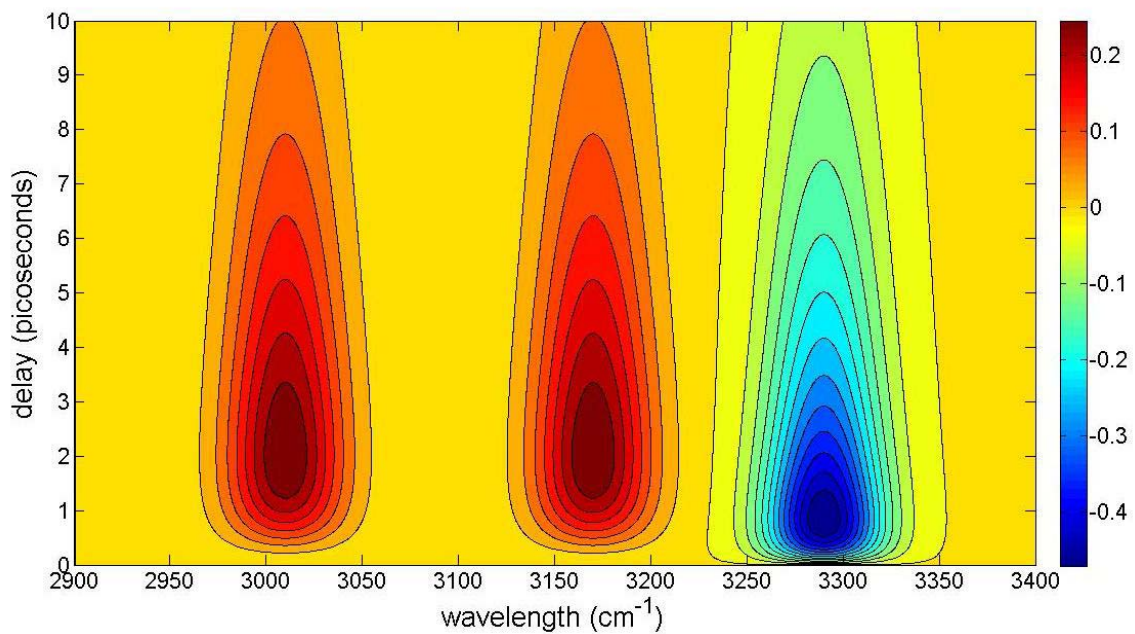


Figure C.9 Simulated pump-probe data based on helical PBLG IR pump-probe data. The two positive (red) peaks correspond to soliton states (TVBS-I, 3160 cm^{-1} ; TVBS-II, 3010 cm^{-1}) and the negative peak (blue) corresponds to the free NH stretch (3290 cm^{-1}).

population transfer into both the soliton peaks, but it is more likely population will transfer first to the TVBS-I soliton state (localization on one peptide unit, 3160 cm^{-1}) before transferring to the into the TVBS-II state (localization on two peptide units, 3010 cm^{-1}). Second, this simulation displays equal lifetime decay of the free state population and the soliton states population but the self-stabilizing nature of solitons suggest that the soliton lifetime should be longer than the free state lifetime resulting in a slower decay for the soliton states. This added complexity is precisely what the research outlined in this proposal aims to unravel. Analysis of experimental pump-probe data will yield new insight to the nature of vibrational soliton formation in α -helical systems.

C.4.b Characterization of soliton propagation

The second goal of the research in this proposal is to address the ability of vibrational solitons to transport energy along α -helices. As with the previously outline experiments, it is imperative that there is no direct excitation at the NH stretch aside from probing purposes. This can be achieved by measuring vibrational mode coupling with dual-frequency two-dimensional infrared (DF-2DIR) spectroscopy. DF-2DIR probes ultrafast dynamics via vibrational mode coupling between modes at different frequencies and has been used to probe both intramolecular and intermolecular vibrational dynamics.¹⁶⁻¹⁹ There are two prerequisites for this approach to yield information about vibrational soliton propagation dynamics: the coupling must probe a vibrational mode that is *spectrally* and *spatially* distinguishable. Isotopic labeling with $^{13}\text{C}^{18}\text{O}$ satisfies both of these conditions and has been used to probe site-specific

dynamics in peptides.²⁰ $^{13}\text{C}^{18}\text{O}$ labeling shifts the CO stretching frequency 60 cm^{-1} to lower energy isolating it from the normal amide-I mode. Figure C.10 illustrates this spectral shift. DF-2DIR spectra will only exhibit coupling between the NH soliton modes and the $^{13}\text{C}^{18}\text{O}$ mode when the soliton resides on the terminal peptide unit. Thus excitation of the chromophore followed by DF-2DIR probing will give a vibrational soliton propagation time.

DF-2DIR is a sophisticated example of photon echo spectroscopy which is analogous to spin echo spectroscopy in nuclear magnetic resonance (NMR) experiments. In photon echo spectroscopy, three coherent light pulses interact resonantly with a sample to generate a fourth (echo) pulse (i.e. transient four-wave mixing). Photon echoes are sensitive measures of both structure and dynamics through environmentally induced fluctuations in transition frequencies.^{21,22} Relative delay between the three excitation pulses yields a time-dependent echo signal. DF-2DIR spectroscopy modifies the basic photon echo experiment in two ways: First, 2DIR echo signals are heterodyne detected with an additional, local oscillator (LO) pulse which provides more detailed information about the echo pulse and consequently sample dynamics. Second, the third excitation pulse and the LO pulse which are spectrally degenerate with the first two excitation pulses are spectrally shifted to probe a different transition. Figure C.11 shows a schematic representation of the 2DIR pulse sequence with the relevant time intervals. 2DIR spectra are generated from raw 2DIR data by Fourier transformation over τ and t ,

$$S(\omega_\tau, T, \omega_t) = \mathcal{F}\{S(\tau, T, t)\}. \quad (\text{C.6})$$

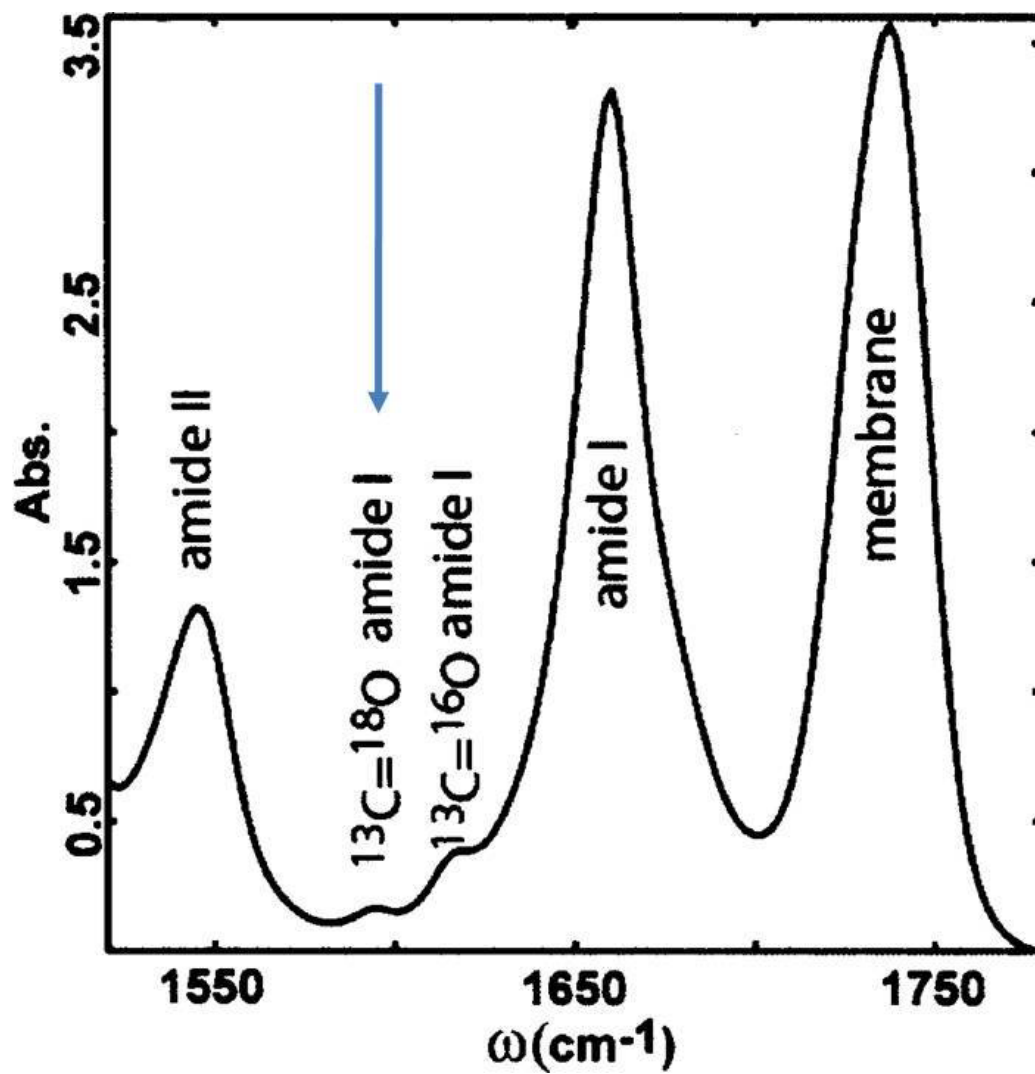


Figure C.10. $^{13}\text{C}^{18}\text{O}$ amide-I isotopic shift. The arrow indicates the 60 cm^{-1} redshifted mode at 1595 cm^{-1} .²⁰

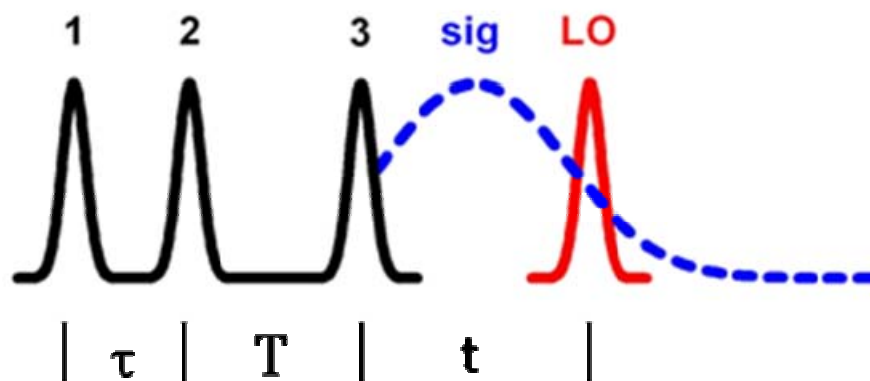


Figure C.11 2DIR pulse sequence. 1, 2, and 3 are the excitation pulses. sig (blue) is the echo signal, and LO (red) is the local oscillator pulse. τ , T , and t are the relative time delays between pulses 1,2; pulses 2,3; and pulses 3,LO respectively.

A 2DIR spectrum reflects the dynamics that have occurred over the time interval T which is known as the population period.

In 2DIR spectra, the peaks along the diagonal correlate approximately with the static absorption spectrum of the sample and off-diagonal or cross peaks indicate coupling between these absorption features. This coupling is strongly distance-dependent as it is a dipole-dipole interaction which falls off with $1/r^6$ where r is the distance between the dipoles. Therefore, 2DIR spectra will exhibit coupling peaks between modes only when two modes are sufficiently close to one another spatially. This provides a convenient method to probe vibrational soliton propagation dynamics along the α -helix; cross peaks will only occur between the soliton modes and the $^{13}\text{C}^{18}\text{O}$ labeled mode when they reside on the same or adjacent peptide units. Figure C.12 shows a simulated DF-2DIR spectrum.

This qualitative simulation is based on soliton and free NH stretch peak widths and positions from PBLG pump-probe data and the $^{13}\text{C}^{18}\text{O}$ amide-I peak position in Ref. 20. This spectrum illustrates coupling between the soliton modes (3160 cm^{-1} , 3010 cm^{-1}) and the $^{13}\text{C}^{18}\text{O}$ amide-I mode (1595 cm^{-1}) through the off-diagonal peaks. Thus this represents a situation where the delay between the second and third pulses in the experiment (population period, T) is sufficiently long for the soliton to propagate along the α -helix to the terminal, labeled peptide unit. Propagation dynamics can be extracted from the 2DIR spectrum by measuring the integrated signal intensity of a particular off-diagonal peak which gives the relative coupling between the two coupled modes. Measuring the coupling between the soliton modes and $^{13}\text{C}^{18}\text{O}$ amide-I mode as

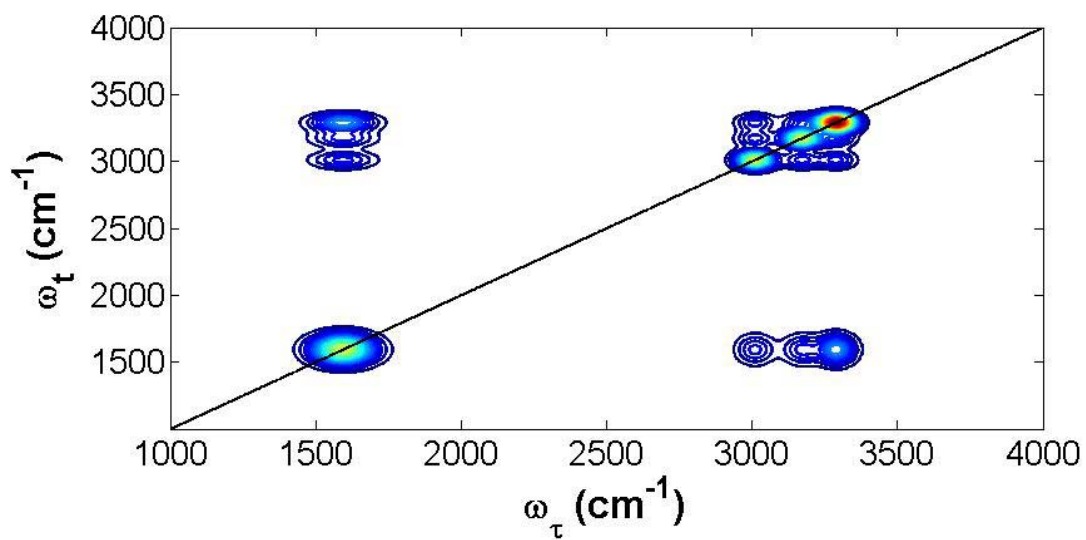


Figure C.12 Simulated DF-2DIR spectrum. The ¹³C¹⁸O labeled mode at 1595 cm⁻¹ exhibits coupling with both the free NH stretch at 3290 cm⁻¹ and the soliton modes at 3160 cm⁻¹ and 3010 cm⁻¹.

a function of the population period will yield a propagation time for a given α -helix chain length. Finally, systematic variation of the chain length will give a more complete picture of how soliton propagation dynamics depend on the helical length. In the simplest case, off-diagonal coupling will show only one characteristic propagation time for a given chain length and the propagation time will depend linearly on the α -helix chain length. Again, in actuality the propagation dynamics may be more complicated and this is precisely what the DF-2DIR studies aim to uncover. Analysis of this DF-2DIR data will provide a wealth of information about vibrational soliton propagation dynamics in α -helices.

References and Notes

- (1) J. Edler, R. P., V. Pouthier, C. Falvo, and P. Hamm *Physical Review Letters* **2004**, *93*, 106405.
- (2) Davydov, A. S. *Journal of Theoretical Biology* **1973**, *38*, 559.
- (3) Davydov, A. S. *Journal of Theoretical Biology* **1977**, *66*, 379.
- (4) Campbell, N. A. *Biology*; 3 ed.; The Benjamin/Cummings Publishing Company, Inc.: Redwood City, CA, 1993.
- (5) Scott, A. *Physics Reports* **1992**, *217*, 1.
- (6) Pouthier, V. *Physical Review E* **2003**, *68*, 021909.
- (7) Falvo, V. P. a. C. *Physical Review E* **2004**, *69*, 041906.
- (8) Cruzeiro-Hansson, L. *Physical Review Letters* **1994**, *73*, 2927.
- (9) Tatulian, L. K. T. a. S. A. *Quarterly Review of Biophysics* **1997**, *30*, 365.

- (10) G. Careri, U. B., F. Carta, E. Gratton, and A. C. Scott *Physical Review Letters* **1983**, *51*, 304.
- (11) G. Careri, U. B., F. Galluzzi, A. C. Scott, E. GRatton and E. Shyamsunder *Physical Review B* **1984**, *30*, 4689.
- (12) A. C. Scott, E. G. E. S., and G. Careri *Physical Review B* **1985**, *32*, 5551.
- (13) V. Helenius, J. K.-T., S. KOTila, J. Nieminen, R. Lohikoski, J. Timonen *Chemical Physics Letters* **1997**, *208*, 325.
- (14) J. Edler, P. H., and A. C. Scott *Physical Review Letters* **2002**, *88*, 067403.
- (15) McHale, J. *Molecular Spectroscopy*; First ed., 1999.
- (16) I. V. Rubtsov, J. W., and R. M. Hochstrasser *Journal of Chemical Physics* **2003**, *118*, 7733.
- (17) I. V. Rubtsov, K. K., and R. M. Hochstrasser *Chemical Physics Letters* **2005**, *402*, 439.
- (18) Dmitry V. Kurochkin, S. R. G. N., and Igor V. Rubtsov *Journal of Physical Chemistry A* **2005**, *109*, 10799.
- (19) Sri Ram G. Naraharisetty, D. V. K., Igor V. Rubstov *Chemical Physics Letters* **2007**, *437*, 262.
- (20) Prabuddha Mukherjee, A. T. K., Eric C. Fulmer, Itamar Kass, Isaiah T. Arkin, and Martin T. Zanni *Journal of Chemical Physics* **2004**, *120*, 10215.
- (21) Mukamel, S. *Principles of Nonlinear Optical Spectroscopy*; Oxford University Press, Inc.: New York, New York, 1995.

(22) Shen, Y. R. *Principles of Nonlinear Optics*; John Wiley & Sons, Inc.: New York, New York, 1984.